UNIVERSITI TEKNOLOGI MARA

BOUNDARY LAYER FLOW AND HEAT TRANSFER CHARACTERISTICS OF DUSTY HYBRID NANOFLUID OVER MULTI-ORIENTED SURFACES WITH VISCOUS DISSIPATION EFFECT

DHIA AZEEM BINTI KHAIRIL ANWAR

MSc

June 2026

UNIVERSITI TEKNOLOGI MARA

BOUNDARY LAYER FLOW AND HEAT TRANSFER CHARACTERISTICS OF DUSTY HYBRID NANOFLUID OVER MULTI-ORIENTED SURFACES WITH VISCOUS DISSIPATION EFFECT

DHIA AZEEM BINTI KHAIRIL ANWAR

Thesis submitted in fullfillment
of the requirements for the degree of
Master of Science
(Mathematics)

Faculty of Computer and Mathematical Sciences

June 2026

CONFIRMATION BY PANEL OF EXAMINERS

I certify that a Panel of Examiners has met on 9 June 2026 to conduct the final examination of Dhia Azeem binti Khairil Anwar on her Master of Science (Mathematics) thesis entitled "Boundary layer flow and heat transfer characteristics of dusty hybrid nanofluid over multi-oriented surfaces with viscous dissipation effect" in accordance with Universiti Teknologi MARA Act 1976 (Akta 173). The Panel of Examiners recommends that the student be awarded the relevant degree. The Panel of Examiners was as follows:

Fariza Hanis Abdul Razak
Associate Professor
Faculty of Computer and Mathematical Sciences
Universiti Teknologi MARA
(Chairman)

Noor Amalina Nisa Ariffin
Senior Lecturer
Faculty of Computer and Mathematical Sciences
Universiti Teknologi MARA
(Internal Examiner)

Norfifah Bachok @ Lati
Associate Professor
Faculty of Science
Universiti Putra Malaysia
(External Examiner)

PROFESSOR DR HJH ZURAEDA IBRAHIM
Dean
Institute of Postgraduates Studies
Universiti Teknologi MARA
Date: 9 June 2026

AUTHOR'S DECLARATION

I declare that the work in this thesis was carried out in accordance with the regulations of Universiti Teknologi MARA. It is original and is the results of my own work, unless otherwise indicated or acknowledged as referenced work. This thesis has not been submitted to any other academic institution or non-academic institution for any degree or qualification.

I, hereby, acknowledge that I have been supplied with the Academic Rules and Regulations for Posgraduate, Universiti Teknologi MARA, regulating the conduct of my study and research.

Name of Student	:	Dhia Azeem binti Khairil Anwar
Student I.D. No.	:	2023709125
Programme	:	Master of Science Mathematics - CS752
Faculty	:	Faculty of Computer and Mathematical Sciences
Thesis Title	:	Boundary layer flow and heat transfer characteristics of dusty hybrid nanofluid over multi-oriented surfaces with viscous dissipation effect
Signature of Student	:	....
Date	:	June 2026

ABSTRACT

Enhancing heat transfer efficiency is crucial for the development of energy and thermal management technologies to develop high-performance systems such as advanced cooling devices, energy-efficient engines, and sustainable power generation units. Previous studies show that using a hybrid nanofluid can improve the heat transfer performance; however, the inclusion of dust particles provides a more realistic and relevant illustration for the flow and heat transfer models, as it constantly influences fluid dynamics. In addition, most studies focus on hybrid nanofluid models, with limited attention given to the combined dusty and hybrid nanofluid with the effects of viscous dissipation and slip conditions. Thus, this research aims to numerically analyse the flow and heat transfer characteristics of a dusty hybrid nanofluid over a multi-oriented stretching/shrinking surface, with the effects of viscous dissipation and slip conditions. The surfaces considered include horizontal, inclined, and vertical orientations, with alumina and copper nanoparticles used as hybrid components. Firstly, the governing equations are formulated according to the problem considered using Tiwari and Das model and are simplified to the boundary layer equations by implementing the boundary layer approximation. Then, the resulting equations are transformed into ordinary differential equations using a similarity transformation by introducing appropriate similarity variables. The transformed ordinary differential equations are solved numerically using the bvp4c function in MATLAB. The influence of pertinent parameters such as dust particle mass concentration, viscous dissipation, inclination angle, nanoparticle volume fraction, mixed convection, velocity slip, thermal slip, stretching/shrinking, and suction parameters is systematically analysed. The results indicate that dual solutions exist for certain ranges of suction and stretching/shrinking parameters. In addition, augmenting certain parameter values, such as dust particle mass concentration, mixed convection parameter, slip conditions, velocity slips, and copper nanoparticle volume fraction contributes to delaying the boundary layer separation. Furthermore, increasing the values of dust particle mass concentrations significantly elevates the skin friction coefficient and diminishes the heat transfer rate at the surface. The consideration of viscous dissipation, represented by the Eckert number, leads to a reduction in the heat transfer rate at the surface, which also depends on the flow configuration and orientation. Additionally, the extensive analysis indicates that horizontal surfaces exhibit the highest rate of heat transfer, followed by inclined and vertical surfaces. Besides that, copper nanoparticles show higher efficiency in comparison to alumina nanoparticles. Thus, the comparative analysis across the three surface orientations highlights the unique contributions of viscous dissipation, gravitational forces, and buoyancy on flow and heat transfer. The findings provide significant insights into engineering and industrial processes related to surface modification, heat exchangers, and hybrid nanofluid applications, where viscous dissipation, slip, and geometric configuration are the essential parameters in designing the devices.

ACKNOWLEDGEMENT

In the name of Allah, the Most Gracious, the Most Merciful.

Alhamdullilah, all praise is due to Allah S.W.T, who granted me the strength, patience, and guidance in completing this thesis and giving me the chance to continue my studies in this Master's Degree. Without His mercy and countless blessings, this journey would not have been possible. May peace and blessings be upon our beloved Prophet Muhammad SAW, whose life and teachings continue to inspire us towards knowledge, sincerity, and perseverance.

I would like to extend my heartfelt appreciation to my supervisor, Assoc. Prof. Dr. Nor Azizah Binti M. Yacob, for her time, continuous support, encouragement, and valuable insights throughout this journey and her guidance which helped me to stay focused and committed until the very end. I would also like to express my gratitude to my co-supervisor Dr. Nor Fadhilah binti Dzulkifli for her supervision and endless support. Not to forget, my sincere thanks to Dr. Mazura for her guidance and support in assisting me with LaTeX during the preparation of this thesis.

I am also sincerely thankful to the faculty and staff of Universiti Teknologi MARA (UiTM) Shah Alam and Pahang, Kampus Jengka for their hard work in managing and facilitating the postgraduate students and not to forget the Ministry of Higher Education who funded the Fundamental Research Grant Scheme (FRGS) grant for these three years of my studies.

Finally, and most importantly, I owe my deepest gratitude to my beloved family, especially, Mummy, Daddy, Mak, Abah, Dania, Putera, Dinie and Darwisya for your endless love, support, and Duas. Thank you for being there and having faith in me, May Allah SWT reward them abundantly in this life and also Hereafter. Last but not least, special thanks to Farah Hazwani, Aiman, and all the ones who had contributed either directly or indirectly, thank you for always being a cheerleader, cheering and supporting me every now and then. Thank you for being part of this chapter of my life.

May this work be accepted as a small contribution to the pursuit of beneficial knowledge, and may it serve as a means of barakah and khayr. Inshaallah.

TABLE OF CONTENTS

LIST OF TABLES

LIST OF FIGURES

LIST OF SYMBOLS

Symbols	
α	Inclination Angle
β_v	Velocity Fluid-Particle Interaction Parameters
β_T	Temperature Fluid-Particle Interaction Parameters
β^*	Volumetric Thermal Expansion Coefficient
δ	Boundary Layer Thickness
ϵ	Specific Heat Parameters Ratio
η	Similarity Variables
θ	Dimensionless Function
θ_p	Dimensionless Function of Dust Particles
λ	Stretching/Shrinking Surface Parameter
λ^*	Mixed Convection Parameter
μ	Dynamic Viscosity
ν	Kinematic Viscosity
ρ	Density
σ_1	Velocity Slip Parameter
σ_2	Thermal Slip Parameter
τ_v	Relaxation Time
τ_T	Thermal Equilibrium Time of Dust Particle
τ_w	Surface Shear Stress
ϕ_1	Alumina Nanoparticle Volume Fraction
ϕ_2	Copper Nanoparticle Volume Fraction
ψ	Stream Function

Subscripts

c	Critical Value
f	Fluid
nf	Nanofluid
hnf	Hybrid Nanofluid
p	Dust Particles
w	Wall
∞	Ambient Condition
1	Alumina Nanoparticle
2	Copper Nanoparticle

Superscripts

$'$	Differentiation with Respect to η

LIST OF NOMENCLATURES

Nomenclatures

A, a, b	Positive Constant
C_f	Skin Friction Coefficient
C_{mf}	Specific Heat of Dust Particles
C_{pf}	Specific Heat of Nanofluids
ρC_p	Specific Heat Capacity
Ec, Ec*	Eckert Number
f	Dimensionless Function
g	Gravity
k	Thermal Conductivity
K	Stokes Drag Coefficient
l	Characteristics Length
L	Dust Particle Mass Concentration
L_s	Velocity Slip Lengths
L_T	Thermal Slip Lengths
m	Dust Particle Mass
N	Dust Particle Number
Nu_x	Local Nusselt Number
p	Pressure
Pr	Prandtl Number
q_w	Surface Heat Flux
Re_x	Local Reynolds Number
s	Suction/ Injection
T	Temperature for Hybrid Nanofluid Phase
T_p	Temperature for Dust Phase
T_w	Wall Temperature
T_∞	Ambient Temperature

u, v	Hybrid Nanofluid Phase Velocity Component in the $x-$ and $y-$ Directions
u_p, v_p	Dust Phase Velocity Component in the $x-$ and $y-$ Directions
U_w	Surface Velocity
U_∞	Free Stream Velocity
v_w	Surface Mass Transfer Velocity
x, y	Constant Coordinates

CHAPTER 1
INTRODUCTION

1.1 Research Background

Fluid flow and heat transfer within the boundary layer are crucial in numerous engineering, industrial, and biomedical applications, particularly those involving thermal systems such as heat exchangers, power generation, electronic cooling, and the development and design of artificial organs. Thus, understanding fluid flow and heat transfer characteristics is essential for ensuring operational stability, reliability, effectiveness, and safety of the heat transfer based engineering devices and systems. Furthermore, the process of heat transfer within the boundary layer is important as it directly reflects the effectiveness of thermal systems.

To enhance heat transfer performance, an advanced working fluid known as nanofluids, consisting of a low thermal conductivity base fluid embedded with nanosized particles, was developed (Izady et al., 2021. Subsequently, to further improve the heat transfer performance, hybrid nanofluids that combine two types of nanoparticles were also introduced (Azman et al., 2021. Hybrid nanofluids demonstrate greater efficiency and heat transfer performance in comparison to nanofluids, which is said to be important in thermal storage, solar heating, refrigeration, lubrication, and so forth. (Hussain et al., 2022. In recent years, dusty hybrid nanofluids have emerged, incorporating both hybrid nanoparticles and suspended dust particles, offering further augmentation in heat transfer properties (Nabwey and Mahdy, 2021. The combination of fluid and dust particles greatly impacts the velocity and temperature distribution within the boundary layer. The boundary layer theory provides a fundamental framework for modelling transport problems in practical applications by simplifying the Navier–Stokes equations within the thin boundary layer adjacent to a solid surface.

Therefore, in this study, the boundary layer flow and heat transfer of a dusty hybrid nanofluid over a stretching or shrinking surface are explored. Stretching and shrinking surfaces represent the predominant type of surfaces examined in the analysis of boundary layer flow and heat transfer. It is extensively utilised in the production of glass fiber, polymer sheet drawing, and various extrusion processes. Previous studies indicate that the stretching surface usually develops stable solutions; however, the shrinking surface results in dual solutions under the same boundary conditions (Yashkun et al., 2020). Furthermore, surface permeability, characterized by suction and injection, significantly influences the boundary layer behavior and is often examined in the majority of studies conducted. Suction facilitates flow stabilisation and delays boundary layer separation, whereas injection has the contrary effect.

Moreover, the classical no-slip boundary conditions are no longer applicable in these contemporary technological contexts, revealing the occurrence of slip conditions, specifically velocity and thermal slip, which, when accounted for, diminish interactions and modifies the temperature distribution between the fluid and the surface. In addition, taking into account the effect of viscous dissipation, indicated by the Eckert number (Ec), is important, especially in conditions involving high-speed or high-viscosity flows, as it transforms kinetic energy to thermal energy due to fluid friction (Farooq et al., 2018). This phenomenon leads to a rise in fluid temperature, consequently influencing the heat transfer rate.

Therefore, understanding the interactions and influences of physical parameters is important, as their consideration impacts flow and heat transfer characteristics. Additionally, developing precise mathematical models and performing comprehensive analysis enhanced theoretical fluid mechanics and develop significant findings for the optimization of thermal management and industrial processes. This research advances knowledge in enhancing thermal systems, minimizing energy consumption, and facilitating the progression of advanced technologies across diverse industries in the future.

1.1.1 Boundary Layer Theory

Boundary layer is a thin layer that develops adjacent to the wall surface as the fluid flows, caused by frictional forces and no-slip conditions. In 1904, Ludwig Prandtl was the first who proposed the boundary layer theory which reduces the mathematical complexity of the Navier-Stokes equation describing the fluid dynamics. Since then, boundary layer theory has been a prominent subject in fluid dynamics, recognized for its significant role in elucidating the characteristics of fluid flow near solid surfaces. Furthermore, as stated by Schlichting (1979), the frictional forces within this thin layer are significant, whereas those outside of it are negligible. Additionally, to this extent, researchers implement boundary layer theory to solve convective heat transfer problems, as it allows a more efficient understanding of fluid flow and heat transfer characteristics across surfaces.

1.1.2 Heat Transfer

Heat transfer refers to the motion of energy from one point to another, driven by temperature differences. The energy typically transmits from a region of higher temperature to one of lower temperature and stops once equilibrium is achieved (Jia, 2020). There are three heat transfer modes: conduction, convection, and radiation. Conduction is a process in which heat is transmitted from a higher temperature region to a lower temperature through a solid or stationary fluid, occurring via physical contact without the involvement of mixing and mass flow. The convection process occurs when fluid interacts with a solid surface and a moving fluid. This process usually occurs on a very thin surface before combining, while, radiation is the phenomenon that occurs through a vacuum or any transparent medium, including solids or liquids. The physical model of heat transfer modes can be seen in Figure 1.1.

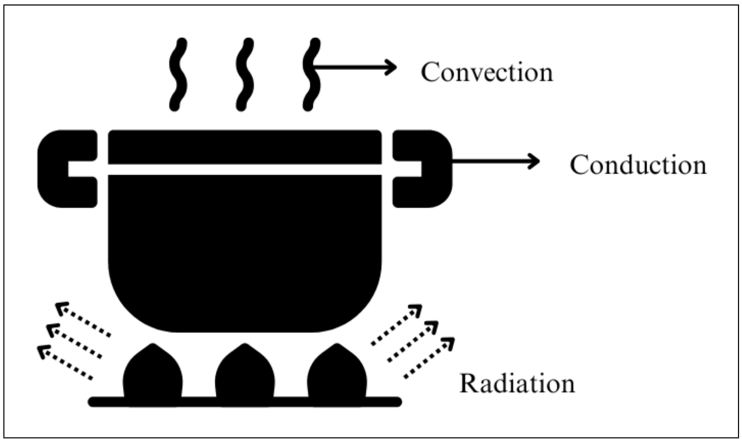

Figure 1.1 Physical Model of Heat Transfer Modes

Given that boundary layer theory is generally applied in understanding and solving convective heat transfer, as previously mentioned, convection will be explored in greater detail. Convection is categorized into three different types, which are forced, free or natural, and mixed convection. Forced convection transpires when fluid movement over a surface is driven by an external source, such as pumps or fans. Free or natural convection occurs when fluid movement is induced by buoyancy, resulting from variations in fluid density owing to temperature gradients, rather than by an external force. In contrast, mixed convection involves both forced and free convection, leading to the occurrence of heat transmission where buoyancy greatly impacts the fluid flow and the pressure gradient differs with the depth of the layers (Deswita et al., 2010). The physical model of convection variations are shown in Figure 1.2. Furthermore, mixed convection flows occur throughout multiple transport processes, whether it happens in natural phenomena or even in engineering or technological applications such as heat exchanges, nuclear reactors, electronic devices. (Farooq et al., 2022).

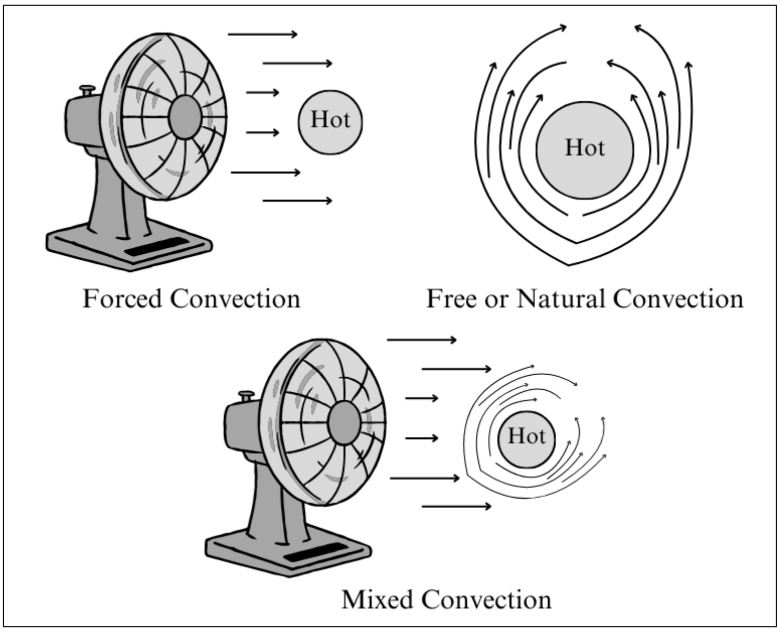

Figure 1.2 Physical Model of Convection Variations

1.1.3 Hybrid Nanofluids

Throughout the years, the application of nanotechnology has been extensively utilized, resulting in increased energy efficiency, improved material qualities, and numerous other developments. Thus, the development of nanotechnology-based heat transfer fluids known as nanofluids gained massive attention among researchers because it leads to higher thermal conductivity and plays a vital role, especially in the engineering field (Nabwey and Mahdy, 2021). Nano itself means diminutive or at a microscopic level. Thus, nanofluids are classified as a group of base fluids that consist of nano-sized particles (1-100 nm) (Farooq et al., 2022). Nanofluids were said to be more effective in heat transfer than traditional fluids such as water, oil, and gasoline, giving them higher thermal conductivity (Kakar et al., 2022). To all knowledge, nanofluids were first proposed by Choi (1995), and most of the traditional heat transfer methods in the industry have been switched to nanofluids, such as in energy conversion, heat exchangers, and cooling systems (Hussain et al., 2022). Nanofluids are developed by dispersing nanoparticles into traditional heat transfer fluids such as water, ethylene glycol, toluene, and engine oil, and the nanoparticles are made of metals, oxides, carbides, nitrides, or nonmetals (Sudarsana Reddy and Chamkha, 2018). The advantages of utilizing nanoparticles include an increased surface area that enhances heat transfer between particles and fluids, improved stability, helps decrease pumping power due to pressure drop, reduced clogging. (Saidur et al., 2011). Adding to that, various models are developed to numerically analyse thermal conductivity and heat transfer rates in the fluid dynamics of nanofluids. The two most commonly utilized models are the Tiwari-Das model and the Buongiorno model, which are also known as the single-phase and two-phase models, respectively (Rossi di Schio et al., 2022). Tiwari-Das model considers the impact of nanoparticles volume fraction on flow characteristics, whereas the Buongiorno model takes into account Brownian motion and thermophoresis mechanism effects in the laminar flow of fluids (Waini et al., 2020).

In the time after, the utilization of nanofluids as a heat transfer medium has become predominant, leading to continuous advancements due to daily innovations, particularly in the fields of science and technology. Hence, an innovative advancement has emerged, namely, hybrid nanofluids. Hybrid nanofluid is said to be more effective as it is more advanced in chemical and thermal characteristics (Hussain et al., 2022). It is made up of two or more nanoparticles suspended in a base fluid. Hybrid nanofluids are used in many distinct fields, especially related to heat transmission technologies, which include mechanical heating elements, plate heat generators, and cylindrical heat generators (Waqas et al., 2021). Copper (Cu) and alumina (Al_2O_3) are employed in this study due to their widespread use in the study of nanofluids. Notably, copper is chosen for its superior thermal conductivity, which optimized the heat transfer rates (Kumar, 2021).

1.1.4 Dusty Fluids

Incorporating milli- or micrometer-sized particles (dust particles) into base fluids known as dusty fluid, improves heat transfer properties (Nabwey and Mahdy, 2021). To the best of our knowledge, Saffman (1961) is the first who propose the boundary layer equations for laminar dusty fluid flow. Moreover, the dusty fluid, also known as the two-phase fluid flow has become significant in the engineering and industrial fields, and it is assumed that one phase is the fluid phase, whereas another is the dust phase. The cross section of dusty hybrid nanofluid is depicted in Figure 1.3. This study considers dusty fluids as they offer a more accurate representation, given that many practical fluid flows are not entirely clean and usually contain dust or solid particles. Additionally, the analysis of dust particles facilitates the investigation of particle-liquid interactions on heat transfer.

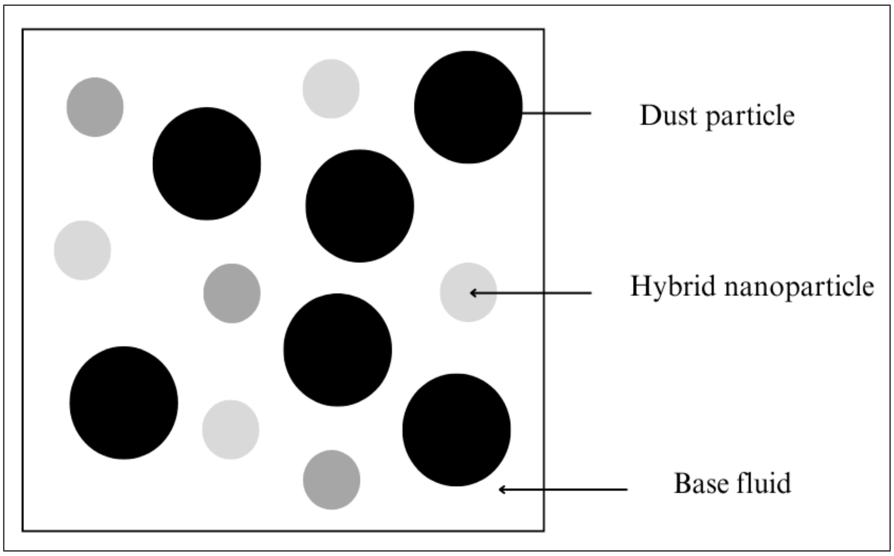

Figure 1.3 Cross Section of Dusty Hybrid Nanofluid

1.1.5 Stretching or Shrinking Surface

In the analysis of boundary layer flow and heat transfer, diverse kinds of surfaces may be explored, including flat plate surfaces, curved surfaces, stretching or shrinking, and rotating or oscillating surfaces. Each of these surfaces exhibits unique characteristics that influence the flow and heat transfer processes. However, in this study, we only focuses on two types of surfaces which are stretching and shrinking. A stretching surface refers to a continuously stretched where the velocity of the fluid flow along the surface increases, leading to the formation of a boundary layer. These kinds of surfaces have been extensively studied in heat and mass transfer fields due to their potential to improve transmission rates (Zhu et al., 2022). The initial discovery of boundary layer flow over a stretched sheet was conducted by Crane (1970). After the discovery, numerous studies have been performed on the stretching of sheets due to its utility for multiple industrial manufacturing operations such as plastic extrusion, wire drawing, metallic cooling processes, and so forth. Different from stretching surfaces, shrinking surfaces are considered unusual due to their contradictory nature, as they create a region that flows in the opposite direction along the surface and it was first discovered by Wang in 1990 (Uddin and Bhattacharyya, 2017). Controlled polymer compression, shrink wrapping, and industries such as aerodynamics and hydrodynamics, as well as biochemical technologies, are some of the sectors that practices shrinking surface. The physical model of stretching and shrinking surfaces are shown in Figure 1.4.

1.1.6 Dual Solutions

The occurrence of dual solutions refers to a condition in which a numerical analysis generates two distinct solutions under the same boundary conditions, both of which are valid. As previously mentioned, the unusual behavior of a shrinking surface results in the destabilization of the boundary layer, as it flows against the pressure gradient and this occurrence leads to the development of dual solutions. Numerous studies have demonstrated that when there are dual solutions, the first solution is typically stable and the second solution often unstable (Anuar et al., 2018; Dzulkifli et al., 2022; Yahaya et al., 2023; Jamrus et al., 2024; Shah et al., 2024). In addition, while shrinking surface and mixed convection parameter are the main causes for the occurrence of dual solutions, parameters such as suction, magnetic field, volume fraction of nanoparticles or dust particles significantly contribute to widening the range of dual solutions (Roy and Pop, 2021). Dual solutions in the

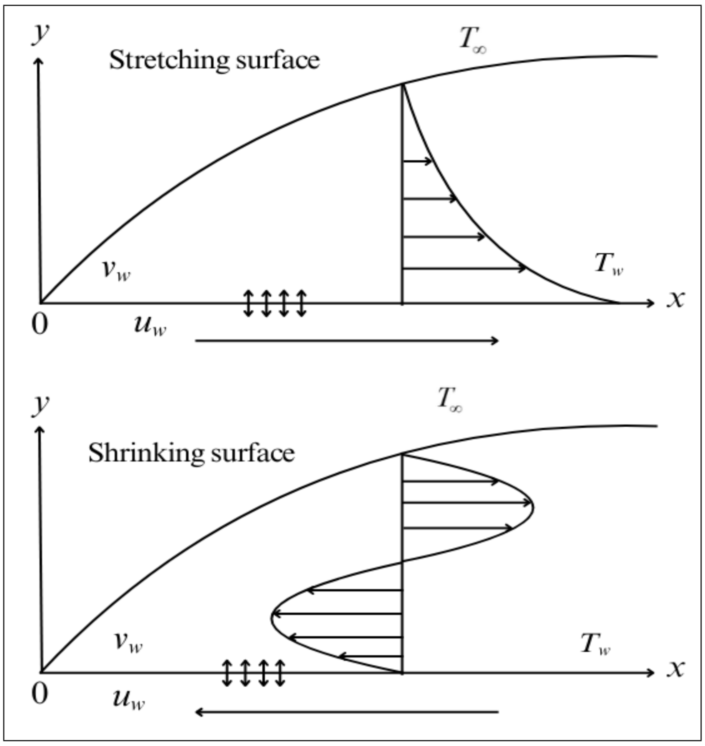

Figure 1.4 Physical Model of Stretching and Shrinking Surfaces

boundary layer are not confined to mathematical analysis, they also have significant implications in predicting the behavior of practical fluid flow and heat transfer system. Experimental studies usually highlight only the stable solution as an example of a real system, however, the unstable solution is important from the point of view of design, as it implies instability, flow separation, or even thermal inefficiency. For example, in the manufacturing industry, parameters such as shrinking surface, mixed convection parameter, suction, and magnetic field contribute to maintaining a stable system. These parameters are crucial for ensuring product quality consistency and improving energy and thermal efficiency.

1.1.7 Types of effects

1.1.7.1 Permeable Surface

It is necessary to acknowledge that in certain boundary layer flow, the surface are not entirely solid but rather porous. The porous media is characterized by its permeability, and it becomes apparent when it enables the motion of particles and fluid through it, in this context, it is either via suction or injection. Suction extracts reactants from the surface, thereby stabilizing the flow, whereas injection offers the contrary effect. Research on boundary layer flow involving suction or injection has been significantly highlighted. Not to mention, the fluid flow, skin friction coefficient, heat transmission rate can be markedly varied with the influence of suction. Additionally, it promotes delaying and eluding boundary layer separation (Kasmani et al., 2017. Adding to that, suction and injection have prompted interest in a wide range of applications, including chemical processing, electrical cooling, water purification, aerodynamics, and both environmental and biological applications.

1.1.7.2 Velocity and Thermal Slip Conditions

In the classical concept of fluid dynamics, the no-slip boundary condition signifies that the velocity of the fluid matches the fluid velocity near the boundary layer, resulting in no relative motion between. Nonetheless, with advances in technology, particularly in the field of nanotechnology, the no-slip condition becomes invalid due to the consideration of velocity and thermal slip conditions, and according to Anuar et al. (2021b), slip boundary conditions were often overlooked by many researchers. Nevertheless, researchers who consider slip condition claims that there were widespread applications for the nanofluids that exhibit boundary slip, including polishing, artificial heart valves, internal cavities, medication delivery systems, micro heat exchangers, and microelectronic cooling devices (Hussain et al., 2022). Slip condition denotes the presence of a velocity or temperature gradient between the fluid and the boundary surface. The presumed no-slip condition in the classical Navier-Stokes equations does not align with physical features, and slip may exist in between them (Wang, 2002). Velocity slip refers to the non-zero velocity present at the boundary layer where the fluid moves along the surface, whilst thermal slip is when there is a temperature difference between the fluid and the surface.

1.1.7.3 Viscous Dissipation

In addition, fluids exhibiting high viscosity are directly related to viscous dissipation, which plays a significant role in the context of energy transmission in boundary layer flow. Viscous dissipation is an irreversible phenomenon in a viscous fluid in which kinetic energy is transformed into thermal energy per unit mass due to the friction of the fluid. This fundamental phenomenon influences the temperature difference and fluid dynamics (Abbas et al., 2024) and is identified by the Ec number (Farooq et al., 2018). Thus, the Ec number will not be zero when viscous dissipation is considered (Desale and Pradhan, 2015). Moreover, viscous dissipation may assist the advancement of technologies that require heating within the fluid and the surface components, overcoming the need for external heating elements. The applications of viscous dissipation can be seen in the industry of polymer and food processing, microfluidics, oil recovery, lubrication of high-viscosity fluids, and heat exchangers.

1.2 Problem Statement

In numerous industrial and engineering applications, including cooling systems, polymer extrusion, and metal processing, understanding and improving the efficiency flow and heat transfer is crucial in order to develop advancement in this field. This is because the efficiency of majority equipment in the industry has improved due to the enhancement of heat transfer rate, since the equipment must rapidly and efficiently transmit heat from one region to another. The utilization of conventional heat transfer fluids such as water, oil, and ethylene glycol, is inefficient due to their relatively low thermal conductivity. Nanofluids were developed by incorporating nanosized particles into the base fluid to overcome the existing limitations. Subsequently, hybrid nanofluids has emerged as an advanced category of nanofluids, offering enhanced performance as heat transfer fluids.

Most existing studies neglects the existence of dust particles in fluids because in practical situations, fluids frequently contain particles such as dust, which can greatly affect flow behavior and thermal performance. This is particularly relevant in applications such as aerodynamics in dusty environments, spray coating, and transportation of fuel for combustion. Next, the consideration of viscous dissipation is also often overlooked, despite its significance in high velocity flows. Additionally, in practical fluid flows, viscous dissipation exists naturally and can influence temperature distribution. Therefore, neglecting viscous dissipation may result in an inaccurate prediction of temperature distribution and heat transfer rate. Besides that, slip conditions has became the subject of intensive study by many researchers due to its significance in heat transfer, which is caused by different fluid velocities near the boundary (Hussain et al., 2022). Hence, slip conditions should be taken into consideration in particular circumstances such as problems involving fluid flow across numerous surfaces, the polishing of mechanical heart valves, and others (Anuar et al., 2021b). In addition, the combined effects of dust particles, viscous dissipation and slip conditions on flow dynamics and thermal performance remain inadequately investigated.

To the best of our knowledge, limited studies have investigated the comparative characteristics of flow and heat transfer of dusty hybrid nanofluids towards horizontal, inclined, and vertical stretching or shrinking surface, particularly under the influence of viscous dissipation and slip conditions. This gap highlights a significant research opportunity. Consequently, examining the behavior of dusty nanofluids across various surface orientations with viscous dissipation and slip conditions effects has become essential, as these factors can notably alter the flow and thermal profiles, and able to determine the most effective orientation for heat transfer. Inspired by the works of Gireesha et al. (2015), Anuar et al. (2021b), Roy et al. (2022), and Ali et al. (2023), the present study aims to numerically analyse the behavior of dusty hybrid nanofluid over a multi-oriented stretching or shrinking surface, incorporating viscous dissipation, velocity, and thermal slip effects. This effort seeks to address the identified research gap and contribute to a deeper understanding of multiphase thermal fluid dynamics.

1.3 Research Questions

The research questions are:

i. How does the mathematical model of dusty hybrid nanofluid flow and heat transfer over a horizontal, inclined, or vertical stretching/shrinking surface with viscous dissipation and slip conditions are formulated?

ii. How does the mathematical model of dusty hybrid nanofluid flow and heat transfer over a horizontal, inclined, or vertical stretching/shrinking surface with viscous dissipation and slip conditions are solved?

iii. How do the dust particle mass concentration, viscous dissipation, inclined surface, nanoparticles volume fraction, stretching/shrinking parameter, mixed convection parameter, velocity, and thermal slip parameter affect the skin friction coefficient, heat transfer rate, velocity, and temperature profiles in boundary layer flow?

1.4 Research Objectives

The objectives of the research are:

i. To formulate the mathematical models of dusty hybrid nanofluid flow and heat transfer over a horizontal, inclined, or vertical stretching/shrinking surface with viscous dissipation and slip conditions using boundary layer approximation and similarity transformation.

ii. To solve the mathematical models of dusty hybrid nanofluid flow and heat transfer over a horizontal, inclined, or vertical stretching/shrinking surface with viscous dissipation and slip conditions by using bvp4c function in MATLAB.

iii. To analyse the effect of dust particle mass concentration, viscous dissipation, inclined surface, nanoparticles volume fraction, stretching/shrinking parameter, mixed convection parameter, velocity, and thermal slip parameter on skin friction coefficient, heat transfer rate, velocity, and temperature profiles in boundary layer flow.

1.5 Scope of Study

The scope of study is limited to analysing the effects of dusty hybrid nanofluid over a stretching or shrinking surface where the

i. flow is assumed incompressible and two-dimensional,

ii. surface considered are horizontal, inclined, and vertical with the influence of viscous dissipation, velocity and thermal slip conditions,

iii. boundary layer theory is applied to formulate the governing equations with appropriate assumptions,

iv. result of the study are numerically executed using a built-in function in MATLAB software called bvp4c,

v. nanoparticles are Cu, and Al_2O_3, and water (H_2O) as the base fluid is utilized,

vi. Prandtl number (Pr) is fixed to 6.2, as water is chosen as the base fluid.

1.6 Significance of Study

The study of numerical solutions of dusty hybrid nanofluids over horizontal, inclined, and vertical stretching or shrinking surface prone to have numerous potential contributions and significant effects to the field of heat transfer and nanofluids. Additionally, this study may lead to an advancement of a new theoretical model in foreseeing behavior of nanofluid, fluid dynamics, and heat transfer which also contributes potential effects for various application in engineering.

Aforementioned, dusty hybrid nanofluid plays a vast role in the technology industry. Thus, further research can be conducted because the combination of some properties in the study has not yet been examined and investigated. The numerical results obtained from this study can be compared with other researchers and can be used as a reference for further research. This study provides useful insights that may guide the design considerations for cooling systems, heat exchangers, and other heat transfer related applications. The combined effects of dust particles, hybrid nanoparticles, viscous dissipation, mixed convection, and slip conditions provide significant recommendations for enhancing heat transfer efficiency, maintaining system performance, improve product quality, reducing energy consumption, among other benefits. In addition, this study could lead to the advancement of technologies that require high thermal efficiency and reliable operation in modern industrial processes.

1.7 Thesis Outline

This thesis includes seven chapters including this introduction chapter. Chapter 1 presents an overview of the research, the background, problem statement, research questions, research objectives, significance of the study and scope of study. Chapter

2 provides a comprehensive literature review based on the previous studies related to the problems considered in this study.

Chapter 3 outlines the mathematical formulation and numerical methodology for the problem considered in Chapter 4, the process begins with governing equations, progresses to the boundary layer approximation, reducing the governing equations to ordinary differential equations (ODEs) using the similarity transformation until the numerical solutions are obtained by using the bvp4c function in MATLAB software. The problems mentioned in Section 1.4 will be discussed in Chapters 4 to 6 and every chapter consists of an introduction, mathematical formulation, numerical solutions, results and discussion, and conclusion.

Chapter 4 discusses on the flow and heat transfer characteristics of dusty hybrid nanofluids over a horizontal stretching or shrinking surface, while considering viscous dissipation and slip conditions. The mathematical formulations are discussed in detail in Chapter 3. The skin friction coefficient, local Nusselt number, and the associated velocity and temperature profiles pertaining to relevant parameters are analysed and presented graphically and in table form.

Meanwhile, Chapter 5 further develops the analysis by investigating the flow and heat transfer behavior on an inclined surface, taking into account the implications of viscous dissipation and slip conditions. This chapter provides insights on how fluid flow and thermal performance are affected by the inclination angle. Besides that, Chapter 6 focuses on the significant influences of vertical surface on the flow and heat transfer characteristics, similar to Problems 1 and 2, but with different surface orientation.

Last but not least, Chapter 7 concludes this thesis by summarizing the key findings and contributions of the study. It also provides recommendations for future research directions.

CHAPTER 2
LITERATURE REVIEW

2.1 Nanofluid

Nanofluid is an innovation of nanotechnology that has been widely used, especially in the engineering industry. Besides that, it had captured the attention of a large number of researchers because of its contribution towards enhancing heat transfer efficiency. Nanofluids consist of nanometer-sized particles suspended in a base fluid and are categorized as heat transfer fluids. The utilization of nanofluids as a heat transfer fluid shows significant potential in both current and future applications, attributed to their improved stability and thermal conductivity. Besides that, in contrast with the normal base fluids, water, and oil, for example, nanofluid shows stronger thermophysical properties such as thermal conductivity, thermal diffusivity, viscosity, and convective heat transfer coefficients (Wong and De Leon, 2010. Thus, many researchers have published their papers related to nanofluids.

2.1.1 Nanofluid Flow Over a Stretching or Shrinking Surface

He and Elazem (2021 presented a research on the boundary layer flow, heat, and mass transfer of nanofluid over a stretching or shrinking, considering the effects of partial slip and temperature jump. The Buongiorno model was employed, and the numerical results were examined using the Chebyshev pseudospectral technique. The numerical analysis indicates that the inclusion of the slip parameter increases the thermal boundary layer thickness in stretching surface, while a contrary pattern was observed in the shrinking surface. Moreover, an increase in the temperature jump parameter enhances the thermal boundary layer thickness on both stretching and shrinking surfaces, thus diminishing the heat transfer rate. Amani et al. (2021 carried out a review analysis on the significance of nanofluids, focuses on a range of parallel surfaces. Based on the reviews, they indicate that the heat transmission rate across parallel surfaces increases with the rise in Rayleigh number, Reynolds number, magnetic number, and Brownian motion. The increment in thermophoresis parameter, Ec number, buoyancy ratio, Hartmann number, and Lewis number diminishes the heat transmission rate. Furthermore, they observed a lack of research addressing the mixed convection of nanofluids in vertical geometries, which then leads to the idea for this study in investigating the gap.

Lanjwani et al. (2022) performed a stability analysis on the flow and heat transfer over a porous stretching or shrinking surface with the influence of radiation effect. Iron (III) oxide (Fe_2O_3) and iron (Fe) are choosen as the nanoparticles, and water as the base fluid. The ODEs were solved numerically by applying the shooting technique implemented in Maple software. Their observations indicate that rising the radiation and nanoparticle volume fraction parameters boosts the temperature profile, but rising the Pr number, thermal slip, and suction parameters diminishes the temperature profile. Moreover, augmenting the velocity slip, and nanoparticle volume percentage, diminishes the temperature profile. Dual solutions exists for a certain range of suction and stretching/shrinking parameters and the stability analysis revealed that one solution is stable, while the other is unstable. Additionally, Fe-H_2O nanofluid exhibits a superior skin coefficient and Nusselt number compared to Fe_2O_3-H_2O nanofluid. Similar to the model employed by He and Elazem (2021), Zhu et al. (2022) also employed the Buongiorno model in their study on heat and mass transfer of Williamson nanofluid over a stretching or shrinking surface. The numerical findings were obtained using the Successive Over Relaxation (SOR) method and Finite Difference Method (FEM), revealing that a rise in the stretching parameter leads to an increase in fluid velocity and thermal boundary layer thickness. Recently, Rana et al. (2025) investigated on the magnetohydrodynamic (MHD) flow and heat transfer. Four distinct types of nanoparticles were chosen which are Cu, Fe_2O_3, silver (Ag), titania (TiO_2), and H_2O as the base fluid. On a stretched surface, Ag nanoparticle exhibits the highest local Nusselt number, while TiO_2 nanoparticle exhibits the lowest local Nusselt number. Conversely, on a shrinking surface, Ag maximizes the skin friction coefficient, while TiO_2 minimizes it.

2.1.2 Nanofluid Flow Over an Inclined Surface

Rafique and Alotaibi (2021) applied the Keller box method to solve the numerical analysis of boundary layer flow passing an inclined stretched surface immersed in the

Williamson nanofluid. The inclination of the angle helps in enhancing the skin friction coefficient; however, velocity profiles were observed to decrease with the inclination of the angle, and a greater local Grashof number increases the rate of heat and mass transmission. Eid et al. (2023) studied on the micropolar magnetic viscous nanofluid flow over a permeable inclined surface. Their study considers the effects of thermal radiation, Dufour effect, viscous dissipation, and magnetic force, employing the bvp4c function in MATLAB to generate the numerical results. An increase in the Dufour and Ec numbers elevates the temperature profile, whereas a rise in the inclination angle results in a decrease in the velocity profile. Besides, Abbas et al. (2024) performed research across a permeable inclined micro-rotations channel. Thermal radiation, buoyancy force, viscous dissipation, magnetic field strength, nanoparticles volume fraction, and vortex viscosity were the parameters analysed. The numerical results show that the rise in Molybdenum disulfide (MoS_2) nanoparticles volume fraction significantly impacted the heat transmission, attributed to the more effective thermal conductivity of MoS_2 in comparison with Fe_2O_3.

2.1.3 Nanofluid Flow Over a Vertical Surface

A research on the steady two-dimensional laminar MHD flow and heat transfer over a vertical stretching surface was conducted by Alarifi et al. (2019). Viscous dissipation, heat source/sink, and magnetic fields are the pertinent parameters analysed, with findings obtained by shooting method and Runge Kutta Fehlberg Integration (RKFI) algorithm. The research indicates that the skin friction coefficient rises with the mixed convection parameter and diminishes with the stretching speed ratio for both assisting and opposing flows. In addition, the heat transfer rate exhibits only an insignificant rise with the increase in the mixed convection parameter. Manjunatha et al. (2021) evaluated the effects of magnetic field, Pr number, wall temperature, wall expansion/contraction, wall permeability strength, and rotation parameter over a vertical upward or downward moving rotating disk. Single-walled carbon nanotubes (SWCNT), and multi-walled carbon nanotubes (MWCNT) were employed along with water-based nanofluid in their study. The Runge-Kutta-Fehlberg's fourth fifth order method (RKF45) and the shooting method were employed to achieve the results. The fluid velocity upsurges with the augmentation of the expanding/contracting parameter, and it is observed to be greater in MWCNT-H_2O than in SWCNT-H_2O nanofluid flow. Furthermore, the elevation in wall temperature rises the temperature profile for both SWCNT and MWCNT-H_2O.

Besides that, Aiyashi et al. (2023) elucidated the heat transfer of an unsteady stagnant point flow of a non-homogeneous nanofluid over a stretching/shrinking vertical plate by taking into account the mixed convection, magnetic, viscous dissipation, Brownian motion, thermophoresis, suction/injection effects. They discovered that considering the influence of viscous dissipation elevates the temperature profile while reducing the skin friction coefficient. Identical to the research by Manjunatha et al. (2021), Kumar et al. (2025) similarly employs SWCNT-H_2O nanofluid to investigate the flow behavior over a vertical porous stretching surface, considering the effects of viscous dissipation and a non-uniform heat source/sink. The findings indicate that, with the presence of viscous dissipation, the velocity profiles augments with the increase of mixed convection parameter and nanotube volume fraction parameter. In addition, they stated that the rate of heat transfer can be efficiently controlled by altering the nanoparticle volume fraction and suction/injection parameters.

In conclusion, prior research indicates that nanofluids significantly enhance heat transfer rate, making them ideal for applications including cooling and heating systems, energy production, and industrial processes.

2.2 Hybrid Nanofluid

Hybrid nanofluid, a new kind of fluid, was then widely used once it was introduced to the industry, as it improves heat transfer efficiency (Anuar et al., 2021b). Furthermore, compared to the normal nanofluid, the hybrid nanofluid shows a higher thermal conductivity, which leads to stronger thermophysical features, which strengthen the fact of having a higher heat transfer rate (Kakar et al., 2022).

2.2.1 Hybrid Nanofluid Flow Over a Stretching or Shrinking Surface

Khan et al. (2021) evaluated a comparative mathematical model of MHD hybrid nanofluid and mono-nanofluid flows with heat flux conditions through a stretching surface. The hybrid nanofluid employed consists of zinc oxide and zirconium dioxide, and the parameters under consideration include viscous dissipation, thermal radiation, and natural convection. The findings reveal that hybrid nanofluid flows have a greater impact on the heat transfer compared to nanofluid, and an increase in the Ec number leads to a reduction in temperature distribution. Kumar (2021) presented a dimensionless study to foresee the effects of hybrid nanoparticles on various physical quantities in copper magnetite ($Cu-Fe_2O_4$)/ethylene glycol-based hybrid nanofluid, also over a stretching surface, and was solved by using Fourth order Runge-Kutta Fehlberg and shooting technique. The influence of porous medium parameter, thermal radiation, magnetic parameter, and Ec number were studied, and they found out that Cu/ethylene glycol-based exhibits the highest heat transfer rate among $Cu-Fe_2O_4$ /ethylene glycol-based nanofluids. In addition, the temperature of the nanofluid increases with the rise of the Ec number.

Mabood and Akinshilo (2021) proposed research on the stability of a flowing viscous hybrid nanofluid over a stretching surface under uniform magnetic effect and radiation. Navier-Stokes model was used to generate the result, but they found that the model was highly non-linear and they decided to apply the Runge-Kutta Fehlberg numerical method instead. The generated result proved that the increase in radiation parameters enhances thermal distribution, and increasing the nanoparticle concentration leads to a decrease in the velocity of the fluid. Rashid et al. (2021) investigate the impact of various nanoparticle shapes on the flow along a stretching/shrinking horizontal cylinder. The three shapes of Ag and TiO_2 utilized are sphere, blade, and lamina. The ODEs were solved by using the homotopy analysis method (HAM), which demonstrates that spherical nanoparticles exhibit greater temperature distribution and heat transfer rates compared to blade and lamina-shaped nanoparticles.

Hussain et al. (2022) conducted a study to clarify the dynamics of water conveying of hybrid nanofluid over an exponentially stretchable surface with the presence of Navier's partial slip and thermal jump condition. In the study, copper oxide (CuO), Al_2O_3, and TiO_2 are used for the nanoparticles, while H_2O is used as the base fluid and was solved numerically using a finite difference scheme based, Lobatto IIIa-bvp4c in MATLAB. Mishra et al. (2022) numerically elucidated the flow, heat, and mass transfer of $CuO\text{-}Al_2O_3/H_2O$ hybrid nanofluid over a stretching surface. The numerical results were obtained utilizing bvp4c function in MATLAB, revealing that the heat transfer rate in hybrid nanofluid surpasses that of both nanofluid and base fluid. Furthermore, an increase in viscous dissipation and stretching parameter leads to a reduction in skin friction coefficient, while an opposite trend is observed with an increase in suction/injection and thermal radiation parameters. Additionally, the inclusion of viscous dissipation augments the thermal diffusion, therefore elevating the fluid temperature. Ali et al. (2024) applied the homotopy pertubation to examine the heat and mass transport of Ree-Eyring hybrid nanofluid flow across a stretching surface.

2.2.2 Hybrid Nanofluid Flow Over an Inclined Surface

The investigation into heat transmission between a water-based hybrid Ag-gold (Au) nanofluid and Ag nanofluids over an inclined microfluidic channel, facilitated by an electroosmotic pumping, was initiated by Akram et al. (2021). The revised Buongiorno model was utilized in the study, incorporating thermophoresis and Brownian motion into the analysis. The outcomes show that hybrid nanofluids demonstrate an elevated heat transfer rate in comparison to mono-nanofluids. Additionally, the thermophysical characteristics are significantly improved when hybrid nanofluids are employed, and the size of nanoparticles also influences the rate of heat transfer. Alabdulhadi et al. (2021) explored on the effect of MHD on the flow and heat transfer. The outcomes indicate, with the consideration of magnetic parameter, dual solutions were obtained with the first solution demonstrating greater stability than the second solution, as validated by stability analysis. Furthermore, the presence of magnetic parameter improved both the skin friction coefficient and heat transfer, and over an inclined shrinking surface, the higher concentration of Ag nanoparticle volume fraction enhances the skin friction coefficient but diminishes the heat transfer between the surface and the fluid.

The work by Arshad et al. (2023) studied on the three-dimensional MHD heat and mass transfer over a permeable dual inclined stretching surface. The governing equations are solved using bvp4c function in MATLAB. According to their analysis, they observed that the heat transfer rate is maximized when the axis of rotation and the inclined magnetic field are aligned, with hybrid nanofluid exhibiting both an increase heat transfer rate and diminish skin friction. Chu et al. (2023) elucidated on the thermal effect of hybrid nanofluid flow across an inclined oscillatory porous surface, utilizing three variants of nanoparticles which are Cu, Al_2O_3, and TiO_2 with water as the base fluid. It is observed that TiO_2-H_2O have significantly better thermal performance in comparison to Cu-H_2O and Al_2O_3-H_2O nanofluids.

Sohut et al. (2023) considered in examining the mixed convection flow across an inclined cylinder accounting the effects of nanoparticles volume fraction, inclination angle, curvature, magnetic, and mixed convection parameters. They came to a conclusion, in comparison to the pure base fluid, and nanofluid, hybrid nanofluid exhibits the highest transfer efficiency and lowers drag force. Jeelani and Abbas (2025) researched on the the Maxwell hybrid nanofluid flow, heat and mass transmission across an inclined stretching porous sheet and adopting the bvp4c function in MATLAB software to solve the ODEs. In their conclusion, they concluded that rising the nanoparticle volume fraction results in improved thermal performance.

2.2.3 Hybrid Nanofluid Flow Over a Vertical Surface

Gumber et al. (2022) applied the RKF-45 and shooting method to solve the numerical analysis of boundary layer flow over a vertical plate immersed in a micropolar hybrid nanofluid. The outcomes indicate that, with the consideration of viscous dissipation, the temperature profile is influenced by the internal friction within the high velocity fluid increases. This study also reveals that the fluid velocity is maximized when lamina-shaped nanoparticles are employed, while it is minimized with hexahedron-shaped nanoparticles. Additionally, an increase in the number of nanoparticles correlates with a temperature rise. A study on the flow and thermal transfer across a vertical porous plate was discovered by Nayan et al. (2022). The focused in examining the influence of aligned magnetic field, magnetic field, nanoparticles volume fraction, local Grashof number, and porous parameter on the velocity and temperature profiles, skin friction and Nusselt number. The analysis reveals that with an upsurge in aligned magnetic field, magnetic parameter, and local Grashof number, results in an elevation of velocity profile, while simultaneously diminishing the temperature profile. Additionally, Ag/CuO-H_2O demonstrates the highest heat transfer rate compared to both the pure fluid and nanofluid, consistent with the findings of Sohut et al. (2023). The impact of various nanoparticle shapes on the flow and heat transmission of MHD Casson hybrid nanofluids across a moving vertical plate was investigated by Zukri et al. (2023). Similar to the study conducted by Zukri et al (2023), Alzu'bi et al. (2024) extended their study by investigating the incompressible MHD flow and heat transmission of Casson ternary hybrid nanofluid over a vertical stretched sheet, considering both magnetic and Newtonian heating.

2.3 Dusty Fluid

Dusty fluid is said to be unique as it consists of a two-phase flow fluid mixed with dust and fluids, and the combination of dust particles with water is an example of dusty fluid. The utilization of dusty fluids is greatly in the fields of environmental pollution, fluidization, combustion, petroleum, polymer, and geophysical processes, refrigeration, polluted soil, air, and water, dust or fumes in the gas cooling system, in agriculture, crude oil purification, and polymer technology (Islam and Nasrin, 2020).

2.3.1 Dusty Fluid Flow Over a Stretching or Shrinking Surface

Gireesha et al. (2014) researched the boundary layer flow and heat transfer of an incompressible nanofluid with homogeneously suspended dust particles over a stretching surface. Partial differential equations are transformed to ordinary differential equations using a similarity transformation. Rungu-Kutta Fehlberg's approach, an effective numerical analysis, is used to find the solutions. The results indicate that an increase in dust particle mass concentration diminishes both the velocity and temperature. Furthermore, in the velocity profile, dusty nanofluid exhibits the lowest velocity, followed by dusty fluid, nanofluid, and ordinary fluid. Noorzehan et al. (2018) also applied the similarity transformations to approximate the governing equations of nonlinear ordinary differential equations to run a study on the effects of the suction parameter and fluid-particle interaction parameter on the boundary layer of the dusty fluid towards a stretching surface. The MATLAB software's bvp4c function was then used to numerically solve the modified equations, and through multiple plots, the impacts of physical parameters on the velocity profiles of the fluid phase and the dust particle phase were determined. They discovered that in the presence of suction, the fluid velocity increases while the particle velocity decreases. In addition, the particle velocity is increased by the fluid-particle interaction parameter.

Punith Gowda et al. (2021) studied the two-phase model known as dusty hybrid nanofluid, which considered both particle and fluid phases. In the study, they considered Darcy-Forchheimer's porous medium and viscous dissipation on the flow of an incompressible dusty hybrid nanofluid over a stretching cylinder. Cu, Al_2O_3, TiO_2, and H_2O were used as the dusty hybrid nanofluid. After the equations are reduced to non-linear ODEs, the shooting method and RKF45 are adapted. The results show that the increase in particle mass concentration enhances heat transmission but decreases the velocity gradient. As the Ec number rises, the temperature profile also increases, whereas the rate of heat transfer diminishes with rising values of the Ec number and fluid velocity interaction parameter. In contrast to the research conducted by Punith Gowda et al. (2021), a scrutiny of an incompressible Fe_2O_3-Cu dusty hybrid nanofluids transversing a stretched melting surface under the influence of a magnetic field was initiated by Radhika et al. (2021). According to their analysis, increasing the values of dust particle mass concentrations elevates the temperature profiles of both fluid and dust phases. Notably, the fluid phase exhibits more significant outcomes in comparison to the dust phase as the values of the temperature interaction parameter rise.

Further, Mallikarjuna et al. (2021) elucidate on the two-phase Darcy-Forchheimer flow of a hybrid nanofluid across a stretchable surface. The melting effect and viscous dissipation are among the pertinent parameters examined in the study. A decreasing trend was observed in the velocity gradient of the nanofluid phase, along with an increase when a higher velocity interaction parameter was taken into account. Conversely, a contrasting observation emerged in the temperature gradient when the thermal interaction parameter was taken into account.

2.3.2 Dusty Fluid Flow Over an Inclined Surface

The impact of convective and Navier slip boundaries towards the MHD stratified fluid flow over an inclined irregular channel with the presence of dust particles was examined in a study by Kalpana and Saleem (2022). The numerical result, which was generated using finite difference technique and Thomas algorithm, shows a high velocity for dusty fluid flow as the permeability of porous medium increases. The temperature profile also increases as the Ec number increases. Khan et al. (2023) performed an analysis to investigate the effect of slipping and relative magnetic field of the two-phase Casson dusty fluid flow over an inclined parallel surface. Further, a research on the aligned MHD flow and heat transmission of two-phase Jeffrey fluid containing Carbon Nanotubes (CNTs) was undertaken by Habib et al. (2024), examining the effects of viscous dissipation and Newtonian heating. A rise in the magnetic field, ratio of relaxation to retardation times, aligned angle parameter and fluid particle interaction causes a decline in the velocity profile. As the aligned angle increases, there is an increase in the temperature profile, while a decrease in the velocity profile. Moreover, the authors stated that the consideration of viscous dissipation and Newtonian heating promotes a thorough comprehension of complicated interactions in the fluid flow system of their study.

An analysis on the flow and convective heat and mass transfer of a second-grade viscoelastic dusty fluid across an inclined parallel plate was performed by Khan et al. (2024). The numerical findings are computed using Zakian's numerical method in MATHCAD software. Based on their analysis, they indicated that the utilizaton of hybrid nanofluid surpasses that of nanofluid, with a heat transfer rate of 25.2% for hybrid nanofluid compared to 14.50% for nanofluid. Furthermore, an increase in nanoparticle volume fraction results in diminished velocity, temperature, and concentration profiles. The effects of thermal buoyancy and viscous dissipation were recently investigated numerically by Awan et al. (2025) in order to maximize the entrophy generation in MHD Maxwell dusty nanofluid over an inclined stretching sheet.

2.3.3 Dusty Fluid Flow Over a Vertical Surface

A steady, two-dimensional two-phase Williamson fluid flow and heat transfer across a vertical stretching sheet with the influence of Newtonian heating was studied by Arifin et al. (2021). The Keller-box approach in MATLAB software is adopted in order to achieve the results. The result implies that the augmenting the Williamson parameter reduces the velocity of the fluid in both fluid and dust phases. Further, a study on MHD $Cu-Al_2O_3$ flow and heat transfer over a shrinking vertical sheet with dust particles was discovered by Waini et al. (2021). The skin friction coefficient and local Nusselt number is seen to rise with higher values of fluid-particle interaction parameter, magnetic parameter, and Cu nanoparticle volume fraction. The stability analysis were performed due to the existence of dual solutions in shrinking case, and it is noted that the first solution is stable compared to the second solution. In addition, Cu nanoparticle volume fraction and fluid-particle interaction parameter contribute in delaying the boundary layer separation. Dey and Chutia (2022) performed a numerical investigation of the two-phase bioconvective boundary layer flow over a vertically stretching flat surface. The research reveals that increasing the mixed convection parameter and Pr number reduces the local skin friction coefficient and local Nusselt number. Tripathy et al. (2024) investigated the two-phase flow and heat transmission over a vertical stretched surface, considering the effects of radiation and viscous dissipation. Enhancing viscous dissipation results in an increased velocity profile for both phases; however, the temperature profile exhibits an increase in the fluid phase, while the dust phase experiences a reduction. Furthermore, the augmentation of the buoyancy parameter results in a reduction of the thermal boundary layer, facilitating surface cooling.

2.4 Boundary Layer Flow and Heat Transfer over Various Surfaces with Viscous Dissipation

Boundary layer analysis has been broadened to include various surface orientations, covering an extensive range of engineering applications. Stretching and shrinking surfaces form the foundation for numerous industrial applications. Researchers have explored flows over rotating disks, inclined surfaces, curved geometries, and oscillating surfaces. Each surface exhibits unique velocity and thermal characteristics, which affect the flow and heat transfer. The incorporation of viscous dissipation also enhances the application by considering internal heating in high-speed flows, which subsequently influences the flow and heat transfer characteristics. This section examines the studies involving various stretching or shrinking surface incorporating viscous dissipation and other relevant parameters.

Afridi et al. (2017) worked on the entropy generation analysis to study the mixed convection flow and heat transfer over an inclined stretching surface with the effect of MHD. In the analysis, the shooting method and the Runge-Kutta method were applied to solve the differential equations, resulting in the thermal boundary layer thickness augmented with the increase of Ec number, whilst decreasing in local Nusselt number. Instead of considering the Tiwari and Das model, El-Zahar et al. (2020) explored the implications of viscous dissipation, Brownian motion, and thermophoresis on an unsteady stretched surface, utilizing the Jeffrey nanofluid, incorporating the Buongiorno model. The outcomes elucidate that an increased Ec number elevates the thermal boundary layer, subsequently leading to a reduction in the Nusselt number. An increase in the Brownian motion and thermophoresis parameters results in a decrease in both the values of the skin friction coefficient and the Nusselt number.

Waqas et al. (2021) studied on vertical stretching cylinder with the effect of thermal radiation and viscous dissipation. Hybrid nanofluids with single-walled and multi-walled nanotubes, SWCNTs, and MWCNTs, respectively, were utilized in their study, and the result shows a significant increase in MWCNTs in comparison to SWCNTs, particularly with a higher Ec number. The heat transfer rate diminishes with a rise in nanoparticles volume fraction, while an increase in the mixed convection parameter leads to a reduction in the skin friction coefficient. Afridi et al. (2017) and Waqas et al. (2021) investigated inclined and vertical stretching surfaces, respectively, while Kho et al. (2021) further extended to include both stretching and shrinking surfaces, with the consideration of viscous dissipation, suction, and nanoparticle volume fraction. The numerical results were obtained using the bvp4c function in MATLAB. Consistent with the findings from other researchers concerning viscous dissipation, the inclusion of viscous dissipation significantly reduces the heat transmission rate but elevates the temperature profile. Higher concentrations of Cu and TiO_2, and suction parameter lead to an increase in the reduced skin friction coefficient but lowers the reduced Nusselt number. Further, the existence of dual solutions for certain parameter ranges were observed, and the stability analysis was performed, revealing that the first solution exhibits greater stability than the second solution.

Besides that, Hamid et al. (2022) numerically scrutinized the study of dusty magnetite ferrofluid over a non-isothermal moving surface. The influence of suction, magnetic field parameter, Pr number, Ec number, stretching/shrinking surface parameter, and nanoparticle volume fraction were analysed. Their findings discovered that, on the stretched or shrunk surface, the ferrofluid flow was slowed down by the magnetic field and dust particles, which also increases the wall friction. Adding to that, dusty magnetite ferrofluid was found to be more effective in kerosene-based fluid than water-based fluid, and due to the presence of dust particles and viscous dissipation, the wall heat transmission diminishes. The research on the non-linear permeable shrinking surface was carried out by Waini et al. (2023). In their research, the parameters of suction, viscous dissipation, stretching or shrinking surface, Pr number, nanoparticle volume fraction, and power law velocity were taken into consideration, and MATLAB software was implemented to execute the results. They proved that the skin friction was reduced by 39.44% and the heat transmission rate was reduced by 11.71% as a result of the rise of the power law. Moreover, a 14.39% reduction in heat transmission rate is discovered due to viscous dissipation, which is represented by the Ec number.

Aiyashi et al. (2023) elucidated the heat transfer of an unsteady stagnant point flow of a viscous laminar fluid over a shrinking or stretching vertical plate by taking into account the mixed convection, magnetic, viscous dissipation, Brownian motion, thermophoresis, and suction or injection effects. Further, Jalili et al. (2023) investigated the viscous fluid flow across a movable plate, accounting for three principal heat transfer effects: radiation, internal heat generation, and viscous dissipation. Alharbi et al. (2024) considered the effect of viscous dissipation and thermal radiation of Al_2O_3-Cu/H_2O across an inclined oscillating disk. The homotopy analysis method was employed to execute the numerical results. Recently, Zeeshan et al. (2025) conducted a research to study the impact of heat source/sink and viscous dissipation on MHD Eyring-Powell CuO-TiO_2/H_2O hybrid nanofluid flow and heat transfer over a horizontal cylinder. Benaissa et al. (2025) conducted a study on the boundary layer flow and heat transfer of Jeffrey fluid over a stretching cylinder, incorporating partial slip and viscous dissipation, with results obtained using the bvp4c solver in MATLAB. The results indicate that an increase in the Ec and Deborah numbers, along with thermal slip, results in a reduction of the local Nusselt number, but an opposite trend is observed with rising Pr number and Jeffrey fluid parameter.

Previous studies collectively conclude that viscous dissipation results in an elevated temperature profile, increases the thermal boundary layer thickness and reduces the heat transfer rate. The findings are consistent with the various surface orientations, which may influence the outcomes presented. Existing studies, however, rarely account for the impact of viscous dissipation on dusty hybrid nanofluid under combined slip conditions and mixed convection parameters. This creates a gap in the literature and forms motivation for the current study.

2.5 Boundary Layer Flow and Heat Transfer over Various Surfaces with Slip Conditions

The classical boundary layer theory assumes that the fluid adheres to the surface with zero relative velocity (the no-slip condition). Experimental and micro-scale studies reveal that partial slip may occur, making the no-slip condition invalid in certain circumstances. Researchers then explored boundary layer flow and heat transfer under slip conditions across various surface orientations. This section discusses studies on various stretching or shrinking surface that include slip conditions and additional parameters.

Mishra and Kumar (2020) evaluated the effects of slip conditions, magnetic field, viscous dissipation, and Joule heating on the flow and heat transfer of $Ag-H_2O$ nanofluid over a permeable stretched cylinder. RKF45 and shooting method were applied to solve the nonlinear equations, and it was noticed that the velocity and temperature profiles decline with an increase in velocity slip and thermal slip parameter, respectively. An increment in values of heat generation absorption, magnetic parameter, and viscous dissipation parameter diminishes the heat transmission, while exhibiting an inverse trend when the velocity slip and suction parameters increase. Kejela et al. (2021) examined the impact of thermal radiation, slip parameters, Ec number, and magnetic field on the MHD Hiemenz flow passing a permeable plate. The ODEs were solved by using the optimal homotopy asymptotic method (OHAM), and the outcome shows that the rise of slip parameters diminishes the fluid flow, thermal boundary layer, and temperature gradient. The fluid temperature increases with the Ec number, whereas the fluid velocity does not change with changes in the Ec number. Besides that, the rising values of the thermal slip parameter result in a reduction of thermal boundary layer thickness, which subsequently decreases the temperature profile.

Meanwhile, Ashraf et al. (2021) conducted a study to analyse the implications of slip flow, thermophoretic motion, and viscous dissipation on the two-dimensional mixed convection flow across various positions of the sphere. Different from the study conducted by Ashraf et al. (2021), Ramzan et al. (2022) considered the influence of slip condition and thermo-diffusion in the problem of unsteady free convection flow passing a vertical rotating inclined plate. A comparative study was conducted to analyse the effects of slip and no-slip conditions. The outcomes depict that an increase in the Grashof number elevates the buoyancy force, thus enhancing both the velocity magnitude and the velocity profile, with slip conditions exhibiting a more notable increasing trend compared to no-slip conditions. Further, an increase in the inclination angle diminishes the velocity magnitude. Dzulkifli et al. (2022) scrutinized on nanofluids considering the slip velocity over a stretching or shrinking surface. The Tiwari and Das model was employed in the formulation, and the ODEs were numerically solved by the bvp4c function in MATLAB. The results show that for a shrinking surface, the local skin friction coefficient and local Nusselt number increase with higher values of velocity slip, but an opposite trend is observed in the stretching surface. Cu demonstrated the highest friction and heat transfer rate in comparison to TiO_2 and Al_2O_3. Stability analysis was performed considering the existence of dual solutions, with the first solution identified as stable.

Rai and Mishra (2022) conducted research similar to that of Mishra and Kumar (2020), involving slip conditions, viscous dissipation, and magnetic fields, but focused on a moving plate. Consistent with the findings of Mishra and Kumar (2020), it was observed that the inclusion of viscous dissipation and magnetic field rises the temperature profile. The increase in velocity slip elevates the temperature profile while diminishing the velocity profile. Abbas et al. (2023) studied the velocity and thermal slip together with multi-mass diffusion through an inclined channel. Three-phase of nanofluids which are the Fe_2O_3/H_2O, Fe_2O_3-Cu/H_2O and $Fe_2O_3-Cu-MoS_2/H_2O$ were used in their study. It was found that the velocity and temperature profile diminish with the increase of inclination angle. Further, as the upper and lower plate of thermal slip rises, the temperature enhances and the $Fe_2O_3-Cu-MoS_2/H_2O$ trihybrid nanofluid shows the highest momentum and heat flow followed by Fe_2O_3-Cu/H_2O hybrid nanofluid, and Fe_2O_3/H_2O nanofluid. Furthermore, an analysis of the convective heat transfer over a porous stretched surface, taking into account nonlinear thermal radiation, buoyancy force, and slip conditions, was examined by Zeeshan et al. (2023). The result shows that the slip effect reduces the frictional force between the fluid and the surface.

Jamrus et al. (2024) numerically examined the mixed convection stagnation point by utilizing the thermally stratified ternary hybrid nanofluids with the impact of suction, MHD, and velocity slip over a stretching/shrinking surface. Based on the outcomes, it is seen that the increment in the velocity slip reduces the friction between the boundary layers, thereby lowering the surface shear stress while enhancing the heat transfer rate. It is also observed that augmenting the velocity slip helps in delaying the boundary layer separation. In addition, the heat transfer rate increased by 1.74% when the TiO_2 volume fraction rose to 6% from 2%, indicating an increase in fluid viscosity and shear stress at the surface. Consequently, it elevates the skin friction coefficient by 7.42%. Further, dual solutions exist in assisting and opposing flow, where the first solution is proven to be stable. Gosty et al. (2024) examined heat and mass transmission in a vertical channel, emphasizing the influence of variable viscosity and velocity slip. Recently, Asghar et al. (2025) studied on MHD hybrid nanofluid flow across a power law form stretching or shrinking surface. Their focus is on evaluating the impact of thermal slip, Joule heating, and magnetic parameters on the reduced skin friction and heat transmission. Ismail et al. (2025) also perform a study on MHD flow limited across a shrinking surface while considering partial slip and heat generation. A decline in the heat transfer rate was seen as the values of the magnetic parameter, thermal slip parameter, and Ec number increased. In addition, they also noted that the first solution exhibited stability.

Therefore, previous studies show a consistent trend across various surfaces where the velocity slip reduces the surface friction by reducing the shear stress, while the thermal slip elevates the fluid temperature, increases the temperature profile, and thickens the thermal boundary layer thickness.

2.6 Bvp4c Function

Khashi'ie et al. (2020) performed a numerical analysis of stagnation point flow over a vertically shrinking and stretching cylinder, incorporating the effects of suction and thermal stratification. Al_2O_3, Cu were dispersed in water to produce a hybrid nanofluid, and the ODEs were computed using the bvp4c solver in MATLAB. The results show that an appropriate ratio of Cu and Al_2O_3 volume fraction in producing hybrid nanofluid yields a better heat transfer rate compared to the Cu/H_2O nanofluid. Further, Al_2O_3/H_2O exhibits the lowest heat transfer rate compared with both Cu/H_2O and Al_2O_3-Cu/H_2O hybrid nanofluids, and the first solution is reported to have a greater stability compared to the second solution, as a stability analysis was performed. Yacob et al. (2021) studied on steady 3D rotating flow and heat transfer of SWCNTs and MWCNTs passing a stretching or shrinking surface. The ODEs were solved numerically using the bvp4c function in MATLAB software, demonstrating that dual solutions exist for a shrinking surface, with only the first solution being stable. Moreover, the heat transfer is greater in MWCNTs-H_2O relative to SWCNTs-H_2O, and kerosene-based CNTs exhibit a greater heat transfer rate than water-based CNTs. An increase in the nanoparticle volume fraction enhances the heat transfer rate whilst diminishing the temperature gradient in both nanofluids.

Research of the implications of slip effect on boundary flow and heat transfer across an exponentially stretching or shrinking cylinder has been extensively studied by Najib et al. (2022). The numerical results were computed using the bvp4c function in MATLAB. Increasing the values of the slip and curvature parameters broadens the range of dual solutions, with the first solution ought to be more stable than the second. Elevating the nanoparticle volume fraction results in an augmentation of the skin friction coefficient and heat transfer rate, with Cu exhibiting the greatest values for both parameters. Yahaya et al. (2023) performed a numerical investigation on the impact of radiation in the flow of Cu-Al_2O_3/H_2O over a biaxially stretching or shrinking surface. Consistent with the findings mentioned previously, the researchers performed a stability analysis of the dual solutions and determined that only the first solution is stable, while the second solution is unstable. In addition, Cu-Al_2O_3/H_2O has the highest temperature profile, followed by Cu/H_2O and Al_2O_3/H_2O, and the increase in radiation parameters elevates the temperature profile of hybrid nanofluid. Rafique et al. (2024) performed a computational analysis by employing bvp4c to analyze the unsteady MHD flow of Al_2O_3-Cu/H_2O hybrid nanofluid past a porous shrinking sheet with heat generation effect.

Recently, numerous studies have computationally solved boundary layer flow and heat transfer using the bvp4c function in MATLAB, including, Divya et al. (2025), Sudarmozhi et al. (2025), Sobale et al. (2025), Al-Sawalha et al. (2025), and Jawad et al. (2025).

CHAPTER 3
GOVERNING EQUATIONS AND RESEARCH METHODOLOGY

3.1 Introduction

This study investigates the flow and heat transfer characteristics of a hybrid nanofluid containing dust particles over three types of permeable surfaces by applying Tiwari and Das model. The first problem focuses on a horizontal stretching or shrinking surface, while the second and third problems address inclined and vertical surfaces, respectively. This chapter presents a comprehensive formulation of the governing equations and details the process leading to the numerical results for the first problem, which are also discussed in Chapter 4. Modifications for the subsequent two problems are outlined in Chapters 5 and 6. The procedure of the research methodology is divided into three phases:

- **Phase 1 - Problem formulation:**
  The governing equations consisting of continuity, momentum, and energy equations are formulated based on the problem considered and subsequently transformed into the boundary layer equations.
- **Phase 2 - Similarity transformation:**
  The boundary layer equations are reduced to the ordinary differential equations using a similarity transformation by introducing appropriate similarity variables.
- **Phase 3 - Numerical method:**
  The ordinary differential equations are solved using bvp4c function in MATLAB software to generate numerical solutions. Then, the numerical results are validated with the previous studies to ensure the formulation and methodology are correct. The findings are presented in tabular and graphical forms and can be analysed.

The flow of the research methodology is summarized in the flowchart given in Figure 3.1.

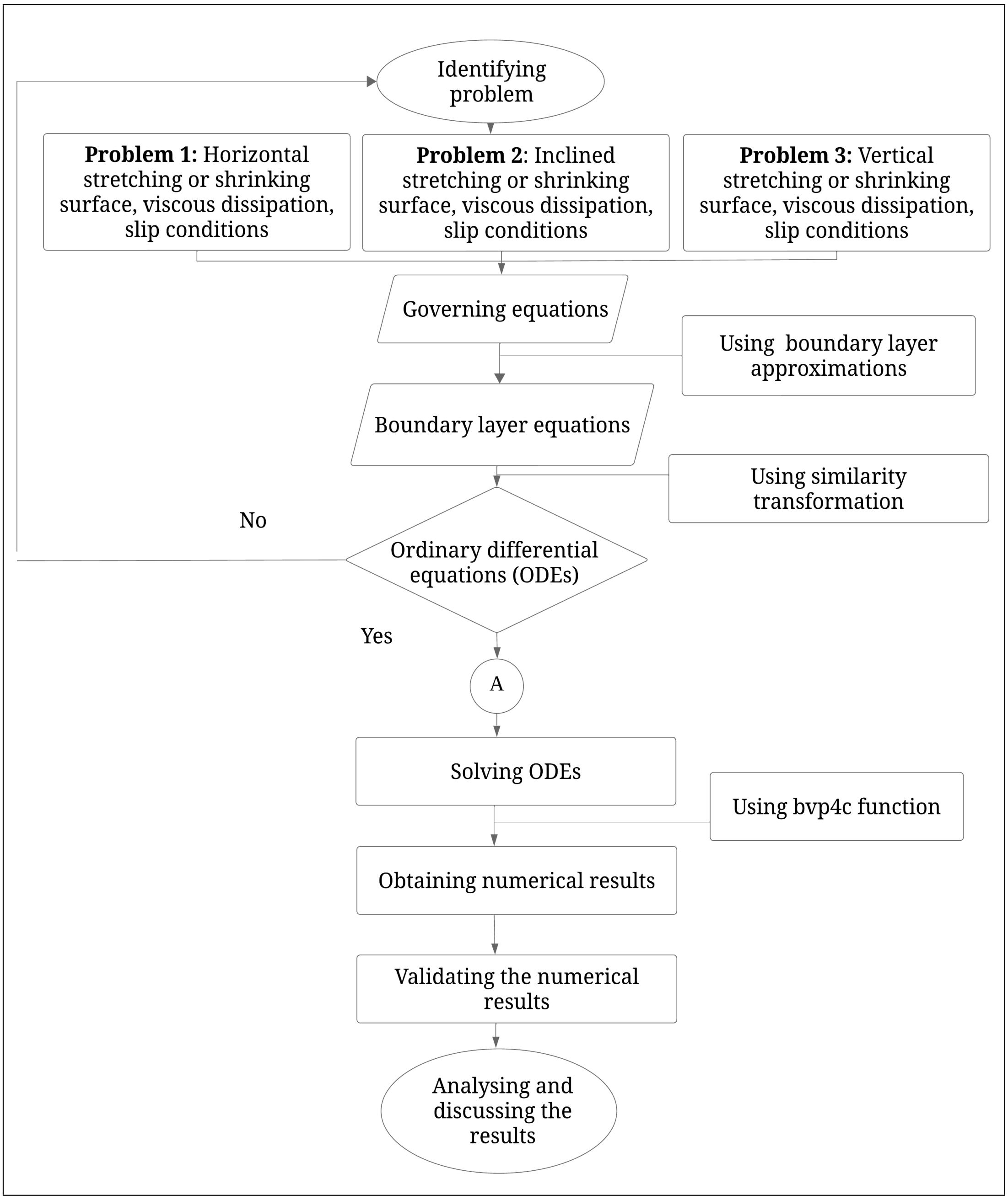

Figure 3.1 Flowchart of the Research Methodology

3.2 Problem Formulation

3.2.1 Governing Equations

Firstly, we consider a problem of steady two-dimensional boundary layer flow towards a horizontal stretching or shrinking surface in a dusty hybrid nanofluid as depicted in Figures 3.2 and 3.3. It is assumed that the velocity of the surface is $U_w(x) = ax$ where a is a positive constant, the surface temperature is T_w and the temperature far from the surface known as the ambient fluid temperature is denoted by T_∞. The surface runs along the x-axis, while the y-axis is perpendicular to it. It is assumed that the size of the dust and nanoparticles are uniform and sphere-shaped (Gireesha et al., 2011). Based on the circumstances, the governing equations of hybrid nanofluid and dust phases are as follows (Gireesha et al., 2015; Anuar et al., 2021b):

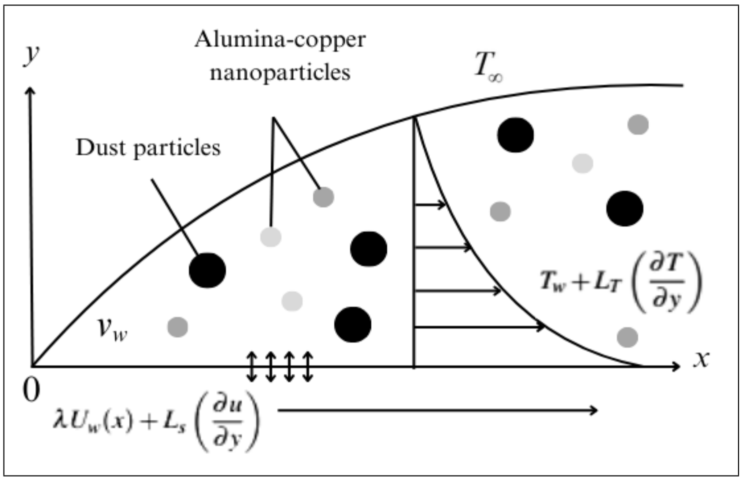

Figure 3.2 Physical Model of a Horizontal Stretching Surface

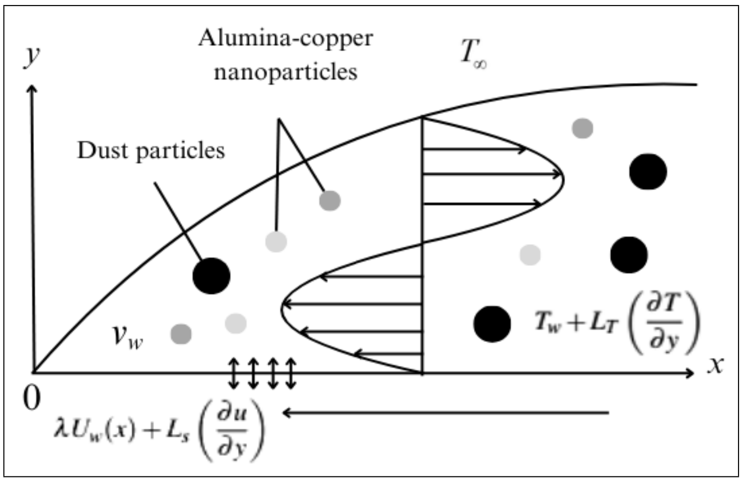

Figure 3.3 Physical Model of a Horizontal Shrinking Surface

i. Hybrid nanofluid phase

Continuity equation:

$$\frac{\partial u}{\partial x}+\frac{\partial v}{\partial y}=0. \tag{3.2.1}$$

Momentum equation in x-component:

$$u\frac{\partial u}{\partial x}+v\frac{\partial u}{\partial y}=-\frac{1}{\rho_{hnf}}\frac{\partial p}{\partial x}+\frac{\mu_{hnf}}{\rho_{hnf}}\left(\frac{\partial^2 u}{\partial x^2}+\frac{\partial^2 u}{\partial y^2}\right)+\frac{KN}{\rho_{hnf}}(u_p-u). \tag{3.2.2}$$

Momentum equation in y-component:

$$u\frac{\partial v}{\partial x}+v\frac{\partial v}{\partial y}=-\frac{1}{\rho_{hnf}}\frac{\partial p}{\partial y}+\frac{\mu_{hnf}}{\rho_{hnf}}\left(\frac{\partial^2 v}{\partial x^2}+\frac{\partial^2 v}{\partial y^2}\right)+\frac{KN}{\rho_{hnf}}(v_p-v). \tag{3.2.3}$$

Energy equation:

$$\begin{aligned}u\frac{\partial T}{\partial x}+v\frac{\partial T}{\partial y}&=\frac{k_{hnf}}{(\rho C_p)_{hnf}}\left(\frac{\partial^2 T}{\partial x^2}+\frac{\partial^2 T}{\partial y^2}\right)+\frac{NC_{pf}}{(\rho C_p)_{hnf}\tau_T}(T_p-T)\\&+\frac{N}{(\rho C_p)_{hnf}\tau_v}(u_p-u)^2+\frac{\mu_{hnf}}{(\rho C_p)_{hnf}}\left(\frac{\partial u}{\partial y}\right)^2.\end{aligned} \tag{3.2.4}$$

ii. Dust phase

Continuity equation:

$$\frac{\partial u_p}{\partial x}+\frac{\partial v_p}{\partial y}=0. \tag{3.2.5}$$

Momentum equation in x-component:

$$u_p\frac{\partial u_p}{\partial x}+v_p\frac{\partial u_p}{\partial y}=\frac{K}{m}(u-u_p). \tag{3.2.6}$$

Momentum equation in y-component:

$$u_p \frac{\partial v_p}{\partial x} + v_p \frac{\partial v_p}{\partial y} = \frac{K}{m}(v - v_p). \tag{3.2.7}$$

Energy equation:

$$u_p \frac{\partial T_p}{\partial x} + v_p \frac{\partial T_p}{\partial y} = \frac{C_{pf}}{C_{mf}\tau_T}(T - T_p). \tag{3.2.8}$$

where u and u_p are the hybrid nanofluid, and dust phases velocity components in x-direction, respectively, while v and v_p are the hybrid nanofluid, and dust phases velocity components in y-direction, respectively, p is the fluid pressure, ρ_{hnf} is the density of hybrid nanofluid, μ_{hnf} is the dynamic viscosity of hybrid nanofluid, while N is the dust particle number, m, and K are dust particle mass, and the Stokes drag coefficient, respectively. Furthermore, T and T_p are the temperature for hybrid nanofluid and dust phases, respectively, k_{hnf} is the thermal conductivity of hybrid nanofluids, and $(\rho C_p)_{hnf}$ is the specific heat capacity of hybrid nanofluid, C_{pf} is the specific heat of nanofluid, C_{mf} is the specific heat of dust particles, τ_v is the dust particles relaxation time and τ_T is the dust particles thermal equilibrium of dusty hybrid nanofluid.

The Tiwari and Das model is implemented in this study where it considers the effects of nanoparticles volume fraction on the boundary layer flow. In addition, both the nanoparticles and the base fluid are presumed to be in thermal equilibrium, with the fluid flowing with uniform velocities. The formulas of the thermophysical properties of nanofluid and hybrid nanofluid, as well as the thermophysical properties of the nanoparticles and fluid employed, are delineated in Tables 3.1 and 3.2, respectively. In Table 3.1, subscript f, nf, and hnf implies the fluid, nanofluid, and hybrid nanofluid, while 1 and 2 implies the first and second nanoparticles.

Table 3.1
Physical Properties of Nanofluid and Hybrid Nanofluid (Anuar et al. (2021b))

Properties	Nanofluid	Hybrid Nanofluid
Density	$\rho_{nf} = (1-\phi_1)\rho_f + \phi_1\rho_1$	$\rho_{hnf} = (1-\phi_2)[(1-\phi_1)\rho_f + \phi_1\rho_1] + \phi_2\rho_2$
Heat Capacity	$(\rho C_p)_{nf} = (1-\phi_1)(\rho C_p)_f + \phi_1(\rho C_p)_1$	$(\rho C_p)_{hnf} = (1-\phi_2)[(1-\phi_1)(\rho C_p)_f + \phi_1(\rho C_p)_1] + \phi_2(\rho C_p)_2$
Dynamic viscosity	$\mu_{nf} = \dfrac{\mu_f}{(1-\phi_1)^{2.5}}$	$\mu_{hnf} = \dfrac{\mu_f}{(1-\phi_1)^{2.5}(1-\phi_2)^{2.5}}$
Thermal conductivity	$\dfrac{k_{nf}}{k_f} = \dfrac{k_1 + 2k_f - 2\phi_1(k_f - k_1)}{k_1 + 2k_f + \phi_1(k_f - k_1)}$	$\dfrac{k_{hnf}}{k_{nf}} = \dfrac{k_2 + 2k_{nf} - 2\phi_2(k_{nf} - k_2)}{k_2 + 2k_{nf} + \phi_2(k_{nf} - k_2)}$ where $\dfrac{k_{nf}}{k_f} = \dfrac{k_1 + 2k_f - 2\phi_1(k_f - k_1)}{k_1 + 2k_f + \phi_1(k_f - k_1)}$

Table 3.2
Thermophysical Properties of Nanoparticles and Base Fluid (Anuar et al. (2021b))

Physical properties	Al_2O_3	Cu	Base fluid (water)
$\rho(kg/m^3)$	3970	8933	997.1
$C_p(J/kgK)$	765	385	4179
$K(W/mK)$	40	400	0.613

3.2.2 Boundary Layer Approximation

The nonlinear partial differential equations (3.2.2)-(3.2.4) and (3.2.6)-(3.2.8) can be simplified by utilizing the boundary layer approximation, which omits one term of the second-order derivative. The procedure is conducted by employing orders of magnitude, with the magnitude of certain components are assumed as follows:

$$x \sim L, \qquad y \sim \delta, \qquad u \sim U_\infty, \qquad T \sim T_\infty, \qquad u_p \sim u, \qquad v_p \sim v, \qquad T_p \sim T, \tag{3.2.9}$$

where L is the length of surface, δ is the thickness of boundary layer, U_∞ is the free stream velocity. In the order of magnitude analysis, the smaller terms within the same equation will be eliminated (Schlichting, 1979; Nakayama, 1995).

i. Hybrid nanofluid phase

Based on equation (3.2.1), each of the term in (3.2.1) can be written as follows:

$$\frac{\partial u}{\partial x} \sim \frac{U_\infty}{L}, \qquad \frac{\partial v}{\partial y} \sim \frac{v}{\delta},$$

and

$$\frac{U_\infty}{L} \sim \frac{v}{\delta},$$

since $\partial v/\partial y$ must be of the same order as $\partial u/\partial x$ and $\partial u/\partial x \neq 0$, thus

$$v \sim \frac{U_\infty \delta}{L}. \tag{3.2.10}$$

Since the assumption of a boundary layer is particularly thin, thus

$$\frac{\delta}{L} \ll 1, \tag{3.2.11}$$

where in a boundary layer, the velocity component normal to the direction of fluid flow u is greater than the velocity component perpendicular to the direction of fluid flow v.

The components of equation (3.2.2) are written as follows:

$$\underbrace{u\frac{\partial u}{\partial x} + v\frac{\partial u}{\partial y}}_{\text{inertia}} = \underbrace{-\frac{1}{\rho_{hnf}}\frac{\partial p}{\partial x}}_{\text{pressure}} + \underbrace{\frac{\mu_{hnf}}{\rho_{hnf}}\left(\frac{\partial^2 u}{\partial x^2} + \frac{\partial^2 u}{\partial y^2}\right)}_{\text{viscosity}} + \underbrace{\frac{KN}{\rho_{hnf}}(u_p - u)}_{\text{dust particle}}.$$

Referring to equation (3.2.9), the orders of magnitude of inertia, pressure, viscosity, and dust particle terms are summarized in Table 3.3. Based on Bernoulli's equation, the pressure inside the boundary layer is assumed approximately equivalent to the pressure outside. In the momentum equation in x-direction is expressed as $p \sim \rho U_\infty^2$. From the result in the final column of Table 3.3, equation (3.2.11) is applied by retaining only the dominant terms, where terms with smaller magnitude are neglected as they approach zero and have negligible influence on the flow behavior.

Table 3.3
Order of Magnitude Analysis for Momentum Equation in x-direction

Terms	Using equation (3.2.9)	Summary	Order of magnitude $\times \frac{L}{U_\infty^2}$	$\delta \leqslant L$
$u\frac{\partial u}{\partial x}$	$U_\infty \frac{U_\infty}{L}$	$\frac{U_\infty^2}{L}$	$O(1)$	retain
$v\frac{\partial u}{\partial y}$	$\frac{U_\infty \delta}{L} \frac{U_\infty}{\delta}$	$\frac{U_\infty^2}{L}$	$O(1)$	retain
$-\frac{1}{\rho_{hnf}} \frac{\partial p}{\partial x}$	$\frac{1}{\rho_{hnf}} \frac{\rho_{hnf} U_\infty^2}{L}$	$\frac{U^2\infty}{L}$	$O(1)$	retain
$\frac{\mu_{hnf}}{\rho_{hnf}} \frac{\partial^2 u}{\partial x^2}$	$\frac{\mu_{hnf}}{\rho_{hnf}} \frac{U_\infty}{L^2}$		$\frac{\mu_{hnf}}{\rho_{hnf}} \frac{1}{LU_\infty}$	since $\frac{\partial^2 u}{\partial y^2} \gg \frac{\partial^2 u}{\partial x^2}$,
$\frac{\mu_{hnf}}{\rho_{hnf}} \frac{\partial^2 u}{\partial y^2}$	$\frac{\mu_{hnf}}{\rho_{hnf}} \frac{U_\infty}{\delta^2}$		$\frac{\mu_{hnf}}{\rho_{hnf}} \frac{L}{U_\infty \delta^2}$	therefore $\frac{\partial^2 u}{\partial x^2}$ can be eliminated.
$\frac{KN}{\rho_{hnf}}(u_p - u)$	$\frac{KN}{\rho_{hnf}} U_\infty$		$\frac{KN}{\rho_{hnf}} \frac{L}{U_\infty}$	retain

The viscous force and inertia force within the boundary layer are assumed to possess similar order of magnitudes. Therefore,

$$\frac{\mu_{hnf}}{\rho_{hnf}} \frac{L}{U_\infty \delta^2} \sim \frac{U_\infty^2}{L}, \tag{3.2.12}$$

which denotes the thickness of boundary layer δ to be

$$\begin{aligned} \delta &\sim \sqrt{\frac{\mu_{hnf}}{\rho_{hnf}} \frac{L}{U_\infty}}, \\ &\sim \sqrt{\nu_f \frac{L}{U_\infty}}, \end{aligned} \tag{3.2.13}$$

where ν_f is the kinematic viscosity of fluid where $\nu_f = \mu_f / \rho_f$. Thus, the assumption of the boundary layer to be particulary thin is true as mentioned in equation (3.2.11) when

$$\frac{\delta}{L} \sim Re_L^{-1/2} \ll 1, \tag{3.2.14}$$

or

$$Re_L \gg 1,$$

and

$$Re_L = \frac{U_\infty L}{\nu_f}. \tag{3.2.15}$$

In boundary layer approximation, the Reynolds number are only valid when $Re \to \infty$ (Schlichting and Gersten, 2017). Therefore, as stated in Table 3.3, $\partial^2 u/\partial y^2 \gg \partial^2 u/\partial x^2$. Thus, the term $\partial^2 u/\partial x^2$ is eliminated. After the execution of the order of magnitude, equation (3.2.2) is transformed into

$$u\frac{\partial u}{\partial x} + v\frac{\partial u}{\partial y} = -\frac{1}{\rho_{hnf}}\frac{\partial p}{\partial x} + \frac{\mu_{hnf}}{\rho_{hnf}}\frac{\partial^2 u}{\partial y^2} + \frac{KN}{\rho_{hnf}}(u_p - u). \tag{3.2.16}$$

The order of magnitude analysis is subsequently conducted on the momentum equation of y-direction as illustrated in Table 3.4. From Table 3.4 it is noticed that all terms can be eliminated except for the pressure term. Therefore, equation (3.2.3) can be written as

$$-\frac{1}{\rho_{hnf}}\frac{\partial p}{\partial y} = 0. \tag{3.2.17}$$

From equation (3.2.17), it is noted that the changes in pressure in y-direction is too small and negligible. Hence, the changes in pressure occur solely in x-direction which can be defined as $\partial p/\partial x = dp/dx$. Additionally, the pressure within the boundary layer is equivalent to the pressure in the free stream for any x-value, and equation (3.2.16) is independent of y, which becomes

$$U_\infty \frac{dU_\infty}{dx} = -\frac{1}{\rho_{hnf}}\frac{dp}{dx}, \tag{3.2.18}$$

which indicates

$$\frac{dp}{dx} = -\rho_{hnf} U_\infty \frac{dU_\infty}{dx}. \tag{3.2.19}$$

Table 3.4
Order of Magnitude Analysis for Momentum Equation in y-direction

Terms	Using equation (3.2.9)	Summary	Order of magnitude $\times \frac{\delta}{U_\infty^2}$	$\delta \leqslant L$
$u\frac{\partial v}{\partial x}$	$U_\infty \frac{U_\infty \delta}{L^2}$	$\frac{U_\infty^2 \delta}{L^2}$	$\frac{\delta^2}{L^2}$	≈ 0
$v\frac{\partial v}{\partial y}$	$\left(\frac{U_\infty \delta}{L}\right)^2 \frac{1}{\delta}$	$\frac{U_\infty^2 \delta}{L^2}$	$\frac{\delta^2}{L^2}$	≈ 0
$-\frac{1}{\rho_{hnf}}\frac{\partial p}{\partial y}$	$\frac{1}{\rho_{hnf}} \frac{\rho_{hnf} U_\infty^2}{\delta}$	$\frac{U_\infty^2}{\delta}$	$O(1)$	retain
$\frac{\mu_{hnf}}{\rho_{hnf}}\frac{\partial^2 v}{\partial x^2}$	$\frac{\mu_{hnf}}{\rho_{hnf}} \frac{U_\infty \delta}{L} \frac{1}{L^2}$	$\frac{\mu_{hnf}}{\rho_{hnf}} \frac{U_\infty \delta}{L^3}$	$\frac{\delta^2}{L^3 U_\infty}$	≈ 0
$\frac{\mu_{hnf}}{\rho_{hnf}}\frac{\partial^2 v}{\partial y^2}$	$\frac{\mu_{hnf}}{\rho_{hnf}} \frac{U_\infty \delta}{L} \frac{1}{\delta^2}$	$\frac{\mu_{hnf}}{\rho_{hnf}} \frac{U_\infty}{L\delta}$	$\frac{1}{LU_\infty}$	≈ 0
$\frac{KN}{\rho_{hnf}}(v_p - v)$	$\frac{KN}{\rho_{hnf}} U_\infty$		$\frac{KN}{\rho_{hnf}} \frac{\delta}{U_\infty}$	≈ 0

Substituting equation (3.2.18) to equation (3.2.16) yields to the following equation:

$$u\frac{\partial u}{\partial x} + v\frac{\partial u}{\partial y} = U_\infty \frac{dU_\infty}{dx} + \frac{\mu_{hnf}}{\rho_{hnf}}\frac{\partial^2 u}{\partial y^2} + \frac{KN}{\rho_{hnf}}(u_p - u). \tag{3.2.20}$$

Given that U_∞ is a constant, equation (3.2.20) can be written as

$$u\frac{\partial u}{\partial x} + v\frac{\partial u}{\partial y} = \frac{\mu_{hnf}}{\rho_{hnf}}\frac{\partial^2 u}{\partial y^2} + \frac{KN}{\rho_{hnf}}(u_p - u). \tag{3.2.21}$$

Further, the order of magnitude for energy equation (3.2.4) is exhibited in Table 3.5.

Table 3.5
Order of Magnitude Analysis for Energy Equation

Terms	Using equation (3.2.9)	Summary	Order of magnitude $\times \frac{L}{U_\infty T_\infty}$	$\delta \leqslant L$
$u\frac{\partial T}{\partial x}$	$U_\infty \frac{T_\infty}{L}$	$\frac{U_\infty T_\infty}{L}$	$O(1)$	retain
$v\frac{\partial T}{\partial y}$	$\frac{U_\infty \delta}{L}\frac{T_\infty}{\delta}$	$\frac{U_\infty T_\infty}{L}$	$O(1)$	retain
$\frac{k_{hnf}}{(\rho C_p)_{hnf}}\frac{\partial^2 T}{\partial x^2}$	$\frac{k_{hnf}}{(\rho C_p)_{hnf}}\frac{T_\infty}{2}$		$\frac{k_{hnf}}{(\rho C_p)_{hnf}}\frac{1}{LU_\infty}$	since $\frac{\partial^2 T}{\partial y^2} \gg \frac{\partial^2 T}{\partial x^2}$,
$\frac{k_{hnf}}{(\rho C_p)_{hnf}}\frac{\partial^2 T}{\partial y^2}$	$\frac{k_{hnf}}{(\rho C_p)_{hnf}}\frac{T_\infty}{\delta^2}$		$\frac{k_{hnf}}{(\rho C_p)_{hnf}}\frac{L}{\delta^2 U_\infty}$	then $\frac{\partial^2 T}{\partial x^2}$ is eliminated.
$\frac{NC_{pf}}{(\rho C_p)_{hnf}\tau_T}(T_p - T)$	$\frac{NC_{pf}T_\infty}{(\rho C_p)_{hnf}\tau_T}$		$\frac{NC_{pf}}{(\rho C_p)_{hnf}\tau_T}\frac{L}{U_\infty}$	retain
$\frac{N}{(\rho C_p)_{hnf}\tau_v}(u_p - u)^2$	$\frac{NU_\infty}{(\rho C_p)_{hnf}\tau_v}$		$\frac{N}{(\rho C_p)_{hnf}\tau_v}\frac{L}{T_\infty}$	retain
$\frac{\mu_{hnf}}{(\rho C_p)_{hnf}}\left(\frac{\partial u}{\partial y}\right)^2$	$\frac{\mu_{hnf}}{(\rho C_p)_{hnf}}\frac{U_\infty}{\delta}$		$\frac{\mu_{hnf}}{(\rho C_p)_{hnf}}\frac{L}{\delta T_\infty}$	retain

Thus, the energy equation (3.2.4) becomes

$$u\frac{\partial T}{\partial x} + v\frac{\partial T}{\partial y} = \frac{k_{hnf}}{(\rho C_p)_{hnf}}\frac{\partial^2 T}{\partial y^2} + \frac{NC_{pf}}{(\rho C_p)_{hnf}\tau_T}(T_p - T) + \frac{N}{(\rho C_p)_{hnf}\tau_v}(u_p - u)^2 + \frac{\mu_{hnf}}{(\rho C_p)_{hnf}}\left(\frac{\partial u}{\partial y}\right)^2. \tag{3.2.22}$$

ii. Dust phase

Based on equation (3.2.5), each of the term in (3.2.5) can be written as follows:

$$\frac{\partial u_p}{\partial x} \sim \frac{U_\infty}{L}, \qquad \frac{\partial v_p}{\partial y} \sim \frac{v}{\delta},$$

and

$$\frac{U_\infty}{L} \sim \frac{v_p}{\delta},$$

since $\partial v_p/\partial y$ must be of the same order as $\partial u_p/\partial x$ and $\partial u_p/\partial x \neq 0$, thus

$$v_p \sim \frac{U_\infty \delta}{L}. \tag{3.2.23}$$

The order of magnitude analysis is performed to the momentum equation in x-direction for the dust phase as shown in Table 3.6.

Table 3.6
Order of Magnitude Analysis for Momentum Equation in x-direction

Terms	Using equation (3.2.9)	Summary	Order of magnitude $\times\frac{L}{U_\infty^2}$	$\delta \leqslant L$
$u_p\left(\frac{\partial u_p}{\partial x}\right)$	$U_\infty \frac{U_\infty}{L}$	$\frac{U_\infty^2}{L}$	$O(1)$	retain
$v_p\left(\frac{\partial u_p}{\partial y}\right)$	$\frac{U_\infty \delta}{L}\frac{U_\infty}{\delta}$	$\frac{U_\infty^2}{L}$	$O(1)$	retain
$\frac{K}{m}(u-u_p)$	$\frac{K}{m}U_\infty$		$\frac{K}{m}\frac{L}{U_\infty}$	retain

From the order of magnitude analysis conducted, it is noted that all the terms are retained, and equation (3.2.6) remains as follows:

$$u_p\frac{\partial u_p}{\partial x} + v_p\frac{\partial u_p}{\partial y} = \frac{K}{m}(u-u_p).$$

Table 3.7 displays the order of magnitude analysis for y-direction for dust phase. Based on the analysis conducted in Table 3.7, all the terms are negligible. Further, the analysis for energy equation (3.2.8) is depicted in Table 3.8. From the order of magnitude analysis, equation (3.2.8) remains as below:

$$u_p\frac{\partial T_p}{\partial x} + v_p\frac{\partial T_p}{\partial y} = \frac{C_{pf}}{C_{mf}\tau_T}(T-T_p).$$

Table 3.7
Order of Magnitude Analysis for Momentum Equation in y-direction

Terms	Using equation (3.2.9)	Summary	Order of magnitude $\times \frac{\delta}{U_\infty^2}$	$\delta \leqslant L$
$u_p \frac{\partial v_p}{\partial x}$	$U_\infty \left(\frac{U_\infty \delta}{L^2}\right)$	$\frac{U_\infty^2 \delta}{L^2}$	$\frac{\delta^2}{L^2}$	≈ 0
$v_p \left(\frac{\partial v_p}{\partial y}\right)$	$\left(\frac{U_\infty \delta}{L}\right)^2 \frac{1}{\delta}$	$\frac{U_\infty^2 \delta}{L^2}$	$\frac{\delta^2}{L^2}$	≈ 0
$\frac{K}{m}(v - v_p)$	$\frac{K}{m} U_\infty$		$\frac{K}{m} \frac{\delta}{U_\infty}$	≈ 0

Table 3.8
Order of Magnitude Analysis for Energy Equation

Terms	Using equation (3.2.9)	Summary	Order of magnitude $\times \frac{L}{U_\infty T_\infty}$	$\delta \leqslant L$
$u_p \frac{\partial T_p}{\partial x}$	$U_\infty \frac{T_\infty}{L}$	$\frac{U_\infty T_\infty}{L}$	$O(1)$	retain
$v_p \frac{\partial T_p}{\partial y}$	$\frac{U_\infty \delta}{L} \frac{T_\infty}{\delta}$	$\frac{U_\infty T_\infty}{L}$	$O(1)$	retain
$\frac{C_{pf}}{C_{mf} \tau_T}(T - T_p)$	$\frac{C_{pf}}{C_{mf} \tau_T} T_\infty$		$\frac{C_{pf}}{C_{mf} \tau_T} \frac{L}{U_\infty}$	retain

The boundary conditions for the first problem considered in Chapter 4 can be presented as follows:

$$
\begin{aligned}
& u = \lambda U_w(x) + L_s \left(\frac{\partial u}{\partial y}\right), v = v_w, T = T_w + L_T \left(\frac{\partial T}{\partial y}\right), \quad \text{at} \quad y = 0, \\
& u \to 0, u_p \to 0, v_p \to v, T_p \to T_\infty, T \to T_\infty, \quad \text{as} \quad y \to \infty,
\end{aligned} \tag{3.2.24}
$$

where $\lambda > 0$ is a stretching surface, $\lambda < 0$ is a shrinking surface, while $\lambda = 0$ is a static surface, L_s is the velocity slip length, and L_T is the thermal slip length.

3.3 Similarity Transformation

The similarity transformation is employed to simplify the complex nonlinear partial differential equations by reducing them to a system of ordinary differential equations, thereby facilitating the solution of the problem under consideration. This approach simplifies two independent variables into one by introducing a set of appropriate similarity variables. Here, the variables x and y are reduced to a new single independent variable, η, where it can be expressed as (Hansen, 1964; Arpaci and Larsen, 1984)

$$\eta = \frac{y}{\delta(x)}, \tag{3.3.1}$$

where the thickness of boundary layer $\delta(x)$ in equation (3.2.13) can be defined as

$$\delta(x) = \left(\frac{\nu_f x}{U_\infty}\right)^{1/2}. \tag{3.3.2}$$

By substituting equation (3.3.2) into equation (3.3.1), η can be stated as

$$\eta = \left(\frac{U_\infty}{\nu_f x}\right)^{1/2} y. \tag{3.3.3}$$

Further, dimensionless velocity can be denoted as (Schlichting, 1979)

$$g(\eta) = \frac{u}{U_\infty}. \tag{3.3.4}$$

The stream function $\psi(x,y)$ is denoted as

$$u = \frac{\partial \psi}{\partial y} \qquad \text{and} \qquad v = -\frac{\partial \psi}{\partial x}, \tag{3.3.5}$$

where it transform the velocity component variables u and v as a function, thus, satisfying the continuity equation of fluid and dust phases of equations (3.2.1) and (3.2.5), respectively as mentioned by Kays, Crawford, and Weigand (1980). The formulation of stream function (ψ) is derived by employing (3.3.4) and u in equation (3.3.5) can be expressed as

$$u = \frac{\partial \psi}{\partial y} = \frac{\partial \psi}{\partial \eta}\frac{\partial \eta}{\partial y}. \tag{3.3.6}$$

Next, the term $\partial\eta/\partial y$ is replaced by differentiating η from equation (3.3.3) with respect to y and substitute the term u from equation (3.3.4) into equation (3.3.6). Hence, we obtain

$$\frac{\partial \psi}{\partial \eta} = U_\infty g(\eta)\left(\frac{\nu_f x}{U_\infty}\right)^{1/2} = \left(\nu_f x U_\infty\right)^{1/2} g(\eta). \tag{3.3.7}$$

Then, to obtain ψ, equation (3.3.7) is integrated with respect to η. Thus, ψ can be written as

$$\begin{aligned} \psi &= \left(\nu_f x U_\infty\right)^{1/2} \int g(\eta) d\eta, \\ \psi &= \left(\nu_f x U_\infty\right)^{1/2} f'(\eta), \end{aligned} \tag{3.3.8}$$

where f represents the dimensionless stream function and $f'(\eta) = g(\eta)$. A similarity variable for the thermal field in the case of constant fixed temperature, as proposed by Polhausen (1921) which known as dimensionless temperature, $\theta(\eta)$ is denoted by

$$\theta(\eta) = \frac{T - T_\infty}{T_w - T_\infty}, \tag{3.3.9}$$

where $\theta(\eta)$ also represents the ratio of temperature difference. The dimensionless temperature for dust phase is denoted by

$$\theta_p(\eta) = \frac{T_p - T_\infty}{T_w - T_\infty}. \tag{3.3.10}$$

In order to obtain the similarity solutions, the temperature at the surface (T_w) are assumed to be

$$T_w = T_\infty + A\left(\frac{x}{l}\right)^2, \tag{3.3.11}$$

where A is a constant and $l = \sqrt{\nu_f / a}$ is the characteristic length.

3.3.1 Formulation of Continuity Equation for Hybrid Nanofluid and Dust Phases

The governing equation for continuity equation of hybrid nanofluid and dust phases, (3.2.1) and (3.2.5), respectively are satisfied by implementing the similarity variables (3.3.3), (3.3.5), and (3.3.8). Therefore, the formulation of continuity equation for hybrid nanofluid are as follows:

i. Hybrid nanofluid phase

$$\frac{\partial u}{\partial x}+\frac{\partial v}{\partial y}=0,$$

where

$$u=\frac{\partial \psi}{\partial y}, v=-\frac{\partial \psi}{\partial x}.$$

By substituting $U_w(x)=ax$ into (3.3.3) and (3.3.8), becomes

$$\eta=\left(\frac{a}{\nu_f}\right)^{1/2} y, \tag{3.3.12}$$

$$\psi=(a\nu_f)^{1/2} x f(\eta). \tag{3.3.13}$$

Differentiating (3.3.12) with respect to x, we obtain

$$\frac{\partial \eta}{\partial x}=0. \tag{3.3.14}$$

Differentiating (3.3.12) with respect to y, we obtain

$$\frac{\partial \eta}{\partial y}=\left(\frac{a}{\nu_f}\right)^{1/2}. \tag{3.3.15}$$

Next, differentiating equation (3.3.13) with respect to x, we obtain

$$\begin{aligned}\frac{\partial \psi}{\partial x}&=(a\nu_f)^{1/2}\left[x\left(\frac{\partial f}{\partial \eta}.\frac{\partial \eta}{\partial x}\right)+f\right],\\ &=(a\nu_f)^{1/2}\left[x\left(\frac{\partial f}{\partial \eta}.0\right)+f\right],\\ &=(a\nu_f)^{1/2} f,\\ v&=-(a\nu_f)^{1/2} f. \end{aligned} \tag{3.3.16}$$

Differentiating equation (3.3.13) with respect to y, we obtain

$$\begin{aligned}
\frac{\partial \psi}{\partial y} &= (a\nu_f)^{1/2} x \frac{\partial f}{\partial\, y}, \\
&= (a\nu_f)^{1/2} x \left(\frac{\partial f}{\partial \eta} . \frac{\partial \eta}{\partial y} \right), \\
&= (a\nu_f)^{1/2} x \frac{\partial f}{\partial \eta} . \left(\frac{a}{\nu_f} \right)^{1/2}, \\
&= axf', \\
u &= axf'. \qquad (3.3.17)
\end{aligned}$$

From equation (3.3.16), differentiate with respect to y, to obtain $\partial v / \partial y$ as follows:

$$\begin{aligned}
v &= -(a\nu_f)^{1/2} f, \\
\frac{\partial v}{\partial y} &= -\left[(a\nu_f)^{1/2} \frac{\partial f}{\partial y} + 0 \right], \\
&= -\left[(a\nu_f)^{1/2} \frac{\partial f}{\partial \eta} . \frac{\partial \eta}{\partial y} + 0 \right], \\
&= -\left[(a\nu_f)^{1/2} \frac{\partial f}{\partial \eta} . \left(\frac{a}{\nu_f} \right)^{1/2} \right], \\
&= -af'. \qquad (3.3.18)
\end{aligned}$$

Then, from equation (3.3.17), differentiate with respect to x, to obtain $\partial u / \partial x$ as follows:

$$\begin{aligned}
u &= axf', \\
\frac{\partial u}{\partial x} &= \left[ax \frac{\partial f'}{\partial x} + af' \right],
\end{aligned}$$

$$
\begin{aligned}
&= \left[ax\frac{\partial f'}{\partial \eta}.\frac{\partial \eta}{\partial x} + af'\right], \\
&= \left[ax\frac{\partial f'}{\partial \eta}.0 + af'\right], \\
&= af'. \qquad (3.3.19)
\end{aligned}
$$

Finally, substitute (3.3.18) and (3.3.19) into continuity equation (3.2.1), we obtain

$$
\begin{aligned}
\frac{\partial u}{\partial x} + \frac{\partial v}{\partial y} &= af' + -af', \\
&= 0.
\end{aligned}
$$

Thus, continuity equation for hybrid nanofluid phase (3.2.1) is satisfied. Futhermore, the formulation of the continuity equation for the dust phase are as follows:

ii. Dust phase

$$
\frac{\partial u_p}{\partial x} + \frac{\partial v_p}{\partial y} = 0.
$$

From equations (3.3.16) and (3.3.17) becomes

$$
u_p = axf_p', v_p = -(a\nu_f)^{1/2} f_p. \qquad (3.3.20)
$$

From equation (3.3.20) differentiate v_p and u_p with the respect to y and x, respectively, as below

$$
\begin{aligned}
v_p &= -(a\nu_f)^{1/2} f_p, \\
\frac{\partial v_p}{\partial y} &= -\left[(a\nu_f)^{1/2}\frac{\partial f_p}{\partial y} + 0\right],
\end{aligned}
$$

$$
\begin{aligned}
&= -\left[(a\nu_f)^{1/2}\frac{\partial f_p}{\partial \eta}.\frac{\partial \eta}{\partial y}+0\right], \\
&= -\left[(a\nu_f)^{1/2}\frac{\partial f_p}{\partial \eta}.\left(\frac{a}{\nu_f}\right)^{1/2}\right], \\
&= -af_p'. \qquad (3.3.21)
\end{aligned}
$$

$$
\begin{aligned}
u_p &= axf_p', \\
\frac{\partial u_p}{\partial x} &= \left[ax\frac{\partial f_p'}{\partial x}+af_p'\right], \\
&= \left[ax\frac{\partial f_p'}{\partial \eta}.\frac{\partial \eta}{\partial x}+af_p'\right], \\
&= \left[ax\frac{\partial f_p'}{\partial \eta}.0+af_p'\right], \\
&= af_p'. \qquad (3.3.22)
\end{aligned}
$$

Finally, substitute (3.3.21) and (3.3.22) into continuity equation for dust phase (3.2.5) and it becomes

$$
\begin{aligned}
\frac{\partial u_p}{\partial x}+\frac{\partial v_p}{\partial y} &= af_p'+-af_p', \\
&= 0.
\end{aligned}
$$

Thus, continuity equation for dust phase (3.2.5) is satisfied.

3.3.2 Formulation of Momentum Equation for Hybrid Nanofluid and Dust Phases

The governing equation for momentum equation of hybrid nanofluid and dust phases, (3.2.21) and (3.2.6), respectively, are reduced to ODE by implementing the similarity variables (3.3.16), (3.3.17), (3.3.19), and (3.3.20). Thus, the formulation of momentum equation for hybrid nanofluid are as follows:

i. Hybrid nanofluid phase

$$u\frac{\partial u}{\partial x}+v\frac{\partial u}{\partial y}=\frac{\mu_{hnf}}{\rho_{hnf}}\frac{\partial^2 u}{\partial y^2}+\frac{KN}{\rho_{hnf}}(u_p-u).$$

Find the values of $u\frac{\partial u}{\partial x}$, $v\frac{\partial u}{\partial y}$, $\frac{\mu_{hnf}}{\rho_{hnf}}\frac{\partial^2 u}{\partial y^2}$, u_p-u, and $\frac{KN}{\rho_{hnf}}(u_p-u)$,

$$u\frac{\partial u}{\partial x}=a^2xf'^2, \tag{3.3.23}$$

$$v\frac{\partial u}{\partial y}=-a^2xff'', \tag{3.3.24}$$

$$\frac{\mu_{hnf}}{\rho_{hnf}}\frac{\partial^2 u}{\partial y^2}=\frac{\mu_{hnf}}{\rho_{hnf}}\frac{a^2xf'''}{\nu_f}, \tag{3.3.25}$$

$$u_p-u=ax\left(f'_p-f'\right), \tag{3.3.26}$$

$$\frac{KN}{\rho_{hnf}}(u_p-u)=\frac{KN}{\rho_{hnf}}\left[ax\left(f'_p-f'\right)\right]. \tag{3.3.27}$$

Next, substitute equations (3.3.23)-(3.3.27) into momentum equation (3.2.21) and the equation becomes

$$a^2xf'^2+\left(-a^2xff''\right)=\frac{\mu_{hnf}}{\rho_{hnf}}\frac{a^2xf'''}{\nu_f}+\frac{KN}{\rho_{hnf}}\left[ax\left(f'_p-f'\right)\right]. \tag{3.3.28}$$

Multiply both sides with $\left(\frac{1}{a^2x}\right)$, becomes

$$\frac{\mu_{hnf}}{\rho_{hnf}}\frac{f'''}{\nu_f}+\frac{KN}{\rho_{hnf}}\left(\frac{1}{a}\right)\left(f'_p-f'\right)-f'^2+ff''=0, \tag{3.3.29}$$

$$\frac{\mu_{hnf}}{\rho_{hnf}}\frac{\rho_f}{\mu_f}f'''+ff''-f'^2+\frac{\left(\frac{m}{\tau_v}\right)N}{\rho_{hnf}}\left(\frac{1}{a}\right)\left(f'_p-f'\right)=0, \tag{3.3.30}$$

where, $K = \left(\dfrac{m}{\tau_v}\right)$

$$\frac{\mu_{hnf}}{\rho_{hnf}}\frac{\rho_f}{\mu_f}f''' + ff'' - f'^2 + \frac{Nm\left(\dfrac{1}{a\tau_v}\right)}{\rho_{hnf}}\left(f_p' - f'\right) = 0. \tag{3.3.31}$$

Then, multiply with $\dfrac{\rho_f}{\rho_f}$, becomes

$$\frac{\mu_{hnf}}{\rho_{hnf}}\frac{\rho_f}{\mu_f}f''' + ff'' - f'^2 + \frac{\dfrac{Nm}{\rho_f}\left(\dfrac{1}{a\tau_v}\right)}{\rho_{hnf}/\rho_f}\left(f_p' - f'\right) = 0, \tag{3.3.32}$$

$$\frac{\mu_{hnf}/\mu_f}{\rho_{hnf}/\rho_f}f''' + ff'' - f'^2 + \frac{L\beta_v}{\rho_{hnf}/\rho_f}\left(f_p' - f'\right) = 0, \tag{3.3.33}$$

where, $L = \dfrac{Nm}{\rho_f}$ and $\beta_v = \dfrac{1}{a\tau_v}$.

Then, substitute the value of physical properties of nanofluid and hybrid nanofluid of $\mu_{hnf} = \dfrac{\mu_f}{(1-\phi_1)^{2.5}(1-\phi_2)^{2.5}}$ and $\rho_{hnf} = (1-\phi_2)\left[(1-\phi_1)\rho_f + \phi_1\rho_1\right] + \phi_2\rho_2$ from Table 3.1 into equation (3.3.33) and it becomes

$$\frac{1}{(1-\phi_1)^{2.5}(1-\phi_2)^{3.5}\left[(1-\phi_1) + \phi_1\dfrac{\rho_1}{\rho_f}\right] + \phi_2\dfrac{\rho_2}{\rho_f}}f''' + ff'' - f'^2$$
$$+ \frac{L\beta_v}{(1-\phi_2)\left[(1-\phi_1) + \phi_1\dfrac{\rho_1}{\rho_f}\right] + \phi_2\dfrac{\rho_2}{\rho_f}}\left(f_p' - f'\right) = 0. \tag{3.3.34}$$

Futhermore, the formulation of the momentum equation for the dust phase are as follows:

ii. Dust phase

$$u_p\frac{\partial u_p}{\partial x} + v_p\frac{\partial u_p}{\partial y} = \frac{K}{m}(u - u_p).$$

Find the values of $u_p \dfrac{\partial u_p}{\partial x}$, $v_p \dfrac{\partial u_p}{\partial y}$, $u - u_p$, and $\dfrac{K}{m}(u-u_p)$,

$$u_p \frac{\partial u_p}{\partial x} = a^2 x f_p'^2, \tag{3.3.35}$$

$$v_p \frac{\partial u_p}{\partial y} = -a^2 x f_p f_p'', \tag{3.3.36}$$

$$u - u_p = ax\left(f' - f_p'\right), \tag{3.3.37}$$

$$\frac{K}{m}(u-u_p) = \frac{K}{m}\left[ax\left(f' - f_p'\right)\right]. \tag{3.3.38}$$

Next, substitute equations (3.3.35)-(3.3.38) into momentum equation (3.2.6) and it becomes

$$a^2 x f_p'^2 + \left(-a^2 x f_p f_p''\right) = \frac{K}{m}\left[ax\left(f' - f_p'\right)\right], \tag{3.3.39}$$

$$a^2 x f_p f_p'' - a^2 x f_p'^2 + \frac{K}{m}\left[ax\left(f' - f_p'\right)\right] = 0. \tag{3.3.40}$$

Then, multiply both sides with $\dfrac{1}{a^2 x}$

$$f_p f_p'' - f_p'^2 + \frac{K}{m}\left[\frac{1}{a}\left(f' - f_p'\right)\right] = 0, \tag{3.3.41}$$

where, $K = \left(\dfrac{m}{\tau_v}\right)$

$$f_p f_p'' - f_p'^2 + \frac{m/\tau_v}{m}\left[\frac{1}{a}\left(f' - f_p'\right)\right] = 0, \tag{3.3.42}$$

$$f_p f_p'' - f_p'^2 + \frac{1}{a\tau_v}\left(f' - f_p'\right) = 0, \tag{3.3.43}$$

$$f_p f_p'' - f_p'^2 + \beta_v\left(f' - f_p'\right) = 0, \tag{3.3.44}$$

where, $\beta_v = \dfrac{1}{a\tau_v}$.

3.3.3 Formulation of Energy Equation for Hybrid Nanofluid and Dust Phases

The governing equation for energy equation of hybrid nanofluid and dust phases, (3.2.22) and (3.2.8), respectively, are reduced to ODE by implementing the similarity variables (3.3.9), (3.3.10), (3.3.11), (3.3.16), (3.3.17), and (3.3.20). Thus, the formulation of energy equation for hybrid nanofluid are as follows:

i. Hybrid nanofluid phase

$$u\frac{\partial T}{\partial x}+v\frac{\partial T}{\partial y}=\frac{k_{hnf}}{(\rho C_p)_{hnf}}\frac{\partial^2 T}{\partial y^2}+\frac{NC_{pf}}{(\rho C_p)_{hnf}\tau_T}(T_p-T)+\frac{N}{(\rho C_p)_{hnf}\tau_v}(u_p-u)^2+\frac{\mu_{hnf}}{(\rho C_p)_{hnf}}\left(\frac{\partial u}{\partial y}\right)^2,$$

where

$$\theta=\frac{T-T_\infty}{T_w-T_\infty},\theta_p=\frac{T_p-T_\infty}{T_w-T_\infty},T_w=T_\infty+A\left(\frac{x}{l}\right)^2.$$

Find the values of T, $\frac{\partial T}{\partial x}$, $u\frac{\partial T}{\partial x}$, $\frac{\partial T}{\partial y}$, $v\frac{\partial T}{\partial y}$, $\frac{\partial^2 T}{\partial y^2}$, T_p-T, $(u_p-u)^2$, $\frac{\partial u}{\partial y}$, $\left(\frac{\partial u}{\partial y}\right)^2$,

$$T=\theta A\left(\frac{x}{l}\right)^2+T_\infty, \tag{3.3.45}$$

$$\frac{\partial T}{\partial x}=\frac{2Ax}{l^2}\theta, \tag{3.3.46}$$

$$u\frac{\partial T}{\partial x}=2Aa\left(\frac{x}{l}\right)^2 f'\theta, \tag{3.3.47}$$

$$\frac{\partial T}{\partial y}=A\left(\frac{x}{l}\right)^2\left(\frac{a}{\nu_f}\right)^{1/2}\theta', \tag{3.3.48}$$

$$v\frac{\partial T}{\partial y}=-Aa\left(\frac{x}{l}\right)^2 f\theta', \tag{3.3.49}$$

$$\frac{\partial^2 T}{\partial y^2}=A\left(\frac{x}{l}\right)^2\left(\frac{a}{\nu_f}\right)\theta'', \tag{3.3.50}$$

$$\frac{\partial u}{\partial y} = axf'' \left(\frac{a}{\nu_f}\right)^{1/2}, \tag{3.3.51}$$

$$\left(\frac{\partial u}{\partial y}\right)^2 = a^2x^2f''^2 \left(\frac{a}{\nu_f}\right), \tag{3.3.52}$$

$$(T_p - T) = A\left(\frac{x}{l}\right)^2 (\theta_p - \theta), \tag{3.3.53}$$

$$(u_p - u)^2 = \left[ax\left(f_p' - f'\right)\right]^2. \tag{3.3.54}$$

Then, substitute equations (3.3.45)-(3.3.54) into $\frac{k_{hnf}}{(\rho C_p)_{hnf}}\frac{\partial^2 T}{\partial y^2}, \frac{NC_{pf}}{(\rho C_p)_{hnf}\tau_T}$ $(T_p - T), \frac{N}{(\rho C_p)_{hnf}\tau_v}(u_p - u)^2, \frac{\mu_{hnf}}{(\rho C_p)_{hnf}}\left(\frac{\partial u}{\partial y}\right)^2$, becomes

$$\frac{k_{hnf}}{(\rho C_p)_{hnf}}\frac{\partial^2 T}{\partial y^2} = \frac{k_{hnf}}{(\rho C_p)_{hnf}}A\left(\frac{x}{l}\right)^2\left(\frac{a}{\nu_f}\right)\theta'', \tag{3.3.55}$$

$$\frac{NC_{pf}}{(\rho C_p)_{hnf}\tau_T}(T_p - T) = \frac{NC_{pf}}{(\rho C_p)_{hnf}\tau_T}\left[A\left(\frac{x}{l}\right)^2(\theta_p - \theta)\right], \tag{3.3.56}$$

$$\frac{N}{(\rho C_p)_{hnf}\tau_v}(u_p - u)^2 = \frac{N}{(\rho C_p)_{hnf}\tau_v}\left[ax\left(f_p' - f'\right)\right]^2, \tag{3.3.57}$$

$$\frac{\mu_{hnf}}{(\rho C_p)_{hnf}}\left(\frac{\partial u}{\partial y}\right)^2 = \frac{\mu_{hnf}}{(\rho C_p)_{hnf}}a^2x^2f''^2\left(\frac{a}{\nu_f}\right). \tag{3.3.58}$$

Next, substitute equation (3.3.55)-(3.3.58) into energy equation (3.2.22) and it becomes

$$\begin{aligned}
2Aa\left(\frac{x}{l}\right)^2 f'\theta - Aa\left(\frac{x}{l}\right)^2 f\theta' &= \frac{k_{hnf}}{(\rho C_p)_{hnf}}A\left(\frac{x}{l}\right)^2\left(\frac{a}{\nu_f}\right)\theta'' \\
&+ \frac{NC_{pf}}{(\rho C_p)_{hnf}\tau_T}\left[A\left(\frac{x}{l}\right)^2(\theta_p - \theta)\right] + \frac{N}{(\rho C_p)_{hnf}\tau_v}\left[ax\left(f_p' - f'\right)\right]^2 \\
&+ \frac{\mu_{hnf}}{(\rho C_p)_{hnf}}a^2x^2f''^2\left(\frac{a}{\nu_f}\right),
\end{aligned} \tag{3.3.59}$$

$$\frac{k_{hnf}}{(\rho C_p)_{hnf}}A\left(\frac{x}{l}\right)^2\left(\frac{a}{\nu_f}\right)\theta''+Aa\left(\frac{x}{l}\right)^2 f\theta'-2Aa\left(\frac{x}{l}\right)^2 f'\theta$$
$$+\frac{NC_{pf}}{(\rho C_p)_{hnf}\tau_T}\left[A\left(\frac{x}{l}\right)^2(\theta_p-\theta)\right]+\frac{N}{(\rho C_p)_{hnf}\tau_v}\left[ax\left(f_p'-f'\right)\right]^2$$
$$\frac{\mu_{hnf}}{(\rho C_p)_{hnf}}a^2x^2f''^2\left(\frac{a}{\nu_f}\right)=0. \tag{3.3.60}$$

Then, multiply with $\left(\frac{1}{Aa}\right)\left(\frac{l}{x}\right)^2$,

$$\frac{k_{hnf}}{(\rho C_p)_{hnf}}\left(\frac{1}{\nu_f}\right)\theta''+f\theta'-2f'\theta+\frac{NC_{pf}}{(\rho C_p)_{hnf}}\frac{1}{a\tau_T}\left[(\theta_p-\theta)\right]$$
$$+\frac{N}{(\rho C_p)_{hnf}}\frac{1}{a\tau_v}\frac{a^2l^2}{A}\left(f_p'-f'\right)^2+\frac{\mu_{hnf}}{(\rho C_p)_{hnf}}\frac{a^2l^2}{A}\left(\frac{1}{\nu_f}\right)f''^2=0, \tag{3.3.61}$$

$$\frac{k_{hnf}}{(\rho C_p)_{hnf}}\left[\frac{(\rho C_p)_f}{k_f Pr}\right]\theta''+f\theta'-2f'\theta+\frac{NC_{pf}\beta_T}{(\rho C_p)_{hnf}}(\theta_p-\theta)$$
$$+\frac{N\beta_v}{(\rho C_p)_{hnf}}\frac{a^2l^2}{A}\left(f_p'-f'\right)^2+\frac{\mu_{hnf}}{(\rho C_p)_{hnf}}\left(\frac{\rho_f}{\mu_f}\right)\frac{a^2l^2}{A}f''^2=0, \tag{3.3.62}$$

where, $\beta_T=\frac{1}{a\tau_T},\beta_v=\frac{1}{a\tau_v},\mathrm{Pr}=\frac{(\mu C_p)_f}{k_f}$

$$\frac{k_{hnf}/k_f}{(\rho C_p)_{hnf}/(\rho C_p)_f}\left(\frac{1}{\mathrm{Pr}}\right)\theta''+f\theta'-2f'\theta+\frac{NC_{pf}\beta_T}{(\rho C_p)_{hnf}}(\theta_p-\theta)$$
$$+\frac{N\beta_v}{(\rho C_p)_{hnf}}\frac{a^2l^2}{A}\left(f_p'-f'\right)^2+\frac{\mu_{hnf}/\mu_f}{(\rho C_p)_{hnf}/\rho_f}\frac{a^2l^2}{A}f''^2=0, \tag{3.3.63}$$

$$\frac{k_{hnf}/k_f}{(\rho C_p)_{hnf}/(\rho C_p)_f}\left(\frac{1}{\mathrm{Pr}}\right)\theta''+f\theta'-2f'\theta+\frac{L\beta_T}{m(\rho C_p)_{hnf}/(\rho C_p)_f}(\theta_p-\theta)$$
$$+\frac{L\beta_v\mathrm{Ec}^*}{m(\rho C_p)_{hnf}/(\rho C_p)_f}\left(f_p'-f'\right)^2+\frac{\mu_{hnf}/\mu_f}{(\rho C_p)_{hnf}/\rho_f}\mathrm{Ec}^*f''^2=0, \tag{3.3.64}$$

where, $\mathrm{Ec}^*=\frac{U_w^2}{(C_p)_f(T_w-T_\infty)}=\frac{a^2l^2}{(C_p)_fA}$.

Then, substitute the value of physical properties of nanofluid and hybrid nanofluid of $\dfrac{k_{hnf}}{k_{nf}} = \dfrac{k_2 + 2k_{nf} - 2\phi_2(k_{nf} - k_2)}{k_2 + 2k_{nf} + \phi_2(k_{nf} - k_2)}$, $\dfrac{k_{nf}}{k_f} = \dfrac{k_1 + 2k_f - 2\phi_1(k_f - k_1)}{k_1 + 2k_f + \phi_1(k_f - k_1)}$, $\mu_{hnf} = \dfrac{\mu_f}{(1-\phi_1)^{2.5}(1-\phi_2)^{2.5}}$, and $(\rho C_p)_{hnf} = (1-\phi_2)\left[(1-\phi_1)(\rho C_p)_f\right.$ $\left.+\phi_1(\rho C_p)_1\right] + \phi_2(\rho C_p)_2$ from Table 3.1 into equation (3.3.64) and it becomes

$$
\begin{aligned}
&\frac{\left[\dfrac{k_2 + 2k_{nf} - 2\phi_2(k_{nf} - k_2)}{k_2 + 2k_{nf} + \phi_2(k_{nf} - k_2)}\right]\left[\dfrac{k_1 + 2k_f - 2\phi_1(k_f - k_1)}{k_1 + 2k_f + \phi_1(k_f - k_1)}\right]}{(1-\phi_2)\left[(1-\phi_1) + \phi_1\dfrac{(\rho C_p)_1}{(\rho C_p)_f}\right] + \phi_2\dfrac{(\rho C_p)_2}{(\rho C_p)_f}}\left(\frac{1}{\mathrm{Pr}}\right)\theta'' + f\theta' - 2f'\theta \\
&+ \frac{L\beta_T}{m(1-\phi_2)\left[(1-\phi_1) + \phi_1\dfrac{(\rho C_p)_1}{(\rho C_p)_f}\right] + \phi_2\dfrac{(\rho C_p)_2}{(\rho C_p)_f}}(\theta_p - \theta) \\
&+ \frac{L\beta_v \mathrm{Ec}^*}{m(1-\phi_2)\left[(1-\phi_1) + \phi_1\dfrac{(\rho C_p)_1}{(\rho C_p)_f}\right] + \phi_2\dfrac{(\rho C_p)_2}{(\rho C_p)_f}}\left(f_p' - f'\right)^2 \\
&+ \frac{1}{(1-\phi_1)^{2.5}(1-\phi_2)^{3.5}\left[(1-\phi_1) + \phi_1\dfrac{(\rho C_p)_1}{(\rho C_p)_f}\right] + \phi_2\dfrac{(\rho C_p)_2}{(\rho C_p)_f}}\mathrm{Ec}^* f''^2 = 0.
\end{aligned}
\tag{3.3.65}
$$

Next, the formulation of the energy equation for the dust phase are as follows:

ii. Dust phase

$$u_p\frac{\partial T_p}{\partial x} + v_p\frac{\partial T_p}{\partial y} = \frac{C_{pf}}{C_{mf}\tau_T}(T - T_p)$$

where

$$T = \theta A\left(\frac{x}{l}\right)^2 + T_\infty, T_p = \theta_p A\left(\frac{x}{l}\right)^2 + T_\infty.$$

Find the values of $\frac{\partial T_p}{\partial x}, u_p \frac{\partial T_p}{\partial x}, \frac{\partial T_p}{\partial y}, v_p \frac{\partial T_p}{\partial y}, (T - T_p)$ and $\frac{C_{pf}}{C_{mf} \tau_T}(T - T_p)$,

$$\frac{\partial T_p}{\partial x} = \frac{2Ax}{l^2} \theta_p, \tag{3.3.66}$$

$$u_p \frac{\partial T_p}{\partial x} = 2Aa \left(\frac{x}{l}\right)^2 f_p' \theta_p, \tag{3.3.67}$$

$$\frac{\partial T_p}{\partial y} = A \left(\frac{x}{l}\right)^2 \left(\frac{a}{\nu_f}\right)^{1/2} \theta_p', \tag{3.3.68}$$

$$v_p \frac{\partial T_p}{\partial y} = -Aa \left(\frac{x}{l}\right)^2 f_p \theta_p' \tag{3.3.69}$$

$$(T - T_p) = A \left(\frac{x}{l}\right)^2 (\theta - \theta_p), \tag{3.3.70}$$

$$\frac{C_{pf}}{C_{mf} \tau_T}(T - T_p) = \frac{C_{pf}}{C_{mf} \tau_T} A \left(\frac{x}{l}\right)^2 (\theta - \theta_p). \tag{3.3.71}$$

Substitute equations (3.3.66)-(3.3.71) into energy equation (3.2.8) and it becomes

$$2Aa \left(\frac{x}{l}\right)^2 f_p' \theta_p + \left[-Aa \left(\frac{x}{l}\right)^2 f_p \theta_p'\right] = \frac{C_{pf}}{C_{mf} \tau_T} A \left(\frac{x}{l}\right)^2 (\theta - \theta_p), \tag{3.3.72}$$

$$Aa \left(\frac{x}{l}\right)^2 f_p \theta_p' - 2Aa \left(\frac{x}{l}\right)^2 f_p' \theta_p + \frac{C_{pf}}{C_{mf} \tau_T} A \left(\frac{x}{l}\right)^2 (\theta - \theta_p) = 0, \tag{3.3.73}$$

Next, multiply with $\left(\frac{1}{Aa}\right)\left(\frac{l}{x}\right)^2$,

$$f_p \theta_p' - 2 f_p' \theta_p + \frac{C_{pf}}{C_{mf}} \frac{1}{a \tau_T} (\theta - \theta_p) = 0, \tag{3.3.74}$$

$$f_p \theta_p' - 2 f_p' \theta_p + \epsilon \beta_T (\theta - \theta_p) = 0, \tag{3.3.75}$$

where, $\epsilon = \frac{C_{pf}}{C_{mf}}$ and $\beta_T = \frac{1}{a \tau_T}$.

3.3.4 Formulation of Boundary Conditions for Hybrid Nanofluid and Dust Phases

Substituting appropriate formulation from previous into boundary condition (3.2.24) to obtain a new set of boundary conditions in ODEs form as follows:

When $y = 0$, then $\eta = \left(\frac{a}{\nu_f}\right)^{1/2} y = 0$,

$$\begin{aligned}
u &= \lambda U_w(x) + L_s \left(\frac{\partial u}{\partial y}\right), \\
axf'(0) &= \lambda ax + L_s \left[axf''(0)\left(\frac{a}{\nu_f}\right)^{1/2}\right], \\
f'(0) &= \lambda + L_s \left[f''(0)\left(\frac{a}{\nu_f}\right)^{1/2}\right], \\
&= \lambda + \sigma_1 f''(0),
\end{aligned} \tag{3.3.76}$$

where, $\sigma_1 = L_s\sqrt{a/\nu_f}$,

$$\begin{aligned}
T &= T_w + L_T\left(\frac{\partial T}{\partial y}\right), \\
\theta(0)\left[A\left(\frac{x}{l}\right)^2\right] + T_\infty &= T_\infty + A\left(\frac{x}{l}\right)^2 + L_T\left[A\left(\frac{x}{l}\right)^2\left(\frac{a}{\nu_f}\right)^{1/2}\theta'(0)\right], \\
\theta(0) &= 1 + L_T\left(\frac{a}{\nu_f}\right)^{1/2}\theta'(0), \\
&= 1 + \sigma_2\theta'(0),
\end{aligned} \tag{3.3.77}$$

where, $\sigma_2 = L_T\sqrt{a/\nu_f}$.

$$\begin{aligned}
v &= v_w, \\
-(a\nu_f)^{1/2} f(0) &= -\sqrt{a\nu_f}s, \\
f(0) &= s.
\end{aligned} \tag{3.3.78}$$

Therefore, from equation (3.3.16), the mass transfer velocity at the surface becomes $v_w = -\left(a\nu_f\right)^{1/2} s$, where s indicates the constant for transpiration rate, which $s > 0$ and $s < 0$ denote the suction and injection parameters, respectively, $s = 0$ denotes an impermeable surface.

When $y \to \infty$, then $\eta = \left(\dfrac{a}{\nu_f}\right)^{1/2} y \to \infty$,

$$\begin{aligned} u &\to 0, \\ axf'(\eta) &\to 0, \\ f'(\eta) &\to 0, \end{aligned} \tag{3.3.79}$$

$$\begin{aligned} u_p &\to 0, \\ axf_p'(\eta) &\to 0, \\ f_p'(\eta) &\to 0, \end{aligned} \tag{3.3.80}$$

$$\begin{aligned} v_p &\to v, \\ -(a\nu_f)^{1/2} f_p(\eta) &\to -(a\nu_f)^{1/2} f(\eta), \\ f_p(\eta) &\to f(\eta), \end{aligned} \tag{3.3.81}$$

$$\begin{aligned} T_p &\to T_\infty, \\ \theta_p(\eta)\left[A\left(\frac{x}{l}\right)^2\right] + T_\infty &\to T_\infty, \\ \theta_p(\eta) &\to 0, \end{aligned} \tag{3.3.82}$$

$$\begin{aligned} T &\to T_\infty, \\ \theta(\eta)\left[A\left(\frac{x}{l}\right)^2\right] + T_\infty &\to T_\infty, \\ \theta(\eta) &\to 0. \end{aligned} \tag{3.3.83}$$

Hence, the new set of boundary conditions are

$$f(0) = s, \qquad f'(0) = \lambda + \sigma_1 f''(0), \qquad \theta(0) = 1 + \sigma_2 \theta'(0),$$
$$f'(\eta) \to 0, f_p'(\eta) \to 0, f_p'(\eta) \to f(\eta), \theta(\eta) \to 0, \theta_p(\eta) \to 0 \qquad \text{as} \quad \eta \to \infty, \tag{3.3.84}$$

where L and ϵ are the mass concentration of dust particle and ratio of specific heat parameters, respectively. Furthermore, β_v and β_T are the fluid-particle interaction parameters for velocity and temperature, σ_1 and σ_2 are the velocity and thermal slip parameters, respectively. Moreover, Ec* is the Eckert number. Note that, the formulation of Eckert number, Ec* in this chapter differs from the Eckert number, Ec presented in Chapters 5 and 6, to achieve similarity transformation.

3.3.5 Formulation of Physical Quantities

The quantities of physical interest are the skin friction coefficient (C_f), and the local Nusselt number (Nu_x) , which are denoted as

$$C_f = \frac{\tau_w}{\rho_f U_w^2}, \quad Nu_x = \frac{x q_w}{k_f (T_w - T_\infty)}, \tag{3.3.85}$$

with the shear stress on the surface (τ_w), and heat flux on the surface (q_w) are given by

$$\tau_w = \mu_{hnf} \left(\frac{\partial u}{\partial y} \right)_{y=0}, \quad q_w = -k_{hnf} \left(\frac{\partial T}{\partial y} \right)_{y=0}. \tag{3.3.86}$$

Substituting equation (3.3.86) into equation (3.3.85), gives

$$C_f = \frac{\mu_{hnf}}{\rho_f U_w^2} \left(\frac{\partial u}{\partial y} \right)_{y=0}, \quad Nu_x = -\frac{x k_{hnf}}{k_f (T_w - T_\infty)} \left(\frac{\partial T}{\partial y} \right) = 0. \tag{3.3.87}$$

Since $U_w = ax$ and $\nu_f = \mu_f / \rho_f$, we obtain

$$
\begin{aligned}
C_f &= \frac{\mu_{hnf}}{\rho_f U_w^2}\left(\frac{\partial u}{\partial y}\right), \\
&= \frac{\mu_{hnf}}{\rho_f (ax)^2}\left[axf''\left(\frac{a}{\nu_f}\right)^{1/2}\right], \\
&= \frac{\mu_{hnf}}{\rho_f \left(ax\right)^2} axf''\left(\frac{a}{\nu_f}\right)^{1/2} \cdot \left(\frac{ax^2}{\nu_f}\right)^{1/2}, \qquad (3.3.88)\\
C_f Re_x^{1/2} &= \frac{\mu_{hnf}}{\rho_f \left(ax\right)^2}\left(ax\right)^2 f''\left(\frac{\rho_f}{\mu_f}\right), \\
&= \frac{\mu_{hnf}}{\mu_f} f''(0), \qquad (3.3.89)
\end{aligned}
$$

$$
\begin{aligned}
Nu_x &= \frac{-xk_{hnf}}{k_f\left(T_w - T_\infty\right)}\left(\frac{\partial T}{\partial y}\right), \\
&= \frac{-xk_{hnf}}{k_f\left(T_w - T_\infty\right)}\left(\frac{Ax^2}{l^2}\right)\left(\frac{a}{\nu_f}\right)^{1/2}\theta', \\
&= \frac{-xk_{hnf}}{k_f\left[T_\infty + A\left(\frac{x}{l}\right)^2 - T_\infty\right]}\left(\frac{Ax^2}{l^2}\right)\left(\frac{a}{\nu_f}\right)^{1/2}\theta', \qquad (3.3.90)\\
Nu_x Re_x^{-1/2} &= \frac{-xk_{hnf}}{k_f}\left(\frac{a}{\nu_f}\right)^{1/2}\theta' \cdot \left(\frac{\nu_f}{ax^2}\right)^{1/2}, \\
&= -\frac{k_{hnf}}{k_f}\theta'(0), \qquad (3.3.91)
\end{aligned}
$$

where Reynolds number, Re_x can be denoted as

$$Re_x = U_w x/\nu_f. \qquad (3.3.92)$$

3.4 Numerical Method

The resulting ordinary differential equation from Phase 2 will be solved using bvp4c function in MATLAB to generate numerical results (Shampine et al., 2000). In this study, we are looking for the physical quantities which are skin friction coefficient (C_f) and local Nusselt number (Nu_x). By using bvp4c function the corresponding values of are skin friction coefficient $f''(0)$ and local Nusselt number $-\theta'(0)$ are generated. The effects of pertinent parameters on the skin friction coefficient, heat transfer, as well as the velocity and temperature profiles are analysed and discussed.

Here are the basic structures of the bvp4c function in MATLAB:

$$sol = bvp4c(OdeBVP, OdeBC, solinit, options)$$

- *sol* is a structure that encompasses the computed numerical solution returned by bvp4c and are divided into two which are:
  - ► sol.x : computes the x-values.
  - ► sol.y : consists of the corresponding values of sol.x.
- *OdeBVP* is a structure which defines the ODE functions to be evaluated in the form of

$$function ff = OdeBVP(x,y)$$

  where x is a scalar, $dydx$ and y are the column vectors. Further, in the ODE function implemented $y(1)$ indicates f, $y(2)$ indicates f' and so forth.
- *OdeBC* is a structure that defines the boundary conditions of the problems considered and expressed by:

$$function res = OdeBC(ya,yb)$$

  which *res* is a column vector representing the residual values of the boundary conditions at the boundary points. Furthermore, *ya* and *yb* are the solutions at two boundary points $x = a$ and $x = b$, respectively.
- *solinit* is a structure which consists of initial guess and denoted as:

$$solinit = bvpinit(x, yinit)$$

which *bvpinit* creates the initial guesses, x defines the initial mesh and *yinit* is a initial guess for the solution.

- *options* is a structure that modifies and controls the relative error in the solution. The *options* structure is in the form of:

$$options = bvpset('stats','off','RelTol',1e-10)$$

where $stats, off$ indicates that the computational cost statistics are not presented as output and $'RelTol', le-10$ refers to the relative error tolerence of $1e-10$.

3.4.1 Bvp4c Function

To solve the boundary layer problem for equations (3.3.34), (3.3.44), (3.3.65), and (3.3.75), the bvp4c function is employed, and new variables are introduced as follows:

$$\begin{aligned} f(\eta) = y(1), f'(\eta) = y(2), f'' = y(3), f_p(\eta) = y(4), f_p' = y(5) \\ \theta(\eta) = y(6), \theta' = y(7), \theta_p = y(8). \end{aligned} \tag{3.4.1}$$

Then, replace the hybrid nanofluid terms into

$$A1 = \frac{1}{(1-\phi_1)^{2.5}(1-\phi_2)^{2.5}}, \tag{3.4.2}$$

$$A2 = (1-\phi_2)\left[(1-\phi_1)+\phi_1\frac{\rho_1}{\rho_f}\right]+\phi_2\frac{\rho_2}{\rho_f}, \tag{3.4.3}$$

$$A3 = (1-\phi_2)\left[(1-\phi_1)+\phi_1\frac{(\rho C_p)_1}{(\rho C_p)_f}\right]+\phi_2\frac{(\rho C_p)_2}{(\rho C_p)_f}, \tag{3.4.4}$$

$$A4 = \frac{k_1+2k_f-2\phi_1(k_f-k_1)}{k_1+2k_f+\phi_1(k_f-k_1)}, \tag{3.4.5}$$

$$A5 = \frac{k_2+2k_{nf}-2\phi_2(k_{nf}-k_2)}{k_2+2k_{nf}+\phi_2(k_{nf}-k_2)}. \tag{3.4.6}$$

Next, substitute (3.4.2)-(3.4.6) into equations (3.3.34), (3.3.44), (3.3.65), and (3.3.75) and the largest degree should be on the left and we obtain

$$f''' = (A2/A1)*(-y(1)*y(3)+((y(2))^2)-((L*Bv)/A2)*(y(5)-y(2))), \quad (3.4.7)$$

$$f_p'' = (1/y(4))*((y(5))^2 - \beta_v*(y(2)-y(5))), \quad (3.4.8)$$

$$\theta'' = ((Pr*A3)/A5)*(-y(1)*y(7)+2*y(2)*y(6)-((L*\beta_T)/(m*A3)) * (y(8)-y(6)) - ((L*\beta_v*Ec)/(m*A3))*((y(5)-y(2))^2) - ((A1/A3) * (Ec*(y(3)^2)))), \quad (3.4.9)$$

$$\theta_p' = (1/y(4))*(2*y(5)*y(8) - \epsilon*\beta_T*(y(6)-y(8))). \quad (3.4.10)$$

$$f(0) = s, \qquad f'(0) = \lambda + \sigma_1 f''(0), \qquad \theta(0) = 1 + \sigma_2 \theta'(0),$$
$$f'(\eta) \to 0, f_p'(\eta) \to 0, f_p'(\eta) \to f(\eta), \theta(\eta) \to 0, \theta_p(\eta) \to 0 \qquad \text{as} \quad \eta \to \infty.$$

At $\eta = 0, y_a(i)$ where i=1,2,3,4,5,6,7,8,

$$y_a(1) = f(0), y_a(4) = f_p(0), y_a(6) = \theta(0), y_a(8) = \theta_p(0),$$
$$y_a(2) = f'(0), y_a(5) = f_p'(0), y_a(7) = \theta'(0),$$
$$y_a(3) = f''(0).$$

At $\eta = \infty, y_a(i)$ where i=1,2,3,4,5,6,7,8,

$$y_b(1) = f(\infty), y_b(4) = f_p(\infty), y_b(6) = \theta(\infty), y_b(8) = \theta_p(\infty),$$
$$y_b(2) = f'(\infty), y_b(5) = f_p'(\infty), y_b(7) = \theta'(\infty),$$
$$y_b(3) = f''(\infty).$$

Therefore, the boundary conditions (3.3.84) can be written as:

$$y_a(1) - s,$$

$$y_a(2) - \lambda - \sigma_1 * y_a(3),$$
$$y_a(6) - 1 - \sigma_2 * y_a(7),$$
$$y_b(2),$$
$$y_b(5),$$
$$y_b(4) - y_b(1),$$
$$y_b(6),$$
$$y_b(8),$$

where subscripts a and b implies the surface conditions, $\eta = 0$ and far field $\eta = \eta_\infty$, respectively. The boundary layer thickness for far-field boundary condition is within the range of $8 < \eta_\infty < 12$ across all considered parameters.

The function ff and res can be implemented in MATLAB as follows:

function ff = OdeBVP $(x, y, Pr, L, Bv, BT, m, Eckert, cepsilon, A1, A2, A3, A5)$

ff =[$y(2)$

$y(3)$

$(A2/A1) * (-y(1) * y(3) + ((y(2))^2) - ((L * Bv)/A2) * (y(5) - y(2)))$

$y(5)$

$(1/y(4)) * ((y(5))^2 - Bv * (y(2) - y(5)))$

$y(7)$

$((Pr * A3)/A5) * (-y(1) * y(7) + 2 * y(2) * y(6) - ((L * BT)/$
$(m * A3)) * (y(8) - y(6)) - ((L * Bv * Eckert)/(m * A3)) * ((y(5) -$
$y(2))^2) - ((A1/A3) * (Eckert * (y(3)^2))))$

$(1/y(4)) * (2 * y(5) * y(8) - cepsilon * BT * (y(6) - y(8)))$];

and

function res = OdeBC $(y_a, y_b, \lambda, s, \sigma_1, \sigma_2)$

$$
\begin{aligned}
res = [&y_a(1) - s,\\
&y_a(2) - \lambda - \sigma_1 * y_a(3),\\
&y_a(6) - 1 - \sigma_2 * y_a(7),\\
&y_b(2),\\
&y_b(5),\\
&y_b(4) - y_b(1),\\
&y_b(6),\\
&y_b(8),];
\end{aligned}
$$

After the residual function is defined, the bvp4c function refines the user provided initial guess until it obtains an accurate numerical solution of the boundary layer problem that satisfies all boundary conditions. In addition, below is the summarization on the bvp4c function:

1. Defining the ODEs function in MATLAB:
   The ODEs function are derived according to the boundary layer problems considered in Chapters 4, 5, and 6 and the higher order ODEs is converted into first order systems.

2. Defining the boundary conditions:
   Develop a function that implements the specified boundary conditions.

3. Providing an initial guess:
   Generate an initial guess and a random estimation solution. bvp may possesses multiple solution; therefore bvp algorithm necessitates to provide an initial guess for the solution. Then, the algoritmhs modifies the mesh to get a precise numerical solution with a limited number of mesh points. Nevertheless, bvp4c employs an unconventional method for error control which enables it to manage an inaccurate estimations effectively (Shampine et al., 2000).

4. Solving the bvp using bvp4c:
   Execute bvp4c with the ODEs function, boundary conditions, and initial guesses

considered. Thus, the numerical solution is computed.

5. Plotting the solutions.

The procedure for the execution of bvp4c is presented in detail in Appendix C, D and E.

CHAPTER 4
BOUNDARY LAYER FLOW AND HEAT TRANSFER OF DUSTY HYBRID NANOFLUID OVER A HORIZONTAL STRETCHING OR SHRINKING SURFACE WITH THE EFFECTS OF VISCOUS DISSIPATION AND SLIP CONDITIONS

4.1 Introduction

The study of flow and heat transfer in dusty hybrid nanofluids has received significant interest due to their enhanced thermal characteristics, making them applicable in numerous industrial and engineering fields, including thermal processing, cooling systems, and advanced material manufacturing. Viscous dissipation, which accounts for the conversion of kinetic energy into heat, plays a crucial role in altering temperature distributions, particularly in high-viscosity or high-speed flows. The presence of slip conditions further alters the behavior of the velocity and thermal boundary layers, collectively impacting the overall flow and heat transfer characteristics. This study aims to investigate the effects of viscous dissipation and slip conditions on flow and heat transfer over a deformable horizontal surface that is either stretching or shrinking in dusty hybrid nanofluids. Additionally, this research expands upon the work of Anuar et al. (2021b, who studied on the flow and heat transfer of dusty hybrid nanofluid over a stretching or shrinking deformable surface with the influence of slip conditions. To the best of our knowledge, limited investigation has been conducted regarding the combined influence of viscous dissipation, dust particles, hybrid nanoparticles, and slip conditions. The mathematical model is reconstructed in a manner that aligns with the presentation in Chapter 3.

4.2 Mathematical Formulation

The steady boundary layer flow and heat transmission of dusty hybrid nanofluid over a horizontal stretching or shrinking surface are examined in this chapter. Two distinct nanoparticles which Al_2O_3 and Cu were chosen as the nanoparticles and water as the base fluid. The detailed mathematical formulations applied in this chapter are discussed in Chapter 3.

4.3 Numerical Solutions

The governing equation (3.2.2)-(3.2.4) and (3.2.6)-(3.2.8) along with the boundary conditions (3.2.24) are transformed into boundary layer equations (3.2.21), (3.2.22), while equations (3.2.6) and (3.2.8) are remained, through the application of boundary layer approximation as presented in Section 3.2.2. Further, the boundary layer equations are reduced into ordinary differential equations (3.3.34), (3.3.44), (3.3.65), and (3.3.75) under boundary conditions (3.3.84) by employing appropriate similarity variables, as elaborated in Chapter 3, Section 3.3.

The ODEs are solved numerically using built in bvp4c function in MATLAB. The initial guess is iteratively refined until the boundary conditions of the velocity and temperature profiles are satisfied. Once the generated profiles satisfied the boundary conditions, the values of $f''(0)$ and $\theta'(0)$ are proven valid. The values of $f''(0)$ and $\theta'(0)$ are subsequently substituted into the formula of the skin friction coefficient ($C_f Re_x^{1/2}$) and the local Nusselt number ($Nu_x Re_x{}^{-1/2}$) to compute their values. After the values of $C_f Re_x^{1/2}$ and $Nu_x Re_x^{-1/2}$ are obtained, the MATLAB plot function is employed to generate the graphs of $C_f Re_x^{1/2}$ and $Nu_x Re_x^{-1/2}$.

Furthermore, this chapter discusses and presents the quantities of physical interest, specifically $C_f Re_x^{1/2}$ and $Nu_x Re_x{}^{-1/2}$, along with the velocity and temperature profiles that satisfy the boundary conditions given in (3.3.84), while considering the effects of pertinent parameters on the flow and heat transfer. The pertinent parameters considered are L, Ec*, σ_1, σ_2, and ϕ. The parameter values employed were chosen according to ranges specified in previous studies to ensure physical accuracy and are consistent with the existing literature. Preliminary computations were conducted to verify the numerical solutions and to identify appropriate parameter ranges resulting in stable and desired solutions. In addition, these equivalent methods and procedures also be implemented in Chapters 5 and 6.

4.4 Results and Discussion

To verify the validity of the current method employed, the comparative results for $f''(0)$ and $-\theta'(0)$ of the current study with several researchers are shown in Tables 4.1 and 4.2, respectively, for the values of $\lambda = 1$, and $\phi_1 = \phi_2 = L = \beta_v = \beta_T = s = \mathrm{Ec}^* = \sigma_1 = \sigma_2 = 0$. Based on the comparative results in Tables 4.1 and 4.2, it depict a strong agreement that proves the validity of the present method utilized.

Table 4.1
Comparative Results of $f''(0)$ for Stretching Surface $(\lambda = 1)$ when $\phi_1 = \phi_2 = L = \beta_v = \beta_T = s = 0$

σ_1	Hayat et al. (2010)	Ibrahim and Shankar (2013)	Anuar et al. (2021b)	Present Results
0	-1.000000	-1.0000	-1.000000	-1.00000056
0.1	-0.872082	-0.8721	-0.872083	-0.872082562
0.2	-0.776377	-0.7764	-0.776377	-0.776377799
0.5	-0.591195	-0.5912	-0.591196	-0.591196705
2.0	-0.283981	-0.2840	-0.283981	-0.283986294
5.0	-0.144841	-0.1448	-0.144842	-0.144842270

Table 4.2
Comparative Results of $-\theta'(0)$ for Stretching Surface $(\lambda = 1)$ when $\phi_1 = \phi_2 = L = \beta_v = \beta_T = s = \mathrm{Ec}^* = \sigma_1 = \sigma_2 = 0$

Pr	Gireesha et al. (2014)	Naramgari and Sulochana (2016)	Punith Gowda et al. (2021)	Anuar et al. (2021b)	Present Results
0.72	1.0885	1.088561	-	1.088527	1.088536003
1	1.3333	1.333333	1.3333	1.333333	1.333333338
10	4.7968	4.796817	4.7969	4.796873	4.796873143

The comparison results of $Nu_x Re_x^{-1/2}$ between Anuar et al. (2021b) and the present study for different shrinking surfaces and (σ_1, σ_2) values are illustrated in Figure 4.1. The comparison is carried out to clarify the significance of considering the effect of viscous dissipation on the flow and heat transfer, as Anuar et al. (2021b) conducted the study without considering viscous dissipation. The figure illustrates that the inclusion of viscous dissipation significantly affects the characteristics of heat transfer, exhibiting contrast characteristic with the usual where negative values of $Nu_x Re_x^{-1/2}$ were denoted and this occurs because the fluid temperature surpasses the surface temperature (Aiyashi et al., 2023; Waini et al., 2023). Furthermore, the influence of L, Ec*, σ_1, σ_2, ϕ_1, and ϕ_2 on $C_f Re_x^{1/2}$ and $Nu_x Re_x^{-1/2}$ for Pr = 6.2, $\lambda = -1, m = \epsilon = 1.0, \beta_v = \beta_T = 0.5$ and $s = 2.0$ of the current study are shown in Table 4.3.

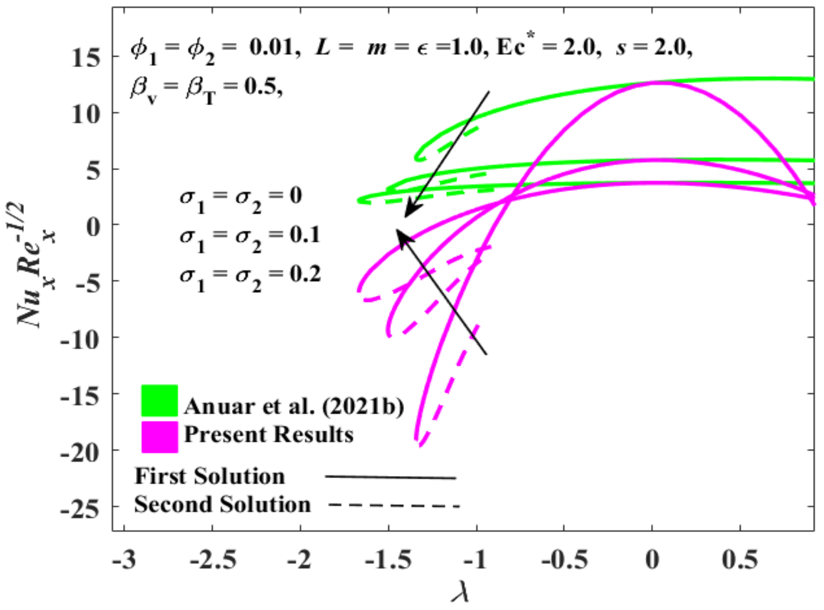

Figure 4.1 Comparison Results of $Nu_x Re_x^{-1/2}$ with Various Slip Parameters for Anuar et al. (2021b) and Present Study

The effect of different values of L and λ on the values of $C_f Re_x^{1/2}$ and $Nu_x Re_x^{-1/2}$ for Pr = 6.2, $\phi_1 = \phi_2 = 0.01$, $m = \epsilon = 1.0, \beta_v = \beta_T = 0.5$ and $s = 2.0$ are depicted in Figures 4.2 and 4.3, respectively. Dual solutions exists indicating non-uniqueness of the flow across the surface within the same parameter, L. Table 4.3 and Figure 4.2 indicate that as L increases from 0 to 0.1, there is an increase in the values of $C_f Re_x^{1/2}$, with an enhancement of 1.78% in the first solution, implying an increase in frictional forces between the dusty hybrid nanofluid flow and the surface, while a decrease of 2.88% in the second solution. Higher values of L indicate greater concentration of dust particle suspended in the fluid, leading to a denser fluid. Besides that, Table 4.3 and Figure 4.3 shows a decline in $Nu_x Re_x^{-1/2}$ values by 0.23% in the first solution and 61.82% in the second solution as L increases, resulting to a reduction in the rate of heat transfer. Further, the increment of L delays the boundary layer separation with the critical points λ_c of -1.2868, -1.2908, and -1.3262 for L = 0, 0.01, and 0.1 and no solutions are found beyond λ_c.

Table 4.3
Influence of L, Ec*, σ_1, σ_2, ϕ_1, and ϕ_2 on $C_f Re_x^{1/2}$ and $Nu_x Re_x^{-1/2}$ for Pr = 6.2, $\lambda = -1.0$ $m = \epsilon = 1.0, \beta_v = \beta_T = 0.5$ and s = 2.0

L	Ec*	σ_1	σ_2	ϕ_1	ϕ_2	$C_f Re_x^{1/2}$		$Nu_x Re_x^{-1/2}$	
						First Solution	Second Solution	First Solution	Second Solution
0	2.0	0.2	0.2	0.01	0.01	1.2844	0.5865	1.3629	-0.3738
0.01	2.0	0.2	0.2	0.01	0.01	1.2868	0.5847	1.3626	-0.3976
0.1	2.0	0.2	0.2	0.01	0.01	1.3072	0.5696	1.3597	-0.6049
1.0	0	0.2	0.2	0.01	0.01	1.4627	0.4797	3.6350	3.5800
1.0	0.5	0.2	0.2	0.01	0.01	1.4627	0.4797	3.0641	2.2074
1.0	2.0	0.2	0.2	0.01	0.01	1.4627	0.4797	1.3514	-2.2781
1.0	2.0	0	0	0.01	0.01	1.8167	0.6337	-3.1369	-7.9534
1.0	2.0	0.1	0.1	0.01	0.01	1.6389	0.5541	0.6579	-2.9937
1.0	2.0	0.2	0.2	0.01	0.01	1.4627	0.4659	1.3514	-2.2781
1.0	2.0	0	0.2	0.01	0.01	1.8167	0.6126	-1.0145	-3.0062
1.0	2.0	0.1	0.2	0.01	0.01	1.6389	0.5463	0.4170	-2.2338
1.0	2.0	0.2	0.2	0.01	0.01	1.4627	0.4659	1.3514	-2.2781
1.0	2.0	0.2	0	0.01	0.01	1.4627	0.4659	4.3697	-7.2082
1.0	2.0	0.2	0.1	0.01	0.01	1.4627	0.4659	2.0567	-3.4394
1.0	2.0	0.2	0.2	0.01	0.01	1.4627	0.4659	1.3514	-2.2781
1.0	2.0	0.2	0.2	0	0.01	1.4279	0.4527	1.3254	-2.2571
1.0	2.0	0.2	0.2	0.01	0.01	1.4627	0.4659	1.3514	-2.2781
1.0	2.0	0.2	0.2	0.02	0.01	1.4978	0.4798	1.3753	-2.2991
1.0	2.0	0.2	0.2	0.01	0	1.3767	0.4595	1.2297	-2.2049
1.0	2.0	0.2	0.2	0.01	0.01	1.4627	0.4659	1.3514	-2.2781
1.0	2.0	0.2	0.2	0.01	0.02	1.5483	0.4728	1.4730	-2.3713

Figures 4.4 and 4.5 shows the velocity and temperature profiles for the fluid phase $f(\eta), \theta(\eta)$ and dust phase $f_p'(\eta)$, $\theta_p(\eta)$ of Figures 4.2 and 4.3, correspondingly. According to Figure 4.4, the inclusion of higher concentration of dust particles into the hybrid nanofluid leads to a decrease in the boundary layer thickness of both phases in the first solution but an increase in the second solution. The increase in the mass concentration of dust particles affects the boundary layer thickness because higher L leads to higher skin friction coefficient which then lowers fluid velocity. Figure 4.5 shows a decreasing trend in both phases for the first solution, while an opposite trend is shown in the second solution. This implies that the local Nusselt number and heat transfer rate in the second solution is less effective compared to the first solution.

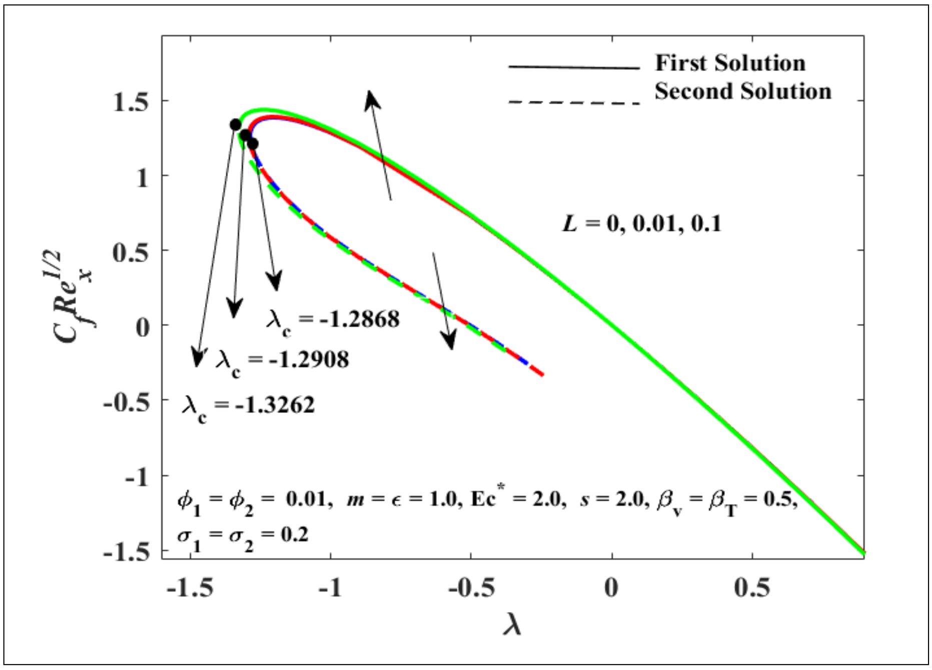

Figure 4.2 $C_f Re_x^{1/2}$ with λ for Different Values of L

The variety of $C_f Re_x^{1/2}$ and $Nu_x Re_x^{-1/2}$ for several values of s and L with Pr = 6.2, $\lambda = -1.0, \phi_1 = \phi_2 = 0.01$, $m = \epsilon = 1.0$, and $\beta_v = \beta_T = 0.5$ are exhibited in Figures 4.6 and 4.7, respectively. Based on the figures, it is shown that rising the values of L, leads to an increment in $C_f Re_x^{1/2}$ in the first solution and decrease in the second solution, while $Nu_x Re_x^{-1/2}$ diminishes in both solutions. As L increases, the concentration of dust particles in the fluid rises, leading to an increase in viscosity and frictional force within the boundary layer region. In addition, an increase in L results in a reduction of heat transfer rate. This occurs because dust particles stores

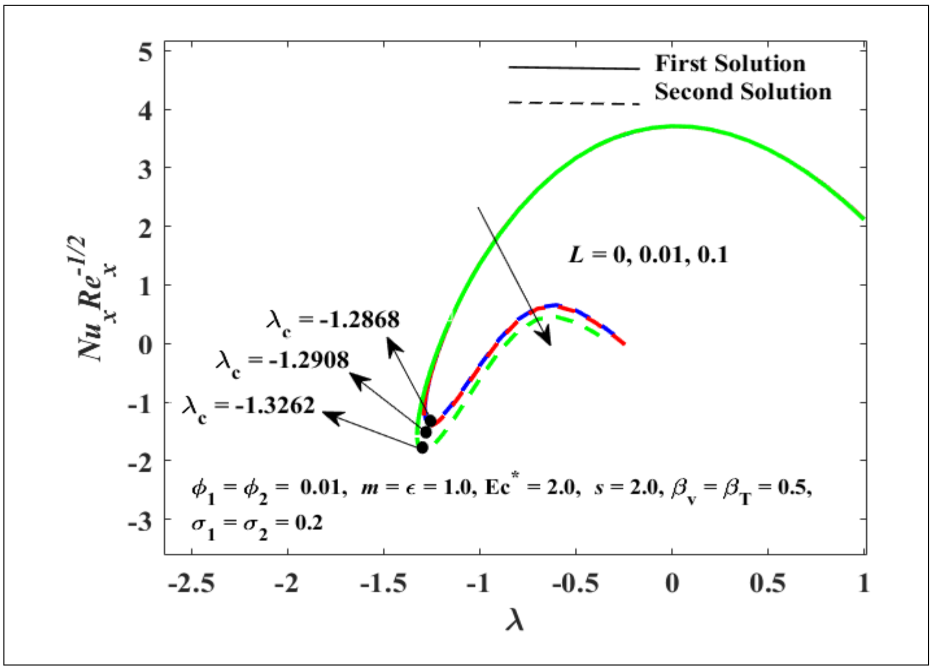

Figure 4.3 $Nu_x Re_x^{-1/2}$ with λ for Different Values of L

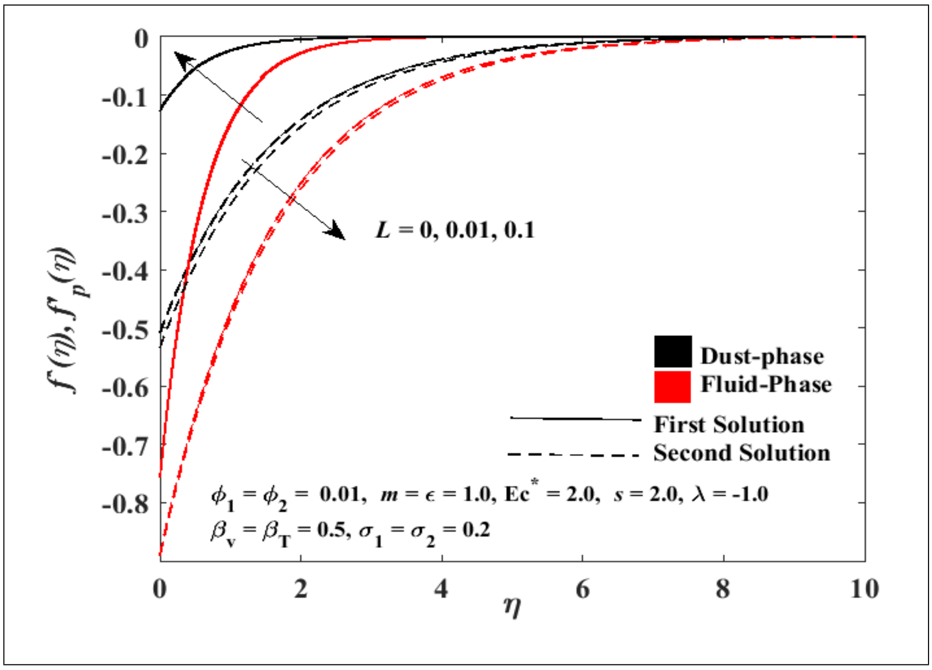

Figure 4.4 Velocity Profile for Different Values of L

more heat, and the combination with viscous dissipation leads to an increased thermal energy, thereby rising the fluid temperature and subsequently diminishing the heat transfer rate (Hamid et al., 2021).

Figures 4.8 and 4.9 illustrates the velocity and temperature profiles of Figures 4.6 and 4.7, respectively. Similar to Figure 4.4, Figure 4.8 illustrates that an increase in

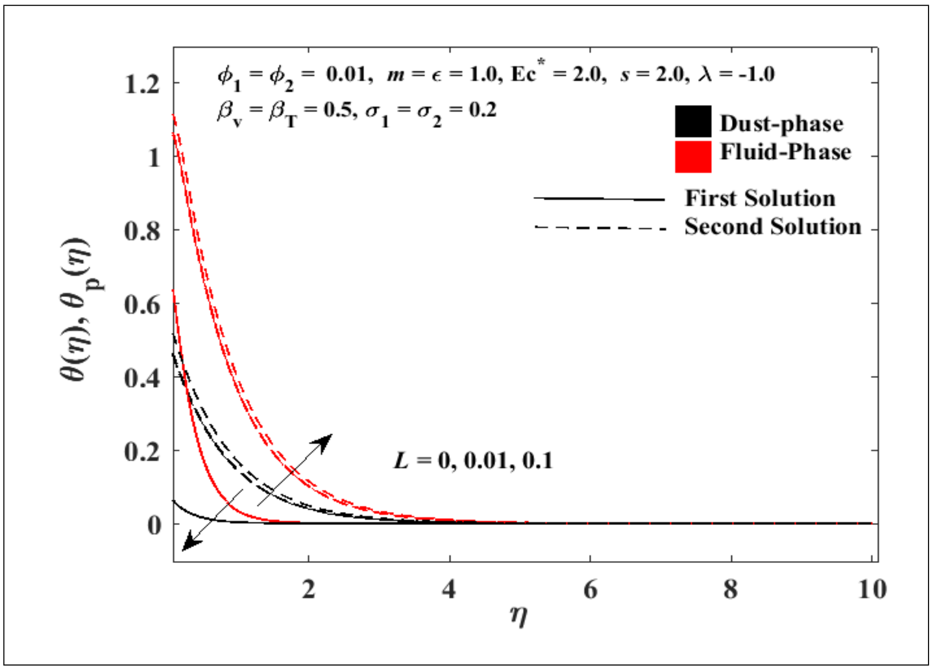

Figure 4.5 Temperature Profile for Different Values of L

the concentration of dust particles in the fluid results in a reduction of boundary layer thickness for the first solution, while it leads to an increase in the second solution for both phases. The velocity gradient enhances, implying an increase in skin friction coefficient, consistent with the results illustrated in Figure 4.6. Furthermore, Figure 4.9 demonstrates a decrease in temperature in the first solution for both the fluid and dust phases, while an increase in the second solution.The boundary layer thickness of the first solution is narrower, this indicates that the local Nusselt number is higher and heat is transferred more efficiently in the first solution compared to the second solution.

Figures 4.10 and 4.11 elucidate the variations of $C_f Re_x^{1/2}$ and $Nu_x Re_x^{-1/2}$ against s for different values of Ec^*. Figure 4.10 portrays that an increase in the Ec^* does not influence the values of $C_f Re_x^{1/2}$ as Ec^* refers to the conversion of kinetic energy to thermal energy in fluid flows. According to Table 4.3 and Figure 4.11, there is a decrease of 62.82% in the first solution and 163.63% in the second solution for the $Nu_x Re_x^{-1/2}$ values as the Ec^* increases. This implies that an increase in Ec^* results in a greater conversion of kinetic to thermal energy, leading to a rise in fluid temperature. As a result, the fluid temperature surpasses the surface temperature, consequently diminishing the heat transfer rate between the fluid and the surface.

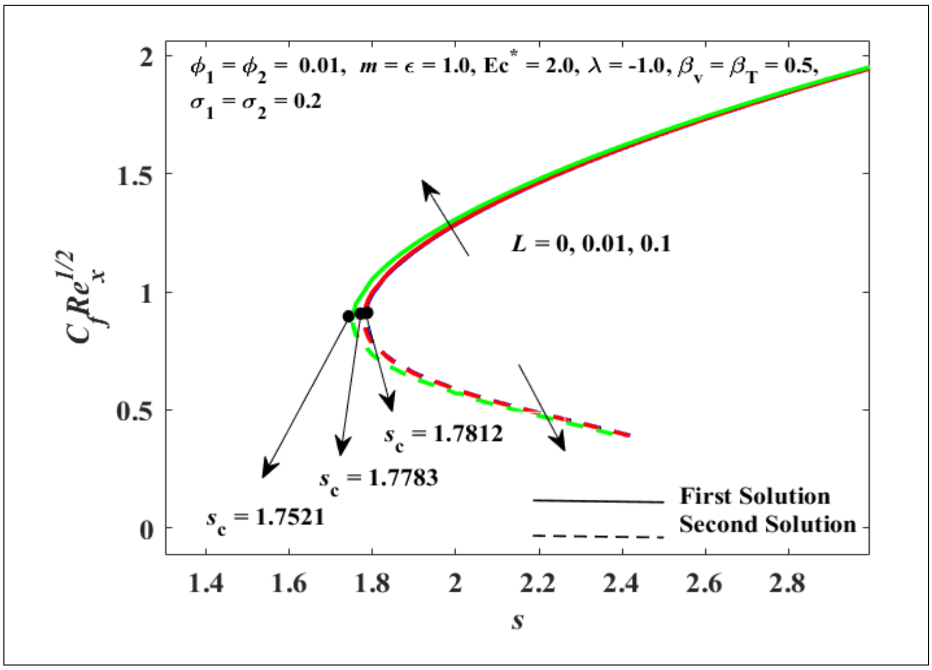

Figure 4.6 $C_f Re_x^{1/2}$ with s for Different Values of L

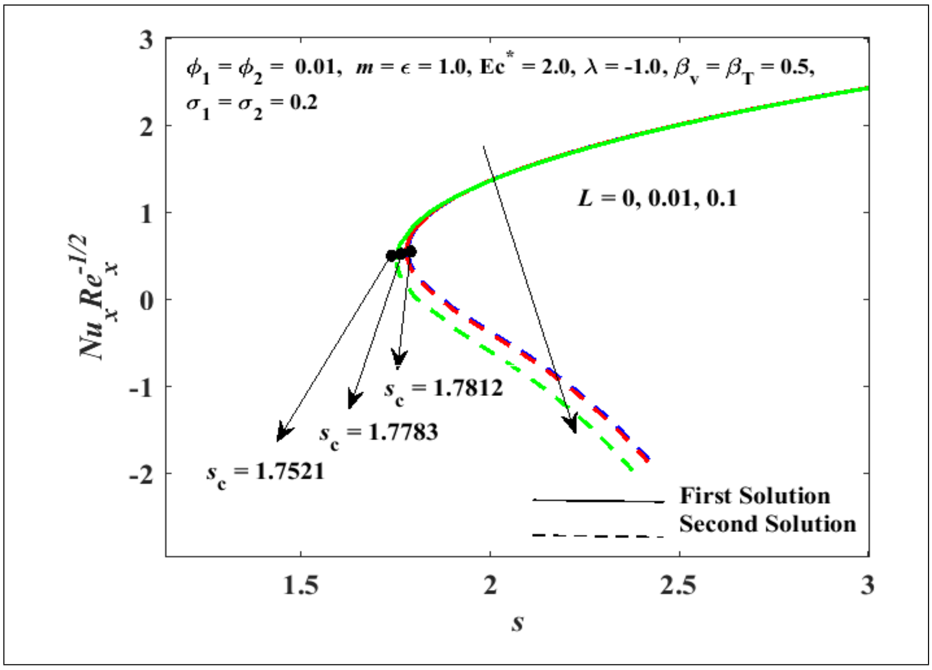

Figure 4.7 $Nu_x Re_x^{-1/2}$ with s for Different Values of L

The corresponding velocity and temperature profiles of Figures 4.10 and 4.11 are illustrated respectively in Figures 4.12 and 4.13. Figure 4.12 demonstrates no variation which implies the rise of Ec* is insignificant in the velocity profile, consistent with the results presented in Figure 4.10. Further, Figure 4.13 shows an increase in temperature profile, which consequently increases the thermal boundary layer thickness in both

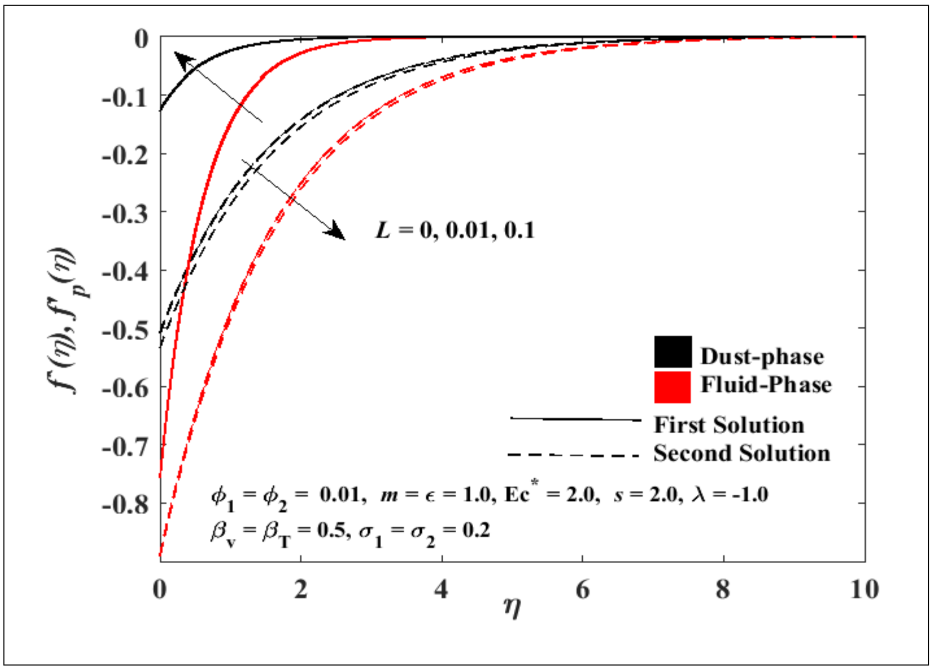

Figure 4.8 Velocity Profile for Different Values of L

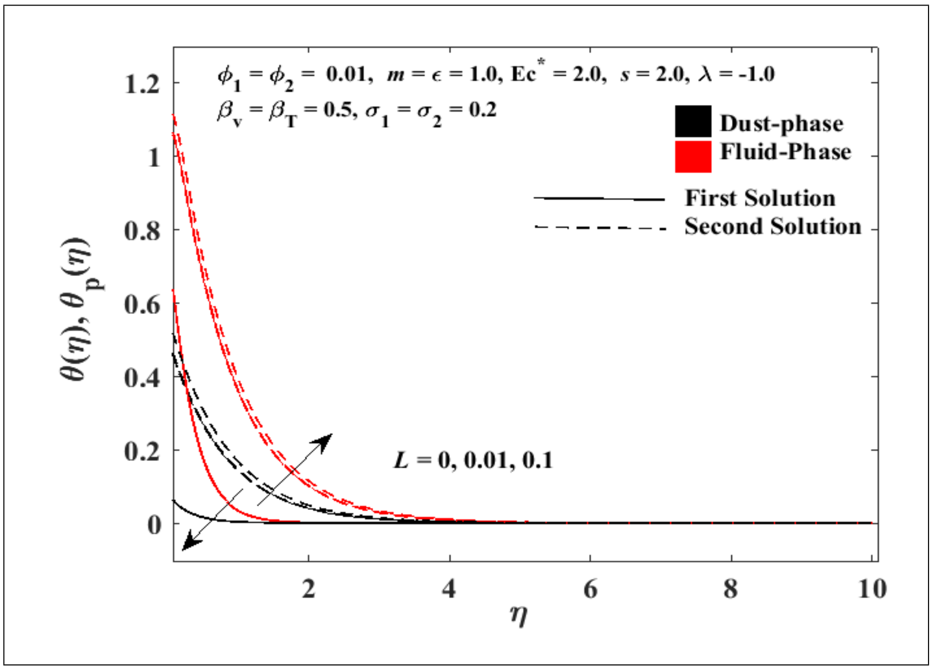

Figure 4.9 Temperature Profile for Different Values of L

phases. This results in a decrease of the temperature gradient, implying a decrease in the local Nusselt number and heat transfer rate, aligned with the findings presented in Figure 4.11.

The variations of $C_f Re_x^{1/2}$ and $Nu_x Re_x^{-1/2}$ for distinct s and σ_1, σ_2 values are shown in Figures 4.14 and 4.15, respectively. The employed slip parameter values are

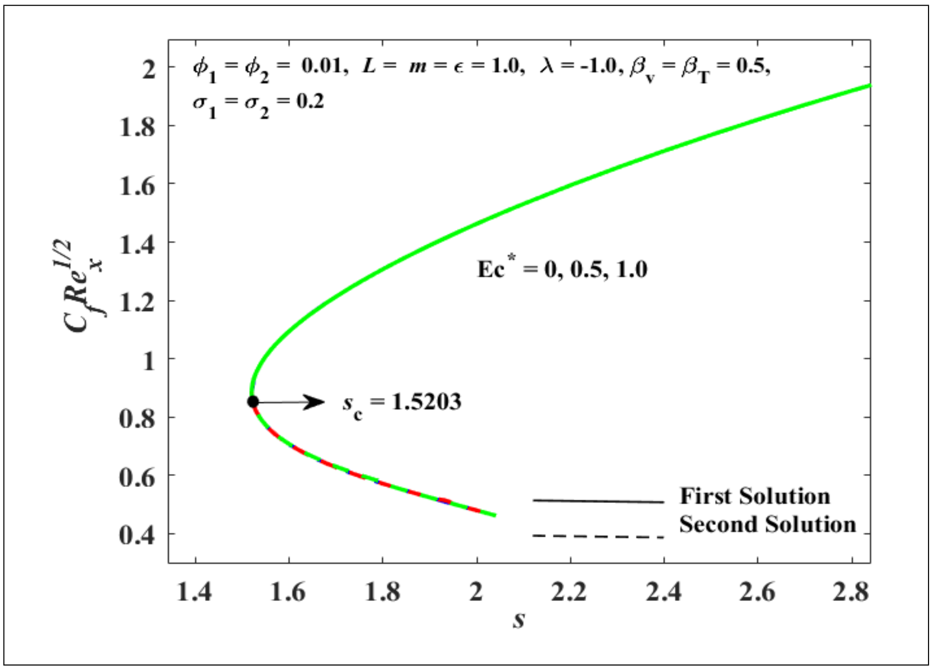

Figure 4.10 $C_f Re_x^{1/2}$ with s for Different Values of Ec* Number

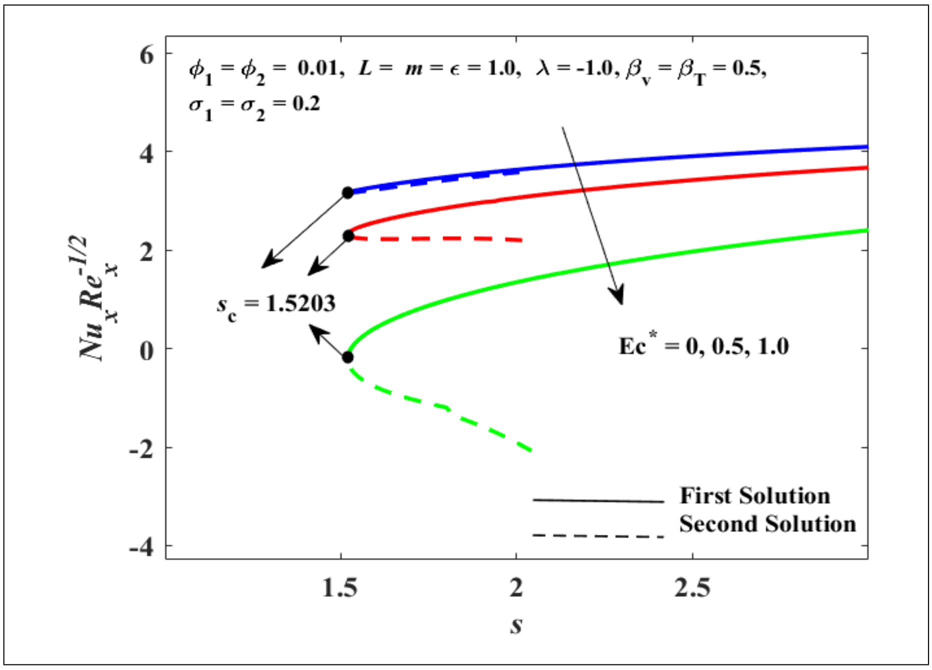

Figure 4.11 $Nu_x Re_x^{-1/2}$ with s for Different Values of Ec* Number

$\sigma_1 = \sigma_2 = 0$ which signifies no-slip parameter, while $\sigma_1 = \sigma_2 = 0.1$ and $\sigma_1 = \sigma_2 = 0.2$ signifies slip parameter. Table 4.3 and Figure 4.14 shows that by increasing the values of σ_1 and σ_2, the values of $C_f Re_x^{1/2}$ decreases by 19.49% and 26.48% for the first and second solutions, respectively. This indicates that increasing the slip parameters can reduce the friction between the fluid and the surface. Besides that, Figure 4.15

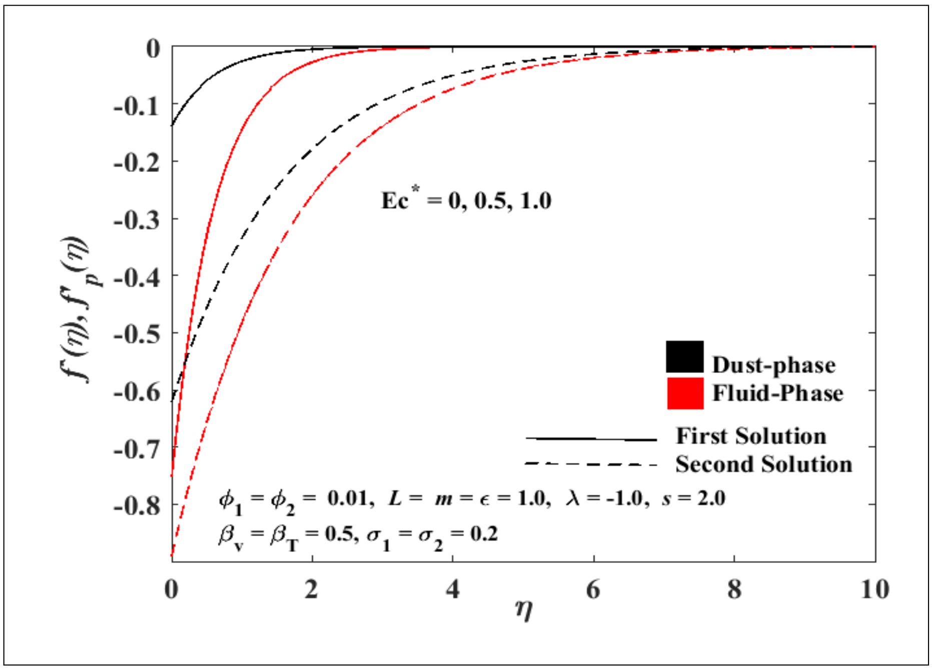

Figure 4.12 Velocity Profile for Different Values of Ec* Number

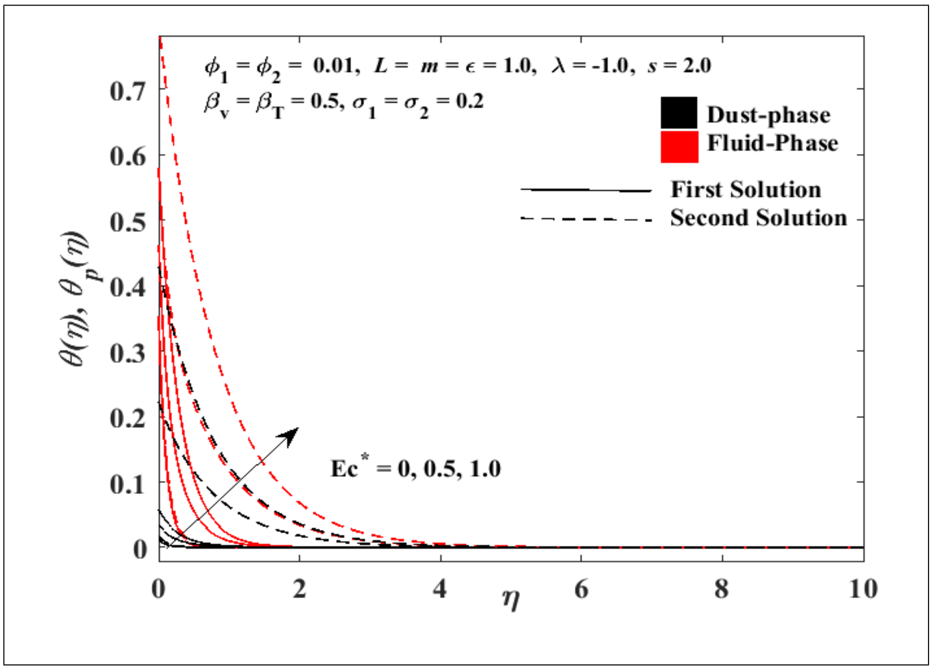

Figure 4.13 Temperature Profile for Different Values of Ec* Number

illustrates that increasing the slip parameter results in a rise of 143.08% and 71.36% in the value of $Nu_x Re_x^{-1/2}$ for the first and second solutions, respectively, indicating enhanced heat transfer at the surface. Additionally, s_c denotes the critical point that connects the first and second solutions. No solution exists beyond the critical point, as this signifies the occurrence of boundary layer separation.

The corresponding velocity and temperature profiles of Figures 4.14 and 4.15 for $f(\eta), \theta(\eta)$ and $f_p'(\eta), \theta_p(\eta)$ are depicted in Figures 4.16 and 4.17, respectively. Figure 4.16 shows that the increment of σ_1 and σ_2 reduces the boundary layer thickness for both phases in the first solution and the velocity gradient at the wall is observed to be steeper, resulting to a reduced skin friction coefficient. Conversely, in the second solution, the boundary layer thickness exhibits an increase. Note that, a steeper velocity gradient often results in a higher skin friction coefficient, but in this case, the skin friction coefficient displays a contradictory pattern, similar to the result depicted by Anuar et al. (2021b) in their study for both of the solutions. The thermal boundary layer thickness in Figure 4.17 exhibits a reduction for the first solution which results to a steeper temperature gradient which indicates an increased local Nusselt number and heat transmission rate, while the second solution shows a contradiction.

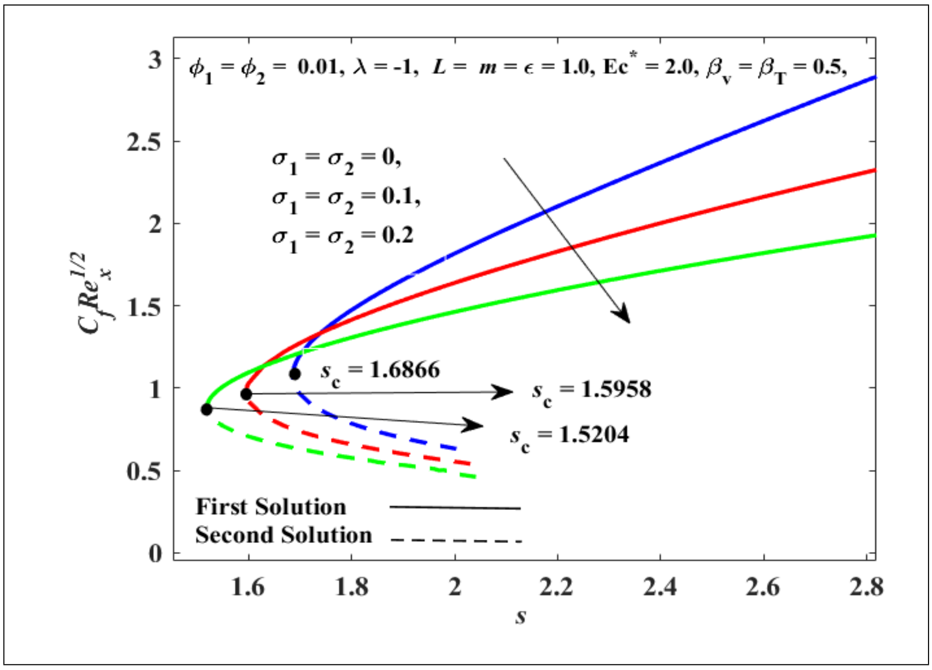

Figure 4.14 $C_f Re_x^{1/2}$ with s for Distinct Values of σ_1 and σ_2

The implication of various values of s and σ_1 on $C_f Re_x^{1/2}$ and $Nu_x Re_x^{-1/2}$ are displayed in Figures 4.18 and 4.19, respectively. According to the figures, the boundary layer separation is delayed as σ_1 increases and the s_c for $\sigma_1 = 0$, 0.1, and 0.2 are 1.6866, 1.5958, and 1.5204. Moreover, Table 4.3, and Figures 4.18, and 4.19 depicts that the upsurge values of σ_1 decreases the values of $C_f Re_x^{1/2}$ by 19.49% for the first solution and 23.95% for the second solution, while the values of $Nu_x Re_x^{-1/2}$

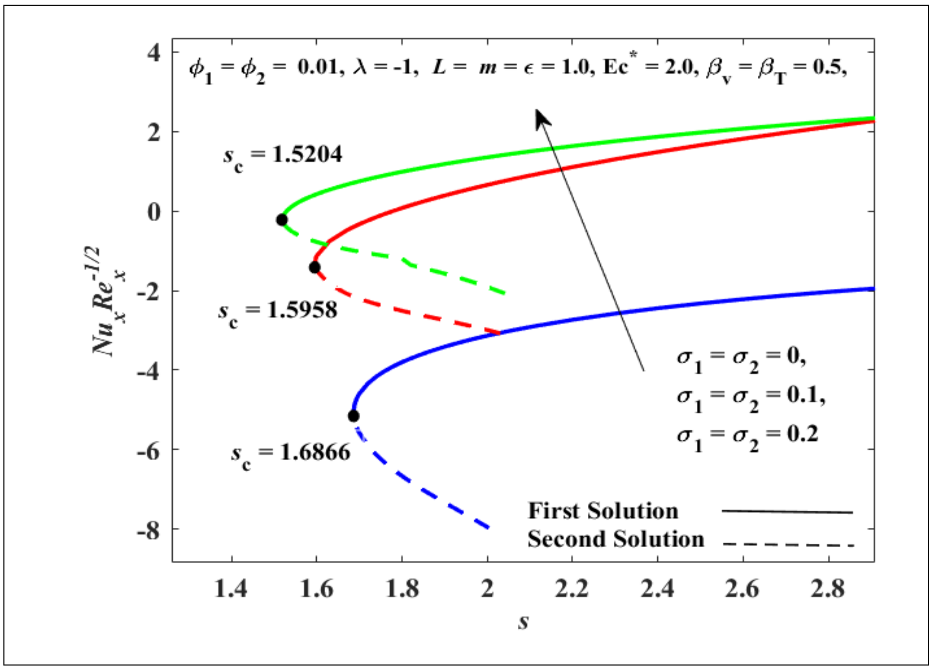

Figure 4.15 $Nu_x Re_x^{-1/2}$ with s for Distinct Values of σ_1 and σ_2

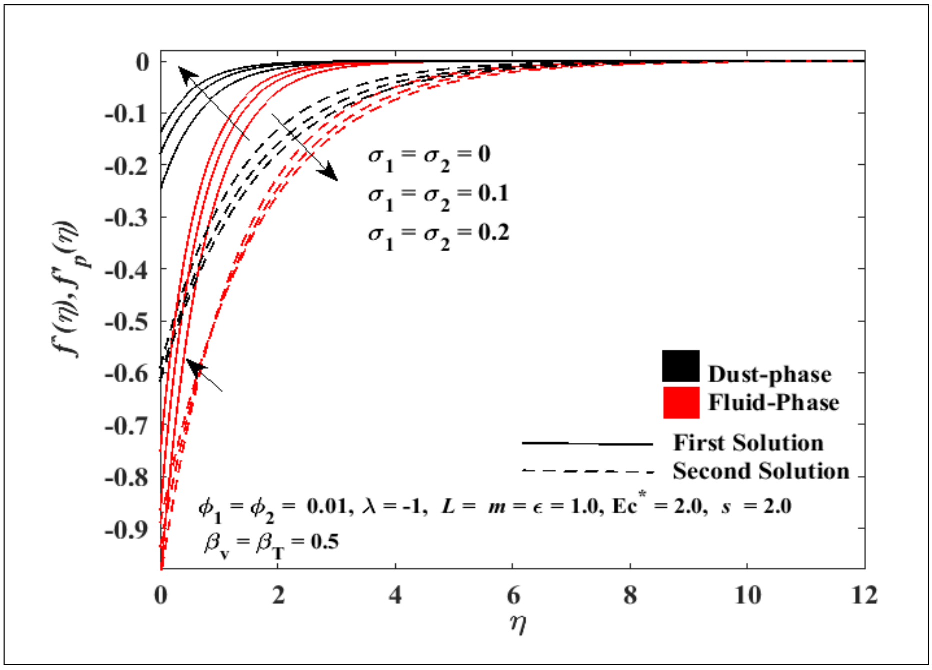

Figure 4.16 Velocity profile with distinct values of σ_1 and σ_2

increases by 233.21% and 24.22% for the first and second solutions, respectively. This demonstrates that higher velocity slip between the fluid and the surface results in an increased slip length which leads to weaker interactions between the fluid and the surface. As a result, this reduces surface friction but enhances the heat transfer rate.

Figures 4.20 and 4.21 illustrate the corresponding velocity and temperature

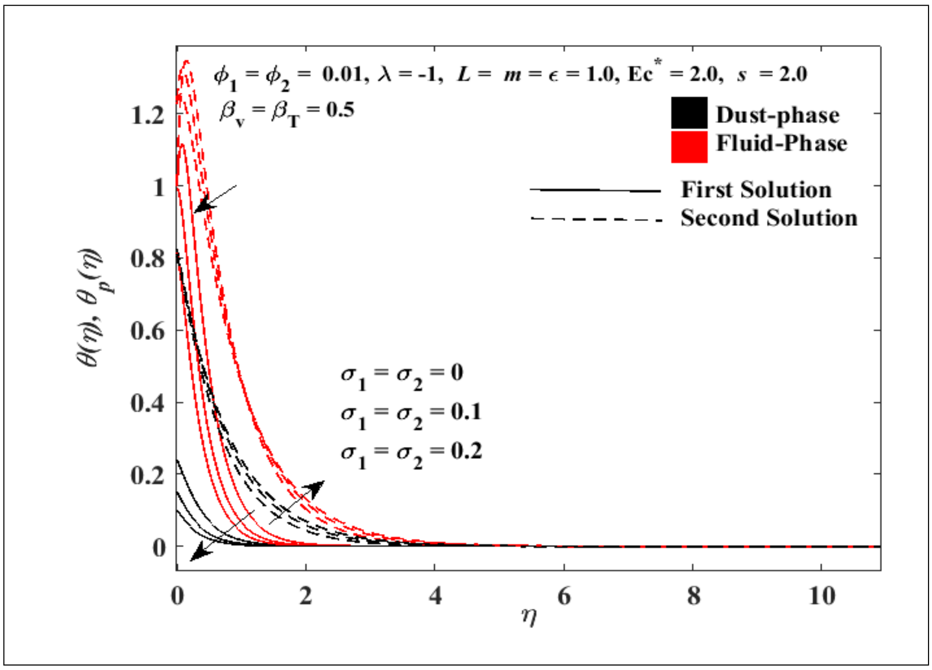

Figure 4.17 Temperature Profile with Distinct Values of σ_1 and σ_2

profile for Figures 4.18 and 4.19, respectively. From Figure 4.20, the velocity profile rises, while the boundary layer thickness diminishes for the first solution of both phases as σ_1 increases which result to a steeper velocity gradient. Similar to the case in Figure 4.16, the velocity gradient shows an increment, however the skin friction coefficient decreases. This indicate a reduction in shear stress and frictional force at the surface. Besides, the second solution of the velocity profile shows an opposite trend for both phases. Figure 4.21 shows that the temperature profile declines for the first solution of both phases, while augments in the second solution. Additionally, the boundary layer thickness narrowed down, leading to a steeper temperature gradient. This indicates a greater local Nusselt number and transmission of heat rate as the velocity slip parameter rises in the first solution.

Distinct values of s and σ_2 for variations values of $C_f Re_x^{1/2}$ and $Nu_x Re_x^{-1/2}$ are depicted in Figures 4.22 and 4.23. The figures demonstrate the existence of dual solutions within the range of $s_c < s < 2.05$ and no solution exists beyond s_c. Based on Figure 4.22, there is no changes in the values of $C_f Re_x^{1/2}$ as σ_2 increases, thus this implies that σ_2 is not significant because no variation in friction as the thermal slip parameter rises. Additionally, $Nu_x Re_x^{-1/2}$ diminishes by 69.07% in the first solution, while rises by 68.4% in the second solution when σ_2 increases, as illustrated in Table

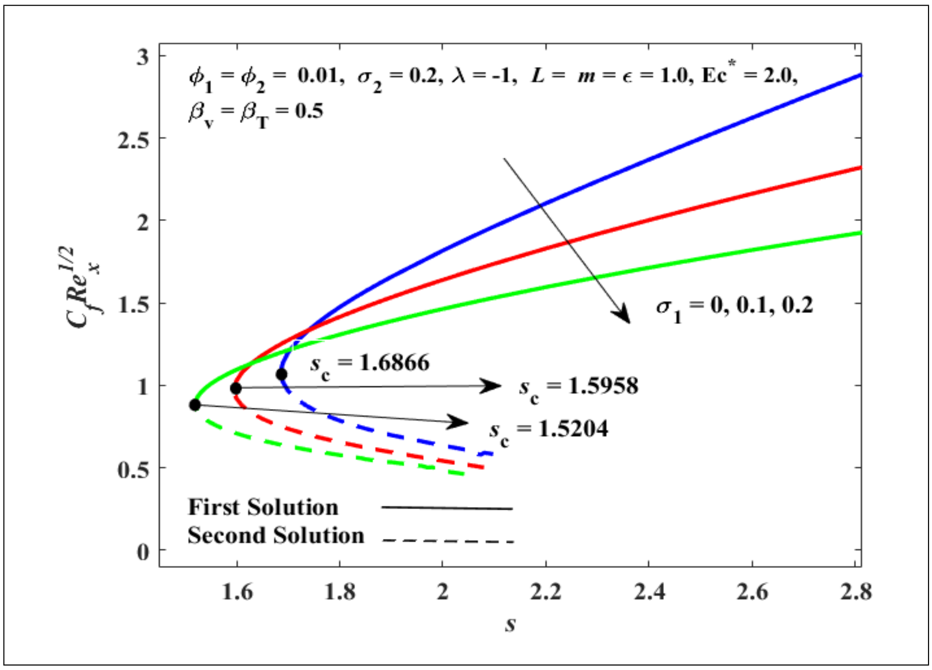

Figure 4.18 $C_f Re_x^{1/2}$ with s for Distinct Values of σ_1

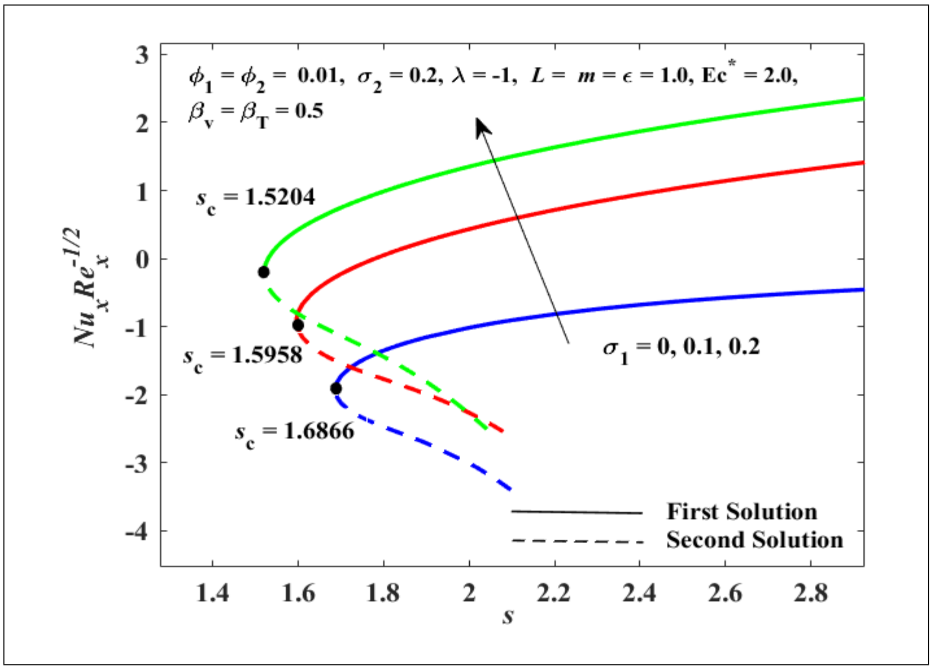

Figure 4.19 $Nu_x Re_x^{-1/2}$ with s for Distinct Values of σ_1

4.3 and Figure 4.23 due to the presence of thermal slip, which acts as a thermal resistance between the fluid and the surface.

The corresponding velocity and temperature profile for $f'(\eta), \theta(\eta)$ and $f_p'(\eta)$, $\theta_p(\eta)$ of Figures 4.22 and 4.23 are presented in Figures 4.24 and 4.25, respectively. Figure 4.24 shows no variation in the velocity profile which indicates no friction

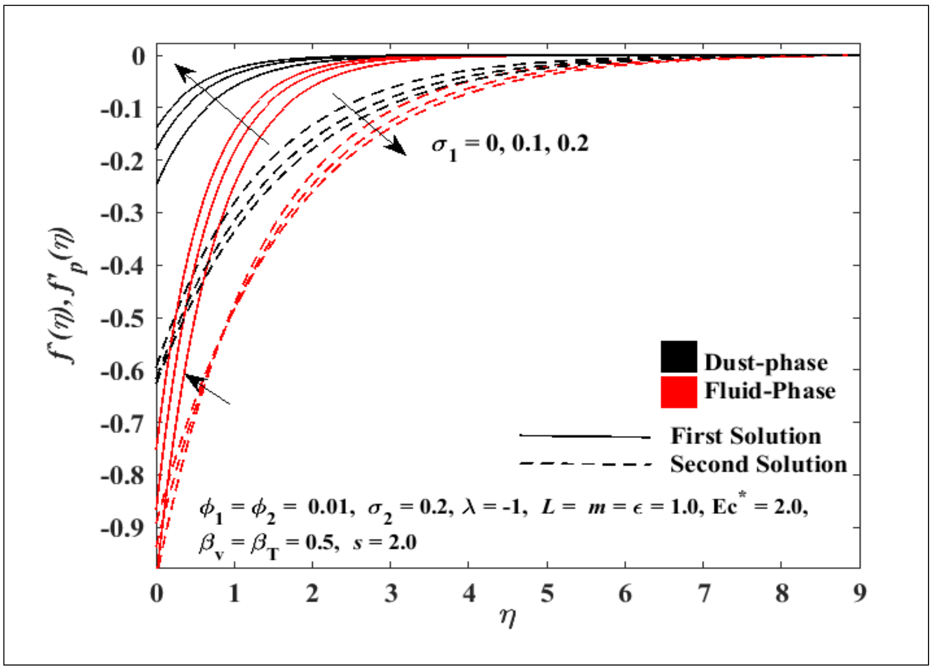

Figure 4.20 Velocity Profile with Distinct Values of σ_1

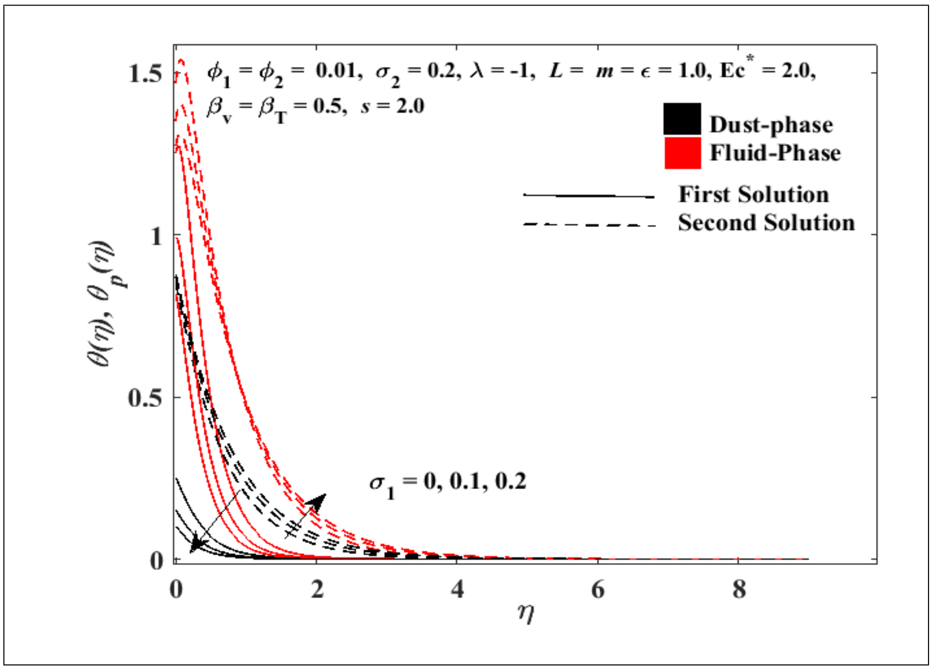

Figure 4.21 Temperature Profile with Distinct Values of σ_1

difference when σ_2 increases as stated in Figure 4.22. Additionally, the temperature profile exhibits a decline in the first solution of both phases and elevates in the second solution, resulting in a thinner boundary layer thickness. The temperature gradient of the second solution reduces as σ_2 increases, leading to reduced local Nusselt number and heat transfer rate.

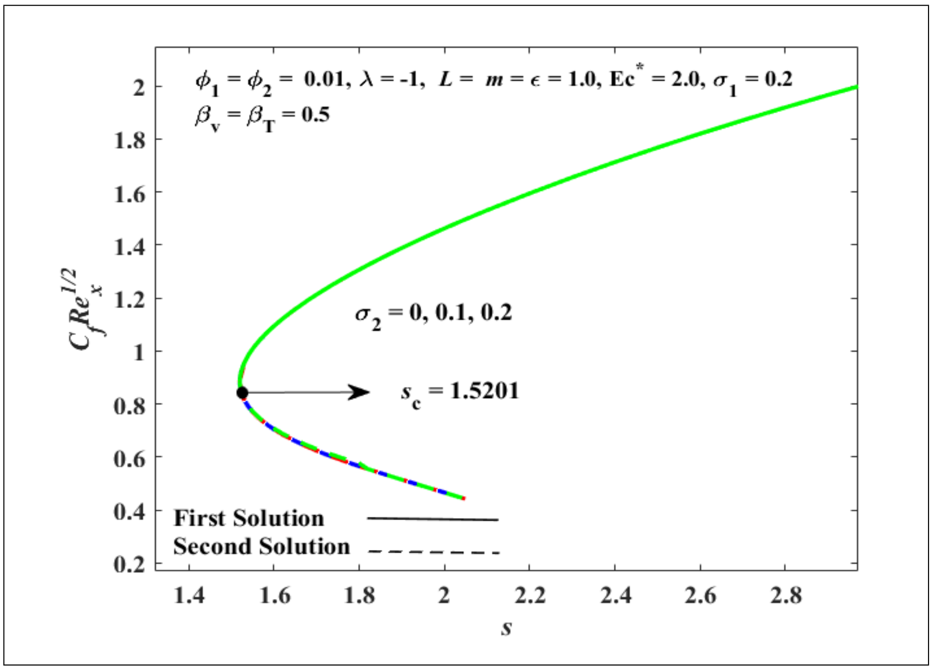

Figure 4.22 $C_f Re_x^{1/2}$ with s for Distinct Values of σ_2

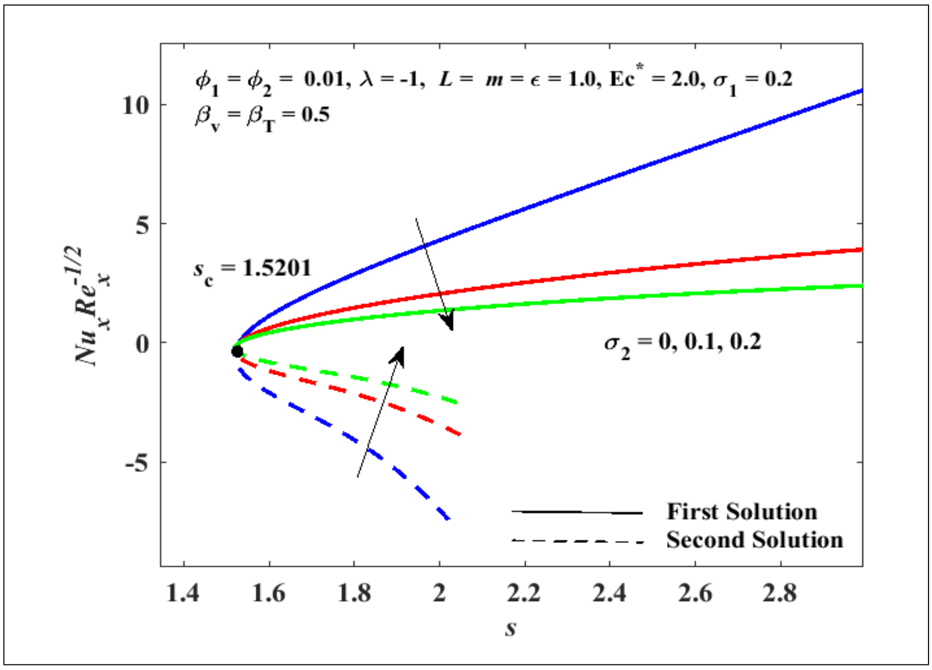

Figure 4.23 $Nu_x Re_x^{-1/2}$ with s for Distinct Values of σ_2

The effect of different values of ϕ_1 and s on the $C_f Re_x^{1/2}$ and $Nu_x Re_x^{-1/2}$ are elucidated in Figures 4.26 and 4.27, respectively. From Table 4.3 and the figures, it can be seen that there is a slight rise in $C_f Re_x^{1/2}$ by 4.9% and 5.99% for the first and second solutions, respectively, while $Nu_x Re_x^{-1/2}$ by 3.76% in the first solution but decreases by 1.86% in second solution when the concentration of ϕ_1 increases. This

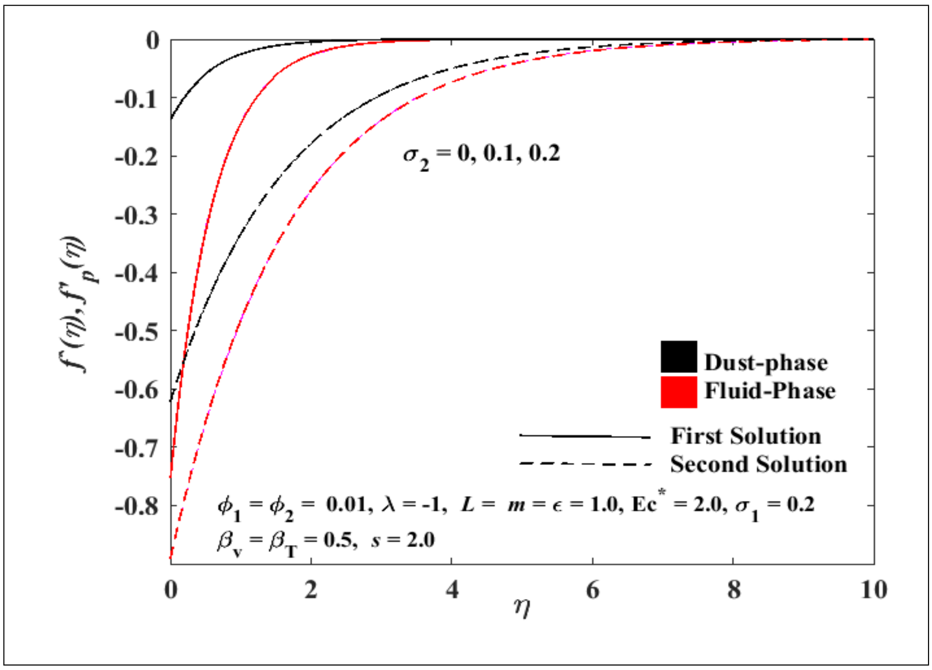

Figure 4.24 Velocity Profile with s for Distinct Values of σ_2

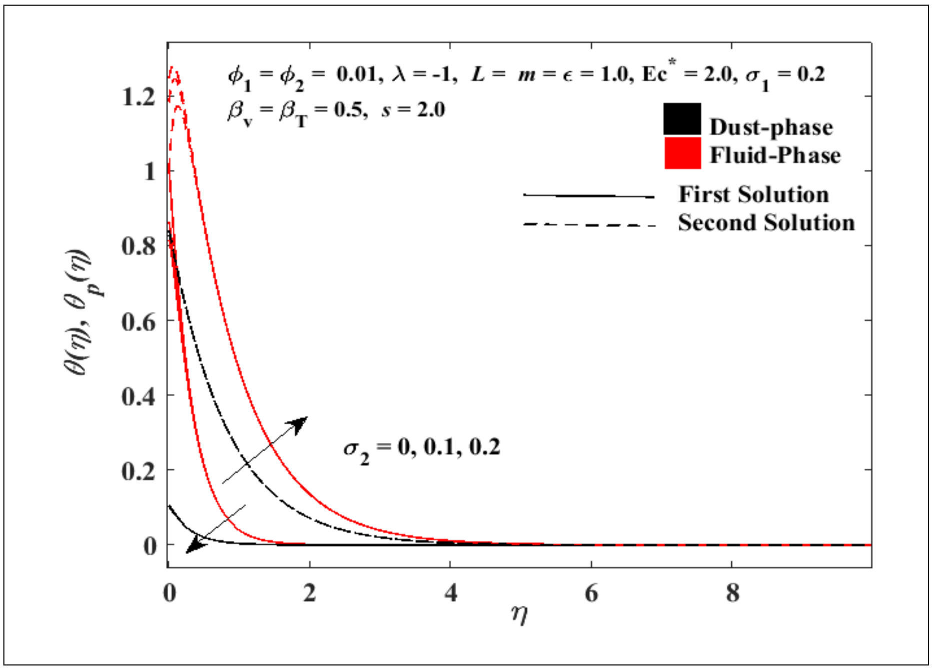

Figure 4.25 Temperature Profile with s for Distinct Values of σ_2

results to an increase in drag forces, resulting in a reduction in fluid velocity while enhancing heat transfer. Dual solutions are observed within the range of $s_c < s < 2.05$ and unique solutions are obtained when $s > 2.05$. Moreover, higher dispersion of Al_2O_3 particles in the base fluid seen to accelerate the boundary layer separation and narrowed down the range of solutions.

Further, the influence of variety ϕ_1 on the velocity and temperature profiles for Figures 4.26 and 4.27 are shown in Figures 4.28 and 4.29, respectively. As presented in Figure 4.28, the addition of ϕ_1 to the base fluid results to an increase in boundary layer thickness, which consequently leads to a less steeper velocity gradient in first solution for both phases, in contrast to the second solution. This signifies an decrease in skin friction, which subsequently enhances the velocity of fluid at the surface. Similar to Figure 4.28, Figure 4.29 depicts a slight increase in thermal boundary layer thickness of the first solution, while a decrease in the second solution for both phases. However, the temperature gradient for the first solution is steeper which implies an enhanced local Nusselt number and heat transmission rate in the first solution compared to the second solution.

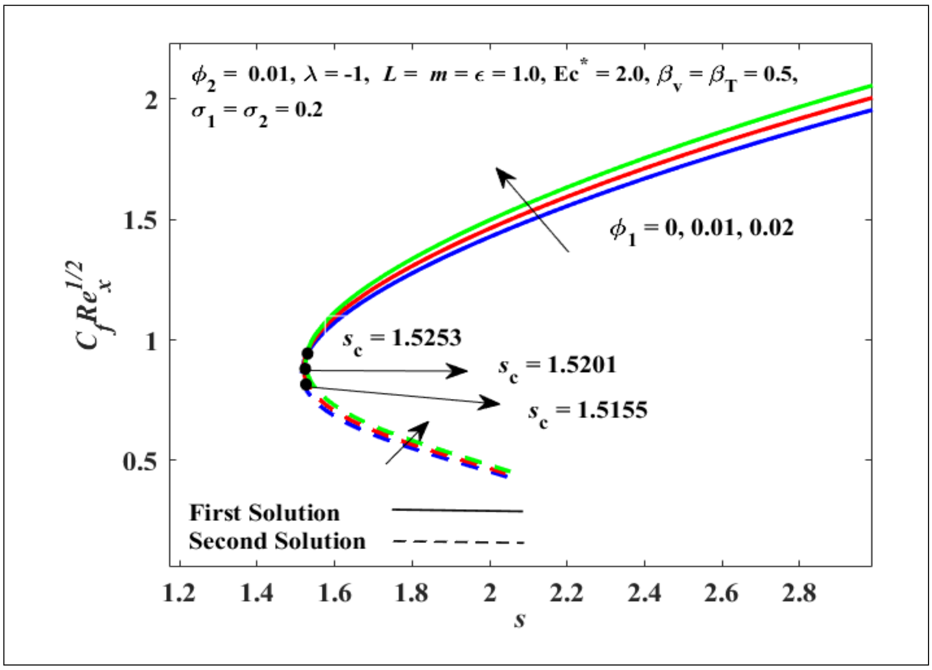

Figure 4.26 $C_f Re_x^{1/2}$ with s for Distinct Values of ϕ_1

The influence of various values of ϕ_2 and s on $C_f Re_x^{1/2}$ and $Nu_x Re_x^{-1/2}$ are displayed in Figures 4.30 and 4.31, respectively. The addition of different concentrations of ϕ_2 into water results in an increment in $C_f Re_x^{1/2}$ and the first solution of $Nu_x Re_x^{-1/2}$ values. Referring to Table 4.3, increasing the concentration of ϕ_2 rises the $C_f Re_x^{1/2}$ by 12.46% and 2.89% in the first and second solutions, respectively, implying an enhanced viscosity, frictional and drag forces which subsequently reduces the fluid velocity. The rate of heat transmission also elevated by 18.97% in the first

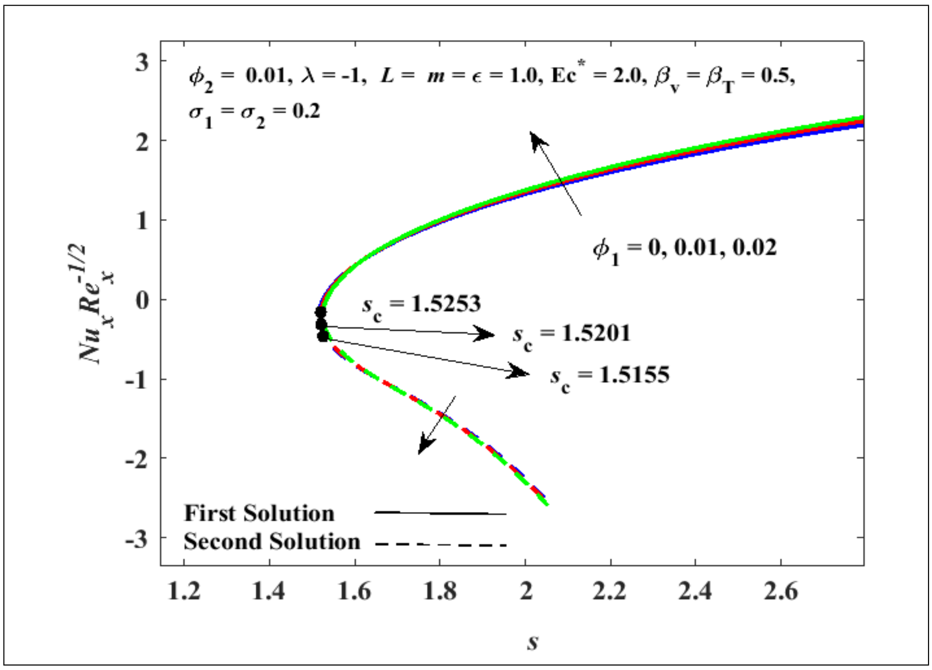

Figure 4.27 $Nu_x Re_x^{-1/2}$ with s for Distinct Values of ϕ_1

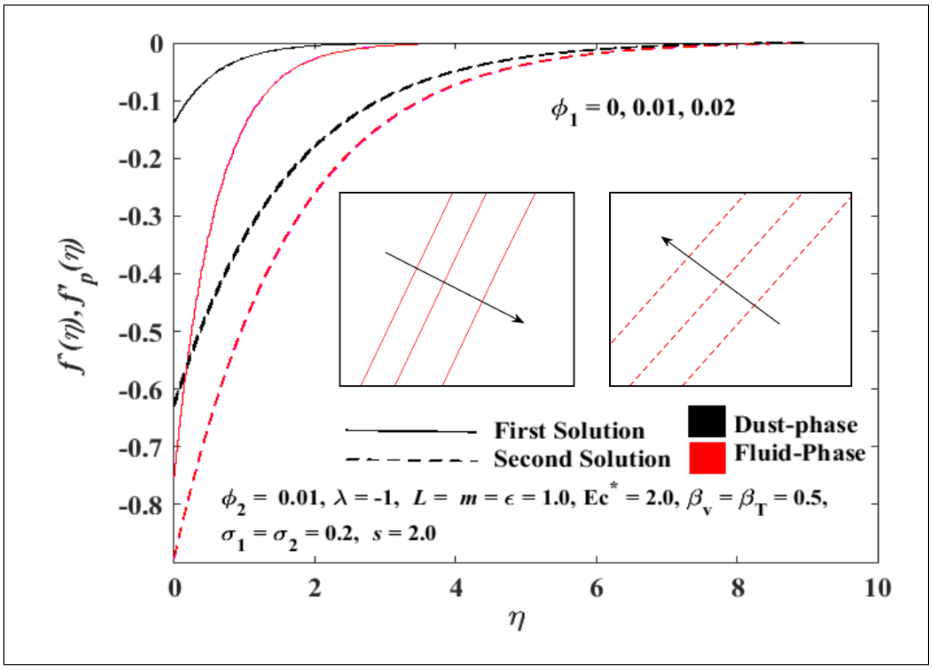

Figure 4.28 Velocity Profile for Distinct Values of ϕ_1

solution and diminishes by 7.55% in the second solution with the increase of the concentration of ϕ_2. Moreover, an increased concentration of ϕ_2 in the base fluid helps in delaying the boundary layer separation, which contradicts the findings presented in Figures 4.26 and 4.27. Further, the dual solutions exist between the range of $s_c < s < 2.05$, and no solutions are found beyond $s < s_c$.

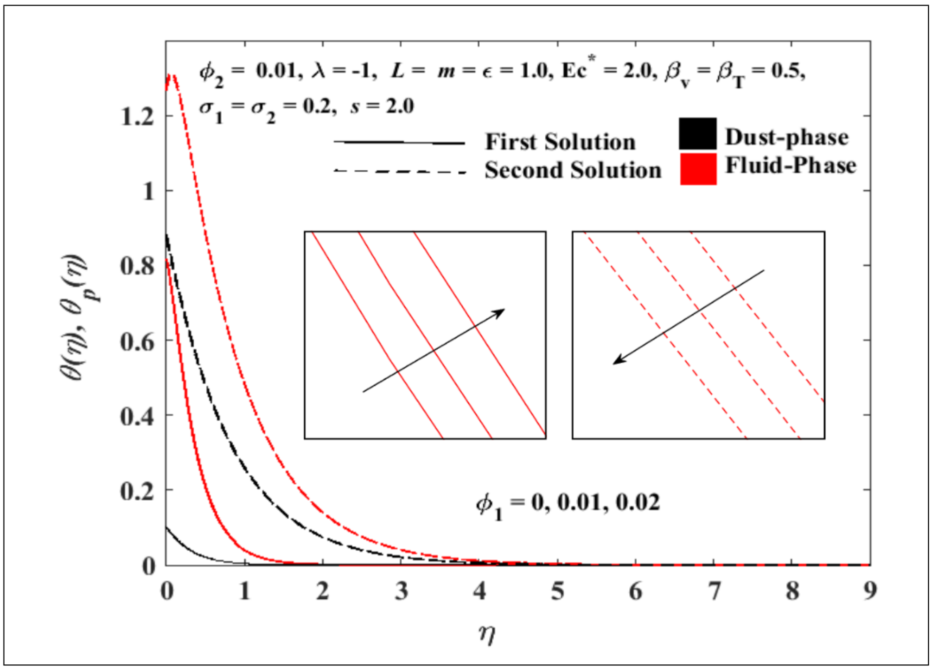

Figure 4.29 Temperature Profile for Distinct Values of ϕ_1

Figures 4.32 and 4.33 show the corresponding velocity and temperature profiles of Figures 4.30 and 4.31, respectively. Based on Figure 4.32, increasing the dispersion of Cu nanoparticle volume fraction into water diminishes the boundary layer thickness of the first solution for both phases, while contradicting pattern in the second solution. This implies that higher concentration of ϕ_2 in the base fluid rises the skin friction coefficient as it increases the effective viscosity and density, which subsequently results in a decrease in fluid velocity at the surface (Palmur et al., 2025). Furthermore, in Figure 4.33 depicts an increase in the concentration of Cu nanoparticle volume fraction reduces the thickness of the thermal boundary layer in the first solution compared to the second solution, indicating more heat is transmitted.

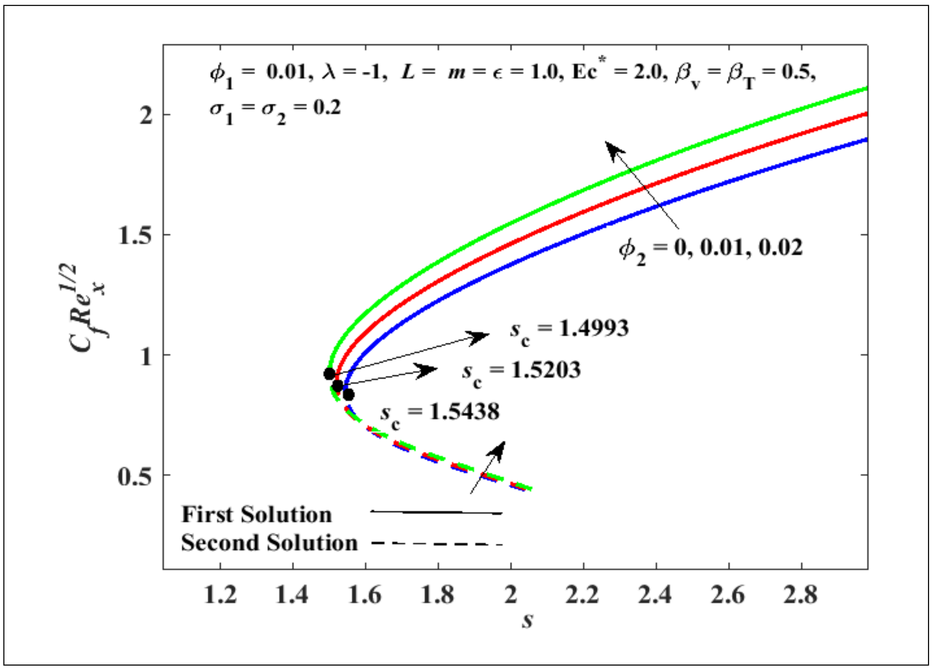

Figure 4.30 $C_fRe_x^{1/2}$ with s for Distinct Values of ϕ_2

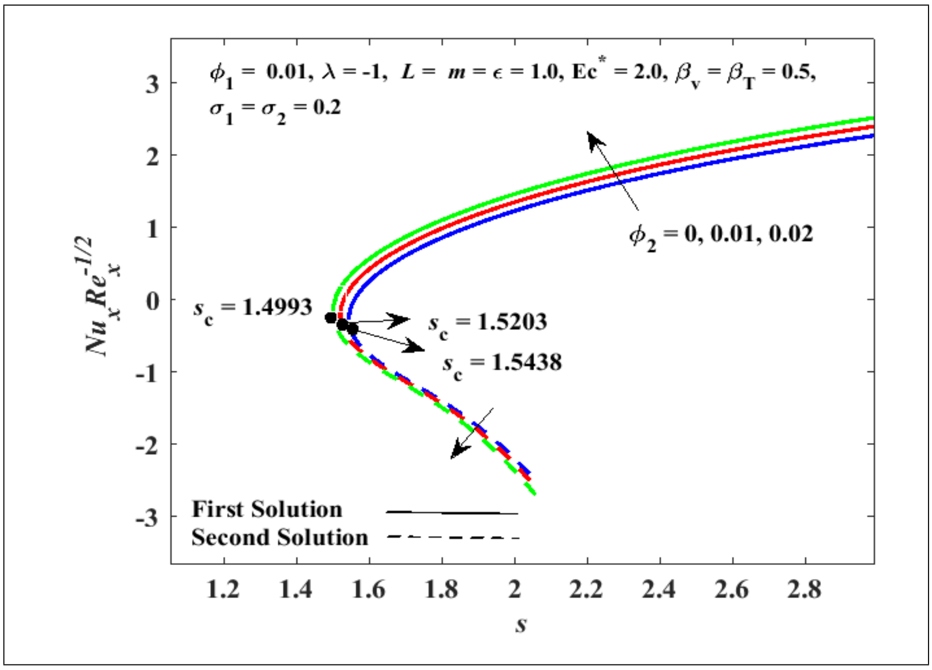

Figure 4.31 $Nu_xRe_x^{-1/2}$ with s for Distinct Values of ϕ_2

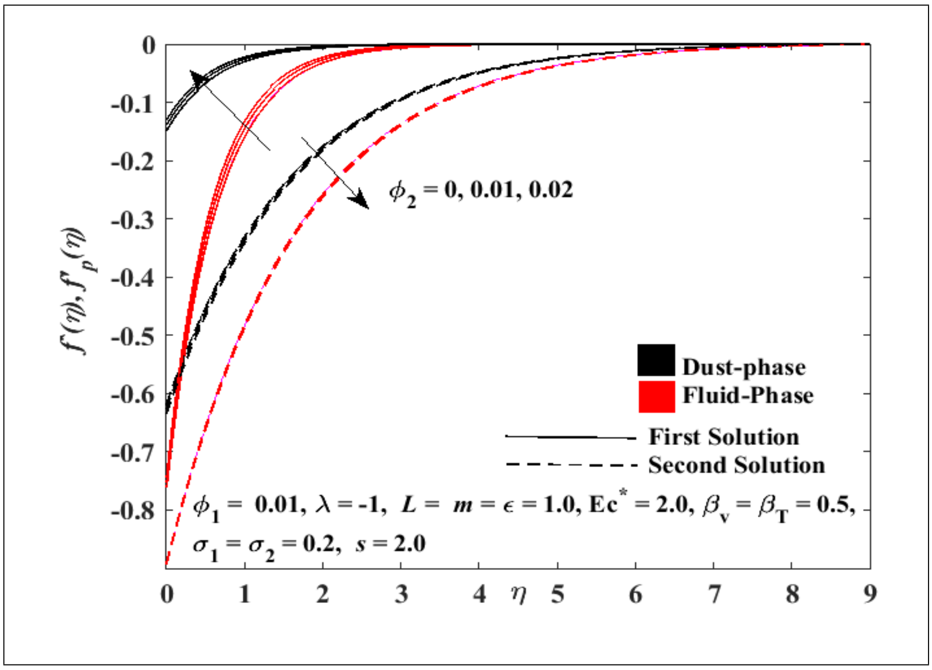

Figure 4.32 Velocity Profile for Distinct Values of ϕ_2

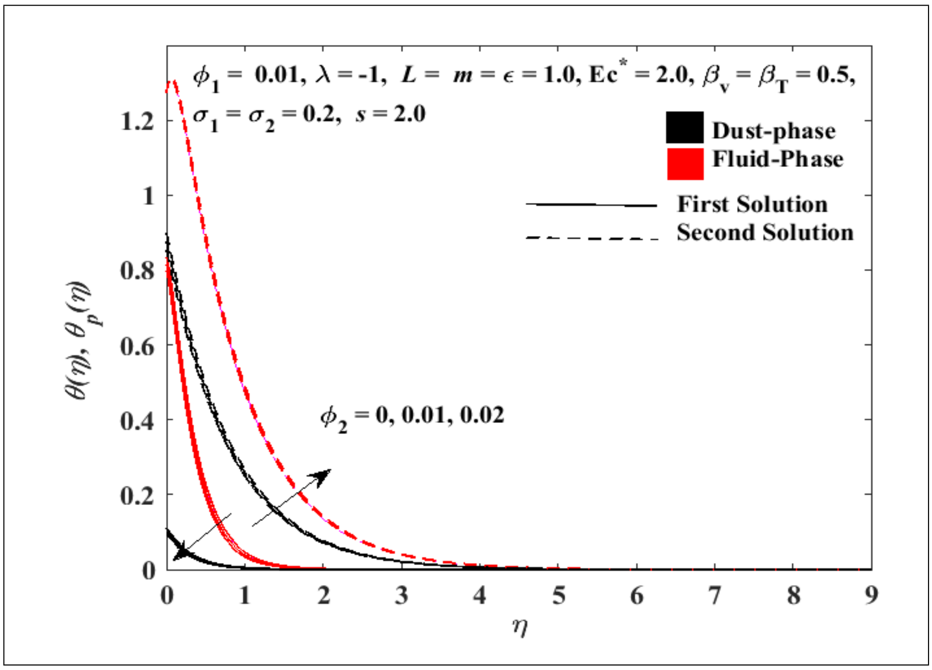

Figure 4.33 Temperature Profile for Distinct Values of ϕ_2

4.5 Conclusions

The steady boundary layer flow over a permeable stretching or shrinking surface with the impact of viscous dissipation, and velocity and thermal slip parameters were investigated in this chapter. Consequently, the conclusions that were derived can be explained as follows:

- The skin friction coefficient increases as the dust particles mass concentration and the addition of different concentrations of alumina and copper nanoparticle volume fraction to the base fluid rises which then elevates the friction between the fluid and the surface due to the upsurge in fluid viscosity, however, as the slip parameters, and velocity slip parameter are considered, it decreases.

- The increase in viscous dissipation (Eckert number) and the thermal slip parameter shows no changes in the values of skin friction coefficient, this is because both parameters influences the thermal energy transport through the energy equation and do not directly affect the momentum equation, thus they insignificantly affect the skin friction coefficient.

- The augmentation in the values of dust particle mass concentration, viscous dissipation, and thermal slip parameter decreases the heat transfer rate, whilst, slip parameters, velocity slip parameter, alumina, and copper nanoparticle volume fractions increase the rate of heat transmission within the surface and the fluid.

- The thermal boundary layer thickness for both fluid and dust phases for temperature profile are generally thinner for the first solution of the parameters examined, implying an improvement in heat transmission compared to the second solution.

- The dual solution exists for the range of $s_c < s < 2.5$, and $\lambda_c < \lambda < -0.1$ for the parameters considered, while unique solutions are obtained beyond $s > 2.5$, and $\lambda > -0.1$. The range of dual solutions were broadened with the increase of dust particle mass concentration, slip parameters, velocity slip parameter, and copper nanoparticle volume fraction.

CHAPTER 5
BOUNDARY LAYER FLOW AND HEAT TRANSFER OF DUSTY HYBRID NANOFLUID OVER AN INCLINED STRETCHING OR SHRINKING SURFACE WITH THE EFFECTS OF VISCOUS DISSIPATION AND SLIP CONDITIONS

5.1 Introduction

This chapter extends the mathematical model presented in Chapter 4 by considering an inclined surface, while the previous chapter focused on a horizontal surface. Inclined surfaces are commonly found in engineering systems such as solar energy collectors, electronic cooling devices, and heat exchangers, where optimizing heat transfer is crucial. Therefore, the analysis of this considered problem is important in enhancing thermal management strategies in practical applications. Furthermore, the inclination of the surface introduces gravitational and buoyancy forces, which significantly affect the flow behavior and heat transfer. In this chapter, the steady boundary layer flow and heat transfer of dusty hybrid nanofluid over an inclined stretching or shrinking surface were examined, incorporating the effects of viscous dissipation, velocity, and thermal slip conditions. Through this analysis, the chapter offers a comprehensive understanding of flow and thermal characteristics over an inclined surface, thereby providing a foundation for future experimental and industrial advancements.

5.2 Mathematical Formulation

Consider a steady two-dimensional boundary layer flow over an inclined permeable stretching or shrinking surface with viscous dissipation, and slip conditions effects in a dusty hybrid nanofluid as illustrated in Figures 5.1 and 5.2.

The governing equations for hybrid nanofluid and dust phases are referred from Afridi et al. (2017, Alabdulhadi et al. (2021, Anuar et al. (2021a, and Anuar et al. (2021b. The continuity and energy equations for the hybrid nanofluid phase, along with the continuity, momentum, and energy equations for the dust phase are aligned

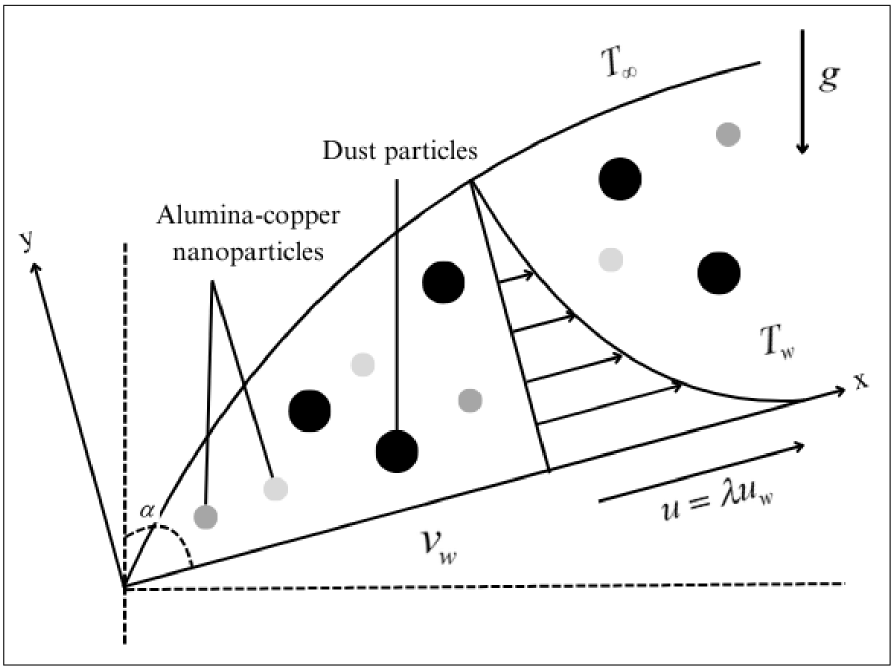

Figure 5.1 Physical Model of an Inclined Stretching Surface

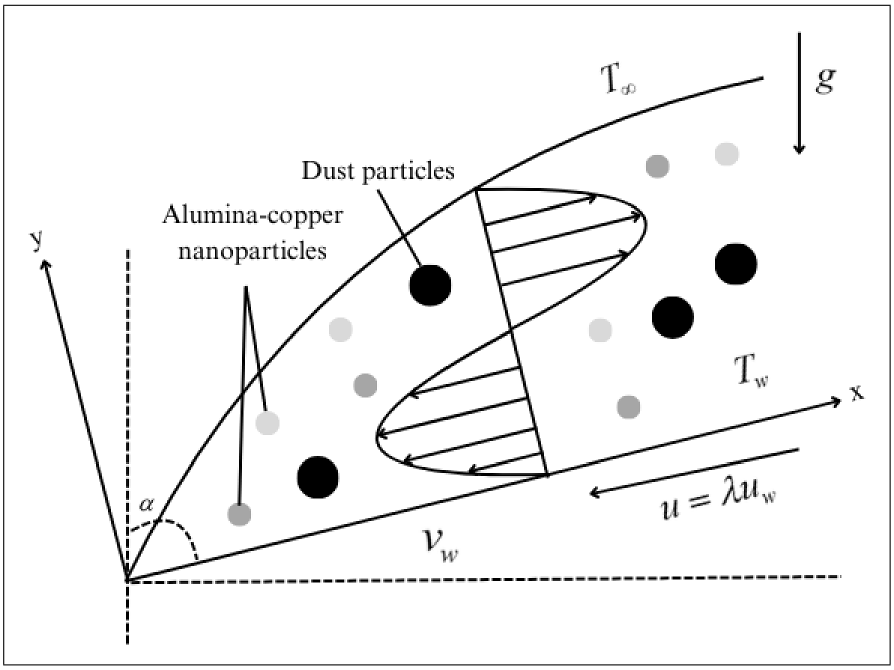

Figure 5.2 Physical Model of an Inclined Shrinking Surface

with (3.2.1) and (3.2.22), as well as (3.2.5), (3.2.6), and (3.2.8), respectively, under the boundary conditions specified in (3.2.24). The exception lies in the momentum equation for the hybrid nanofluid phase. Since we have considered inclined surface, thus there is an extra term in the momentum equation and is detailed as follows:

i. Hybrid nanofluid phase

Momentum equation:

$$u\frac{\partial u}{\partial x}+v\frac{\partial u}{\partial y}=-\frac{1}{\rho_{hnf}}\frac{\partial p}{\partial x}+\frac{\mu_{hnf}}{\rho_{hnf}}\frac{\partial^2 u}{\partial y^2}+\frac{KN}{\rho_{hnf}}(u_p-u)+g\beta^*(T-T_\infty)\,cos\alpha. \tag{5.2.1}$$

Further, to achieve the similarity transformation, T_w and Ec are assumed to be

$$T_w=T_\infty+bx^2, \qquad \mathrm{Ec}=\frac{a^2}{(C_p)_f b} \tag{5.2.2}$$

different with the T_w and Ec^* that were considered in Chapter 4, where b is a constant. In addition, we consider the volumetric thermal expansion coefficient to be $\beta^*=nx^{-1}$ to obtain the similarity equations (Afridi et al., 2017) and equations (3.3.3), (3.3.9), (3.3.10), (3.3.16), (3.3.17), and (3.3.20) are employed to reduce the governing equations to ordinary differential equations are expressed as follows:

$$\frac{\mu_{hnf}/\mu_f}{\rho_{hnf}/\rho_f}f'''+ff''-f'^2+\frac{L\beta_v}{\rho_{hnf}/\rho_f}\left(f_p'-f'\right)+\lambda^*\theta cos\alpha=0, \tag{5.2.3}$$

where λ^* is the mixed convection parameter, $\lambda^*>0$ implies the assisting buoyant force, $\lambda^*<0$ implies the opposing buoyant force, and α is the inclination angle. Then, equation (5.2.3) are converted to (5.2.4) by employing the physical properties of nanofluid and hybrid nanofluid in Table 3.1.

$$\begin{aligned}&\frac{1}{(1-\phi_1)^{2.5}(1-\phi_2)^{3.5}\left[\left[(1-\phi_1)+\phi_1\frac{\rho_1}{\rho_f}\right]+\phi_2\frac{\rho_2}{\rho_f}\right]}f'''+ff''-f'^2\\&+\frac{L\beta_v}{(1-\phi_2)\left[\left[(1-\phi_1)+\phi_1\frac{\rho_1}{\rho_f}\right]+\phi_2\frac{\rho_2}{\rho_f}\right]}\left(f_p'-f'\right)+\lambda^*\theta cos\alpha=0,\end{aligned} \tag{5.2.4}$$

subjected to boundary conditions (3.3.84)

$$\begin{aligned}&f(0)=s, \qquad f'(0)=\lambda+\sigma_1 f''(0), \qquad \theta(0)=1, \qquad \theta(0)=1+\sigma_2\theta'(0),\\&f'(\eta)\to 0, f_p'(\eta)\to 0, f_p'(\eta)\to f(\eta), \theta(\eta)\to 0, \theta_p(\eta)\to 0 \qquad \text{as} \quad \eta\to\infty.\end{aligned}$$

5.3 Results and Discussion

The numerical solutions of the ordinary differential equations (3.3.44), (3.3.65), (3.3.75), and (5.2.4) under the boundary conditions (3.3.84) were generated by the computation of bvp4c function in MATLAB, and the results are presented in tabular and graphical form. Table 5.1 presents the numerical results of the current study for the impact of L, Ec, α, σ_1, σ_2, ϕ_1, and ϕ_2 on $C_f Re_x^{1/2}$ and $Nu_x Re_x^{-1/2}$ for the values Pr = 6.2, $\lambda = -1, m = \epsilon = 1.0, \beta_v = \beta_T = 0.5$ and $s = 2.0$.

The influence of various values of L on $C_f Re_x^{1/2}$ and $Nu_x Re_x^{-1/2}$ against λ are demonstrated in Figures 5.3 and 5.4, respectively. Based on Table 5.1 and Figure 5.3, the increment in dust particles concentration results in elevated $C_f Re_x^{1/2}$ values by 1.77% in the first solution but decreases by 2.86% in the second solution. This occurs due to an increased suspension of dust particles in the fluid, resulting in an augmented flow resistance (Alarabi et al., 2024). Additionally, a decline in the values of $Nu_x Re_x^{-1/2}$ is noted, with a 0.07% decrease in the first solution and a 30% reduction in the second solution, as shown in Table 5.1 and Figure 5.4, indicating a reduction in the heat transfer rate as L increases. Furthermore, dual solutions arise for the shrinking surfaces, and no solutions were identified beyond the critical point λ_c.

The corresponding profiles of velocity and temperature for Figures 5.3 and 5.4 are portrayed in Figures 5.5 and 5.6, respectively. The velocity profile depicted in Figure 5.5 shows an increase for the first solution, whereas a decrease is observed in the second solution for both phases. The boundary layer thickness of the first solution is thinner compared to the second solution, indicating a higher velocity gradient that results in a higher skin friction coefficient and a decrease in fluid flow velocity. Moreover, the temperature profile illustrated in Figure 5.6 shows a reduction in the boundary layer thickness in the first solution for both phases, whereas it shows an increase in the second solution. It indicates that the local Nusselt number which implies the rate of heat transfer is higher in the first solution than the second solution.

The implication of suspending distinct values of L in the base fluid on $C_f Re_x^{1/2}$ and $Nu_x Re_x^{-1/2}$ with various values of s are displayed in Figures 5.7 and 5.8. These figures implies that more than one solution are identified as L rises, and no solutions are obtained over the critical point $s < s_c$. Adding to that, it is observed that an

Table 5.1
Impact of L, Ec, α, σ_1, σ_2, ϕ_1, and ϕ_2 on $C_f Re_x^{1/2}$ and $Nu_x Re_x^{-1/2}$ for Pr = 6.2, $\lambda = -1, m = \epsilon = 1.0, \beta_v = \beta_T = 0.5$ and $s = 2.0$

L	Ec	α	σ_1	σ_2	ϕ_1	ϕ_2	$C_f Re_x^{1/2}$		$Nu_x Re_x^{-1/2}$	
							First Solution	Second Solution	First Solution	Second Solution
0	2.0	$\pi/4$	0.2	0.2	0.01	0.01	1.2847	0.5867	1.1085	-0.8241
0.01	2.0	$\pi/4$	0.2	0.2	0.01	0.01	1.2871	0.5849	1.1084	-0.8496
0.1	2.0	$\pi/4$	0.2	0.2	0.01	0.01	1.3075	0.5699	1.1077	-1.0713
1.0	0	$\pi/4$	0.2	0.2	0.01	0.01	1.4628	0.4798	3.6350	3.5800
1.0	0.5	$\pi/4$	0.2	0.2	0.01	0.01	1.4628	0.4800	3.0053	2.0664
1.0	2.0	$\pi/4$	0.2	0.2	0.01	0.01	1.4629	0.4667	1.1160	-2.8848
1.0	2.0	$\pi/6$	0.2	0.2	0.01	0.01	1.4630	0.4669	1.1160	-2.8861
1.0	2.0	$\pi/4$	0.2	0.2	0.01	0.01	1.4629	0.4667	1.1160	-2.8848
1.0	2.0	$\pi/3$	0.2	0.2	0.01	0.01	1.4629	0.4664	1.1160	-2.8832
1.0	2.0	$\pi/4$	0	0	0.01	0.01	1.8172	0.6134	-4.5836	-11.1975
1.0	2.0	$\pi/4$	0.1	0.1	0.01	0.01	1.6392	0.5421	0.1622	-4.3153
1.0	2.0	$\pi/4$	0.2	0.2	0.01	0.01	1.4629	0.4667	1.1160	-2.8848
1.0	2.0	$\pi/4$	0	0.2	0.01	0.01	1.8172	0.6134	-1.4824	-3.6742
1.0	2.0	$\pi/4$	0.1	0.2	0.01	0.01	1.6392	0.5293	0.1069	-3.1905
1.0	2.0	$\pi/4$	0.2	0.2	0.01	0.01	1.4629	0.4667	1.1160	-2.8848
1.0	2.0	$\pi/4$	0.2	0	0.01	0.01	1.4629	0.4667	3.5528	-8.8855
1.0	2.0	$\pi/4$	0.2	0.1	0.01	0.01	1.4629	0.4667	1.6985	-4.3556
1.0	2.0	$\pi/4$	0.2	0.2	0.01	0.01	1.4629	0.4667	1.1160	-2.8848
1.0	2.0	$\pi/4$	0.2	0.2	0	0.01	1.4281	0.4534	1.1600	-2.6866
1.0	2.0	$\pi/4$	0.2	0.2	0.01	0.01	1.4629	0.4667	1.1160	-2.8848
1.0	2.0	$\pi/4$	0.2	0.2	0.02	0.01	1.4793	0.4806	1.0670	-3.0881
1.0	2.0	$\pi/4$	0.2	0.2	0.01	0	1.3768	0.4601	1.1612	-2.3777
1.0	2.0	$\pi/4$	0.2	0.2	0.01	0.01	1.4629	0.4667	1.1160	-2.8848
1.0	2.0	$\pi/4$	0.2	0.2	0.01	0.02	1.5485	0.4738	1.0649	-3.4357

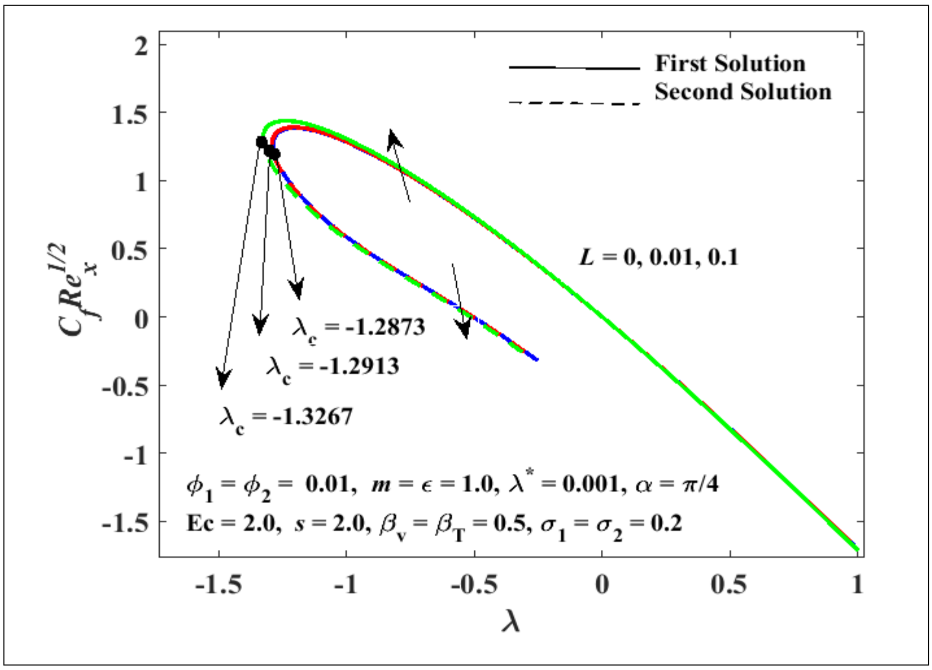

Figure 5.3 $C_f Re_x^{1/2}$ with λ for Various Values of L

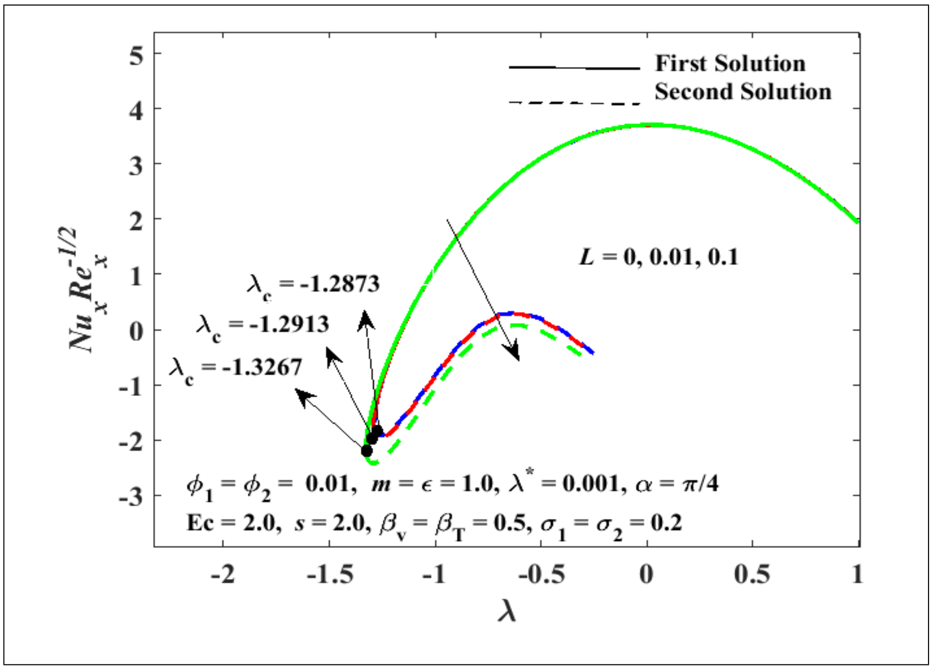

Figure 5.4 $Nu_x Re_x^{-1/2}$ with λ for Various Values of L

increase in the concentration of dust particles in the fluid enhances the fluid to adhere to the surface, thereby helps in delaying the boundary layer separation. According to Figure 5.7, the values of $C_f Re_x^{1/2}$ increase with the suspension of additional dust particles. This is due to the elevated concentration of dust particles within the fluid which increases the friction as the fluid flows. Meanwhile, in Figure 5.8, the values

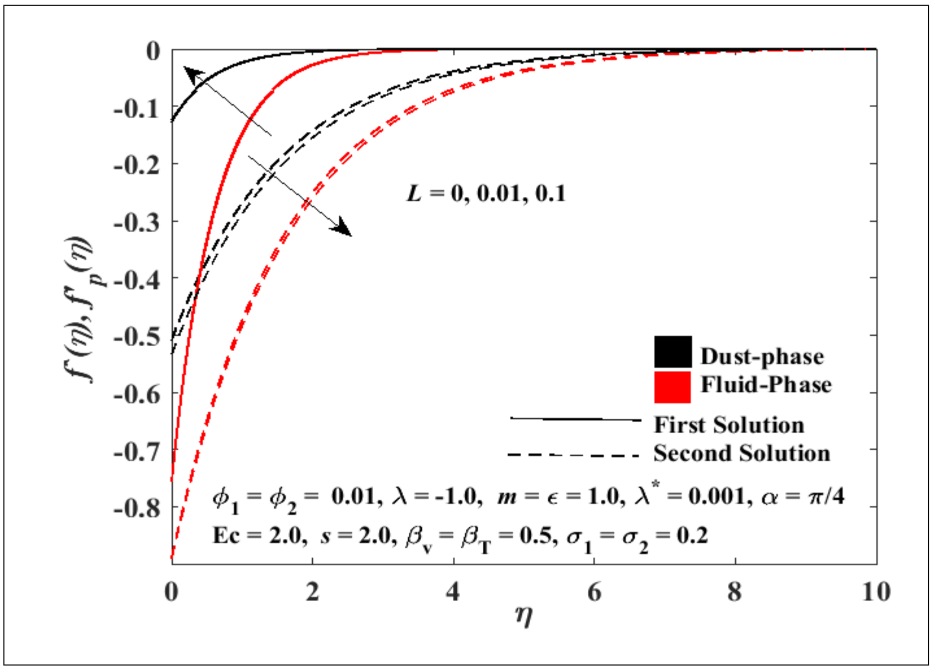

Figure 5.5 Velocity Profile for Various Values of L

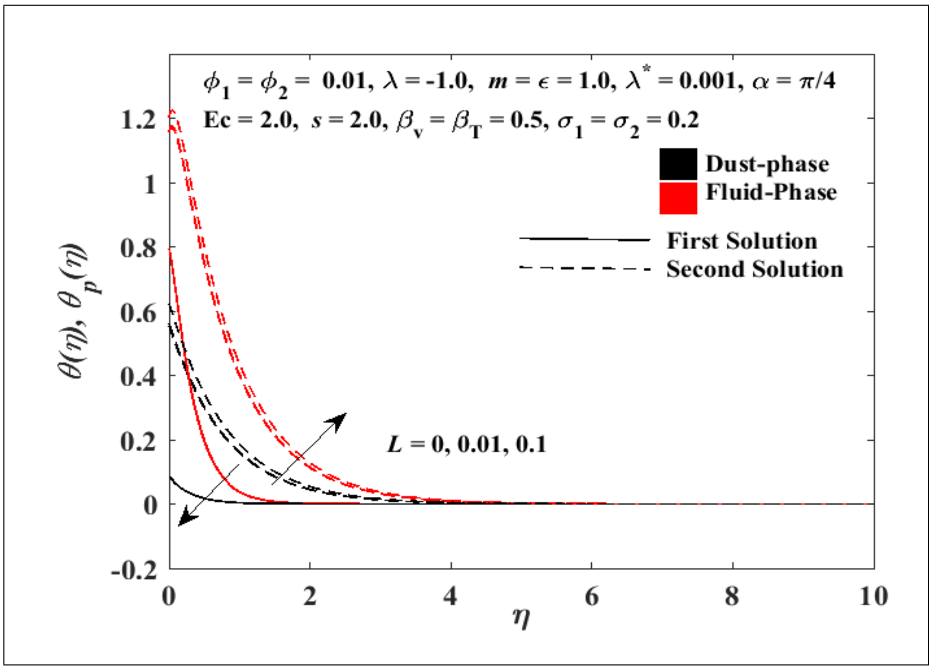

Figure 5.6 Temperature Profile for Various Values of L

$Nu_x Re_x^{-1/2}$ diminishes as L increases which lowers down the heat transfer rate at the surface.

The velocity and temperature profiles for some values of L over a shrinking surface for Figures 5.7 and 5.8 are presented in Figures 5.9 and 5.10, correspondingly.These profile are equivalent to the profiles shown in Figures 5.5

and 5.6 as same parameters are utilized. Rising the values of dust particles mass concentration has elevated the velocity profile of the first solution and decreased for the second solution for both phases. The thickness of the velocity boundary layer decreases in the first solution of both phases, subsequently increasing the velocity gradient, which in turn augments the skin friction coefficient in the boundary layer flow. Additionally, there is a reduction in temperature also for the first solution and increases for the second solution of both phases. The boundary layer thickness of the first solution is notably smaller than the second solution indicating an increase in local Nusselt number and more efficient heat transfer in the first solution compared to the second solution.

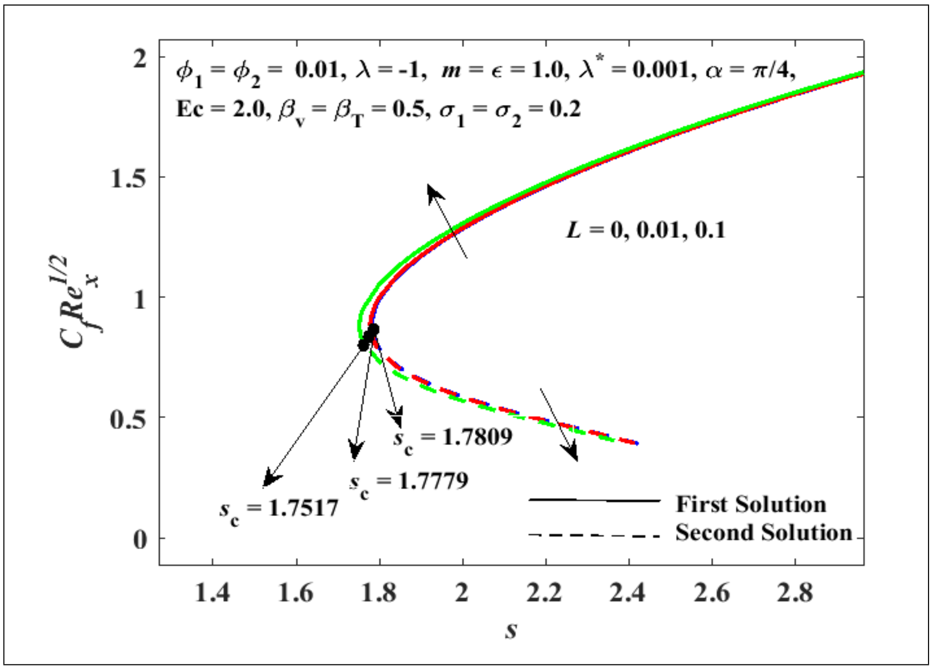

Figure 5.7 $C_f Re_x^{1/2}$ with s for Distinct Values of L

The quantities of physical interest which are the $C_f\ Re_x^{1/2}$ and $Nu_x Re_x{}^{-1/2}$ for distinct values of Ec number are illustrated in Figures 5.11 and 5.12, respectively. The dual solution are observed in the range $s_c < s < 2.1$, while no solutions can be found when $s < s_c$ as it implies the occurrence of boundary layer separation. According to Table 5.1 and Figure 5.11, the values of $C_f Re_x^{1/2}$ shows a 0.007% increase for the first solution and 2.73% decrease for the second solution with the increasing Ec number, whereas $Nu_x Re_x^{-1/2}$ values decrease by 69.30% and 180.58% for the first and second solutions, respectively, as Ec number rises. This decline occurs because more kinetic

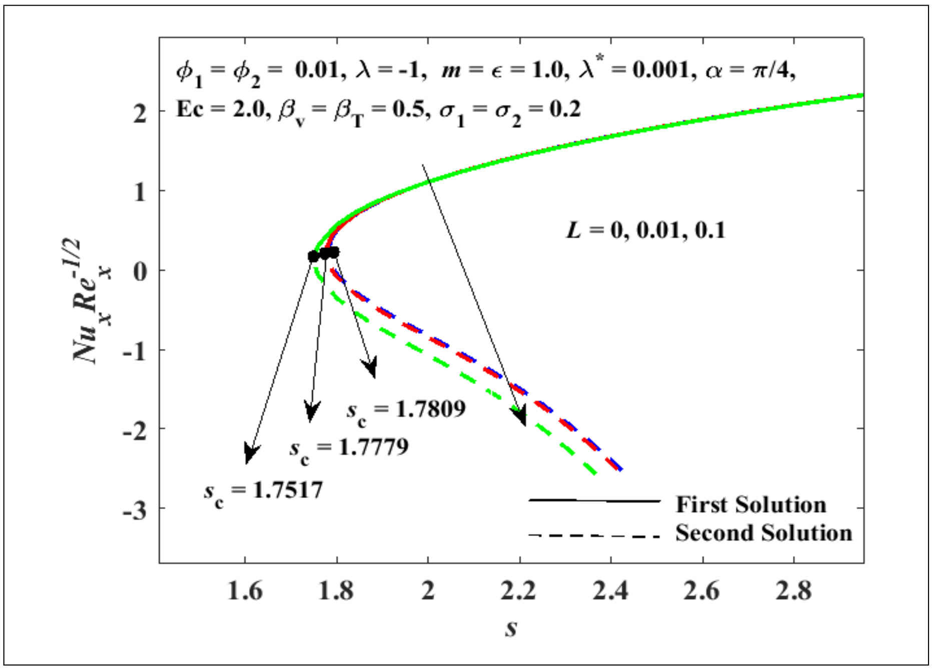

Figure 5.8 $Nu_x Re_x^{-1/2}$ with s for Distinct Values of L

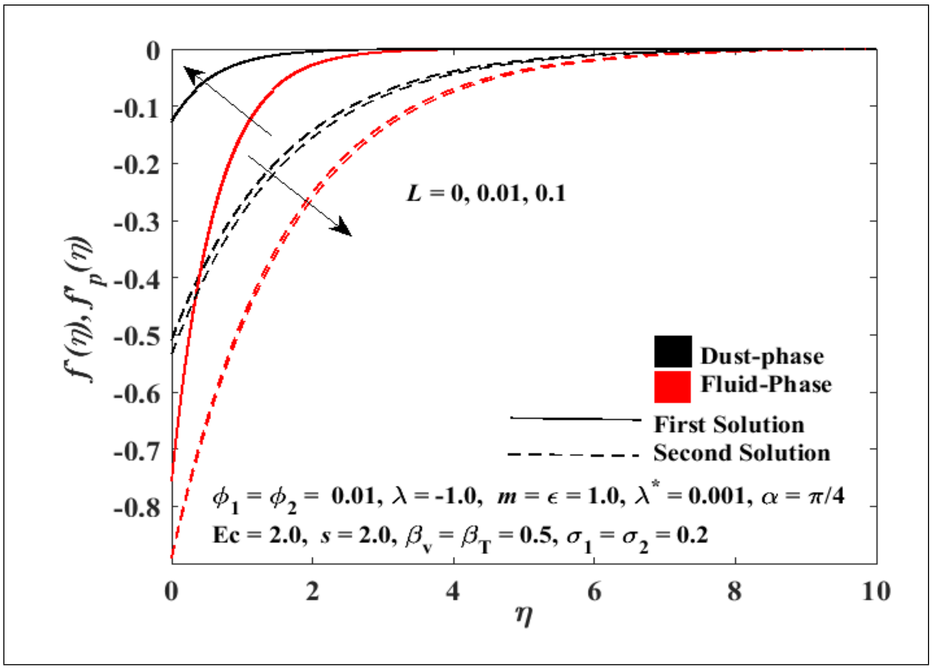

Figure 5.9 Velocity Profile for Distinct Values of L

energy is converted to thermal energy, resulting in an elevated fluid temperature due to the thermal energy retained in the fluid (Tripathy et al., 2024). Thus, the rate of heat transfer within the surface reduces.

Figures 5.13 and 5.14 displays the velocity and temperature profiles for $f'(\eta)$, $\theta(\eta)$ and $f'_p(\eta), \theta_p(\eta)$ of Figures 5.11 and 5.12, respectively. The velocity profile

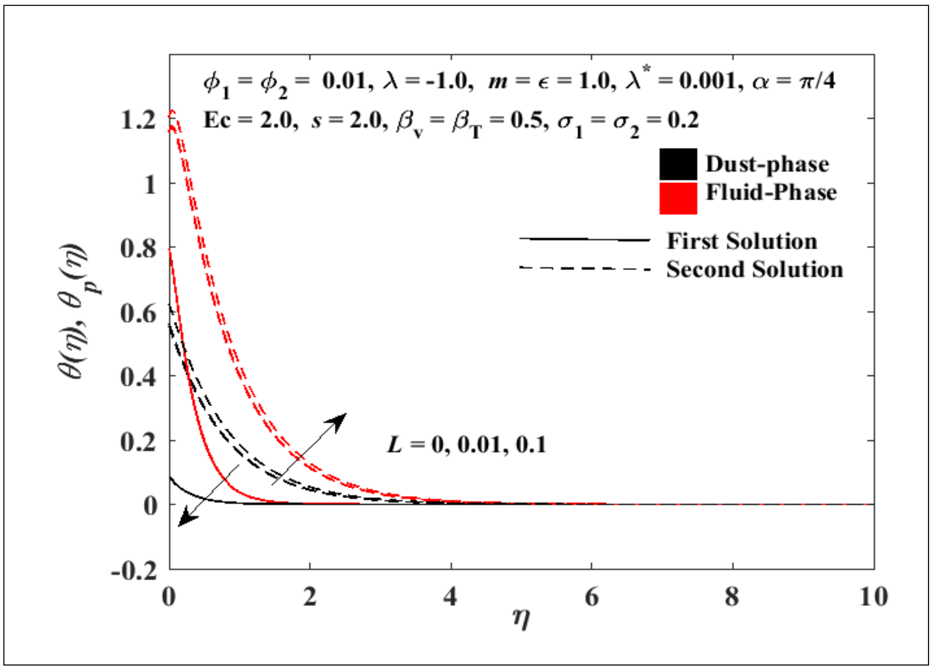

Figure 5.10 Temperature Profile for Distinct Values of L

exhibits minimal changes in both solution for both phases, validating the findings shown in Figure 5.11. In contrast, temperature profile in Figure 5.14 demonstrates an increase with rising Ec numbers. The boundary layer thickness also increases, indicating a decrease in local Nusselt number and heat transfer rate in both solutions and phases.

The findings of $C_f Re_x^{1/2}$ and $Nu_x Re_x^{-1/2}$ for variety values of of s and α are elucidated in Figures 5.15 and 5.16, respectively. The transitions of surface from vertical to horizontal results in a minimal diminishing trend in both the values of $C_f Re_x^{1/2}$ and $Nu_x Re_x^{-1/2}$. Based on Table 5.1 and Figure 5.15, a decrease of 0.007% and 0.11% for the first and second solutions, respectively for the values of $C_f Re_x^{1/2}$ are noted, while for $Nu_x Re_x^{-1/2}$ a very minimal decrease in the first solution and 0.1% increase in the second solution. Thus, it can be conclude that increasing the angle, reduces the frictional force and heat transfer between the fluid flow and the surface (Uddin et al., 2024). Furthermore, the rise in α accelerates the boundary layer separation.

Besides that, the profiles of velocity and temperature for $f'(\eta)$, $\theta(\eta)$ and $f_p'(\eta)$, $\theta_p(\eta)$ of Figures 5.15 and 5.16 are presented in Figures 5.17 and 5.18,

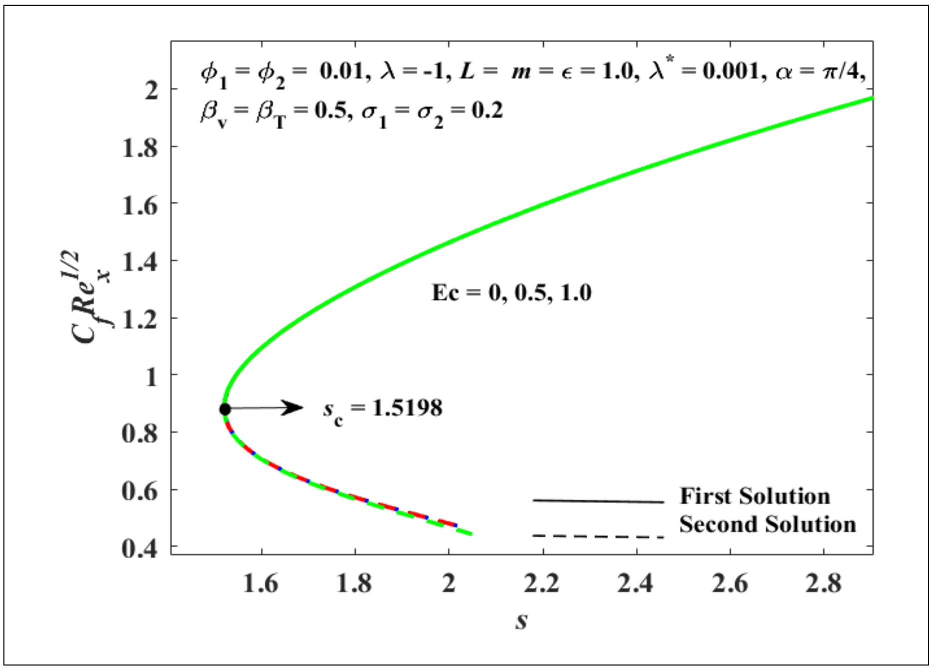

Figure 5.11 $C_f Re_x^{1/2}$ with s for Distinct Values of Ec Number

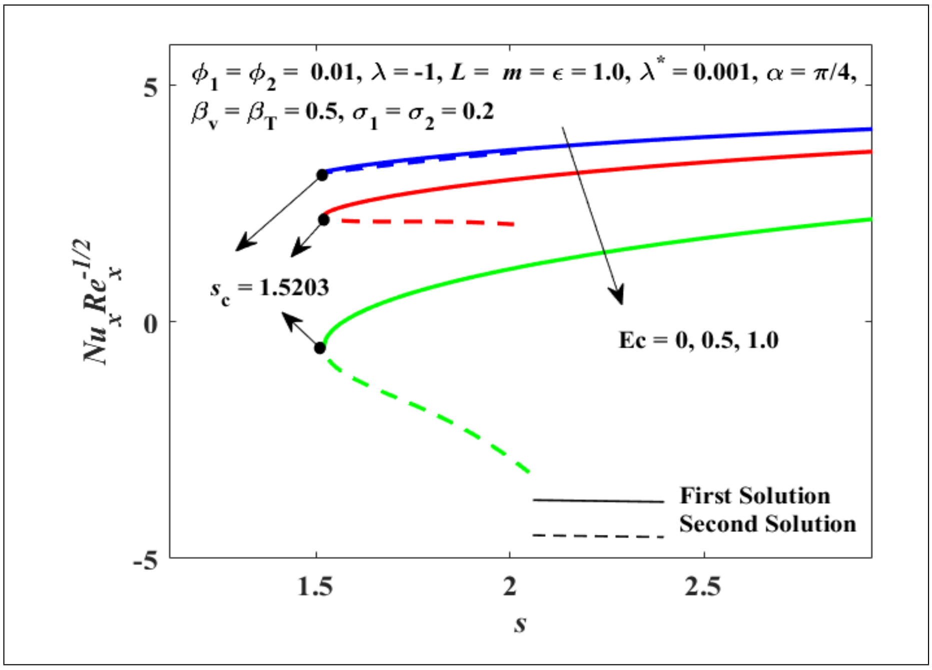

Figure 5.12 $Nu_x Re_x^{-1/2}$ with s for Distinct Values of Ec Number

correspondingly. Analysis of Figure 5.17 reveals that the velocity profile decreases for the first solution but increases in the second solution for both phases leading to an increase in boundary layer thickness and decreased velocity gradient. Consistent with the results shown in Figure 5.15. Further, in Figure 5.18, the temperature profile increases for the first solution, while a decrease in the second solution for both phases.

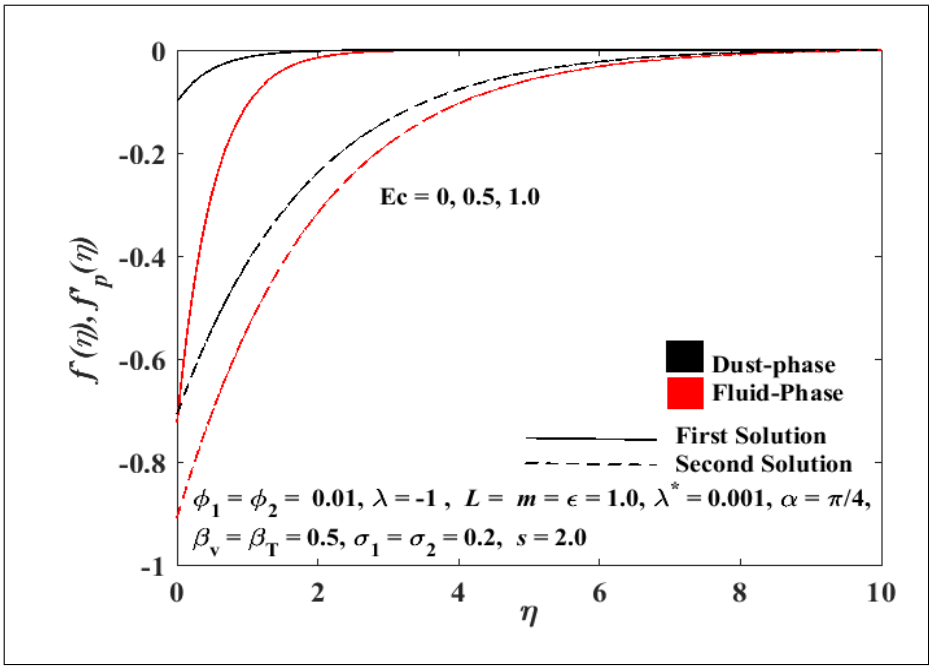

Figure 5.13 Velocity Profile for Distinct Values of Ec Number

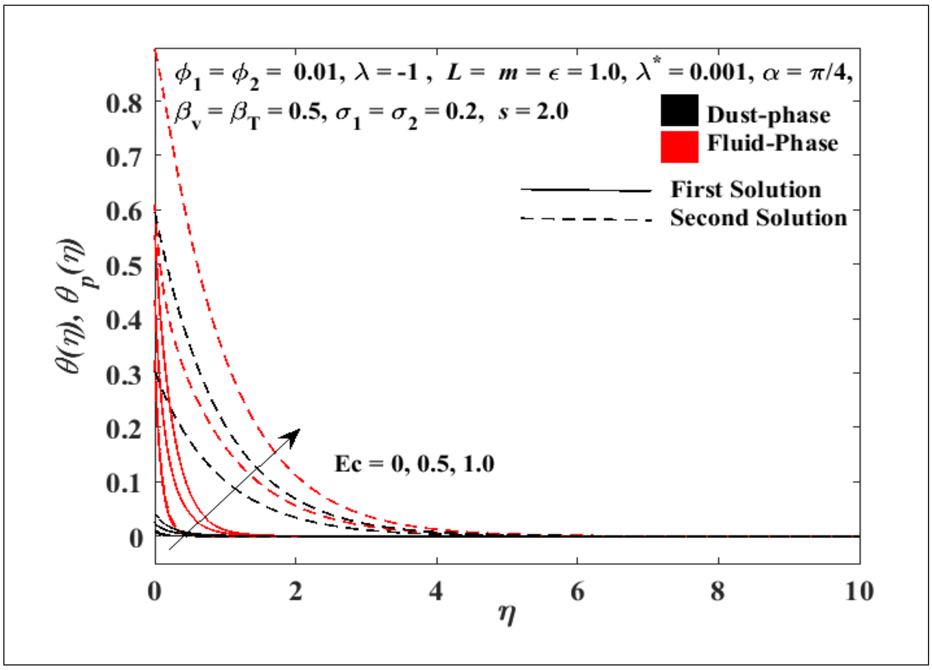

Figure 5.14 Temperature Profile for Distinct Values of Ec Number

This implies that there is an increase in the boundary layer thickness for the first solution, resulting to a reduced local Nusselt number and heat transfer rate.

The effect of different values of s, σ_1 and σ_2 on $C_f Re_x^{1/2}$ and $Nu_x Re_x{}^{-1/2}$ over shrinking surface are shown in Figures 5.19 and 5.20 respectively. Dual solutions are found to exist within the range of $s_c < s < 2.1$ and no solution is achievable beyond

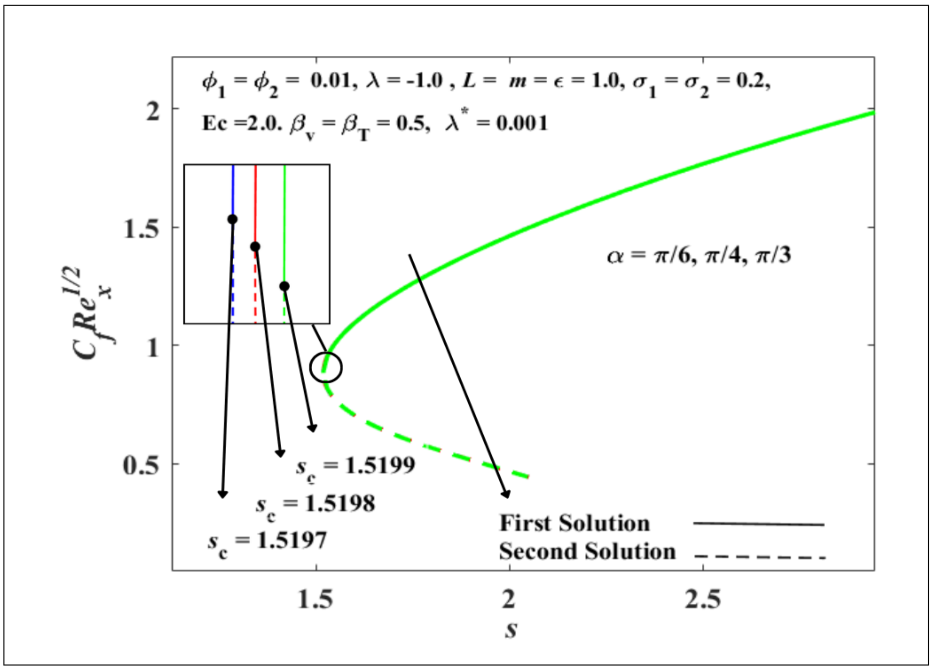

Figure 5.15 $C_f Re_x^{1/2}$ with s for Variety Values of α

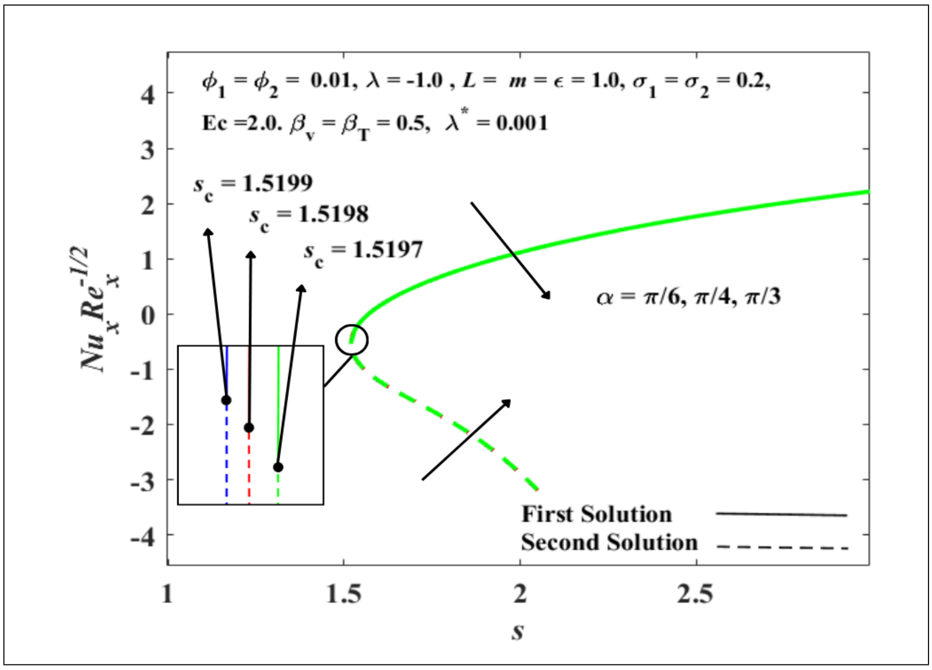

Figure 5.16 $Nu_x Re_x^{-1/2}$ with s for Variety Values of α

$s < s_c$ as it indicates the occurrence of boundary layer separation. Based on Table 5.1 and Figure 5.19, the increment of slip parameters decreases the $C_f Re_x^{1/2}$ values by 19.5% for the first solution and 23.92% for the second solution. As for the $Nu_x Re_x^{-1/2}$ values, it increases by 124.35% in the first solution and 74.24% in the second solution. In other words, increasing the slip parameter results in a greater flow of heat from the

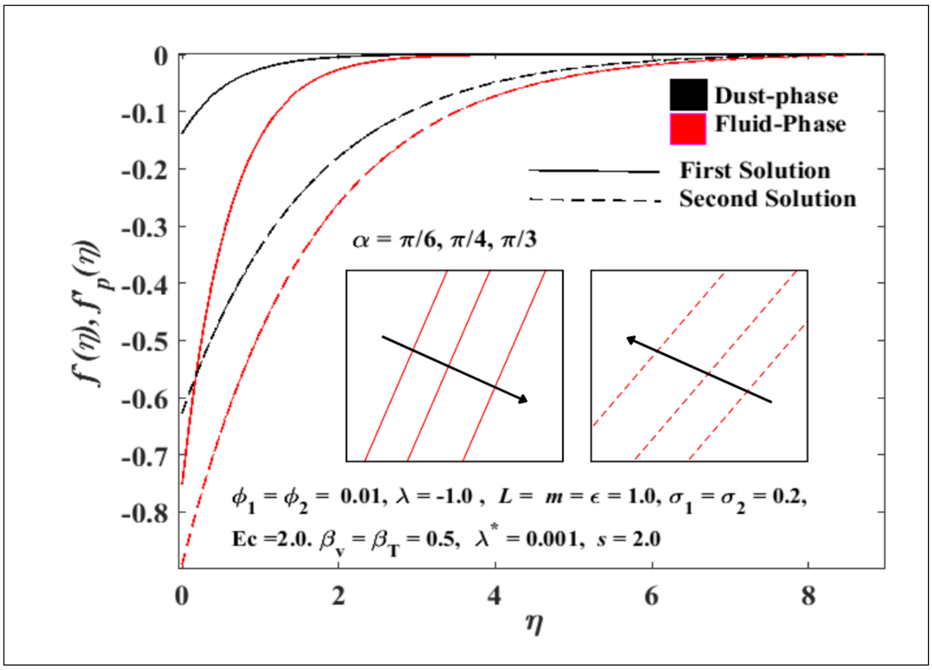

Figure 5.17 Velocity Profile for Distinct Values of α

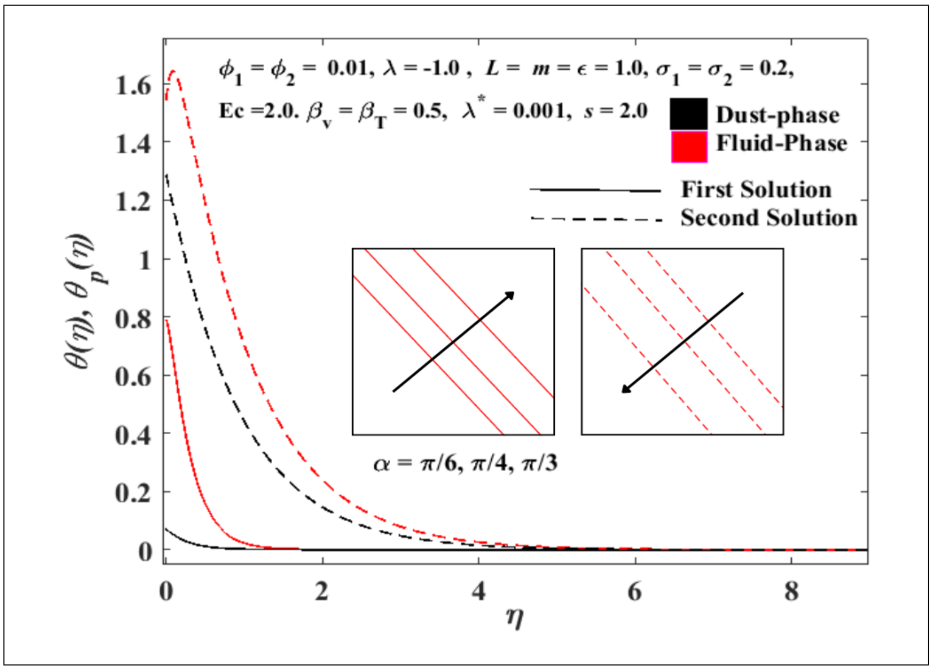

Figure 5.18 Temperature Profile for Distinct Values of α

surface into the fluid while diminishing the friction between them (Najib et al., 2022). Besides that, the increase of slip parameter also delays the boundary layer separation.

The corresponding velocity and temperature profiles of Figures 5.19 and 5.20 are displayed in Figures 5.21 and 5.22, respectively. From figure 5.21, it can be noted that the increase in slip parameter leads to a decrease in the velocity boundary layer thickness for the first solution of both phases while increases in the second solution. The reduction in boundary layer thickness illustrated in Figure 5.21 shows an increase in the velocity gradient, but the skin friction coefficient depicted in Figure 5.19 shows a decrease, demonstrating a contradiction to typical observations. Observations reveal that the skin friction coefficient typically increases with a rising velocity gradient, however, this case presents a contradiction to that trend. Furthermore, Figure 5.22 shows a decline in the temperature profile in the first solution and an increase in the second solution of both phases. The boundary layer thickness of temperature profile is gradually decreasing which increases the temperature gradient and implies a rise in local Nusselt number and heat transmission rate.

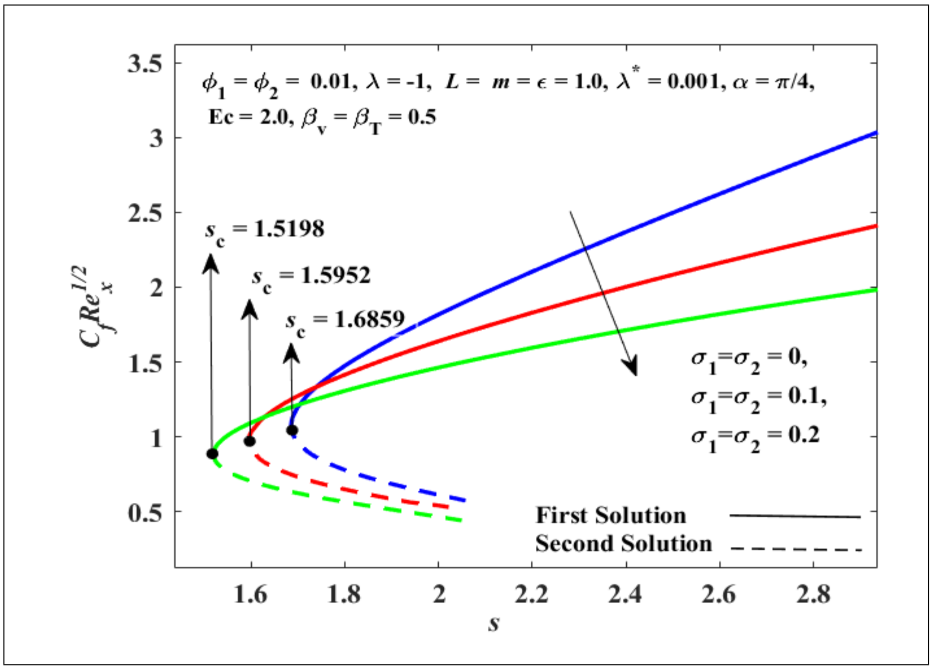

Figure 5.19 $C_f Re_x^{1/2}$ with s for Distinct Values of σ_1 and σ_2

The variation of $C_f Re_x^{1/2}$ and $Nu_x Re_x^{-1/2}$ for distinct values of σ_1 is presented in Figures 5.23 and 5.24, respectively. Based on the figures, non-unique solutions are obtained when s is more than the critical point s_c and 1.6859, 1.5952, and 1.5198 are the critical points for $\sigma_1 = 0$, 0.1 and 0.2. Further, the retardation of boundary layer separation is observable as σ_1 rises. As referred to Table 5.1, and Figure 5.23, the $C_f Re_x^{1/2}$ is seen to decrease by 19.5% in the first solution and 23.92% in the second solution as the value of σ_1 increases indicating a reduction in friction between fluid and the surface. In addition, a rise in the velocity slip parameter correspond to a larger slip

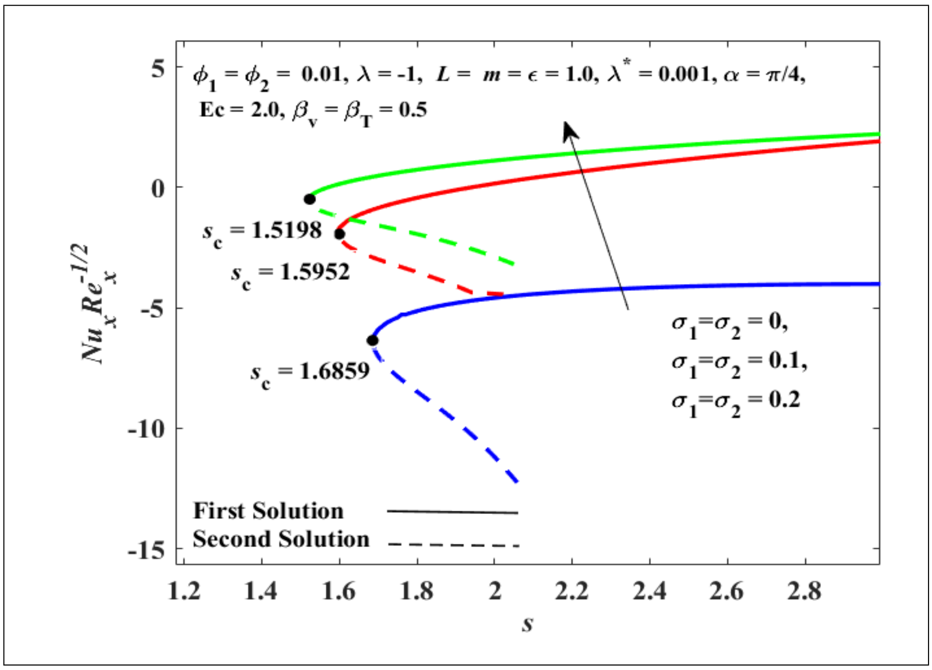

Figure 5.20 $Nu_xRe_x^{-1/2}$ with s for Distinct Values of σ_1 and σ_2

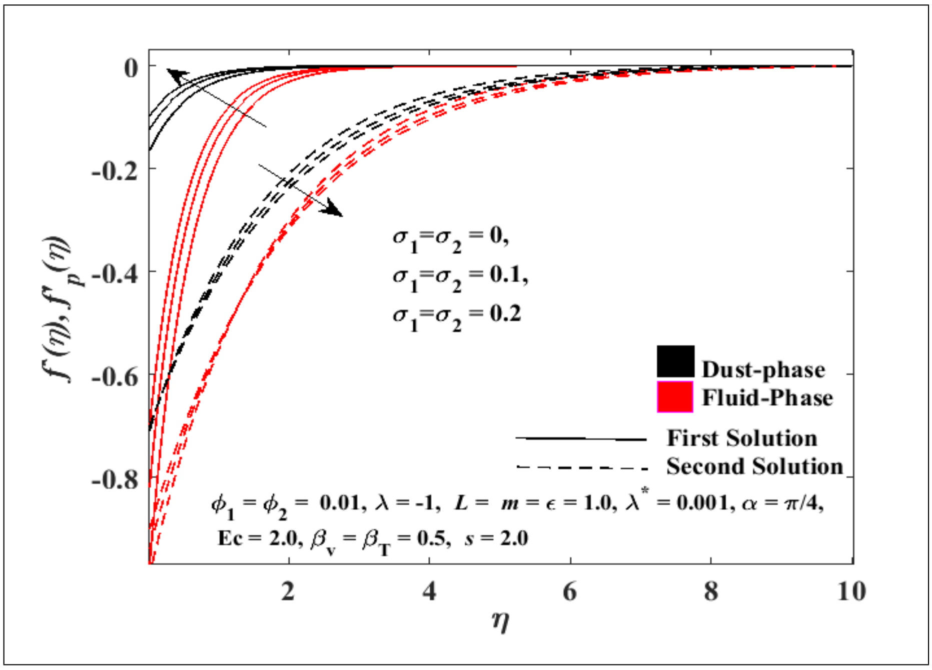

Figure 5.21 Velocity Profile with Distinct Values of σ_1 and σ_2

length. As a result, the fluid slips more readily along the surface, further diminishing the resistance to flow (Pandey and Kumar, 2016). Furthermore, in Table 5.1, and Figure 5.24, the values of $Nu_xRe_x^{-1/2}$ seen to increase by 175.28% and 21.48% for the first and second solutions, respectively with greater σ_1, which implies an enhance in the heat transfer rate.

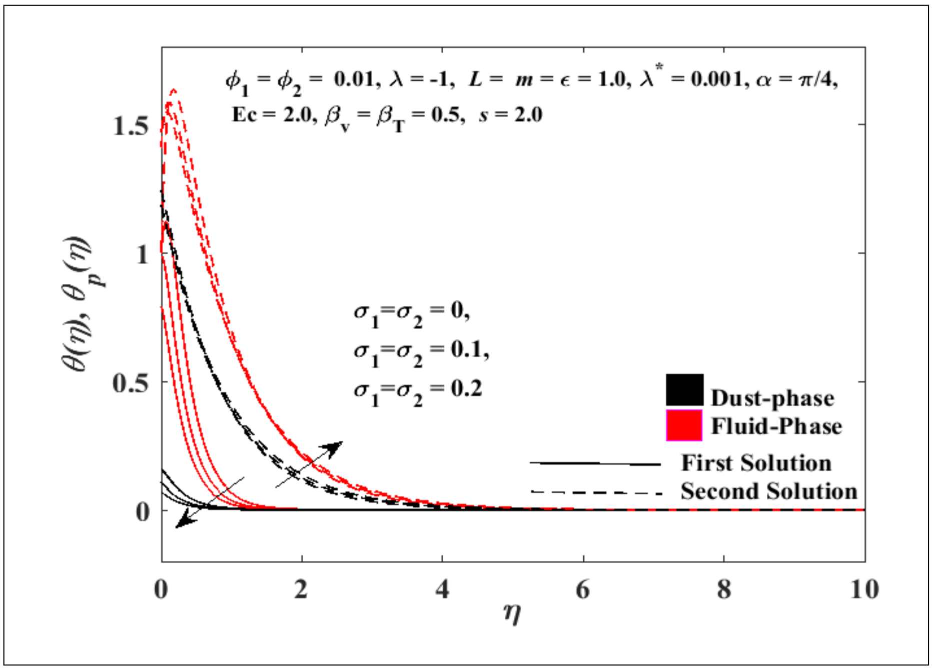

Figure 5.22 Temperature Profile with Distinct Values of σ_1 and σ_2

The velocity and temperature profiles for some values of σ_1 over a shrinking surface are illustrated in Figures 5.25 and 5.26, respectively. Increasing the velocity slip parameter has increased the velocity profile of the first solution for both phases in Figure 5.25 but decreases in the second solution. The boundary layer thickness diminishes resulting to a steeper velocity gradient. Nonetheless, the skin friction coefficient exhibits a decline, which contradicts its usual behaviour, as illustrated in Figure 5.21. The temperature profile demonstrate a decrease in the first solution, but an increase in the second solution for both phases as shown in Figure 5.26. Further, the boundary layer thickness becomes thinner in the first solution than the second solution, consistent with the findings in Figure 5.24 which implies a higher temperature gradient and heat transfer rate within the boundary layer.

Figures 5.27 and 5.28 display the implications of some values of σ_2 and s on $C_f Re_x^{1/2}$ and $Nu_x Re_x^{-1/2}$ towards a shrinking surface $(\lambda = -1)$. Figure 5.27 reveals that there is no changes in the skin friction coefficient as the thermal slip parameter value rises. Hence, this evidence that thermal slip is insignificant as the thermal slip rises. Figure 5.28 demonstrates a reduction in the first solution and an increase in the second solution. Furthermore, as referred to Table 5.1 and Figure 5.28, the $Nu_x Re_x^{-1/2}$ of the first solution reduces by 68.59%, while the second solution rises by 67.53%. The

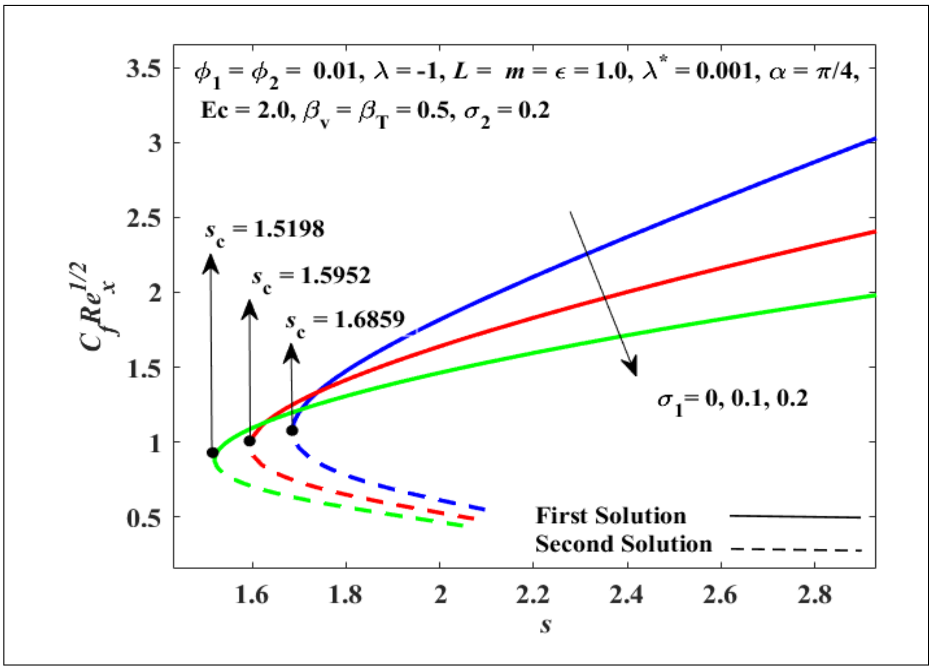

Figure 5.23 $C_f Re_x^{1/2}$ with s for Distinct Values of σ_1

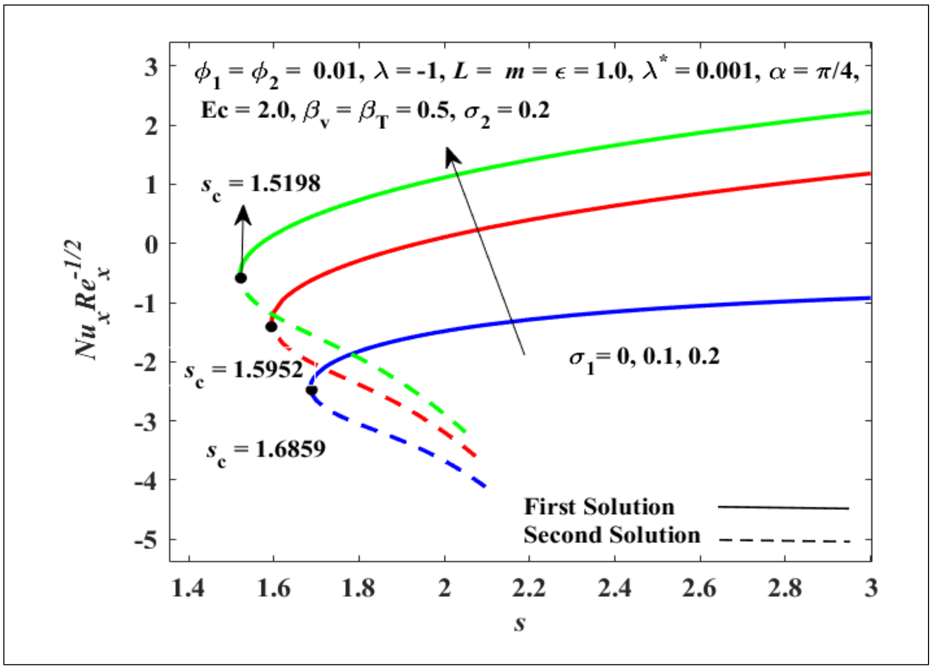

Figure 5.24 $Nu_x Re_x^{-1/2}$ with s for Distinct Values of σ_1

increase in the values of σ_2 corresponds with a reduction in the rate of heat transfer in the first solution within the surface and the fluid flow. This is because an increase in the thermal slip parameter reduces the thermal coupling between the fluid and the surface (Wahid et al., 2020). In addition, the value of s_c for all three values of σ_2 are identical, yielding a value of 1.5198.

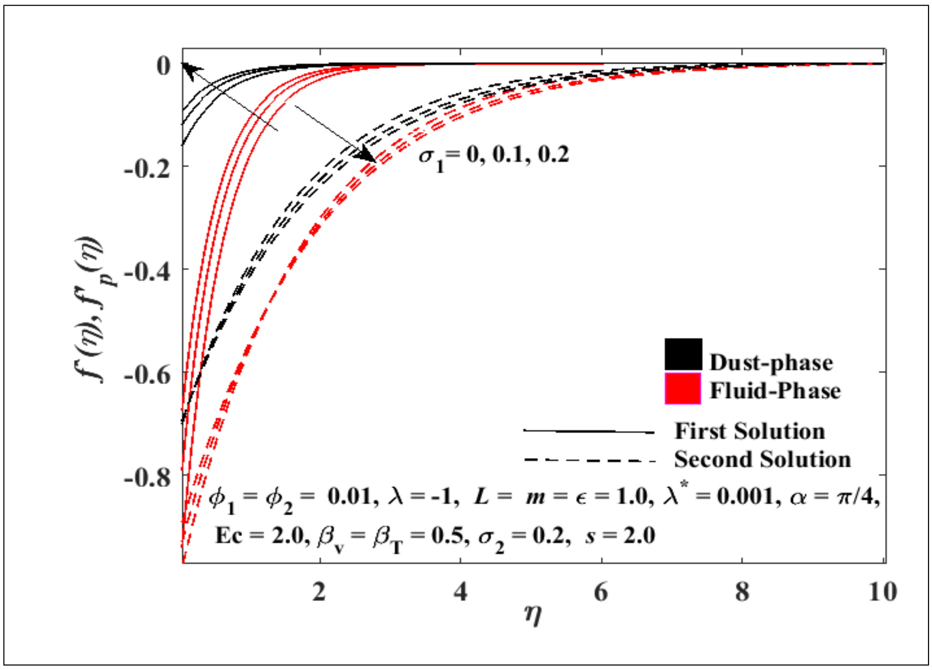

Figure 5.25 Velocity Profile with Distinct Values of σ_1

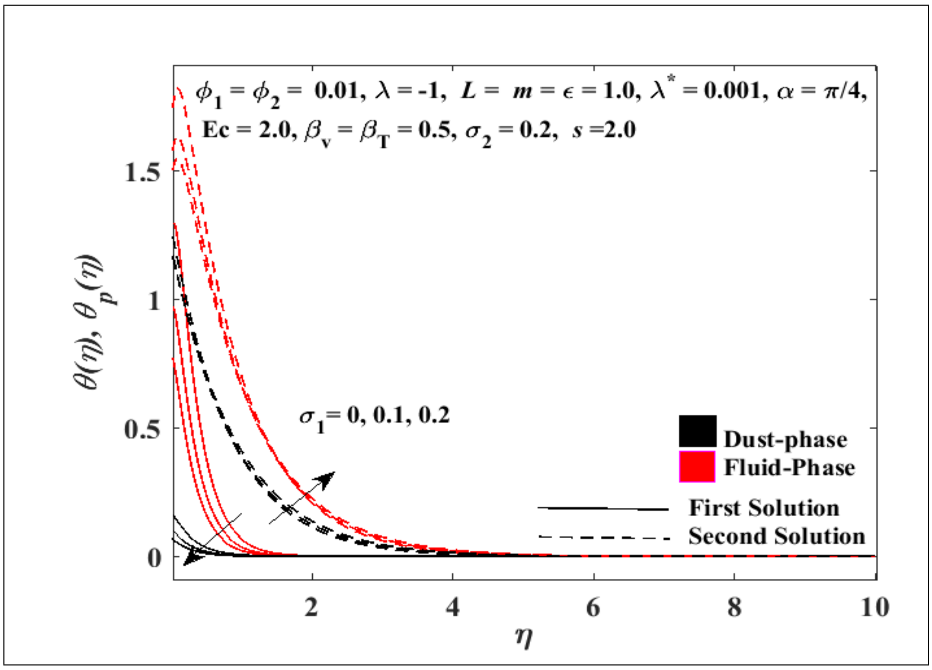

Figure 5.26 Temperature Profile with Distinct Values of σ_1

The impact of variety σ_2 on the velocity and temperature profiles for $f'(\eta)$, $\theta(\eta)$ and $f'_p(\eta), \theta_p(\eta)$ of Figures 5.27 and 5.28 are presented in Figures 5.29 and 5.30, correspondingly. Based on Figure 5.29, only a minimal diminution can be seen in the first solution and a minimal increment in the second solution of both phases for the velocity profile. The increase in σ_2 values results in a increased boundary layer thickness for the first solution of both phases, subsequently decreasing the velocity gradient and skin friction coefficient. Figure 5.30 displays a reduction in boundary layer thickness for both phases in the first solution as σ_2 increases, however an opposite pattern is observed in the second solution implying a decrease in local Nusselt number and heat transfer efficiency.

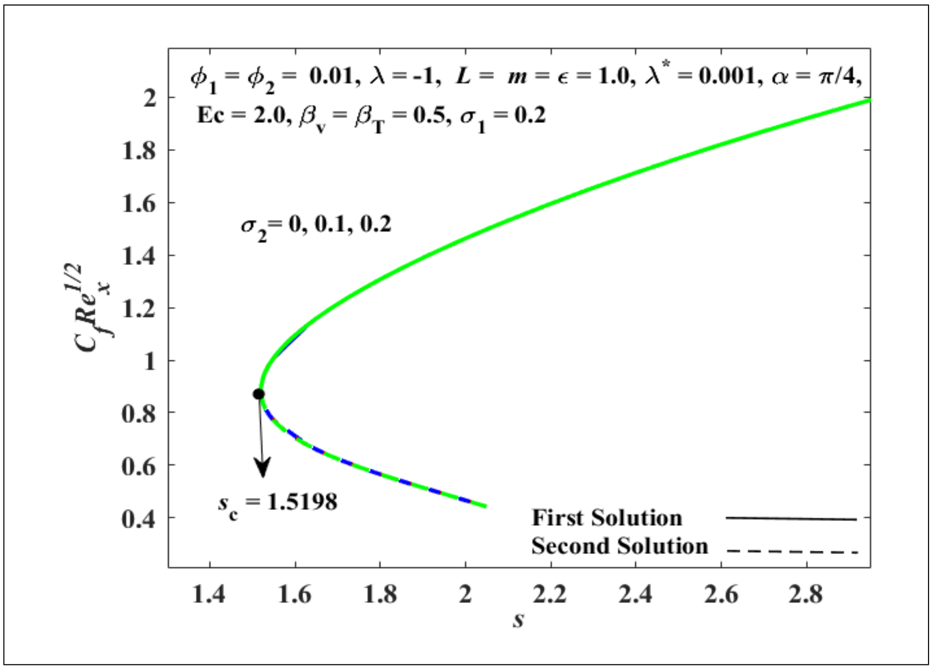

Figure 5.27 $C_f Re_x^{1/2}$ with s for Distinct Values of σ_2

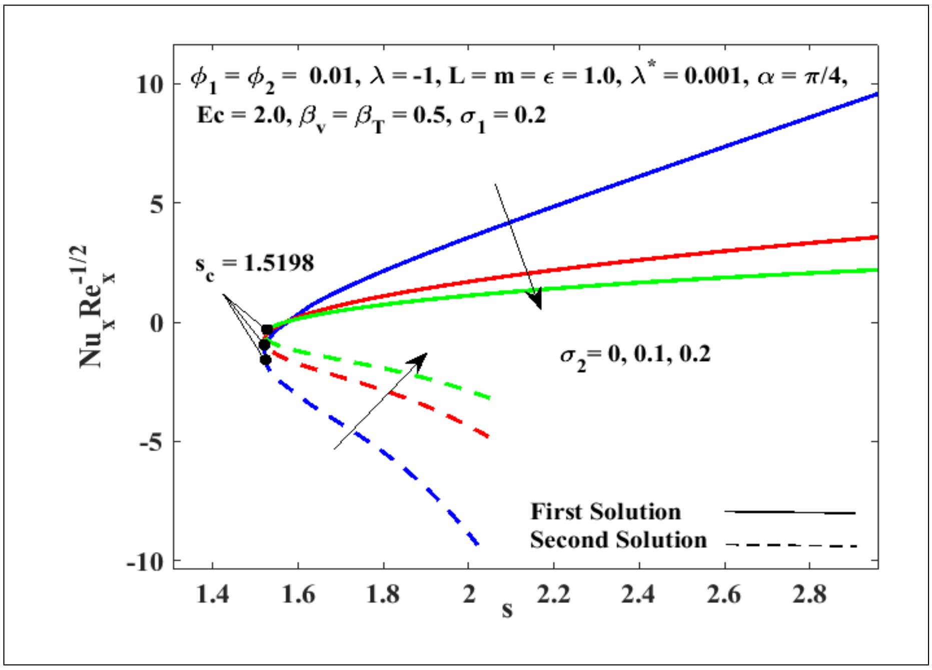

Figure 5.28 $Nu_x Re_x^{-1/2}$ with s for Distinct Values of σ_2

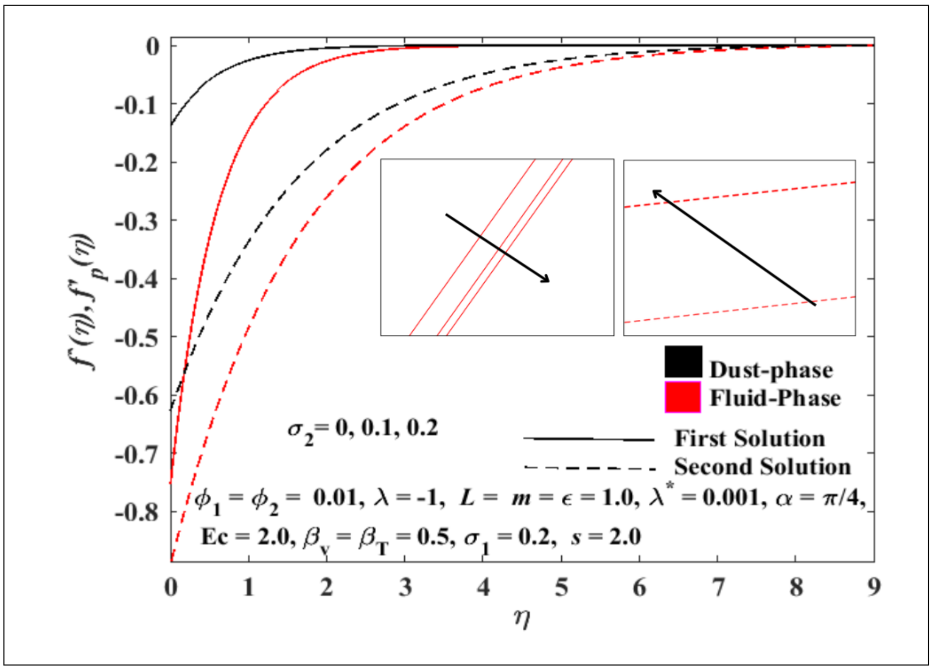

Figure 5.29 Velocity Profile with s for Distinct Values of σ_2

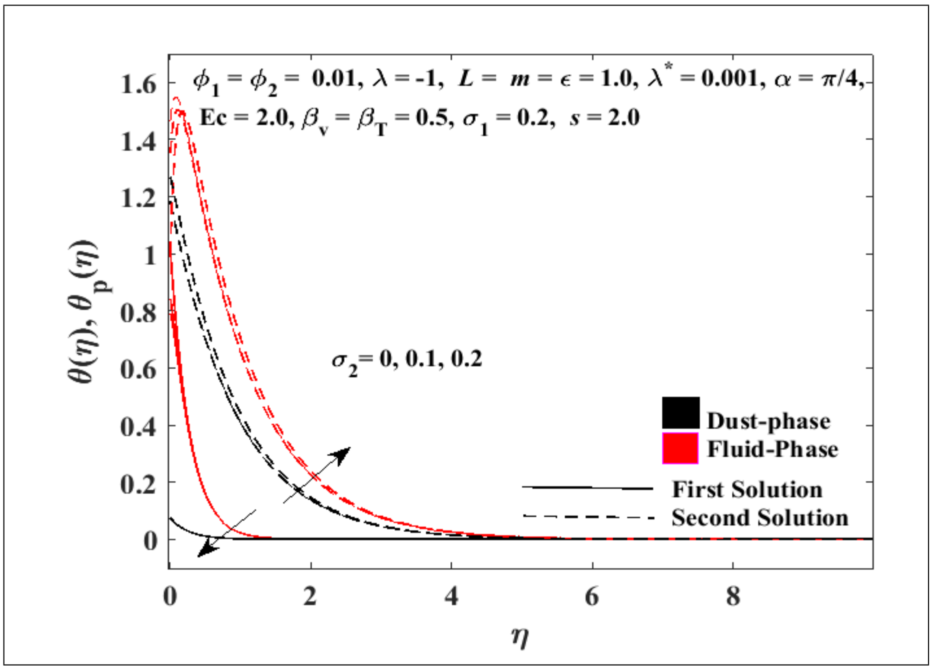

Figure 5.30 Temperature Profile with s for Distinct Values of σ_2

The influence of variation ϕ_1 and s towards the $C_f Re_x^{1/2}$ and $Nu_x Re_x^{-1/2}$ are shown in Figures 5.31 and 5.32, respectively. From Table 5.1 and Figure 5.31, it is noticed that when the parameter of ϕ_1 increases, the $C_f Re_x^{1/2}$ values increases by 3.59% and 6% for the first and second solutions, respectively. However, a reverse trend can be seen in Figure 5.32 where the $Nu_x Re_x^{-1/2}$ values diminished by 8.02% for the first solution and 14.94% for the second solution for a greater value of ϕ_1 . This implies that with a higher volume of Al_2O_3 nanoparticle volume fraction dispersed in the base fluid, it increases the viscosity of the fluid (Yusuf et al., 2025), while decreases the heat transfer rate. In addition, the retardation of boundary layer separation is faster as the volume of Al_2O_3 is greater.

The velocity and temperature profiles for various of ϕ_1 are elucidated in Figures 5.33 and 5.34, respectively and it corresponds to the figures shown in Figures 5.31 and 5.32. According to Figure 5.33, a minimal increase in the boundary layer thickness for the first solution of both phases while decreases for the second solution as the value of Al_2O_3 nanoparticle volume fraction gets higher. This indicates that a higher volume of nanoparticle volume fraction leads to an increase skin friction coefficient which slows down the velocity of the fluid flow. Whereas, Figure 5.34, shows a rising pattern in both solutions of both phases showing an increase in boundary layer thickness and less steep temperature gradient. This implies that the local Nusselt number and heat transfer rate diminishes as ϕ_1 increases equivalent to the result shown in Figure 5.32.

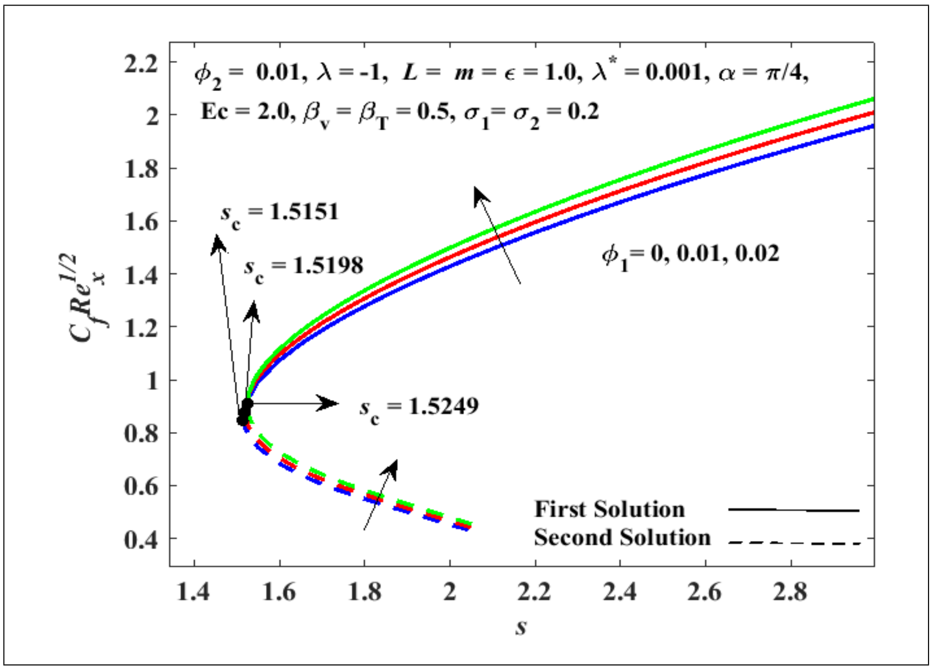

Figure 5.31 $C_f Re_x^{1/2}$ with s for Distinct Values of ϕ_1

The influence of increasing ϕ_2 and s for the values of $C_f Re_x^{1/2}$ and $Nu_x Re_x{}^{-1/2}$ are demonstrated in Figures 5.35 and 5.36, respectively. Based on Table 5.1, and Figures 5.35 and 5.36, increment in the values of Cu nanoparticle volume fractions

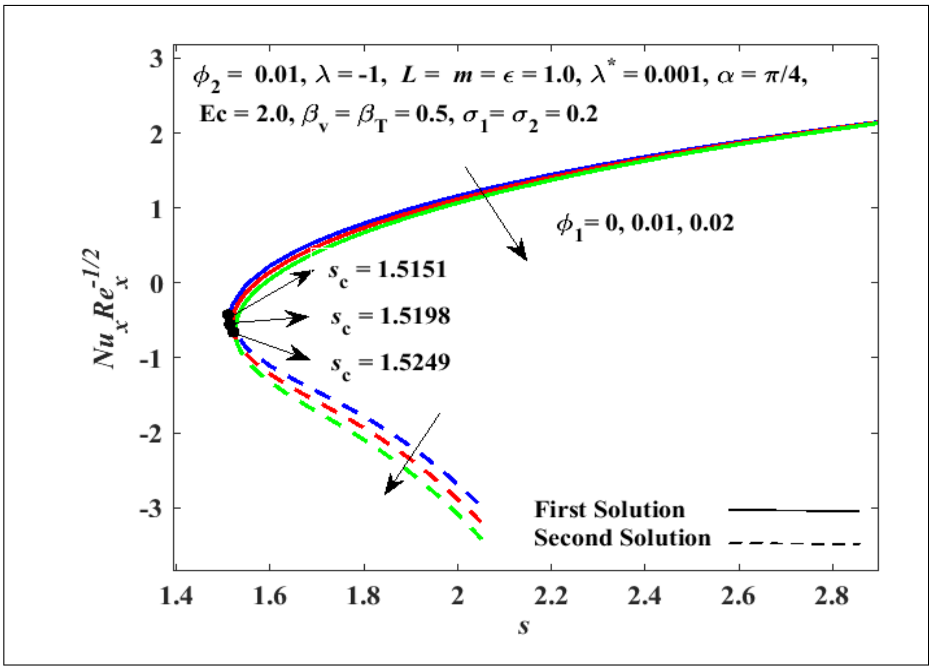

Figure 5.32 $Nu_x Re_x^{-1/2}$ with s for Distinct Values of ϕ_1

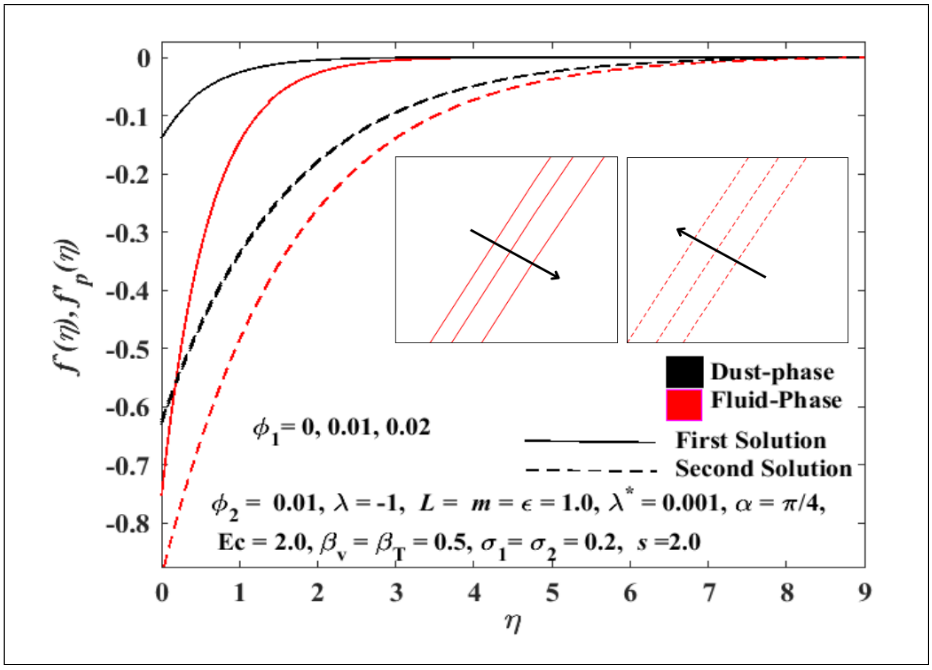

Figure 5.33 Velocity Profile for Distinct Values of ϕ_1

leads to an increase in the $C_f Re_x^{1/2}$ values by 12.47% for the first solution and 2.98% for the second solution, while a decrease in $Nu_x Re_x^{-1/2}$ values by 8.29% and 44.5% for the first and second solutions, respectively. Thus, it can be deduced that a higher concentration of ϕ_2 rises the frictional force and drag force within the fluid and the surface, while diminishes the heat transfer rate. In addition, the critical values decrease

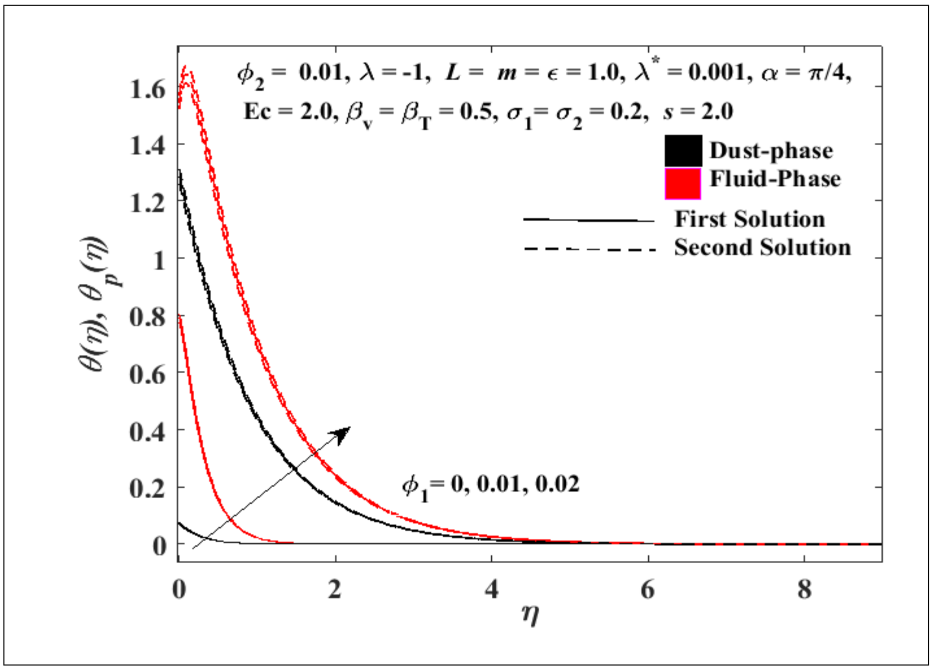

Figure 5.34 Temperature Profile for Distinct Values of ϕ_1

which then means there is a delay in the boundary layer separation where no solutions are found across the critical points.

Meanwhile, Figures 5.37 and 5.38 illustrate the corresponding velocity and temperature profiles of Figures 5.35 and 5.36. Figure 5.37 depicts that an increase in the concentration of Cu nanoparticle volume fraction into the base fluid decreases the boundary layer thickness of the first solution but increases in the second solution of both phases. This results in a steeper velocity gradient, with the skin friction coefficient exhibiting an increase in the first solution in comparison to the second solution. Moreover, an opposite pattern can be seen in Figure 5.38, where an increment in Cu nanoparticle volume fraction decreases the temperature profile of the first solution and increases in the second solution of both phases. The boundary layer thickness of the second solution is greater compared to the first solution which shows that the local Nusselt number heat transmission rate of the second solution is less efficient.

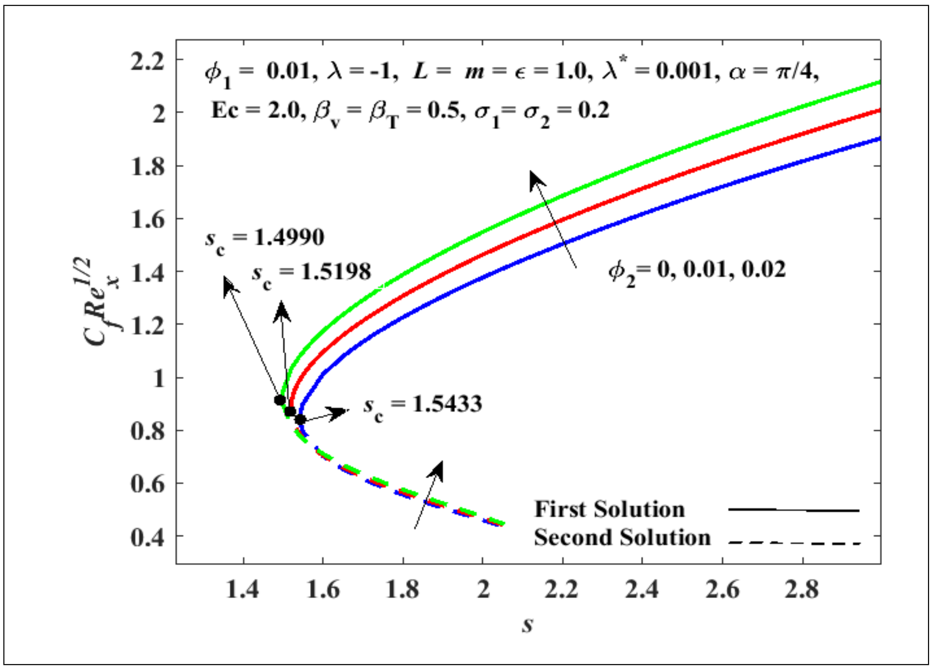

Figure 5.35 $C_f Re_x^{1/2}$ with s for Distinct Values of ϕ_2

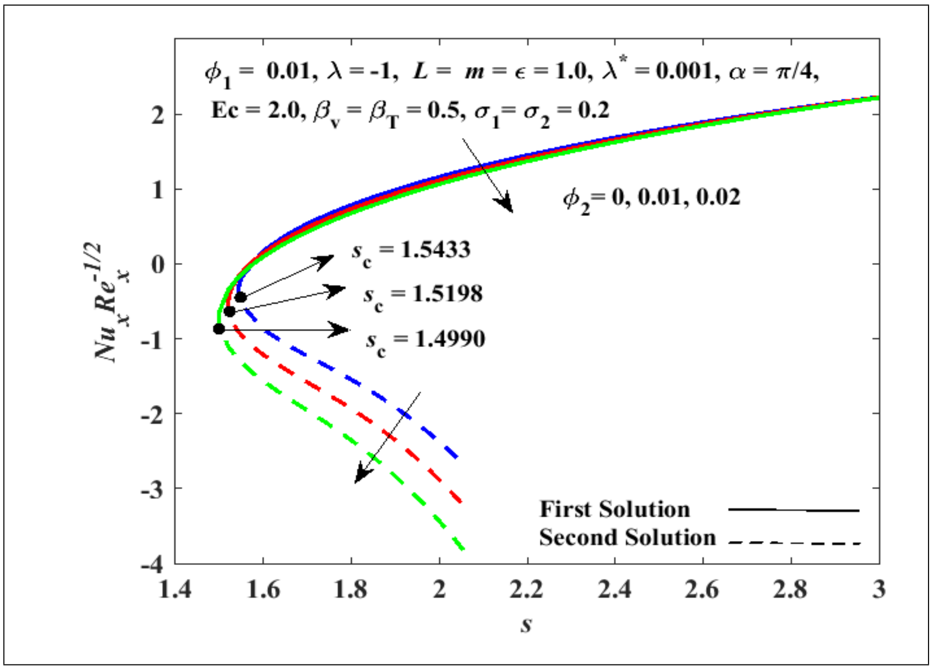

Figure 5.36 $Nu_x Re_x^{-1/2}$ with s for Distinct Values of ϕ_2

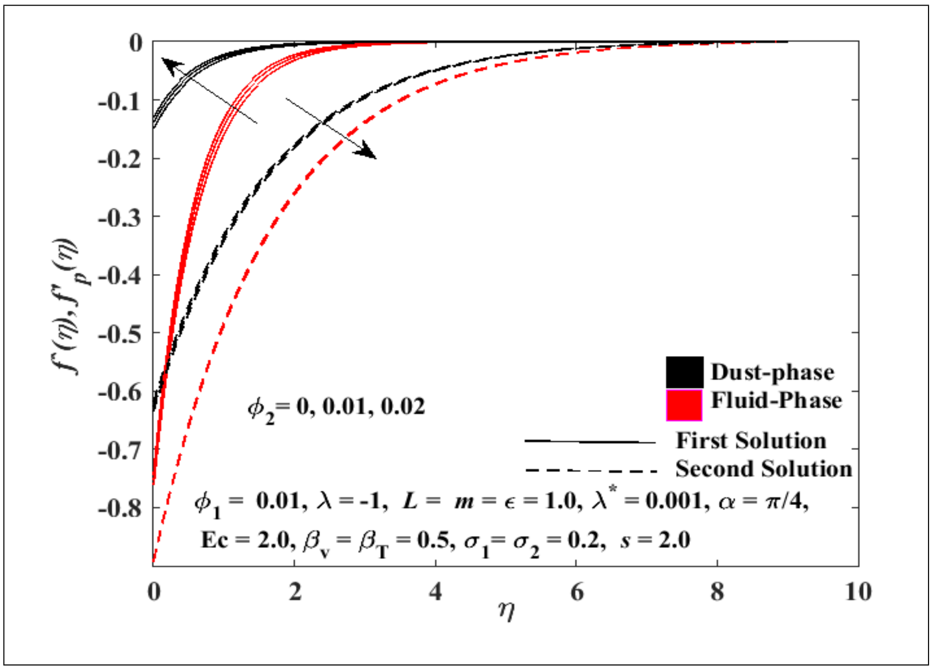

Figure 5.37 Velocity Profile for Distinct Values of ϕ_2

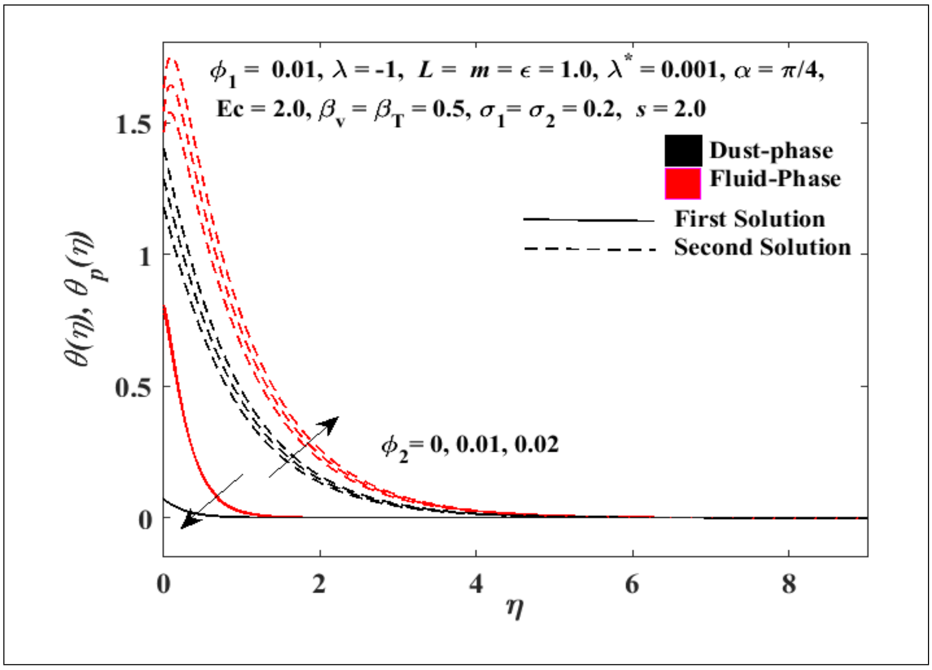

Figure 5.38 Temperature Profile for Distinct Values of ϕ_2

5.4 Conclusions

This chapter elucidates the boundary layer flow and heat transfer occurring over an inclined stretching or shrinking surface that is immersed in a hybrid nanofluid with the presence of dust particles. The influences of dust particle mass concentation, viscous dissipation, slip parameters including velocity slip and thermal slip, as well as the volume fractions of alumina nanoparticles, and copper nanoparticles were observed. The outcomes of this chapter can be summarized as follows:

- The skin friction coefficient rises as the dust particles mass concentration, volume fraction of both alumina and copper nanoparticles increases. A diminishing pattern is observed as the inclination angle, slip parameters, and velocity slip parameter values increase. The increase in dust particles mass concentration, nanoparticle volume fractions enhances both the frictional force and drag force within the boundary layer, while an increase in inclination angle, slip parameter, and velocity slip parameter values results in a reduction of friction between fluid flow and the surface.
- The local Nusselt number declines with an increase in dust particles mass concentration, viscous dissipation (via Eckert number), inclination angle, thermal slip parameter, alumina, and copper nanoparticles volume fraction, while it rises with an increase in slip parameters and velocity slip parameter. This reveals that an increase in dust particles mass concentration, viscous dissipation (via Eckert number), thermal slip, alumina and copper nanoparticle volume fractions results to a reduced heat transfer rate. Conversely, an opposing trend was seen when examining slip parameters and velocity slip parameter.
- The temperature profile depicts a declining trend for the first solution in both fluid and dust phases, subsequently resulting in an increased temperature gradient and reduced boundary layer thickness. This implies the enhanced heat transmission rate within the boundary layer.
- The dual solution is present for the interval $s_c < s < 2.5$, and $\lambda_c < \lambda < -0.1$ for all examined parameters, however, unique solutions are discovered for $s > 2.5$, and $\lambda > -0.1$. The range of dual solutions were expanded with the rise of dust

particle mass concentration, slip parameters, velocity slip parameter, and copper nanoparticle volume fraction, while the increase of inclination angle reduces the range of dual solutions.

CHAPTER 6
BOUNDARY LAYER FLOW AND HEAT TRANSFER OF DUSTY HYBRID NANOFLUID OVER A VERTICAL STRETCHING OR SHRINKING SURFACE WITH THE EFFECT OF VISCOUS DISSIPATION AND SLIP CONDITIONS

6.1 Introduction

This chapter extends the mathematical model from Chapter 4 to study the flow and heat transfer on a vertical surface instead of a horizontal surface. This alternative orientation includes a wide range of engineering and industrial applications, particularly those where vertical surfaces are essential, such as heat exchangers, electronic cooling units, chemical processing, and energy generation. Employing this orientation provides clearer insight into the behaviour of fluid flow and heat transfer under realistic operational situations. Since the vertical surface is considered, the effect of mixed convection is considered in this analysis, as the buoyancy force is present. Therefore, this chapter evaluates the steady laminar mixed convection flow and heat transfer of a dusty hybrid nanofluid over a vertical stretched or shrunk surface, incorporating the effects of viscous dissipation, velocity, and thermal slip conditions. Similar parameters examined in Chapter 4 are also taken into account.

6.2 Mathematical Formulation

Consider a steady mixed convection boundary layer flow and heat transfer of hybrid nanofluid with dust particles passing a vertical stretching or shrinking surface with viscous dissipation, and velocity and thermal slip conditions. Figure 6.1 illustrates the physical model of a vertical surface.

In the analysis of this third problem, vertical surface is examined, thus, there is an additional term in the governing equation for momentum of the hybrid nanofluid phase which implies the buoyant force. Other equations, including continuity and energy for the hybrid nanofluid phase and the equations for dust phase remain consistent with those derived in Chapters 3 and 5. The governing equations were expressed as below by referring to Gireesha et al. (2011), Desale and Pradhan (2015), Afridi et al. (2017), Anuar et al. (2021b), Kho et al. (2021), and Hamid et al. (2022).

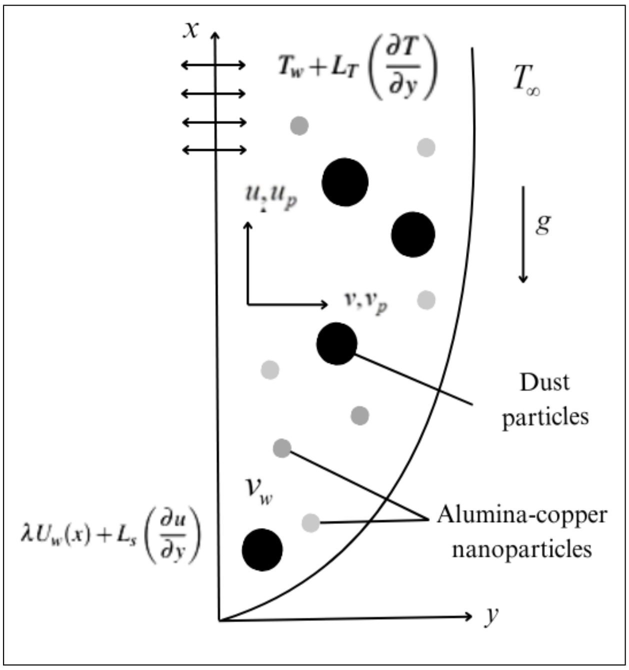

Figure 6.1 Physical Model of a Vertical Surface

i. Hybrid nanofluid phase

Momentum equation:

$$u\frac{\partial u}{\partial x}+v\frac{\partial u}{\partial y}=-\frac{1}{\rho_{hnf}}\frac{\partial p}{\partial x}+\frac{\mu_{hnf}}{\rho_{hnf}}\frac{\partial^2 u}{\partial y^2}+\frac{KN}{\rho_{hnf}}(u_p-u)+g\beta^*\left(T-T_\infty\right). \quad (6.2.1)$$

Similar to what was discussed in Chapter 5, the surface temperature, and volumetric thermal expansion coefficient are assumed to be $T_w = T_\infty + bx^2$, and $\beta^* = nx^{-1}$, respectively, and $\mathrm{Ec} = a^2/\left(C_p\right)_f b$ to achieve the similarity transformation. Moreover, to reduce to ordinary differential equations, equations (3.3.3), (3.3.9), (3.3.10), (3.3.16), (3.3.17), and (3.3.20) are employed, resulting to

$$\frac{\mu_{hnf}/\mu_f}{\rho_{hnf}/\rho_f}f'''+ff''-f'^2+\frac{L\beta_v}{\rho_{hnf}/\rho_f}\left(f_p'-f'\right)+\lambda^*\theta=0. \quad (6.2.2)$$

Furthermore, utilizing the physical properties of nanofluid and hybrid nanofluid presented in Table 3.1, equation (6.2.2) is modified from the ODEs as follows:

$$
\begin{aligned}
&\frac{1}{(1-\phi_1)^{2.5}(1-\phi_2)^{3.5}\left[(1-\phi_1)+\phi_1\dfrac{\rho_1}{\rho_f}\right]+\phi_2\dfrac{\rho_2}{\rho_f}} f'''+ff''-f'^2 \\
&+\frac{L\beta_v}{(1-\phi_2)\left[(1-\phi_1)+\phi_1\dfrac{\rho_1}{\rho_f}\right]+\phi_2\dfrac{\rho_2}{\rho_f}}\left(f_p'-f'\right)+\lambda^*\theta=0
\end{aligned}
\tag{6.2.3}
$$

along with boundary conditions (3.3.84)

$$
\begin{aligned}
&f(0)=s, \qquad f'(0)=\lambda+\sigma_1 f''(0), \qquad \theta(0)=1, \qquad \theta(0)=1+\sigma_2\theta'(0), \\
&f'(\eta)\to 0, f_p'(\eta)\to 0, f_p'(\eta)\to f(\eta), \theta(\eta)\to 0, \theta_p(\eta)\to 0 \qquad \text{as} \quad \eta\to\infty.
\end{aligned}
$$

6.3 Results and Discussion

The ordinary differential equations (3.3.44), (3.3.65), (3.3.75), and (6.2.3) were numerically solved employing the bvp4c function in MATLAB as mentioned in Section 3.4 in Chapter 3, with the outcomes shown in tables and graphs. Further, the full program of MATLAB is included in Appendix E. Table 6.1 illustrates, the effect of various parameters such as L, λ^*, σ, σ_1, σ_2, ϕ_1, and ϕ_2 on $C_f Re_x^{1/2}$ and $Nu_x Re_x^{-1/2}$ for the specified values Pr = 6.2, $\lambda = -1, m = \epsilon = 1.0, \beta_v = \beta_T = 0.5$ and $s = 2.0$ of the current study which emphasizes the distinct outcomes resulting from the effects of these pertinent parameters mentioned.

Various values of L over a vertical stretching and shrinking surfaces on the values of $C_f Re_x{}^{1/2}$ and $Nu_x Re_x^{-1/2}$ are elucidated in Figures 6.2 and 6.3, respectively. The rise in parameter L leads to a corresponding rise for the values of $C_f Re_x^{1/2}$ by 1.77% for the first solution and a decrease by 2.86% in the second solution, as shown in Table 6.1 and Figure 6.2. This is attributed to the presence of dust particles suspended in the fluid, which enhances the drag force between the fluid and the surface. As the concentration of dust particles increases, the overall resistance to flow becomes more significant, thereby reducing the fluid velocity. Conversely, a rise in L results in a decrease of 0.06% and 29.96% in the first and second solutions, respectively for $Nu_x Re_x^{-1/2}$ values, as illustrated in Table 6.1 and Figure 6.3. This reduction in heat transfer efficiency is due to the energy retaining characteristics of dust particles, which slows down thermal energy exchange between the fluid and the surface. In addition, the rise in L also delays the boundary layer separation with the values of λ_c = -1.2875, -1.2915, and -1.3269 for L = 0, 0.01, and 0.1.

Figures 6.4 and 6.5 present the velocity and temperature profiles of Figures 6.2 and 6.3, respectively. In the velocity profile displayed in Figure 6.4 demonstrate that in both the fluid and dust phases, when L increases, the thickness of the boundary layer decreases in the first solution and increases in the second solution. This results in a steeper velocity gradient, signifying an increase in skin friction coefficient. Further, in terms of thermal characteristics, the temperature profile in Figure 6.5 shows a decrease in the boundary layer thickness for the first solution and an increase in the second solution for both phases with higher values of L. This elucidates that the local Nusselt

Table 6.1
Influence of L, Ec, λ^*, σ_1, σ_2, ϕ_1, and ϕ_2 on $C_f Re_x^{1/2}$ and $Nu_x Re_x^{-1/2}$ for Pr = 6.2, $\lambda = -1, m = \epsilon = 1.0, \beta_v = \beta_T = 0.5$ and $s = 2.0$

L	Ec	λ^*	σ_1	σ_2	ϕ_1	ϕ_2	$C_f Re_x^{1/2}$		$Nu_x Re_x^{-1/2}$	
							First Solution	Second Solution	First Solution	Second Solution
0	2.0	0.001	0.2	0.2	0.01	0.01	1.2848	0.5868	1.1085	-0.8253
0.01	2.0	0.001	0.2	0.2	0.01	0.01	1.2872	0.5800	1.1084	-0.8508
0.1	2.0	0.001	0.2	0.2	0.01	0.01	1.3076	0.5700	1.1078	-1.0726
1.0	0	0.001	0.2	0.2	0.01	0.01	1.4630	0.4800	3.6350	3.5800
1.0	0.5	0.001	0.2	0.2	0.01	0.01	1.4635	0.4688	3.0054	1.9597
1.0	2.0	0.001	0.2	0.2	0.01	0.01	1.4651	0.4769	1.1168	-2.9679
1.0	2.0	-0.001	0.2	0.2	0.01	0.01	1.4605	0.4686	1.1150	-2.4549
1.0	2.0	0	0.2	0.2	0.01	0.01	1.4627	0.4797	1.1159	-2.4741
1.0	2.0	0.001	0.2	0.2	0.01	0.01	1.4651	0.4769	1.1168	-2.9679
1.0	2.0	0.001	0	0	0.01	0.01	1.8237	0.6340	-4.6035	-11.3952
1.0	2.0	0.001	0.1	0.1	0.01	0.01	1.6449	0.5390	0.1664	-4.9356
1.0	2.0	0.001	0.2	0.2	0.01	0.01	1.4651	0.4769	1.1168	-2.9679
1.0	2.0	0.001	0	0.2	0.01	0.01	1.8240	0.6367	-1.4889	-3.4678
1.0	2.0	0.001	0.1	0.2	0.01	0.01	1.7406	0.4875	0.2615	-3.8715
1.0	2.0	0.001	0.2	0.2	0.01	0.01	1.4651	0.4769	1.1168	-2.9679
1.0	2.0	0.001	0.2	0	0.01	0.01	1.4607	0.4938	3.5129	-7.6075
1.0	2.0	0.001	0.2	0.1	0.01	0.01	1.4652	0.4915	1.6998	-3.7781
1.0	2.0	0.001	0.2	0.2	0.01	0.01	1.4651	0.4769	1.1168	-2.9679
1.0	2.0	0.001	0.2	0.2	0	0.01	1.4301	0.4777	1.1608	-2.3130
1.0	2.0	0.001	0.2	0.2	0.01	0.01	1.4651	0.4769	1.1168	-2.9679
1.0	2.0	0.001	0.2	0.2	0.02	0.01	1.5003	0.4913	1.0679	-3.1800
1.0	2.0	0.001	0.2	0.2	0.01	0	1.3789	0.4682	1.1620	-2.4436
1.0	2.0	0.001	0.2	0.2	0.01	0.01	1.4651	0.4769	1.1168	-2.9679
1.0	2.0	0.001	0.2	0.2	0.01	0.02	1.5508	0.4865	1.0657	-3.5404

number is higher and heat is transferred more effectively in the first solution compared to the second solution as the mass concentration of dust particles rises.

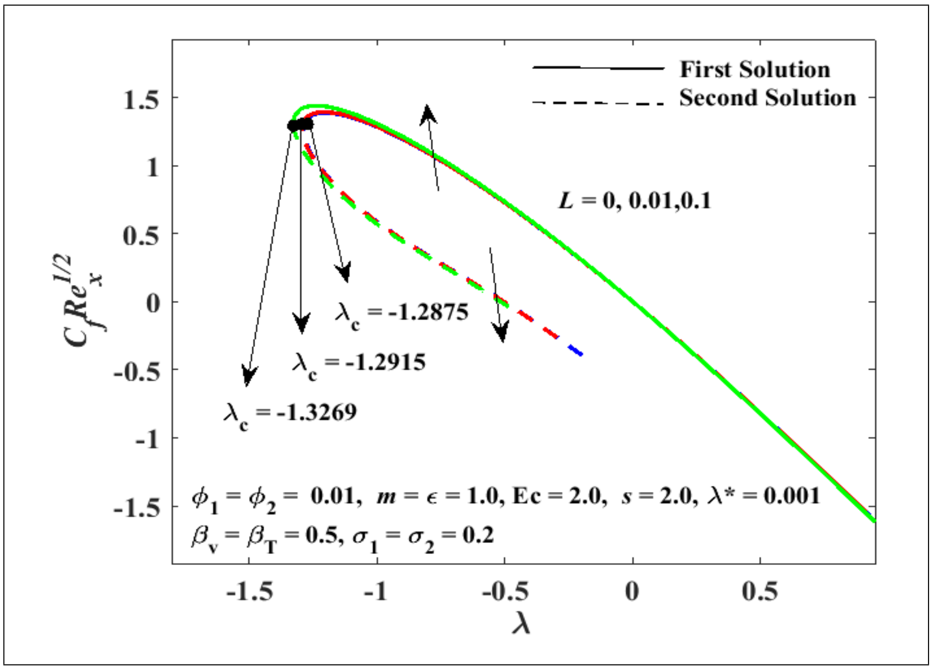

Figure 6.2 $C_f Re_x^{1/2}$ with λ for Various Values of L

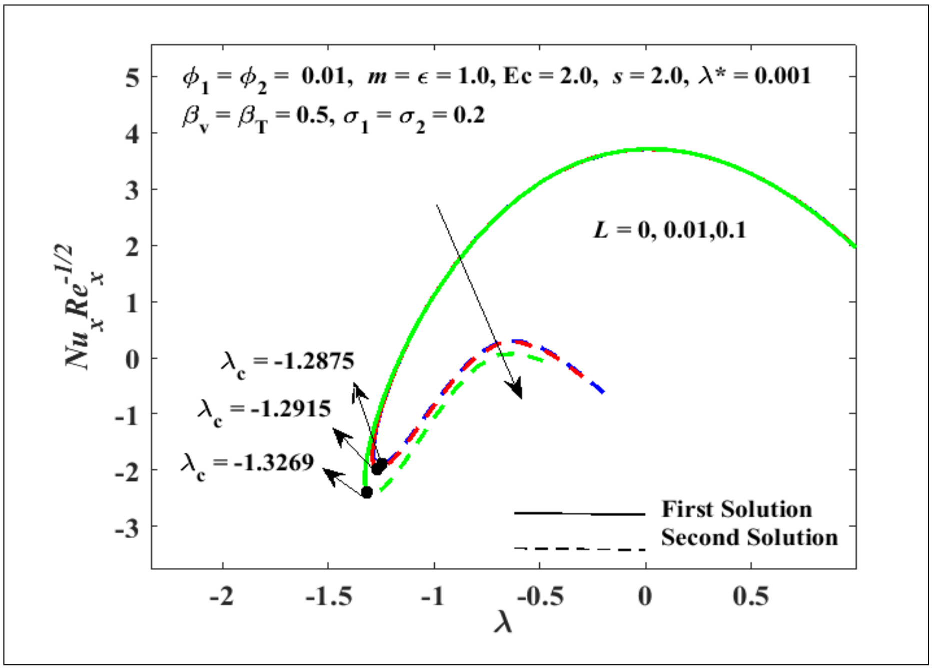

Figure 6.3 $Nu_x Re_x^{-1/2}$ with λ for Various Values of L

Different values of s and L for the values of $C_f Re_x^{1/2}$ and $Nu_x Re_x^{-1/2}$ are demonstrated respectively in Figures 6.6 and 6.7. Based on Figure 6.6, the rise in mass concentration of dust particles leads to an augmentation to the values of $C_f Re_x^{1/2}$

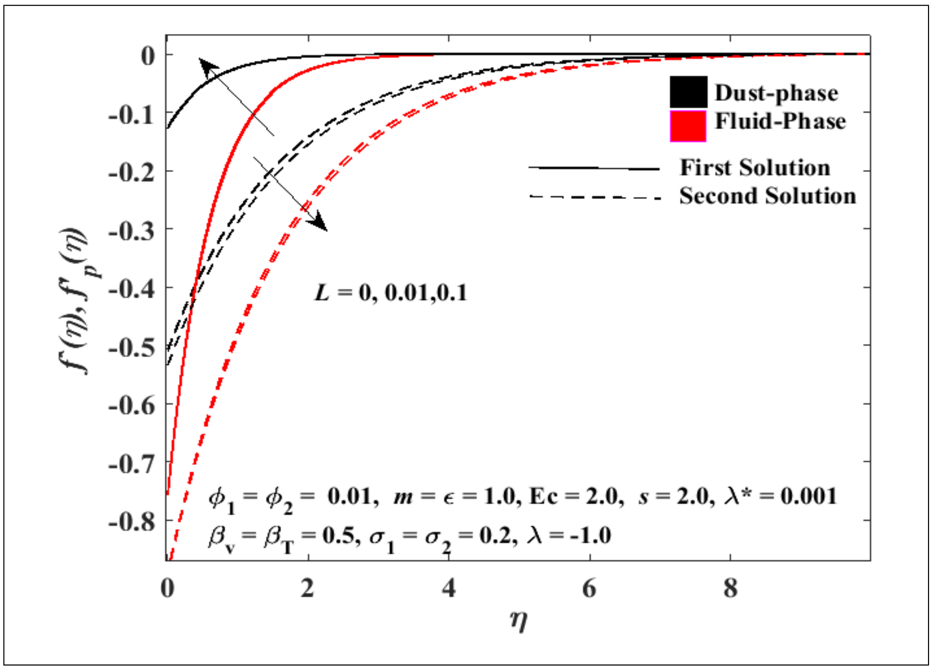

Figure 6.4 Velocity Profile with Various Values of L

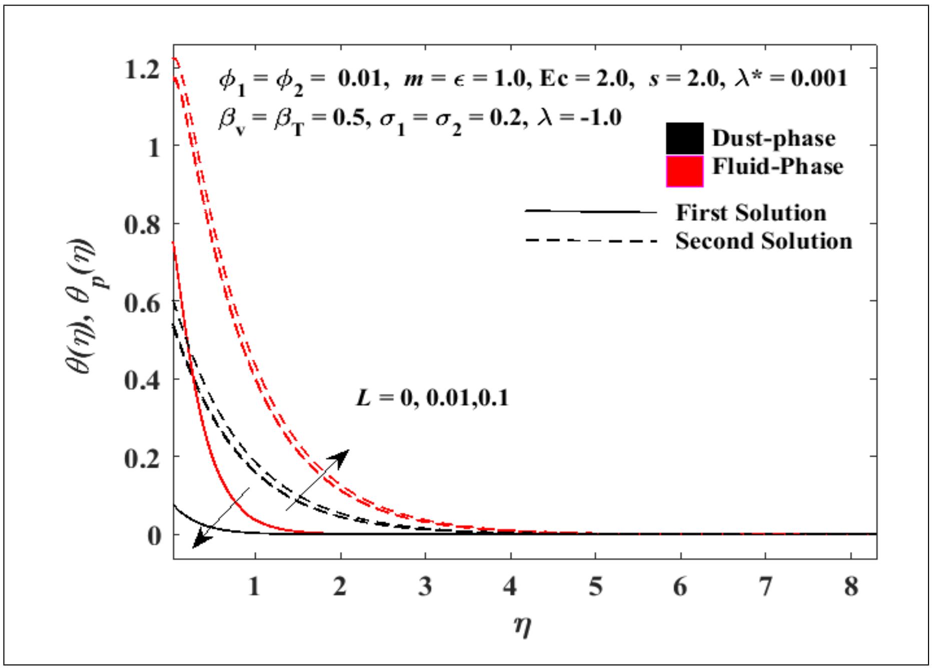

Figure 6.5 Temperature Profile with Various Values of L

in the first solution but diminishes in the second solution. Meanwhile, the elevated mass concentration of dust particles results in a reduction of the $Nu_x Re_x^{-1/2}$ values. This implies that the combined of enhanced suction and dust particles contributes in intensifying the drag force between the fluid and the surface. Physically, a stronger suction effect draws the fluid closer to the surface which elevates the shear stress.

Similarly, a greater dust particle mass concentration increases the viscosity in the boundary layer, contributing to higher frictional forces. An increase in the values of L leads to a decrease in the value of $Nu_x Re_x^{-1/2}$, which subsequently results in diminished heat transfer performance. The occurrence is attributed to the dust particles, which have been known to store heat, thus retaining internal heat instead of effectively transferring it at the surface.

The velocity and temperature profiles for $f'(\eta), \theta(\eta)$ and $f'_p(\eta), \theta_p(\eta)$ of Figures 6.6 and 6.7 are correspondingly shown in Figures 6.8 and 6.9. The velocity profile shows a rise in the first solution of both phases, indicating a decrease in boundary layer thickness as the dust particles mass concentration rises. This occurs as a result of the increased mass concentration of dust particles, which causes a steeper velocity gradient at the surface and a higher skin friction coefficient, implying that the system experiences greater resistance. Figure 6.9 shows a decrease in the boundary layer thickness of the first solution for both phases, while an increase in the second solution. This results in a thinner boundary layer thickness in the first solution than the second solution, indicating a higher local Nusselt number and heat transfer rate in the first solution.

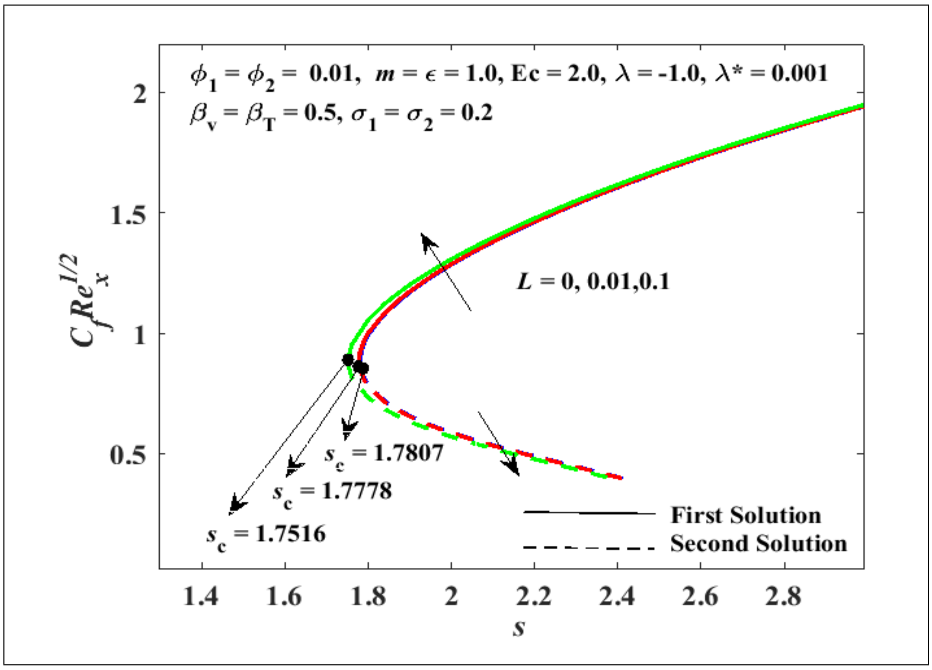

Figure 6.6 $C_f Re_x^{1/2}$ with s for Different Values of L

The effect of considering distinct values of λ^* over stretching and shrinking

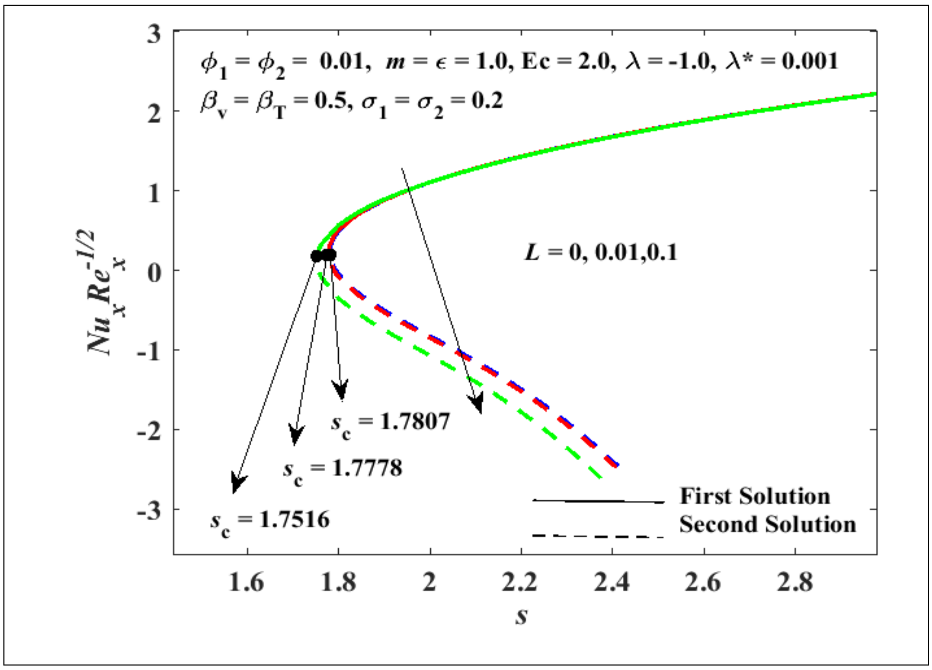

Figure 6.7 $Nu_x Re_x^{-1/2}$ with s for Different Values of L

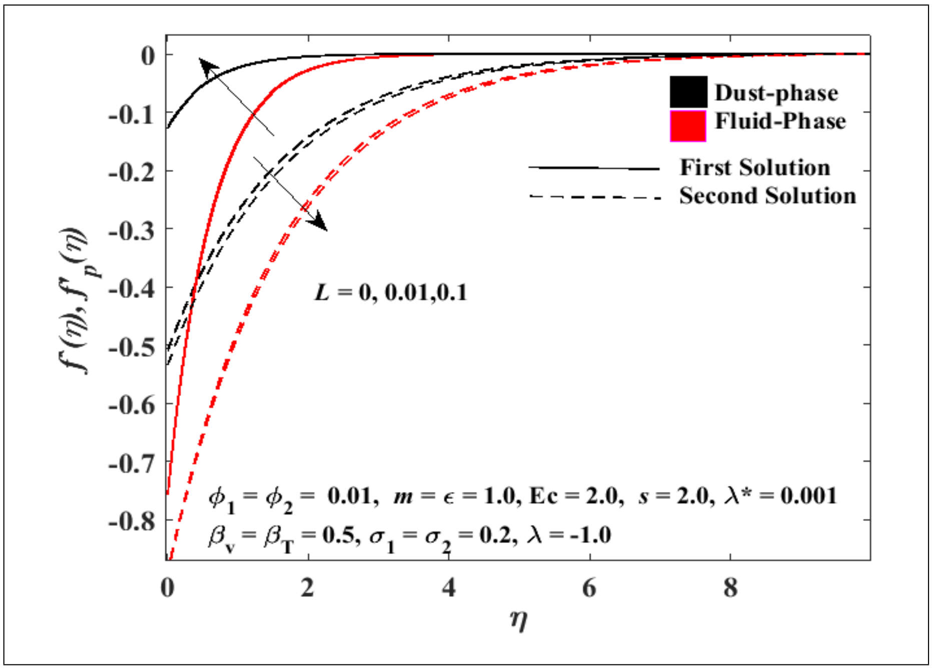

Figure 6.8 Velocity Profile with Different Values of L

surfaces for the values of $C_f\ Re_x^{1/2}$ and $Nu_x Re_x^{-1/2}$ are illustrated in Figures 6.10 and 6.11, respectively. The numerical results shows the presence of dual solutions for certain ranges of the shrinking surface. An increase in λ^* was found to delay boundary layer separation, particularly in shrinking surface cases and no solutions were found beyond the critical point $\lambda < \lambda_c$. Analysis of Figures 6.10 and 6.11,

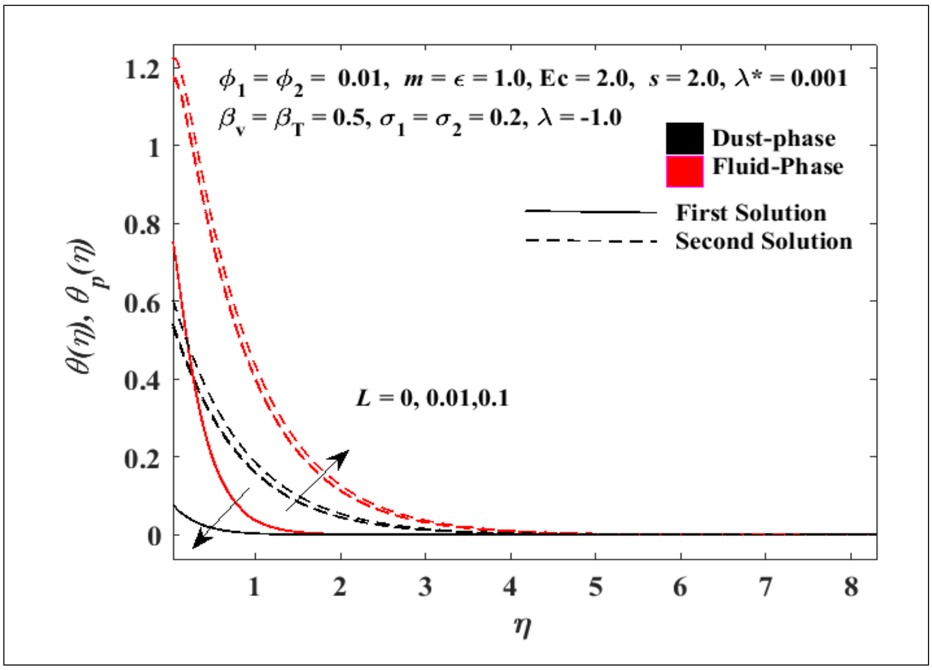

Figure 6.9 Temperature Profile with Different Values of L

and Table 6.1 reveals that for both stretching and shrinking surfaces, there is a slight increase of 0.31% and 1.77% for the first and second solutions for the value of $C_f Re_x^{1/2}$, respectively. Further, the first solution shows an increase of 0.16%, while the second solution exhibits a decrease of 20.9% for the value of $Nu_x Re_x^{-1/2}$ as λ^* increases. This is because, the increase in the mixed convection parameter results to a stronger buoyancy force, causing the fluid near the surface to accelerate upwards with greater intensity. This, consequently, enhances the drag force and improves the efficiency of heat transfer.

The corresponding profiles of Figures 6.10 and 6.11 are shown in Figures 6.12 and 6.13, respectively. Based on the profiles presented, a diminishing trend can be seen in the first solutions across both phases which leads to a steeper velocity and temperature gradient, respectively. This indicates that an increase in λ^* resulting to a diminished boundary layer thickness which then enhance the skin friction coefficient and local Nusselt number between the fluid and the surface within the boundary layer. Meanwhile, the second solution demonstrates a contrasting trend.

Figures 6.14 and 6.15 illustrates the numerical findings for variety values of s, and λ^* for $C_f Re_x^{1/2}$ and $Nu_x Re_x^{-1/2}$ values, respectively. Similar to the findings shown in Figures 6.10 and 6.11, both solutions of the skin friction coefficient and the

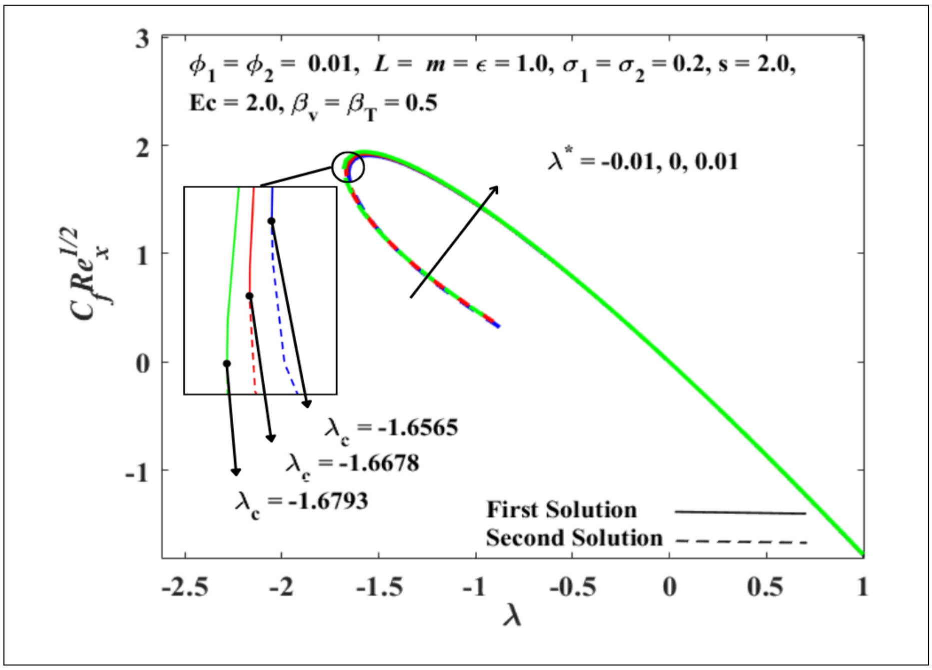

Figure 6.10 $C_f Re_x^{1/2}$ with λ for Distinct Values of λ^*

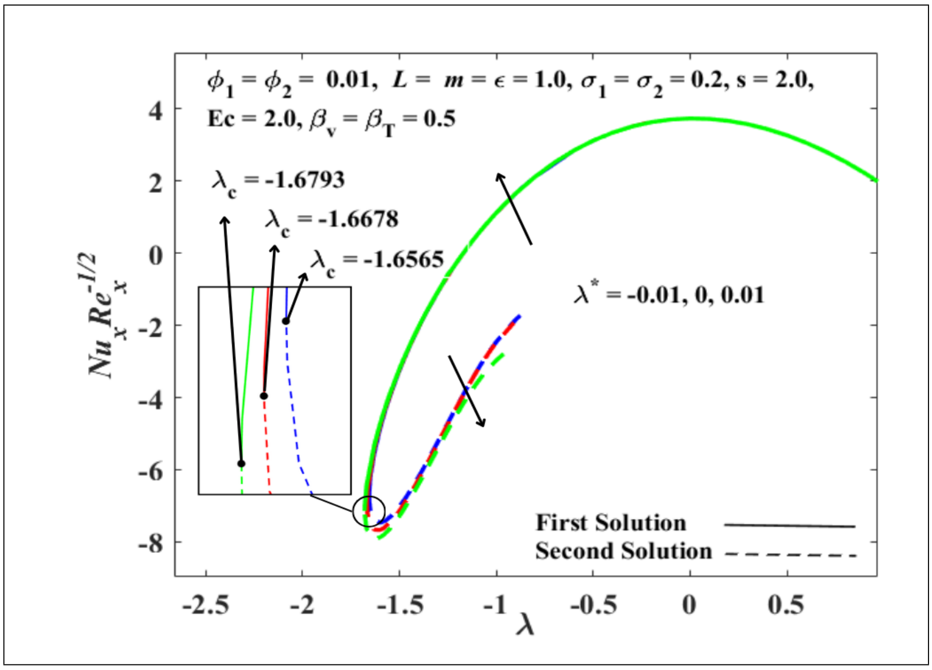

Figure 6.11 $Nu_x Re_x^{-1/2}$ with λ for Distinct Values of λ^*

first solution of local Nusselt number values exhibit a slight but consistent increasing trend as λ^* increases. This highlights the influence of buoyancy-driven convection in enhancing drag forces and heat transfer rate at the surface.

Figures 6.16 and 6.17 elucidates the velocity and temperature profiles of Figures 6.14 and 6.15, respectively. A rise in the mixed convection parameter leads to an

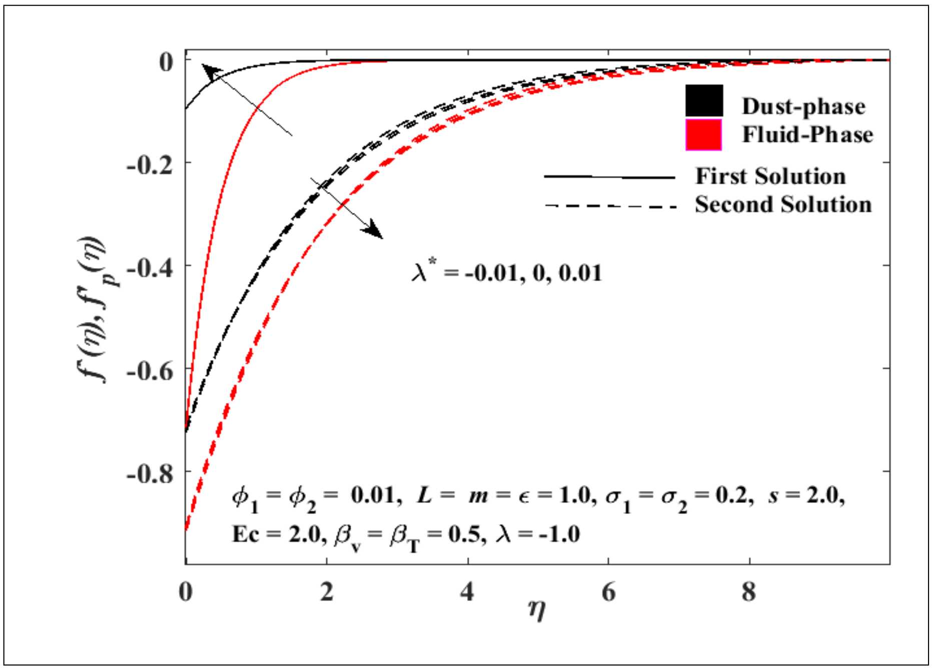

Figure 6.12 Velocity Profile with Distinct Values of λ^*

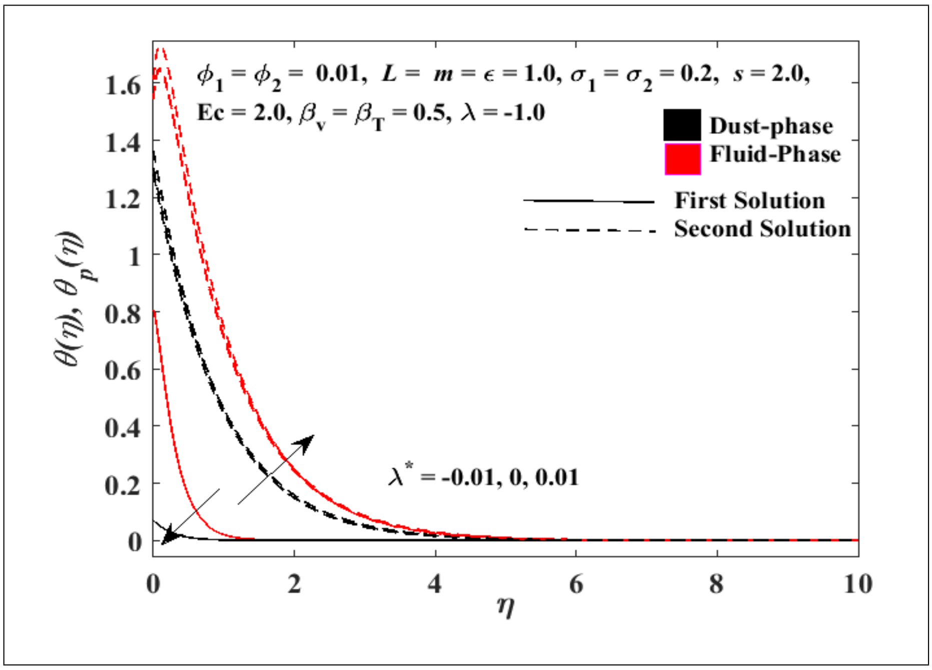

Figure 6.13 Temperature Profile with Distinct Values of λ^*

enhanced buoyancy force, this results to an decrease in the boundary layer thickness in the first solution of both phases due to the additional upward force, whereas the second solution shows an opposite trend. It therefore results in an elevated velocity gradient, subsequently increasing the skin friction coefficient. Furthermore, in terms of the temperature profile, the boundary layer shows a thinning effect in the first solution, which enhances the temperature gradient and results in a higher local Nusselt number and heat transfer rate compared to the second solution.

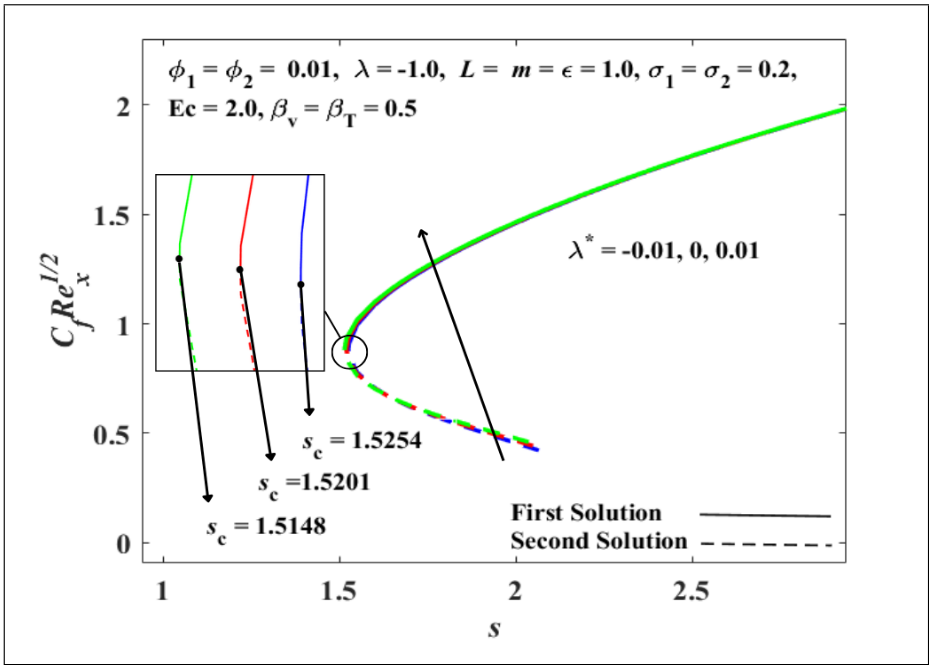

Figure 6.14 $C_f Re_x^{1/2}$ with s for Variety Values of λ^*

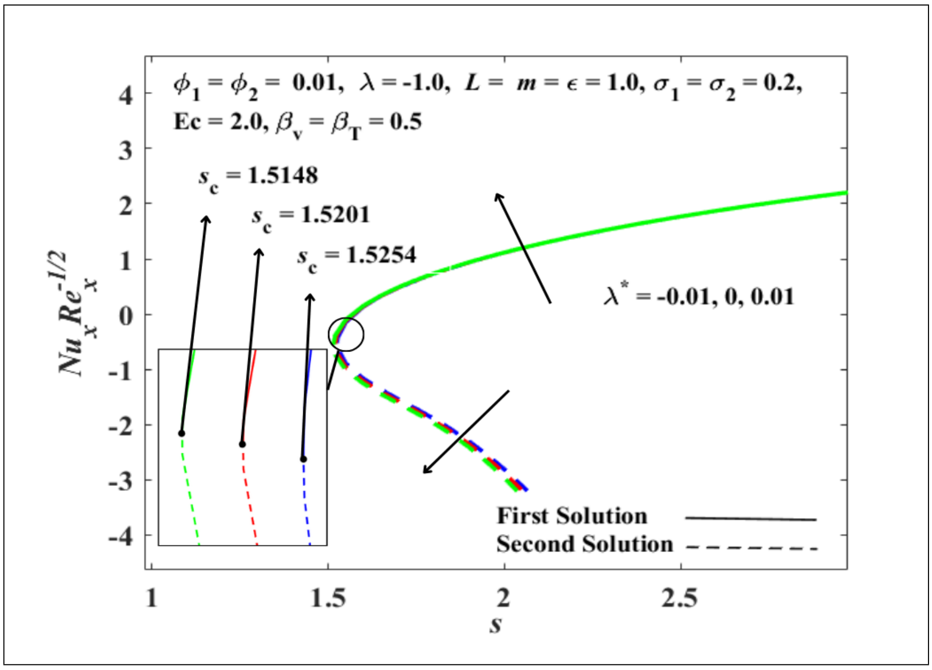

Figure 6.15 $Nu_x Re_x^{-1/2}$ with s for Variety Values of λ^*

Figures 6.18 and 6.19 depicts the values of $C_f Re_x^{1/2}$ and $Nu_x Re_x^{-1/2}$ against s for different values of Ec. As depicted in Table 6.1 and Figure 6.18, the values of $C_f Re_x^{1/2}$ shows a minimal increase of 0.14% in the first solution, while 0.65% decrease in

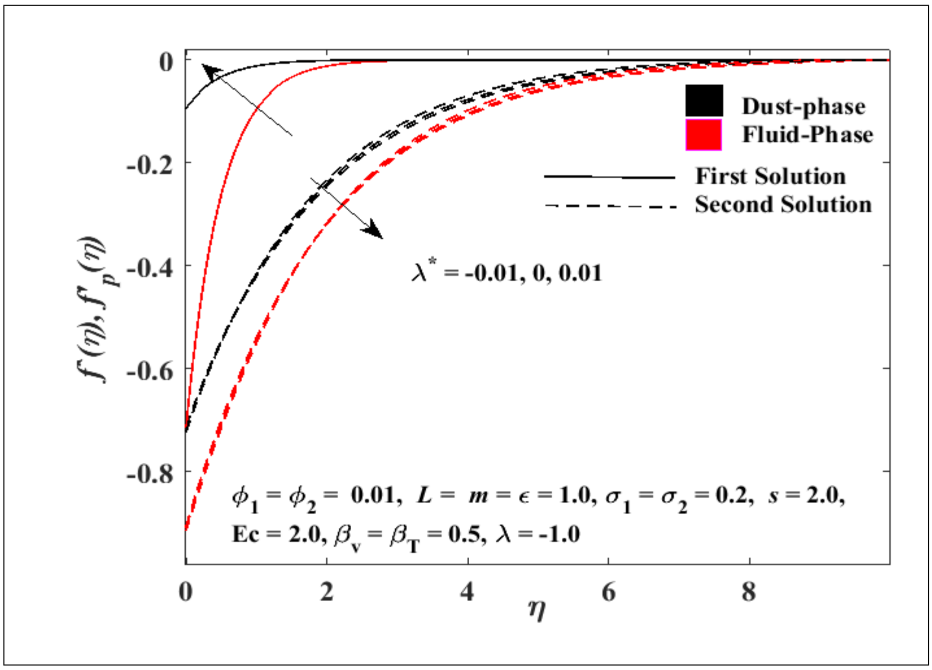

Figure 6.16 Velocity Profile with Variety Values of λ^*

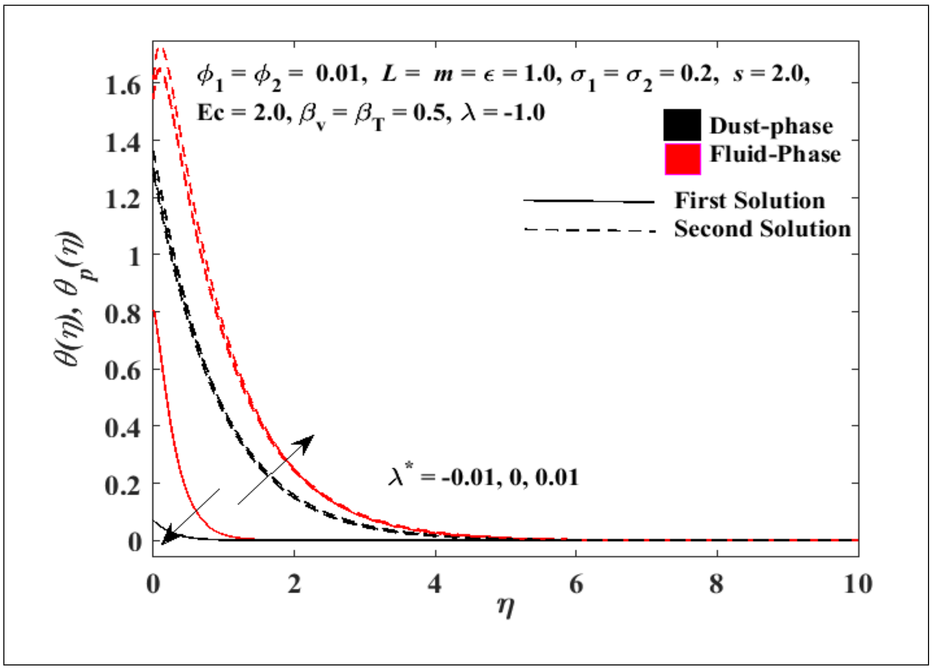

Figure 6.17 Temperature Profile with Variety Values of λ^*

the second solution as Ec increases. This is due to the fact that Ec implies viscous dissipation, which relates to the transformation of kinetic energy into thermal energy, thus, Ec is insignificant for the skin friction coefficient. Furthermore, referring to Table 6.1 and Figure 6.19, there is a noticeable diminishing trend of approximately 69.28% in the first solution and 182.9% in the second solution for the $Nu_x Re_x^{-1/2}$

values as the Ec number increases. This can be concluded that, with higher Ec number values, it increases the amount of thermal energy being converted, which subsequently rises the fluid temperature and lowers the rate of heat transfer.

Figures 6.20 and 6.21 shows the corresponding profiles of Figures 6.18 and 6.19, respectively. Figure 6.20 illustrates a consistent result for velocity profile, aligning with the observations noted in Figure 6.18. However, in Figure 6.21, an increase in the temperature profile can be seen with a greater Ec number. The thickness of the thermal boundary layer rises in both solutions for both phases, implying a reduced local Nusselt number and heat transfer rate, equivalent to the results presented in Figure 6.19. This happens because, as the Ec number rises, it simultaneously elevates the fluid temperature, which subsequently diminishes the heat transfer between the fluid and the surface.

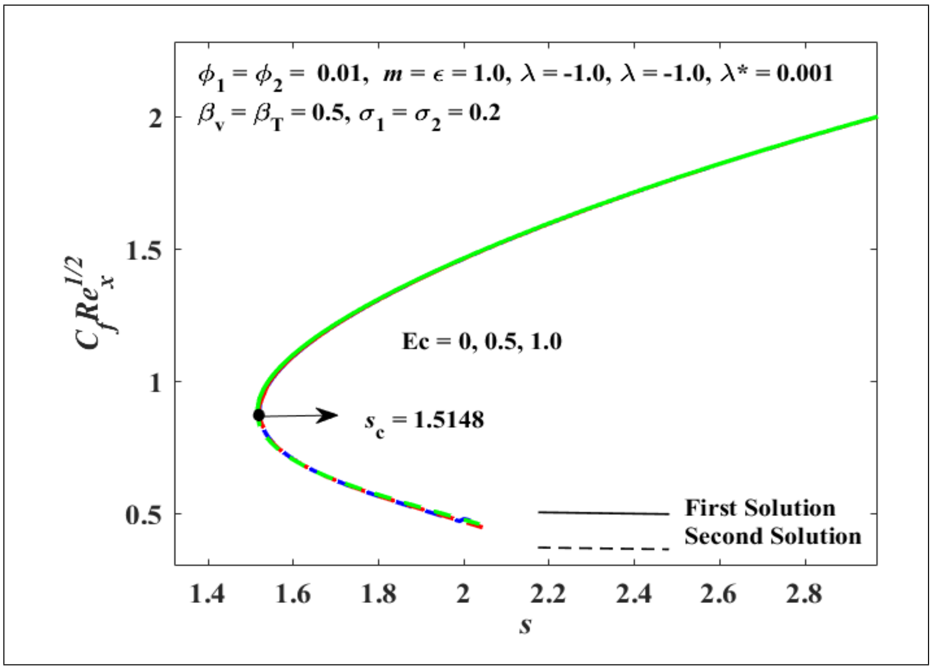

Figure 6.18 $C_f Re_x^{1/2}$ with s for Different Values of Ec Number

The variation of $C_f Re_x^{1/2}$ and $Nu_x Re_x^{-1/2}$ across a shrinking surface for some values of s and σ_1, σ_2 are presented in Figures 6.22 and 6.23 respectively. Based on both figures, it can be seen that within the range of $s_c < s < 2.1$, dual solutions exists, and when $s < s_c$ no solution exists which indicates the formation of boundary layer separation. Furthermore, Table 6.1 and Figure 6.22 show a diminishing pattern of 19.66% and 24.78% for the first and second solutions, respectively, for the $C_f Re_x^{1/2}$

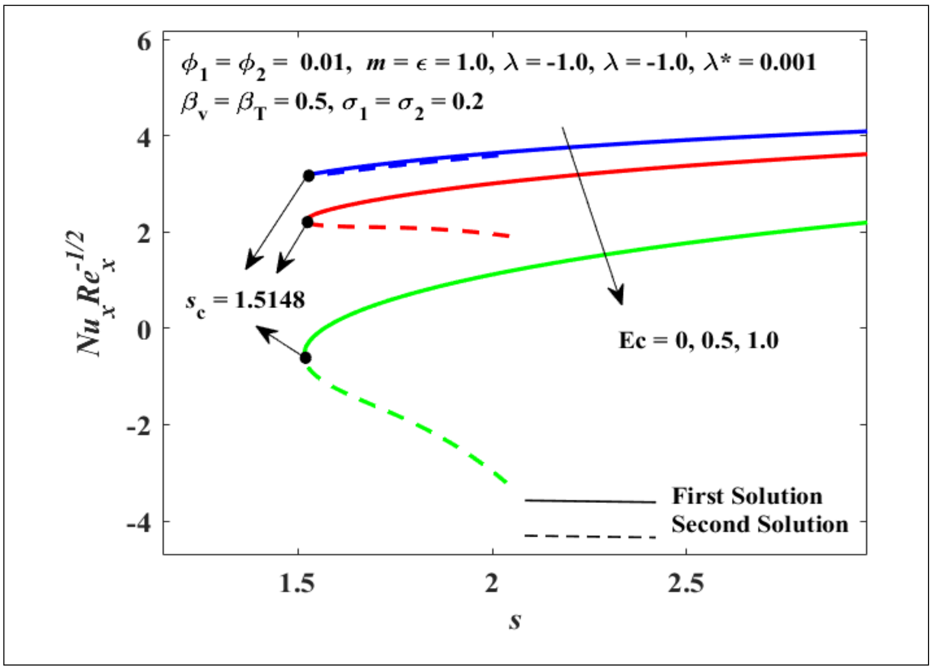

Figure 6.19 $Nu_x Re_x^{-1/2}$ with s for Different Values of Ec Number

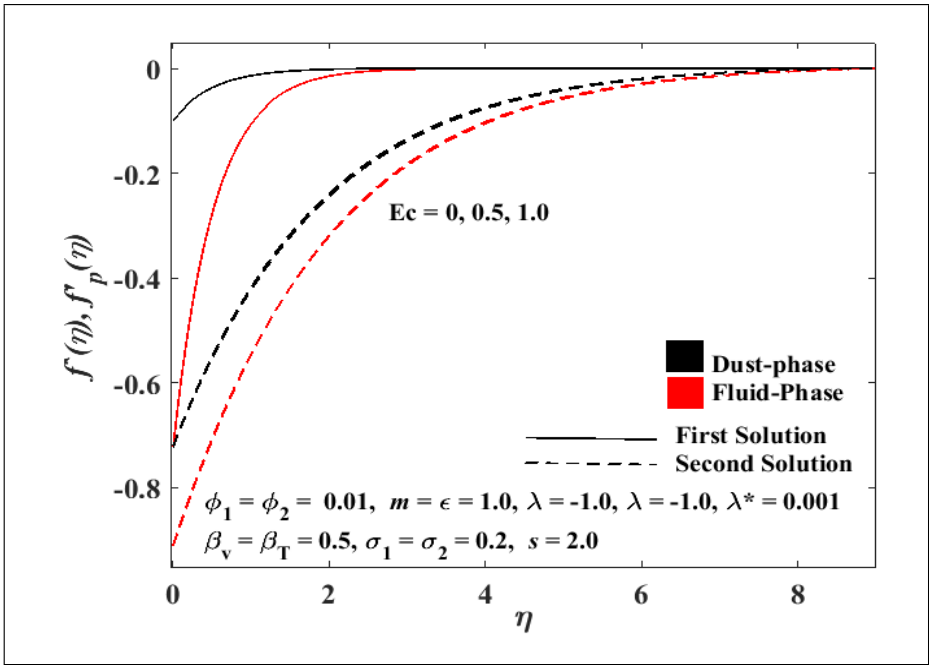

Figure 6.20 Velocity Profile with Different Values of Ec Number

as the values of slip parameter rises, contradict to the outcomes shown in Figure 6.23, where an increase of 124.26% and 73.95% for the first and second solutions, respectively. This indicates that the rising values of slip parameters reduces the resistance and frictional force, while increases heat transmission within the boundary layer. Besides that, the boundary layer separation is also seen to be delayed with the

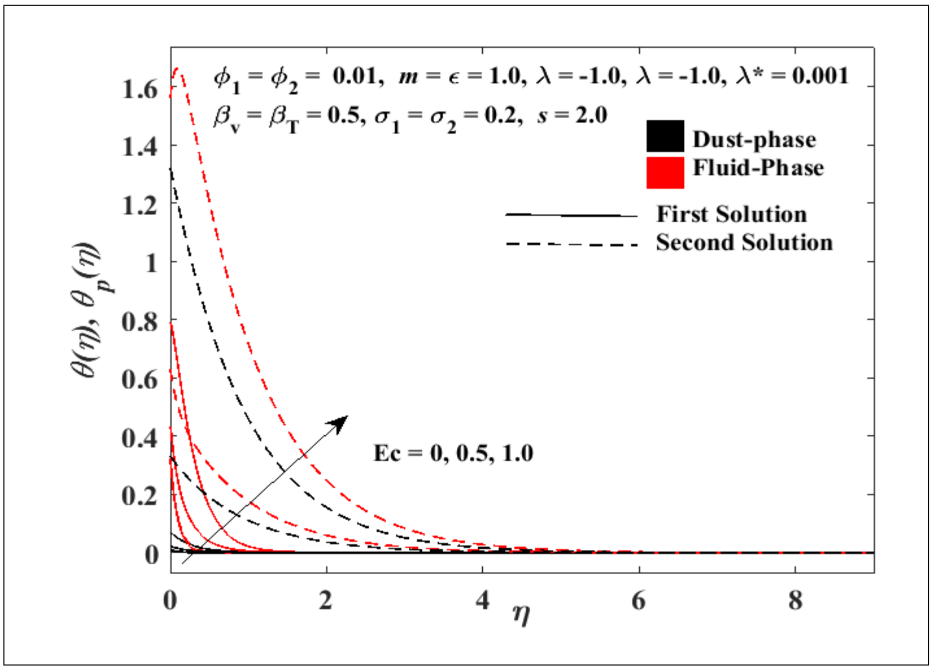

Figure 6.21 Temperature Profile with Different Values of Ec Number

increasing values of σ_1 and σ_2.

The corresponding profiles of velocity and temperature for fluid phase and dust phase of Figures 6.22 and 6.23 for different values of slip parameters are displayed in Figures 6.24 and 6.25, respectively. The profiles satisfy the specified boundary conditions, confirming the reliability of the numerical solutions. In addition, the occurrence of dual solutions in Figures 6.22 and 6.23 are proven. As depicted in Figure 6.24, the boundary layer thickness of the velocity profile for the first solution of both phases is seen to decrease than the second solution with greater values of slip parameters, which then increases the velocity gradient. However, the skin friction coefficient is observed to be diminishing, which contradicts to its typical trend. Figure 6.25 shows a reduction in the temperature profile, implying thinning of boundary layer thickness in the first solution for both phases but increases in the second solution. This pattern elevates the temperature gradient, resulting in a greater local Nusselt number and heat transmission rate.

Figures 6.26 and 6.27 demonstrates the influence of σ_1 on $C_f Re_x^{1/2}$ and $Nu_x Re_x^{-1/2}$, respectively. Dual solutions occurs in the range of $s_c < s < 2.2$, while no solution can be found beyond the range as it indicates the separation of the boundary layer from the surface. Adding to that, rising the values of σ_1 leads to a retardation

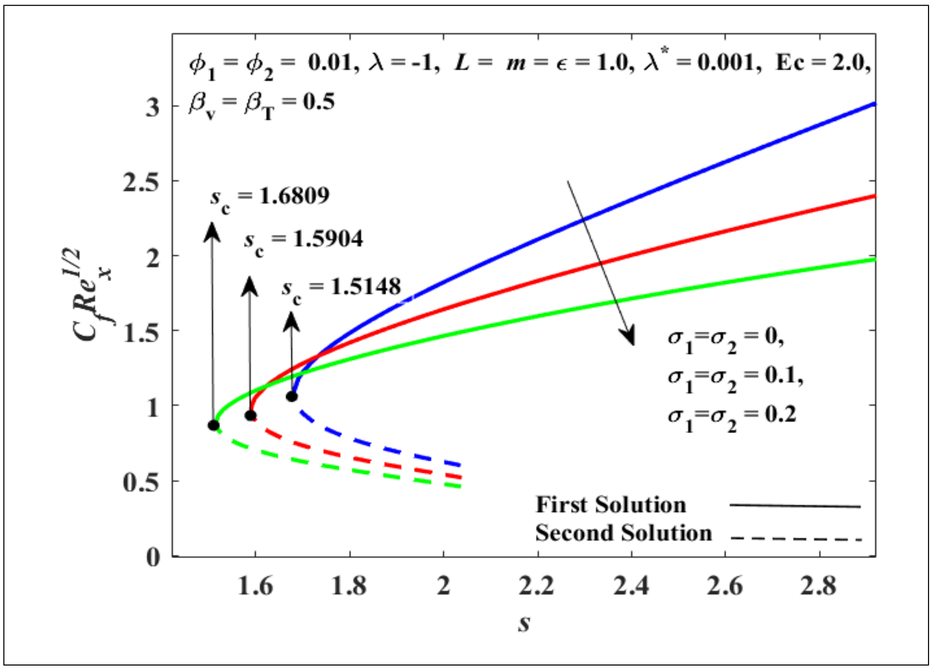

Figure 6.22 $C_f Re_x^{1/2}$ with s for Distinct Values of σ_1 and σ_2

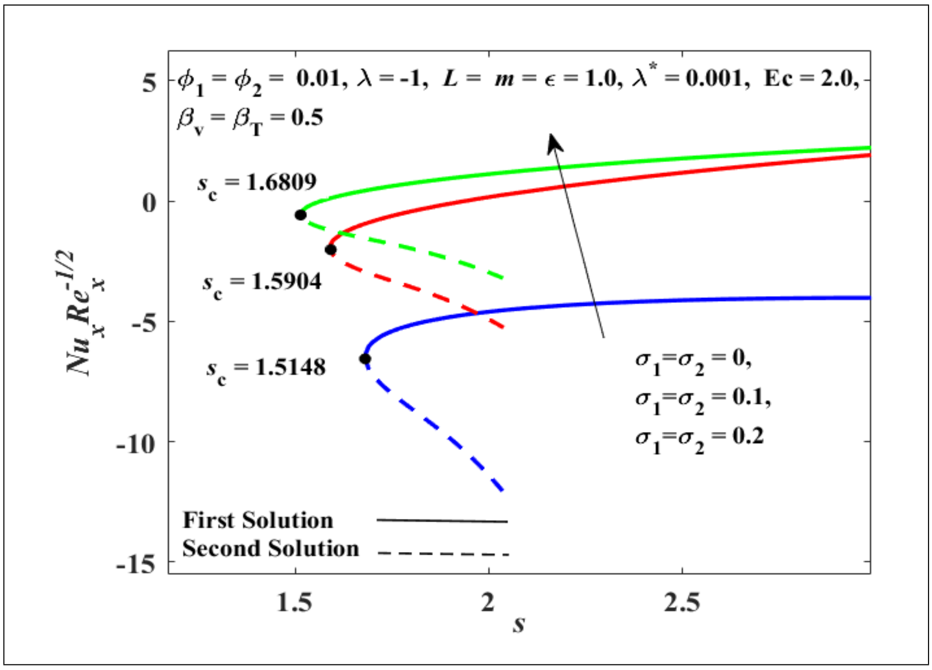

Figure 6.23 $Nu_x Re_x^{-1/2}$ with s for Distinct Values of σ_1 and σ_2

of boundary layer separation. According to Table 6.1 and Figure 6.26, the values of $C_f Re_x^{1/2}$ decreases by 19.68% for the first solution and 25.1% for the second solution with an increase of σ_1. This implies that an increase in velocity slip lengths which differentiates the velocity between the fluid and boundary layer, results in a reduction of frictional and drag forces at the surface. Meanwhile, Figure 6.27 illustrates an

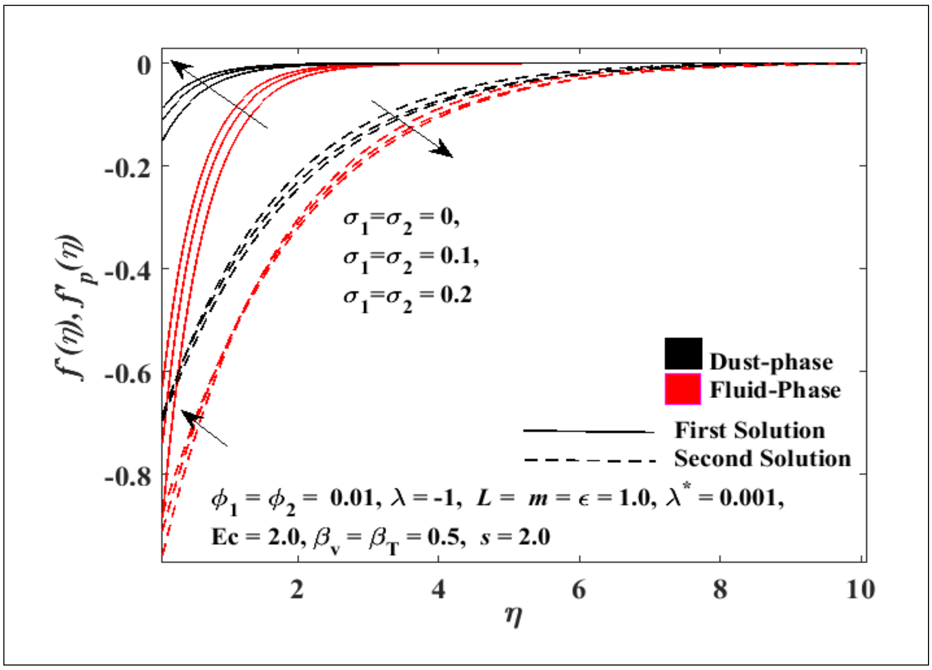

Figure 6.24 Velocity Profile with Distinct Values of σ_1 and σ_2

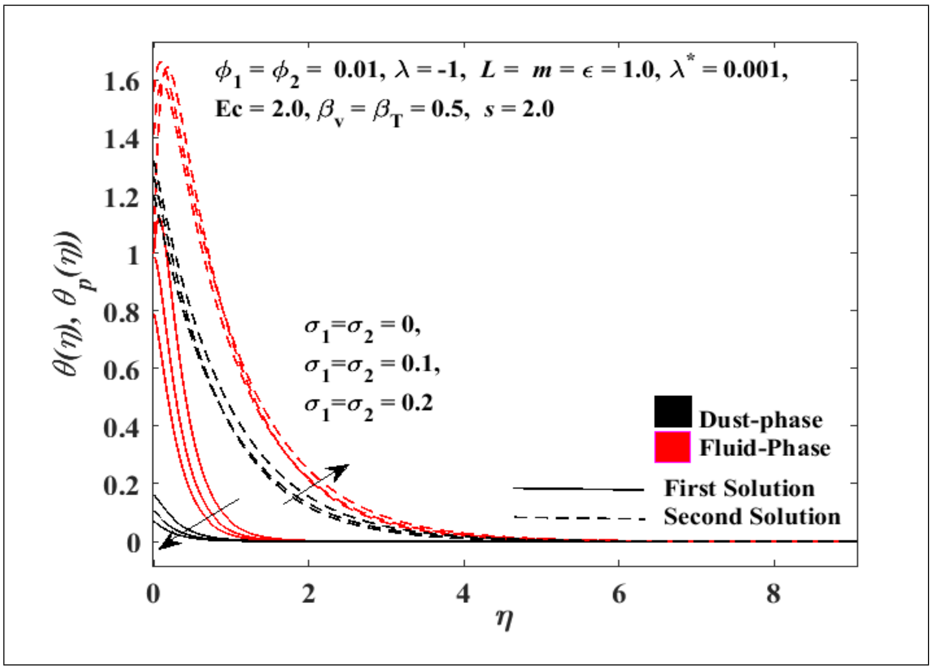

Figure 6.25 Temperature Profile with Distinct Values of σ_1 and σ_2

increment by 175% and 14.42% for the first and second solutions, respectively, in the $Nu_x Re_x^{-1/2}$ values as σ_1 rises.

The velocity and temperature profiles for some values of σ_1 for $f'(\eta), \theta(\eta)$ and $f'_p(\eta), \theta_p(\eta)$ are shown in Figures 6.28 and 6.29, respectively which also are the corresponding profiles of Figures 6.26 and 6.27 above. Figure 6.28 depicts the increasing values of σ_1 leading to an increase of the first solution while a decrease in the second solution for both phases of the velocity profile. The boundary layer thickness of the first solution appears to be reduced, similar to the findings shown in Figure 6.24 resulting in an increased velocity gradient. However, there is a declining trend in the skin friction coefficient. Additionally, Figure 6.29 illustrates a decreasing trend in the temperature profile across the first solution for both phases, implying improved local Nusselt number and heat transmission characterized by a steeper temperature gradient.

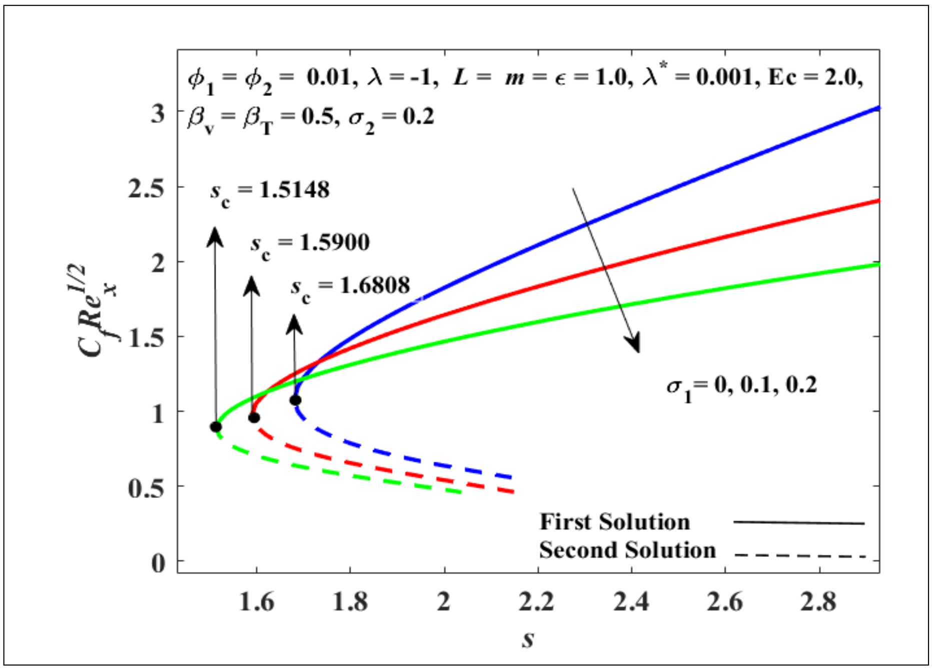

Figure 6.26 $C_f Re_x^{1/2}$ with s for Distinct Values of σ_1

The implication of different values of σ_2 towards a shrinking surface for $C_f Re_x^{1/2}$ and $Nu_x Re_x^{-1/2}$ are displayed in Figures 6.30 and 6.31 respectively. Based on these figures, non-unique solutions are observed within the range of $s_c < s < 2.1$ and s_c remains consistent across all three increasing values of σ_2, specifically at 1.5148. Table 6.1 and Figure 6.30 shows that increasing σ_2 has minimal increasing effect of 0.3% in the first solution, while 3.42% decreases in the second solution on $C_f Re_x^{1/2}$, indicating increasing values of σ_2 gives an insignificant effect to $C_f Re_x^{1/2}$. Moreover, based on Figure 6.31, a declination of 68.21% in the first solution and an inclination of 60.99% in the second solution is noticed in the $Nu_x Re_x^{-1/2}$ values as σ_2 augments. It can concluded the inclusion of the thermal slip parameter has minimal effect on the

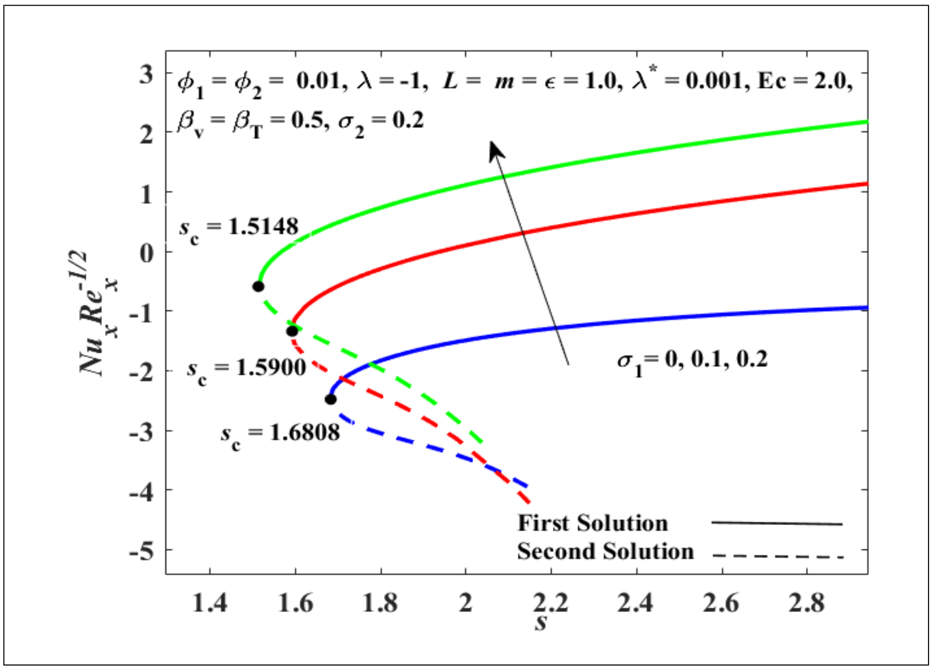

Figure 6.27 $Nu_x Re_x^{-1/2}$ with s for Distinct Values of σ_1

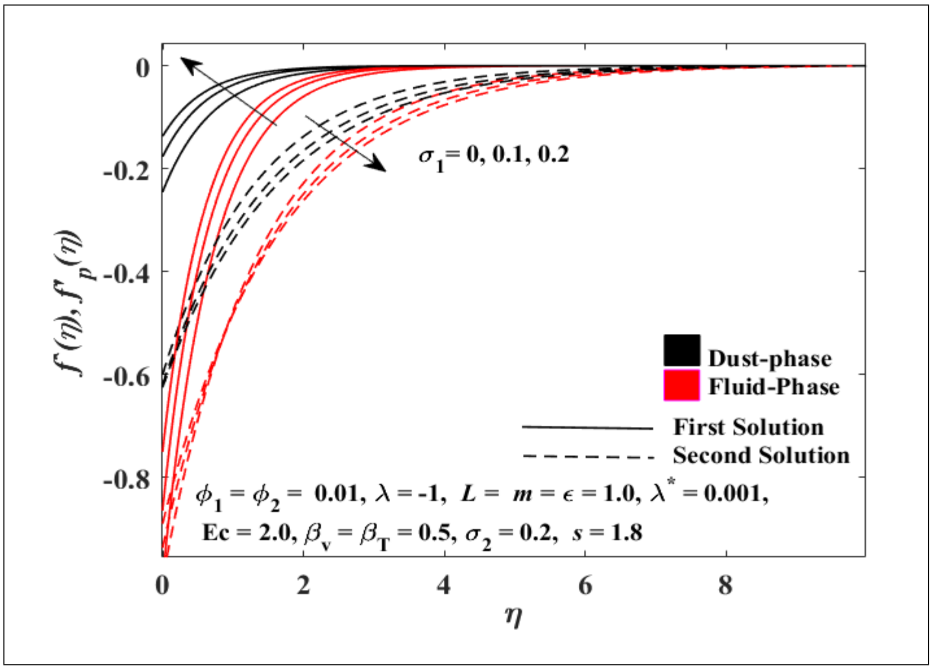

Figure 6.28 Velocity Profile with Distinct Values of σ_1

frictional and drag force on the surface, but diminishes the efficiency of high thermal conductivity fluid, resulting in lowering the local Nusselt and heat transfer rate.

The profiles of velocity and temperature for $f'(\eta), \theta(\eta)$ and $f'_p(\eta), \theta_p(\eta)$ of Figures 6.30 and 6.31 are demonstrated in Figures 6.32 and 6.33 respectively. Figure 6.32 displays a consistent result to Figure 6.30, where the velocity profile

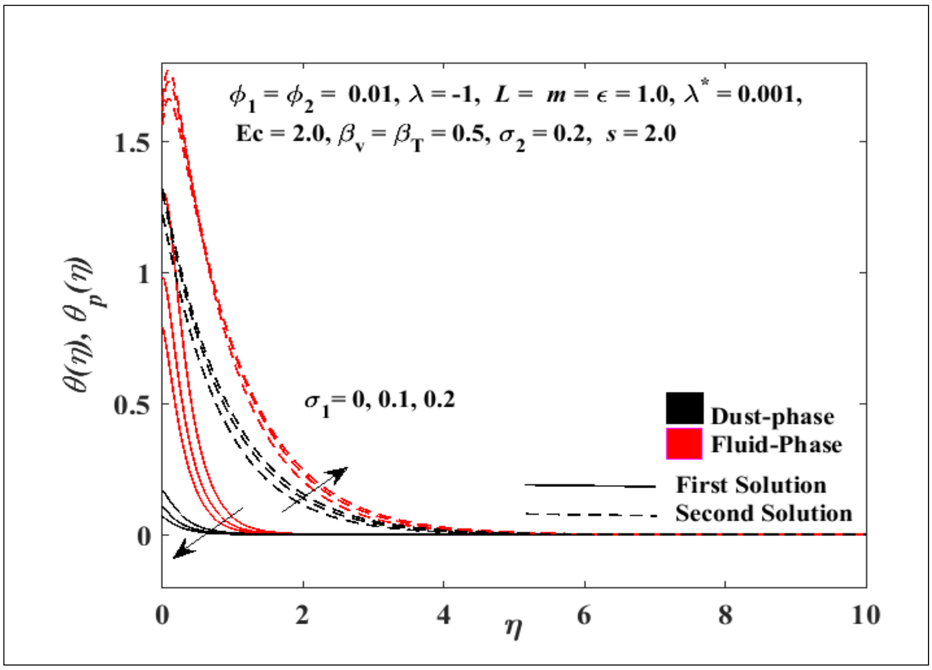

Figure 6.29 Temperature Profile with Distinct Values of σ_1

shows minimal changes as σ_2 increases. This is because alterations in thermal slip only affects the thermal boundary conditions, not the velocity boundary conditions (Bhattacharyya et al., 2011). Aside from that, a decrease in the first solution of the temperature profile is illustrated in Figure 6.33 and the boundary layer thickness of the first solution of both phases is seen to be thinner which indicates the higher local Nusselt number and effectiveness of the heat transmission rate compared to the second solution.

The effect of dispersing distinct values of ϕ_1 into water on $C_f Re_x^{1/2}$ and $Nu_x Re_x^{-1/2}$ are depicted in Figures 6.34 and 6.35 respectively. According to Table 6.1, and Figures 6.34 and 6.35, the increased values of ϕ_1 upsurges the value of $C_f Re_x^{1/2}$ by 4.91% in the first solution and 2.85% in the second solution, while for the values of $Nu_x Re_x^{-1/2}$ it diminishes by 8% and 37.48% in the first and second solutions, respectively. This further implies the incorporation of alumina nanoparticles raises the viscosity of the fluid, subsequently leading to an increment of the frictional force and drag force within the boundary layer. Meanwhile, as the $Nu_x Re_x^{-1/2}$ values diminishes, it indicates a decrease in the rate of heat transfer, signifying diminished heat transfer efficiency of the fluid . Additionally, the increase in alumina nanoparticle volume fraction is seen to fasten the retardation in the boundary layer separation.

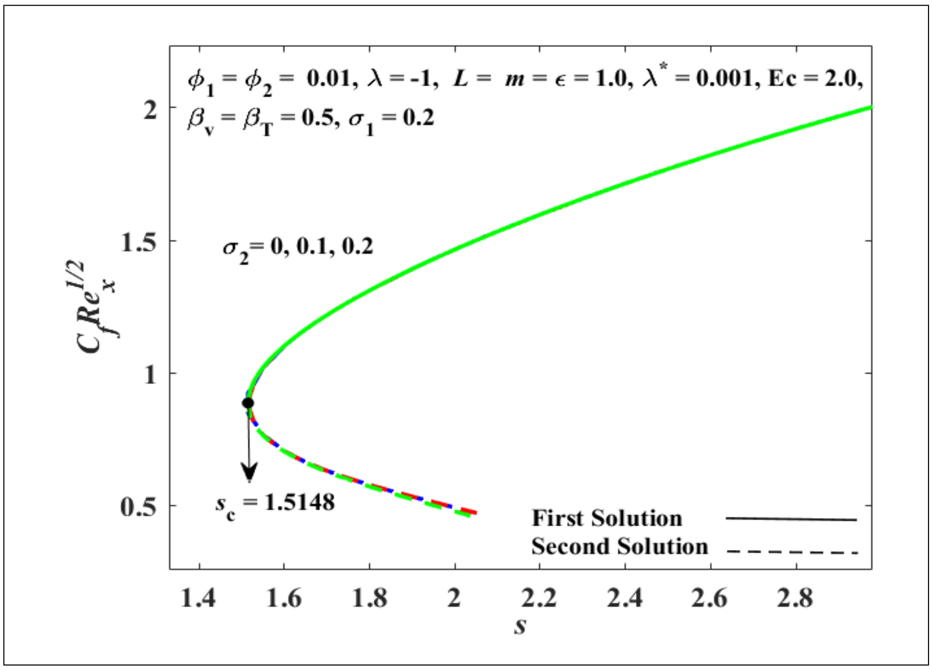

Figure 6.30 $C_f Re_x^{1/2}$ with s for Distinct Values of σ_2

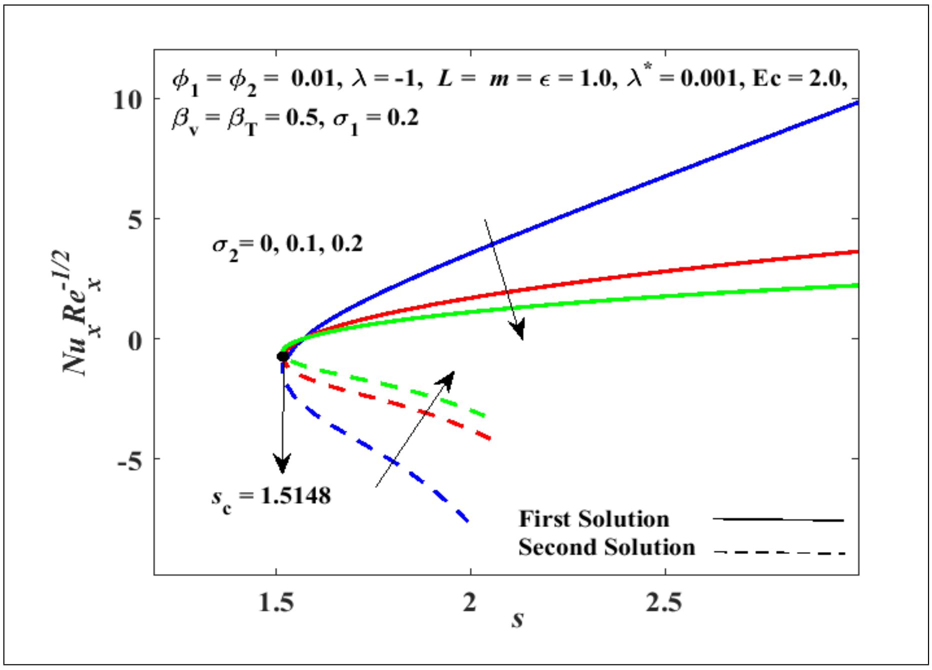

Figure 6.31 $Nu_x Re_x^{-1/2}$ with s for Distinct Values of σ_2

The increasing values of ϕ_1 on the velocity and temperature profiles of Figures 6.34 and 6.35 are correspondingly illustrated in Figures 6.36 and 6.37. The boundary conditions outlined in equation (3.3.84) are thoroughly satisfied showing a good correlation and dependability of the numerical findings achieved. Based on the figures, the boundary layer thickness increases in the first solution for both phases

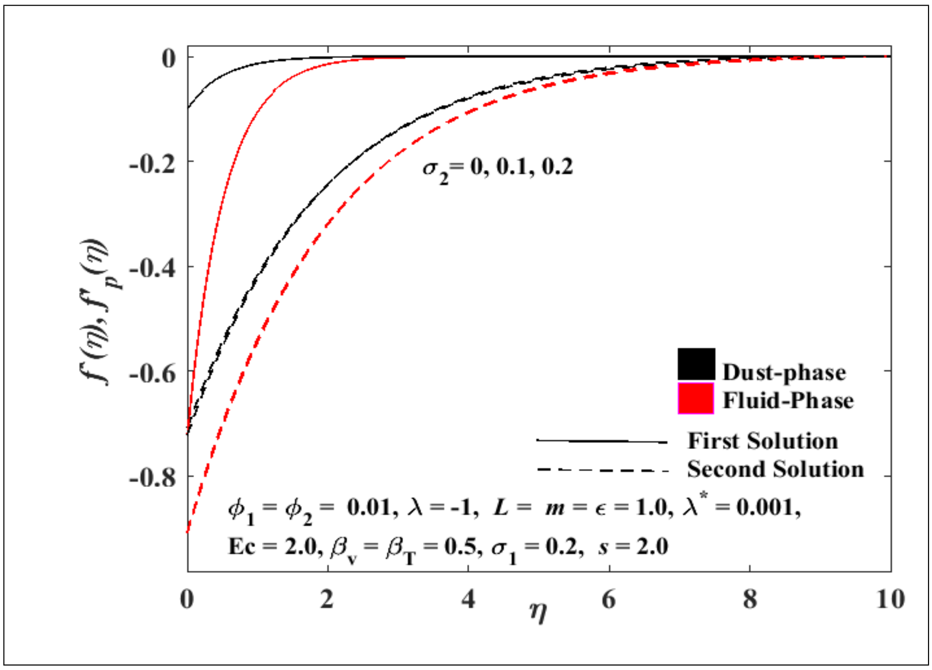

Figure 6.32 Velocity Profile with s for Distinct Values of σ_2

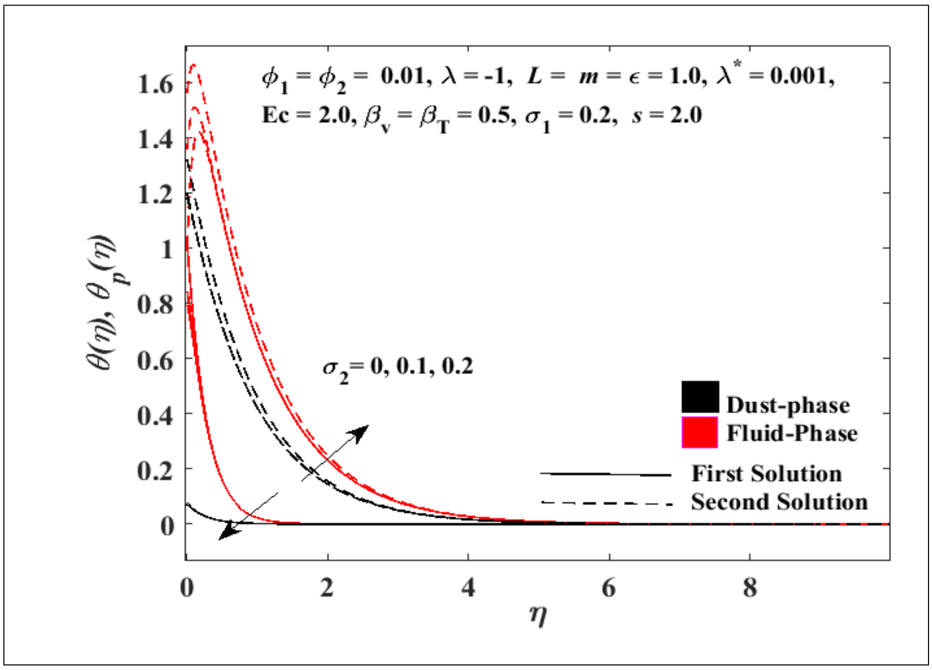

Figure 6.33 Temperature Profile with s for Distinct Values of σ_2

as ϕ_1 rises, which then leads to a less steep velocity and temperature gradient. The temperature profile results are consistent with those presented in Figure 6.35, indicating that the local Nusselt number and heat transfer rate decrease with ϕ_1.

The $C_f Re_x^{1/2}$ and $Nu_x Re_x\ ^{-1/2}$ for different values of ϕ_2 over a shrinking surface are shown in Figures 6.38 and 6.39 respectively. Based on both of the figures, similar

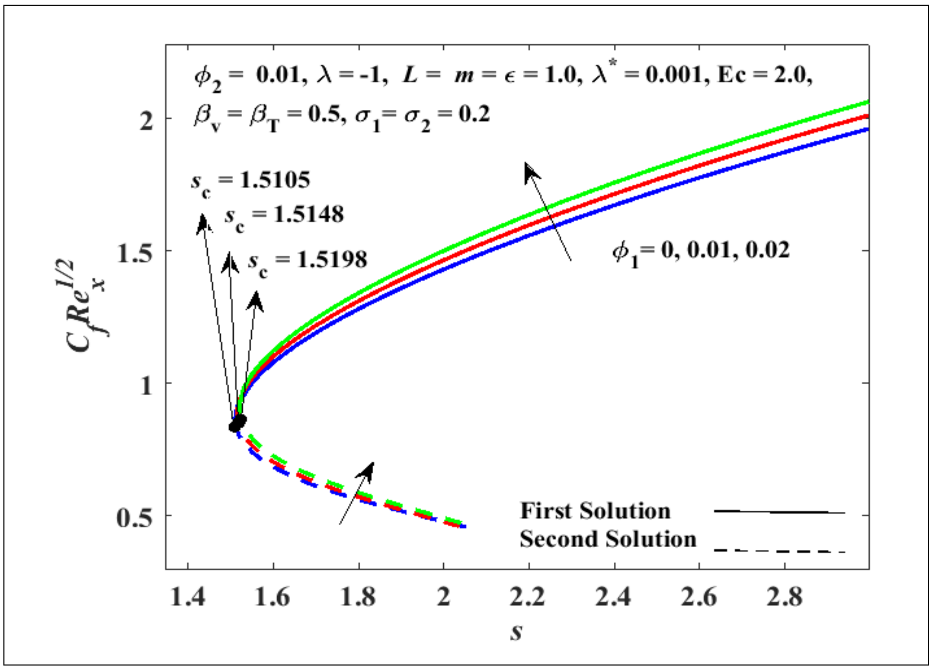

Figure 6.34 $C_f Re_x^{1/2}$ with s for Distinct Values of ϕ_1

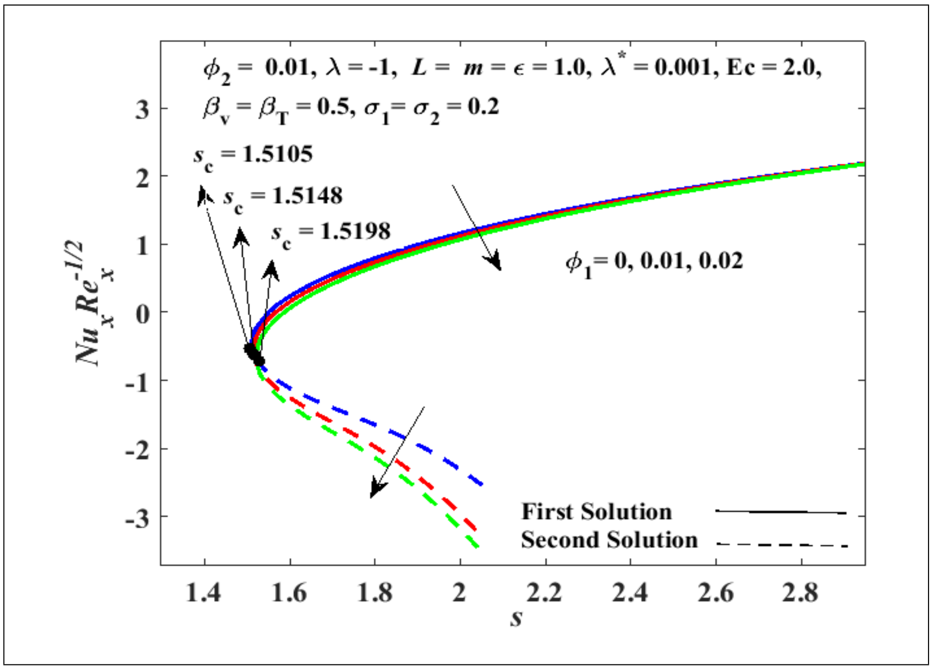

Figure 6.35 $Nu_x Re_x^{-1/2}$ with s for Distinct Values of ϕ_1

patterns are noticed compared to the Figures 6.34 and 6.35 above. The values of $C_f Re_x^{1/2}$ is seen to increase by 12.47% and 3.91% in the first and second solutions, respectively, with a greater amount of Cu nanoparticles added into the base fluid indicating greater friction at the surface, while a decrease in the values of $Nu_x Re_x^{-1/2}$ by 8.29% and 44.88% in the first and second solutions, respectively, indicating a lower

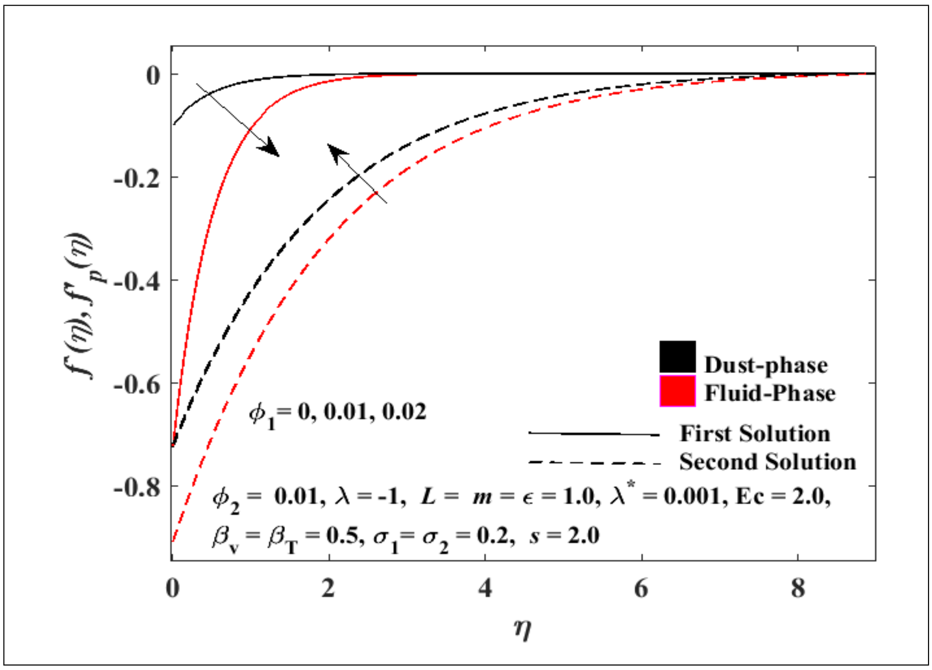

Figure 6.36 Velocity Profile for Distinct Values of ϕ_1

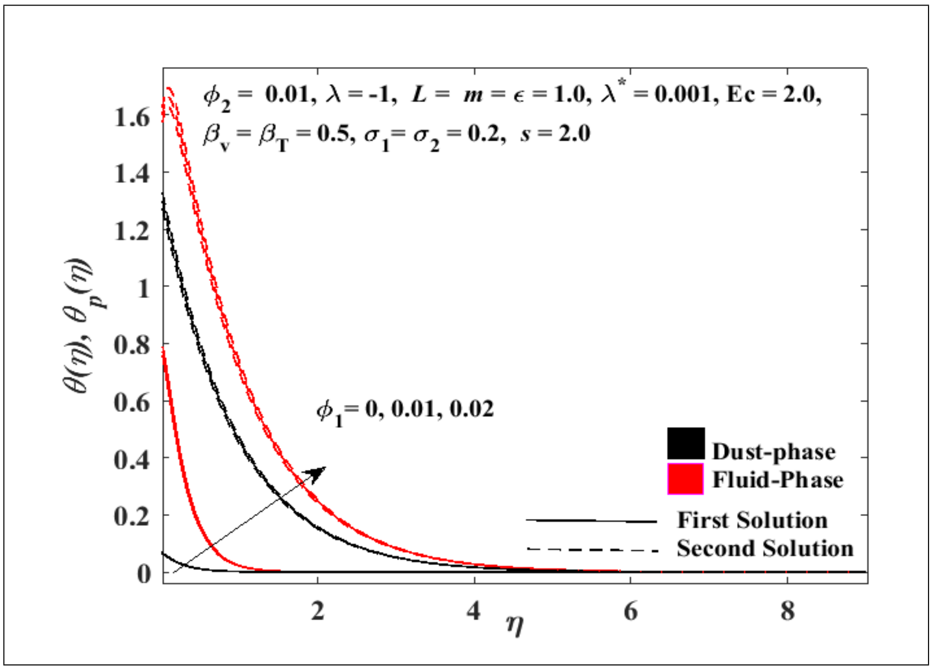

Figure 6.37 Temperature Profile for Distinct Values of ϕ_1

rate of heat transfer. Adding to that, the boundary layer separation of Figures 6.38 and 6.39 are delayed as values of the critical point are lower which indicates that greater dispersion of Cu nanoparticles into base fluid slows down the separation of the boundary layer. Furthermore, the existence of a dual solution is notable within the range of $s_c < s < 2.2$.

The corresponding velocity and temperature profiles of Figures 6.38 and 6.39 for $f'(\eta), \theta(\eta)$ and $f_p'(\eta), \theta_p(\eta)$ are demonstrated in Figures 6.40 and 6.41. Figure 6.40 shows an increment in the first solution of both phases whilst a decrease in the second solution also for both phases of the velocity profile. Further, the boundary layer thickness of the first solution is thinner than the second solution showing a higher velocity gradient in the first solution which implies a higher skin friction coefficient. Next, a decrease in the temperature profile for the first solution of both phases is seen in Figure 6.41. The thickness of the boundary layer of the first solution of both phases is thinner which signifies the local Nusselt number and heat transmission of the second solution is less efficient in comparison to the first solution as the values of ϕ_2 rise.

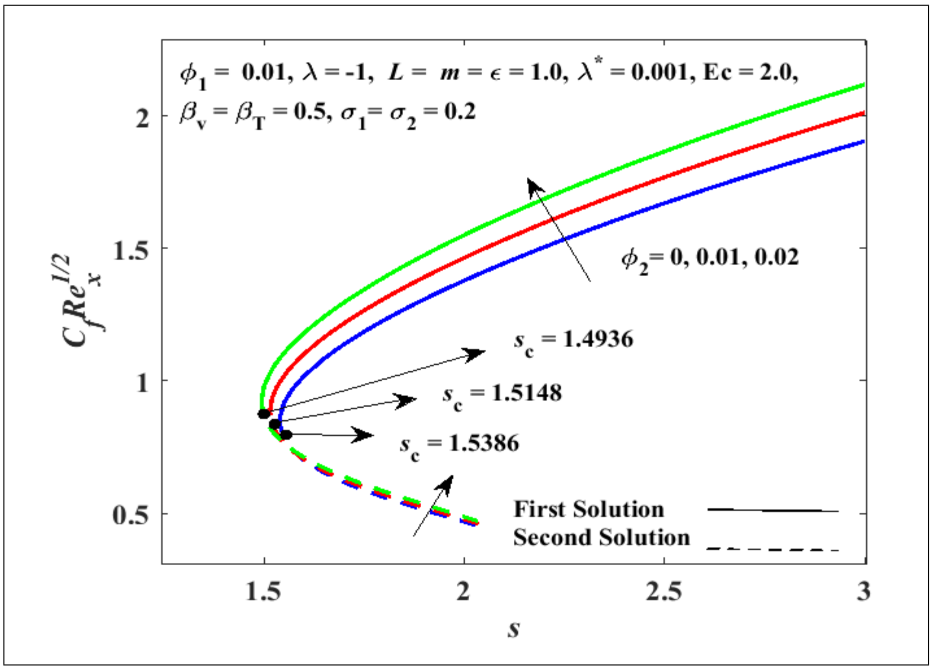

Figure 6.38 $C_f Re_x^{1/2}$ with s for Distinct Values of ϕ_2

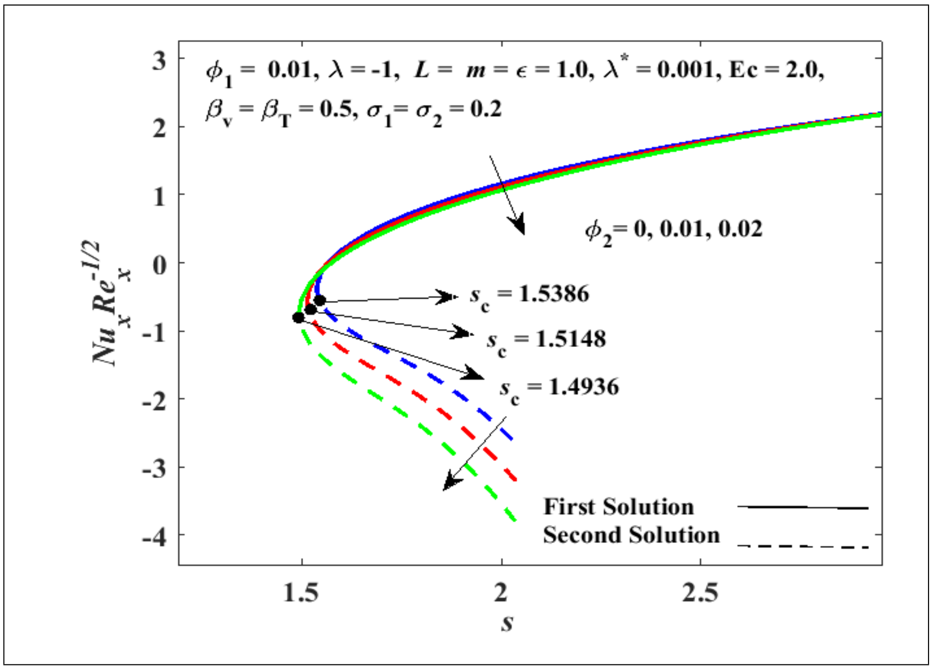

Figure 6.39 $Nu_x Re_x^{-1/2}$ with s for Distinct Values of ϕ_2

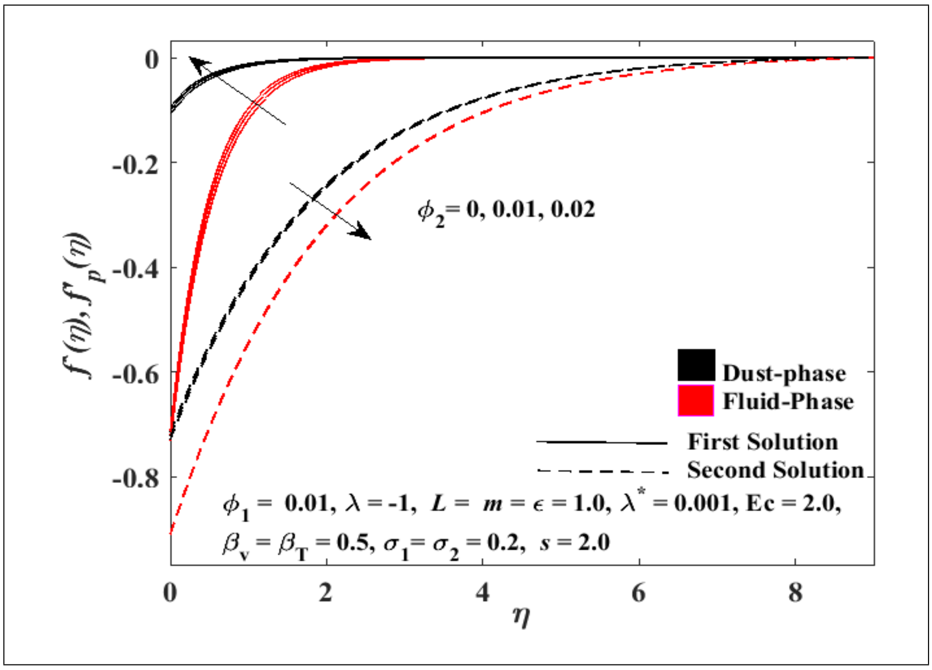

Figure 6.40 Velocity Profile for Distinct Values of ϕ_2

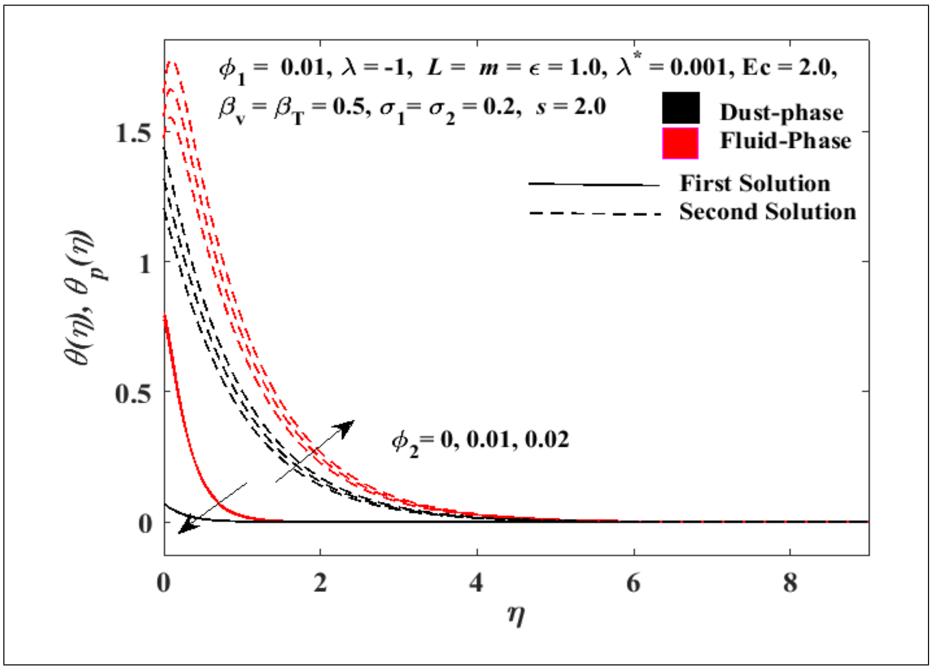

Figure 6.41 Temperature Profile for Distinct Values of ϕ_2

6.4 Conclusions

The two-phase flow and heat transfer characteristics of hybrid nanofluids passing a vertical permeable stretching or shrinking surface with viscous dissipation and slip conditions effects are explored in this chapter. Therefore, the conclusions that have been drawn are

- The skin friction coefficient upsurges with the rising values of dust particles mass concentration, viscous dissipation, mixed convection parameter, thermal slip parameter, alumina and copper nanoparticles volume fractions, but a reverse trend is noticed for slip parameters and velocity slip parameter. Thus, the presence of dust particles, viscous dissipation, mixed convection parameter, thermal slip parameter, alumina and copper nanoparticles volume fractions results in an increase of frictional force, thereby rising the drag force within the boundary layer.

- The decrease of the local Nusselt number values are observed with an elevation in dust particles mass concentrations, viscous dissipation, thermal slip parameters, alumina and copper nanoparticle volume fractions, while other parameters which include, mixed convection parameter, slip parameters, and velocity slip parameter exhibits an increase.

- The thickness of the boundary layer in the temperature profile diminishes in first solution of the fluid and dust phases as the dust particles mass concentration, mixed convection parameter, slip parameters, velocity and thermal slip parameters and copper nanoparticle volume fraction indicating an increment in heat transmission rate. Conversely, the analysis of viscous dissipation and alumina nanoparticle volume fraction reveals a contrary trend.

- The occurrence of the dual solutions is observed within the range of $s_c < s < 2.5$, and $\lambda_c < \lambda < -0.1$ for the parameters under consideration, whereas unique solutions are identified when $s > 2.5$, and $\lambda > -0.1$. The range of dual solutions were widened with augmentation of dust particle mass concentration, mixed convection parameter, slip parameters, velocity slip parameter, and copper nanoparticle volume fraction.

CHAPTER 7
CONCLUSION AND RECOMMENDATIONS

7.1 Conclusion

In this study, mathematical models were developed to investigate and analyse the behavior of the boundary layer flow and heat transfer over various stretching or shrinking surface by employing the Tiwari and Das model for the three problems, where the first problem concerns the flow and heat transfer over a permeable horizontal stretching or shrinking surface, the second discusses the flow and heat transfer over a permeable inclined stretching or shrinking surface, and the last problem involves the flow and heat transfer over a vertical permeable stretching or shrinking surface. The dusty hybrid nanofluid is developed by scattering copper and alumina nanoparticles along with dust particles into water. The influence of dust particle mass concentration, viscous dissipation, suction, stretching or shrinking, mixed convection, velocity and thermal slip, and the nanoparticles volume fraction were studied. However, the mixed convection parameter is not considered in the first problem since it involves a horizontal surface. Further, the mathematical models of the aforementioned problems were transformed into boundary layer equations employing the boundary layer approximation and subsequently reduced to ordinary differential equations through similarity transformation. The first objective of formulating the mathematical models for the problems considered has been achieved through the formulation of the mathematical models.

The reduced ordinary differential equations were then solved by utilising the bvp4c function in MATLAB to generate numerical results. The initial guesses are refined iteratively until the boundary conditions for the velocity and temperature profiles are satisfied, then the values of f'' and $-\theta'$ are substituted into the formula of the skin friction coefficient and local Nusselt number. Subsequently, graphs of skin friction coefficient and local Nusselt number are generated utilizing the MATLAB plot function. Therefore, the second objective, which is focused on solving the mathematical models using the bvp4c function in MATLAB is achieved. Next, the third objective, which aims to analyse the effects of various pertinent parameters on the skin friction coefficient and local Nusselt number, as well as the velocity and temperature profiles for all the problems, is achieved. Additionally, to verify the reliability and validity of the employed method, a comparison analysis was made with several researchers, and it shows a good agreement.

Based on the analysis, the increase in dust particle mass concentration, alumina, and copper nanoparticles volume fraction increases the skin friction coefficient in all surface orientations. The heat transfer rate reduces across all surface orientations as the dust particle mass concentration increases. This leads to the enhancement of energy storage which then increases the fluid temperature and reduces the heat transfer efficiency (Alarabi et al., 2024) On the other hand, for alumina and copper nanoparticles volume fraction, the heat transfer rate increases on horizontal surfaces but decreases on inclined and vertical surfaces. This contradictory trend arises due to the interaction of buoyancy and viscous effects associated with surface orientation. For the horizontal surface, the buoyancy effect is minimal; thus, the enhancement in thermal conductivity due to the increase in nanoparticle volume fraction dominates, which enhances the heat transfer. However, for inclined and vertical surfaces, the rate of heat transfer is observed to decrease, which is because of the influence of buoyancy, which reduces the velocity of fluid and the temperature gradient as more forces are required for the fluid to flow at the surface.

Next, the increase in viscous dissipation (represented by the Eckert number) does not affect the skin friction coefficient of the horizontal and inclined surfaces, but a minimal increase is observed on the vertical surface. This is because the fluid flow along the vertical surface is driven by buoyancy, leading to a steeper velocity gradient near the surface, which in turn increases the skin friction coefficient. As for the horizontal and inclined surfaces, the buoyant force is insignificant, thus it does not significantly affect the skin friction coefficient. The rate of heat transfer diminishes with the increase in viscous dissipation for all surface orientations, as the increase in viscous dissipation results in greater conversion of kinetic energy into thermal energy within the fluid. This process elevates the fluid temperature higher than the surface temperature, resulting in a reduced heat transfer rate. Therefore, although viscous dissipation enhances thermal energy in fluid flow, the skin friction coefficient is affected only when the surface is vertical, indicating that viscous dissipation is surface-dependent and varies with flow direction.

The velocity slip parameter lowers the skin friction coefficient and enhances the rate of heat transfer across all surface orientations. Further, the increase in thermal slip does not affect the skin friction coefficient across the horizontal and inclined surfaces but increases on the vertical surface. This is because the thermal slip has an insignificant effect on the skin friction coefficient, as it only affects the thermal boundary conditions; however, with the presence of buoyancy in the vertical surface, the skin friction coefficient is affected. The heat transfer rate lowers with the increase in thermal slip over all surface orientations. This indicates that accounting for thermal slip results in less the transmission of heat between the surface and the fluid (Kejela et al., 2021).

Therefore, based on the overall analysis, it can be concluded that the consideration of viscous dissipation decreases the heat transfer rate, while velocity and thermal slip, increases and decreases the heat transfer rate, respectively. Next, according to the surface orientations, horizontal surface exhibits the highest heat transfer rate, followed by inclined and vertical surfaces, and lastly, copper nanoparticle is seen to be more effective compared to alumina nanoparticle.

7.2 Suggestions for future research

The current study suggests several promising directions for future research, such as:

- Performed the stability analysis to determine the physically stable solution between the dual solutions.
- Inclusion of other physical effects such as magnetic field and radiation effect to broaden the applicability of the model.
- Considers different nanoparticle combination for hybrid nanofluid such as copper and magnetite, copper and magnesium oxide, copper and iron (iii) oxide.
- Extension to non-Newtonian fluid such as ferrofluid, Williamson fluid, Eyring-Powell fluid, and others.

- Examine various types of surfaces, including curved surfaces, rotating disks, circular cylinders, and others to analyse their effects on flow and heat transfer.
- Consider a time-dependent stretching or shrinking surface.

REFERENCES

Abbas, K., Xinhua, W., Rasool, G., Sun, T., Razzaq, I. (2024). Thermal optimization of buoyancy driven radiative engine-oil based viscous hybrid nanofluid flow observing the micro-rotations in an inclined permeable enclosure. *Case Studies in Thermal Engineering*, 60, 104774.

Abbas, Z., Rahim, T., Hasnain, J., Abid, N., Shah, Z. M. (2023). Entropy generation analysis of multi-mass diffusion in a nanofluid-interfaced three-phase viscous fluid in an inclined channel. *Case Studies in Thermal Engineering*, 49, 103368.

Afridi, M. I., Qasim, M., Khan, I., Shafie, S., Alshomrani, A. S. (2017). Entropy generation in magnetohydrodynamic mixed convection flow over an inclined stretching sheet. *Entropy* , 19(1).

Aiyashi, M. A., Abo-Dahab, S. M., Albalwi, M. D. (2023). Effect of viscous dissipation and induced magnetic field on an unsteady mixed convective stagnation point flow of a nonhomogenous nanofluid. *Scientific Reports*, 13(1), 1–14.

Ajeeb, W., Thieleke da Silva, R. R. S., Murshed, S. M. S. (2023). Experimental investigation of heat transfer performance of Al_2O_3 nanofluids in a compact plate heat exchanger. *Applied Thermal Engineering*, 218, 119321.

Akram, J., Akbar, N. S., Tripathi, D. (2021). A theoretical investigation on the heat transfer ability of water-based hybrid (Ag–Au) nanofluids and Ag nanofluids flow driven by electroosmotic pumping through a microchannel. *Arabian Journal for Science and Engineering*, 46(3), 2911–2927.

Alabdulhadi, S., Waini, I., Ahmed, S. E., Ishak, A. (2021). Hybrid nanofluid flow and heat transfer past an inclined surface. *Mathematics*, 9(24).

Alarabi, T., Mahdy, A., Alzahrani, S., Abo-Zaid, O. A. (2024). Dusty non-Newtonian nanofluid flow along a stretching curved sheet via chemically reactive and heat source/sink imapct: Two-phase model. *Partial Differential Equations in Applied Mathematics*, 9, 100646.

Alharbi, A. F., Alhawiti, M., Usman, M., Ullah, I., Alam, M. M., Bilal, M. (2024). Enhancement of heat transfer in thin-film flow of a hybrid nanofluid over an inclined rotating disk subject to thermal radiation and viscous dissipation. *International Journal of Heat and Fluid Flow*, 107, 109360.

Ali, F., Zaib, A., Faizan, M., Zafar, S., Alkarni, S., Shah, N. A., Chung, J. D. (2024). Heat and mass exchanger analysis for Ree-Eyring hybrid nanofluid through a stretching sheet utilizing the homotopy perturbation method. *Case Studies in Thermal Engineering*, 54, 104014.

Ali, B., Jubair, S., Duraihem, F. Z. (2023). Numerical analysis of viscous dissipative unsteady darcy forchhemier hybrid nanofluid flow subject to magnetic effect across a stretching cylinder. *Materials Today Communications*, 36, 106532.

Al-Sawalha, M. M., Zidan, A. M., Jan, W. U., Saeed, A. M., Shafee, A., Jebran, S. (2025). Investigation of Alumina-Cu/$C_2H_6O_2$+H_2O flows for improved heat transfer through efficient thermal deposition and internal heat generation. *Boundary Value Problems*, 2025(1).

Alzu'bi, O. a. S., Qabaah, A. S., Faqih, F. M. A., Yaseen, N., Shawaqfeh, S. a. M., Swalmeh, M. Z. (2024). Newtonian heating on Casson mixed convection transport by ternary hybrid nanofluids over vertical stretching sheet: Numerical Study. *Journal of Advanced Research in Fluid Mechanics and Thermal Sciences*, 115(1), 166–180.

Amani, M., Amani, P., Bahiraei, M., Ghalambaz, M., Ahmadi, G., Wang, L. P., Wongwises, S., Mahian, O. (2021). Latest developments in nanofluid flow and heat transfer between parallel surfaces: A critical review. *Advances in Colloid and Interface Science*, 294, 102450.

Anuar, N. S., Bachok, N., Pop, I. (2018). A stability analysis of solutions in boundary layer flow and heat transfer of carbon nanotubes over a moving plate with slip effect. *Energies*, 11(12).

Anuar, N. S., Bachok, N., Pop, I. (2021a). Influence of buoyancy force on Ag-MgO/water hybrid nanofluid flow in an inclined permeable stretching/shrinking sheet. *International Communications in Heat and Mass Transfer*, 123, 105236.

Anuar, N. S., Bachok, N., Pop, I. (2021b). Numerical computation of dusty hybrid nanofluid flow and heat transfer over a deformable sheet with slip effect. *Mathematics*, 9(6).

Arpaci, V. S., Larsen, P. S. (1984). *Convection heat transfer* (Vol. 90). Prentice-Hall Englewood Cliffs, NJ.

Arshad, M., Alharbi, F. M., Hassan, A., Haider, Q., Alhushaybari, A., Eldin, S. M., Ahmad, Z., Al-Essa, L. A., Galal, A. M. (2023). Effect of inclined magnetic field on radiative heat and mass transfer in chemically reactive hybrid nanofluid flow due to dual stretching. *Scientific Reports*, 13(1), 7828.

Asghar, A., Govindarajoo, M. V., Ara, H., Zaimi, K., Ying, T. Y. (2025). Effect of water-based Alumina-copper MHD hybrid nanofluid on a Power-law form stretching/shrinking sheet with joule heating and slip condition : Dual Solutions Study. *CFD Letters*, 17(4), 119–135.

Ashraf, M., Abbas, A., Oztop, H. F., Nisar, K. S., Khan, I. (2021). Computations of mixed convection slip flow around the surface of a sphere: Effects of thermophoretic transportation and viscous dissipation. *Heat Transfer*, 50(7), 7349–7362.

Azman, A., Yusoff, M. Z., Mukhtar, A., Gunnasegaran, P., Hamid, N. A., Ching, N. K. (2021). Numerical study of heat transfer enhancement for mono and hybrid nanofluids flow in a straight pipe. *CFD Letters*, 13(2), 49–61.

Awan, A. U., Niazai, S., Hussain, M., Ali, B., Ahammad, N. A., Gamaoun, F., Nadeem, S. (2025). Optimizing entropy generation in MHD Maxwell dusty nanofluid flow via nanoparticle radius and inter-particle spacing on an inclined stretching sheet. *Scientific Reports*, 15(1), 38931.

Benaissa, M., Rafiq, M., Shahzad, H., Zayani, H. M., Khedher, N. B. (2025). Boundary layer formation over a stretchable cylinder in a viscoelastic fluid with partial slip and viscous dissipation effects. *Case Studies in Thermal Engineering*, 74, 106894.

Bhattacharyya, K., Mukhopadhyay, S., Layek, G. (2011). Steady boundary layer slip flow and heat transfer over a flat porous plate embedded in a porous media. *Journal of Petroleum Science and Engineering*, 78(2), 304–309.

Cheng, L., Nawaz, M., Kaneez, H., Alaoui, M. K., Selmi, A., Li, C., Assilzadeh, H. (2021). Flow and heat transfer analysis of elastoviscoplastic generalized non-Newtonian fluid with hybrid nano structures and dust particles. *International Communications in Heat and Mass Transfer*, 126, 105275.

Choi, S. U. S. (1995). Enhancing thermal conductivity of fluids with nanoparticles. *American Society of Mechanical Engineers, Fluids Engineering Division (Publication) FED*, 231, 99–105.

Chu, Y., Alzahrani, F., Mopuri, O., Ganteda, C., Khan, M., Lakshmi, P. J., Khan, S. U., Eldin, S. M. (2023). Thermal impact of hybrid nanofluid due to inclined oscillatory porous surface with thermo-diffusion features. *Case Studies in Thermal Engineering*, 42, 102695.

Crane, L. J. (1970). Flow past a stretching plate. *Zeitschrift für angewandte Mathematik und Physik ZAMP*, 21, 645-647.

Desale, S., Pradhan, V. H. (2015). Numerical solution of boundary layer flow equation with viscous dissipation effect along a flat plate with variable temperature. *Procedia Engineering*, 127, 846–853.

Deswita, L., Nazar, R., Ishak, A., Ahmad, R., Pop, I. (2010). Similarity solutions for mixed convection boundary layer flow over a permeable horizontal flat plate.

Applied Mathematics and Computation, 217(6), 2619–2630.

Dey, D., Chutia, B. (2022). Dusty nanofluid flow with bioconvection past a vertical stretching surface. *Journal of King Saud University - Engineering Sciences, 34* (6), 375–380.

Divya, A., Alasiri, A., Jawad, M., Garalleh, H. A. (2025). Mixed convection and heat transfer in williamson fluid bounded by nonlinear curved surface with heat sink/source. *Case Studies in Thermal Engineering*, 73, 106673.

Dzulkifli, N. F., Bachok, N., Yacob, N. A., Pop, I., Arifin, N., Rosali, H. (2022). Stability solution of unsteady stagnation-point flow and heat transfer over a stretching/shrinking sheet in nanofluid with slip velocity effect. *CFD Letters*, 14(1), 66–86.

El-Zahar, E. R., Rashad, A. M., Seddek, L. F. (2020). Impacts of viscous dissipation and brownian motion on Jeffrey nanofluid flow over an unsteady stretching surface with thermophoresis. *Symmetry*, 12(9), 1–12.

Elboughdiri, N., Nazir, U., Sohail, M., Mousa, A. A. A. (2024). Combine thermal performance based on dust particles and Hall and ion slip currents including tetra-hybrid nanoparticles on Howarth's wavy pipe. *Results in Engineering*, 23, 102666.

Farooq, Umer, Afridi, M. I., Qasim, M., Lu, D. C. (2018). Transpiration and viscous dissipation effects on entropy generation in hybrid nanofluid flow over a nonlinear radially stretching disk. *Entropy*, 20(9).

Farooq, Umar, Waqas, H., Imran, M., Albakri, A., Muhammad, T. (2022). Numerical investigation for melting heat transport of nanofluids due to stretching surface with Cattaneo-Christov thermal model. *Alexandria Engineering Journal* 61(9), 6635–6644.

Gireesha, Bijjanal Jayanna, Ramesh, G. K., Lokesh, H. J., Bagewadi, C. S. (2011). Boundary layer flow and heat transfer of a dusty fluid over a stretching vertical surface. *Applied Mathematics*, 02(04), 475–481.

Gireesha, B. J., Chamkha, A. J., Rudraswamy, N. G., Krishnamurthy, M. R. (2014). MHD flow and heat transfer of a nanofluid embedded with dust particles over a stretching sheet. *Journal of Nanofluids*, 4(1), 66–72.

Gireesha, B. J., Mahanthesh, B., Manjunatha, P. T., Gorla, R. S. R. (2015). Numerical solution for hydromagnetic boundary layer flow and heat transfer past a stretching surface embedded in non-Darcy porous medium with fluid-particle suspension. *Journal of the Nigerian Mathematical Society*, 34(3), 267–285.

Gosty, V., Srinivas, G., Suresh Babu, B. (2024). Numerical investigation of slip effects on heat and mass transfer in a vertical channel with immiscible micropolar and viscous fluids of variable viscosity. *Heat Transfer*, 58.

Gul, T., Nasir, S., Berrouk, A. S., Raizah, Z., Alghamdi, W., Ali, I., Bariq, A. (2023). Simulation of the water-based hybrid nanofluids flow through a porous cavity for the applications of the heat transfer. *Scientific Reports*, 13(1), 1–12.

Gumber, P., Yaseen, M., Rawat, S. K., Kumar, M. (2022). Heat transfer in micropolar hybrid nanofluid flow past a vertical plate in the presence of thermal radiation and suction/injection effects. *Partial Differential Equations in Applied Mathematics*, 5, 100240.

Habib, N. A. N. N., Arifin, N. S., Zokri, S. M., Kasim, A. R. M. (2024). MHD flow of dusty jeffrey fluid flow containing carbon nano tubes (CNTs) under influences of viscous dissipation and newtonian heating. *Malaysian Journal of Mathematical Sciences*, 18(2), 445–468.

Hamid, R. A., Nazar, R., Naganthran, K., Pop, I. (2022). Dusty ferrofluid transport phenomena towards a non-isothermal moving surface with viscous dissipation. *Chinese Journal of Physics*, 75, 139–151.

Hansen, A. G. (1964). Similarity analyses of boundary value problems in engineering. Prentice-Hall.

Hayat, T., Qasim, M., Mesloub, S. (2010). MHD flow and heat transfer over permeable stretching sheet with slip conditions. *International Journal for Numerical Methods in Fluids*, 66(8), 963–975.

He, J., Elazem, N. Y. A. (2021). Insights into partial slips and temperature jumps of a nanofluid flow over a stretched or shrinking surface. *Energies*, 14(20), 6691.

Hussain, S. M., Sharma, R., Chamkha, A. J. (2022). Numerical and statistical explorations on the dynamics of water conveying Cu-Al_2O_3 hybrid nanofluid flow over an exponentially stretchable sheet with Navier's partial slip and thermal jump conditions. *Chinese Journal of Physics*, 75, 120–138.

Ibrahim, W., Shanker, B. (2013). MHD boundary layer flow and heat transfer of a nanofluid past a permeable stretching sheet with velocity, thermal, and solutal slip boundary conditions. *Computers Fluids*, 75, 1-10.

Islam, M. R., Nasrin, S. (2020). Dusty fluid flow past between two parallel riga plates embedded in a porous medium. The International. *Journal of Advances in Applied Mathematics and Mechanics*, 8(2), 1–14.

Ismail, N. S., Mohd Shaipullah, N., Azhar, S. A., Md Arifin, N., Ramli, N., Mohamed Isa, S. S. P. (2025). Influence of MHD flow on shrinking sheet with partial slip and heat generation at stagnation point. *Journal of Advanced Research in Numerical Heat Transfer*, 28(1), 43–54.

Izady, M., Dinarvand, S., Pop, I., Chamkha, A. J. (2021). Flow of aqueous Fe_2O_3 hybrid nanofluid over a permeable stretching/shrinking wedge: A development on Falkner–Skan problem. *Chinese Journal of Physics*, 74, 406–420.

Jalili, B., Emad, M., Jalili, P., Domiri Ganji, D., Saleem, S., Tag-eldin, E. M. (2023). Thermal analysis of boundary layer nanofluid flow over the movable plate with internal heat generation, radiation, and viscous dissipation. *Case Studies in Thermal Engineering*, 49, 103203.

Jamrus, F. N., Waini, I., Khan, U., Ishak, A. (2024). Effects of magnetohydrodynamics and velocity slip on mixed convective flow of thermally stratified ternary hybrid nanofluid over a stretching/shrinking sheet. *Case Studies in Thermal Engineering*, 55.

Jawad, M., Ali, A. B., Abdelfattah, W., Bognár, G. (2025). Numerical modelling of heat transfer and flow efficiency in the stretching process and extrusion of Jeffrey fluid in a heated cylinder. *International Journal of Thermofluids*, 29, 101395.

Jeelani, M. B., Abbas, A. (2025). Energy transport in MHD Maxwell hybrid nanofluid flow over inclined stretching porous sheet with effects of chemical reaction, solar radiation and porous medium. *Case Studies in Thermal Engineering* , 68, 105915.

Jia, D. E. (2020). Heat and mass transfer. *Essentials of Fluidization Technology*, 291–331.

Kakar, N., Khalid, A., Al-Johani, A. S., Alshammari, N., Khan, I. (2022). Melting heat transfer of a magnetized water-based hybrid nanofluid flow past over a stretching/shrinking wedge. *Case Studies in Thermal Engineering*, 30.

Kalpana, G., Saleem, S. (2022). Heat transfer of Magnetohydrodynamic stratified dusty fluid flow through an inclined irregular porous channel. *Nanomaterials*, 12(19), 3309.

Kasmani, R. M., Sivasankaran, S., Bhuvaneswari, M., Hussein, A. K. (2017). Analytical and numerical study on convection of nanofluid past a moving wedge with soret and dufour effects. *International Journal of Numerical Methods for Heat and Fluid Flow*, 27(10), 2333–2354.

Kays, W. M., Crawford, M. E., Weigand, B. (1980). *Convective heat and mass transfer* (Vol. 4). New York: McGraw-Hill.

Kejela, S. B., Daba, M., Girum, A. (2021). Investigation of effects of thermal radiation, magnetic field, Eckert number, and thermal slip on MHD hiemenz flow by optimal homotopy asymptotic method. *Journal of Mathematics*.

Khan, D., Kumam, P., Sitthithakerngkiet, K. (2024). Convective heat and mass transfer in inclined parallel plates with fractional model: Dusty hybrid nanofluid. *Engineering Reports*, 1–24.

Khan, D., Kumam, P., Kumam, W., Suttiarporn, P., Rehman, A. (2023). Relative magnetic field and slipping effect on Casson dusty fluid of two phase fluctuating flow over inclined parallel plate. *South African Journal of Chemical Engineering*, 44, 135–146.

Khan, S. A., Waqas, H., Muhammad, T., Farooq, U., Alghamdi, M. (2021). Recent progress in melting phenomenon for magnetized hybrid nanofluid flow over a stretching surface with temperature dependent viscosity: a comparative study. *Journal of Materials Research and Technology*, 15, 3965–3973.

Khashi'ie, N. S., Hafidzuddin, E. H., Arifin, N. M., Wahi, N. (2020). Stagnation point flow of hybrid nanofluid over a permeable vertical stretching/shrinking cylinder with thermal stratification effect. *CFD Letters, 12* (2), 80–94.

Kho, Y. B., Jusoh, R., Salleh, M. Z., Mohamed, M. K. A., Ismail, Z., Hamid, R. A. (2021). Inclusion of viscous dissipation on the boundary layer flow of Cu-TiO_2 hybrid nanofluid over stretching/shrinking sheet. *Journal of Advanced Research in Fluid Mechanics and Thermal Sciences*, 88(2), 64–79.

Kumar, T. S. (2021). Hybrid nanofluid slip flow and heat transfer over a stretching surface. *Partial Differential Equations in Applied Mathematics*, 4, 0–7.

Kumar, S., Choudhary, S., Kumari, K., Sharma, A., Choudhary, P. (2025). MHD darcy-forchheimer flow of SWCNT-H_2O nanofluid over a porous stretching sheet. *International Journal of Thermofluids*, 26, 101064.

Lanjwani, H. B., Chandio, M. S., Malik, K., Shaikh, M. M. (2022). Stability analysis of boundary layer flow and heat transfer of Fe_2O_3 and Fe-water base nanofluid over a stretching/shrinking sheet with radiation effect. *Engineering, Technology Applied Science Research*, 12–12(1), 8114–8122.

Low, E., Mansur, S., Choy, Y. Y., Low, E. (2022). Flow and heat transfer of MHD dusty nanofluid toward moving plate with convective boundary condition. *Journal of Advanced Research in Fluid Mechanics and Thermal Sciences*, 89(2), 43–55.

Mabood, F., Pochai, N., Shateyi, S. (2016). Stagnation point flow of nanofluid over a moving plate with convective boundary condition and magnetohydrodynamics. *Journal of Engineering (United Kingdom)*.

Mabood, F., Akinshilo, A. T. (2021). Stability analysis and heat transfer of hybrid Cu-Al_2O_3/H_2O nanofluids transport over a stretching surface. *International Communications in Heat and Mass Transfer*, 123.

Mallikarjuna, H. B., Nirmala, T., Punith Gowda, R. J., Manghat, R., Varun Kumar, R. S. (2021). Two-dimensional Darcy–Forchheimer flow of a dusty hybrid nanofluid over a stretching sheet with viscous dissipation. *Heat Transfer* 50(4), 3934–3947.

Manjunatha, P., Gowda, R. P., Kumar, R. N., S, S., Sarwe, D. U. (2021). Numerical simulation of carbon nanotubes nanofluid flow over vertically moving disk with rotation. *Partial Differential Equations in Applied Mathematics*, 4, 100124.

Mebarek-Oudina, F., Chabani, I. (2022). Review on nano-fluids applications and heat transfer enhancement techniques in different enclosures. *Journal of Nanofluids*, 11(2), 155–168.

Mishra, S., Swain, K., Dalai, R. (2022). Heat and mass transfer of water-based copper and alumina hybrid nanofluid over a stretching sheet. *Heat Transfer*, 52(2), 1198–1214.

Mishra, A., Kumar, M. (2020). Velocity and thermal slip effects on MHD nanofluid flow past a stretching cylinder with viscous dissipation and Joule heating. *SN Applied Sciences*, 2(8), 1–13.

Nabwey, H. A., Mahdy, A. (2021). Transient flow of micropolar dusty hybrid nanofluid loaded with Fe_3O_4-Ag nanoparticles through a porous stretching sheet. *Results in Physics*, 21.

Najib, N., Bachok, N., Dzulkifli, N. F., Pop, I. (2022). Numerical results on slip effect over an exponentially stretching/shrinking cylinder. *Mathematics*, 10(7), 1114.

Nakayama, A. (1995). PC-aided numerical heat transfer and convective flow. *CRC press*.

Naramgari, S., Sulochana, C. (2016). MHD flow of dusty nanofluid over a stretching surface with volume fraction of dust particles. *Ain Shams Engineering Journal*, 7(2), 709–716.

Nayan, A., Fauzan, N. I. F. A., Ilias, M. R., Zakaria, S. F., Aznam, N. H. Z. (2022). Aligned Magnetohydrodynamics (MHD) flow of hybrid nanofluid over a vertical plate through porous medium. *Journal of Advanced Research in Fluid Mechanics and Thermal Sciences, 92* (1), 51–64.

Noorzehan, F. M. S., Anati, A., Syahira, M., Radiah, M., Nurul, A. J. (2018). Boundary layer of a dusty fluid flow over a stretching sheet. *International Journal of Engineering Technology*, 7(4.30), 462–464.

Palmur, S., Chandarki, I., Venkateswarlu, B. (2025). Stagnation point flow of Cu-Al_2O_3/H_2O hybrid nano-fluid with MHD convection over an anti-logarithmically stretching/shrinking sheet under velocity and thermal slips. *Discover Mechanical Engineering*, 4(1).

Pandey, A. K., Kumar, M. (2016). Effect of viscous dissipation and suction/injection on MHD nanofluid flow over a wedge with porous medium and slip. *Alexandria Engineering Journal*, 55(4), 3115–3123.

Pohlhausen, K. (1921). Zur näherungsweisen Integration der Differentialgleichung der Grenzschicht. *Zeitschrift für Angewandte Mathematik und Mechanik*,1(4), 252–268.

Punith Gowda, R. J., Naveen Kumar, R., Prasannakumara, B. C. (2021). Two-phase darcy-forchheimer flow of dusty hybrid nanofluid with viscous dissipation over a cylinder. *International Journal of Applied and Computational Mathematics* 7(3), 1–18.

Radhika, M., Punith Gowda, R. J., Naveenkumar, R., Siddabasappa, Prasannakumara, B. C. (2021). Heat transfer in dusty fluid with suspended hybrid nanoparticles over a melting surface. *Heat Transfer*, 50(3), 2150–2167.

Rafique, K., Mahmood, Z., Adnan, Khan, U., Muhammad, T., Mir, A., Aich, W., Kolsi, L. (2024). Unsteady MHD flow analysis of hybrid nanofluid over a shrinking surface with porous media and heat generation: Computational study on entropy generation and Bejan number. *International Journal of Heat and Fluid Flow* , 107, 109419.

Rafique, K., Alotaibi, H. (2021). Numerical simulation of Williamson nanofluid flow over an inclined surface: Keller box analysis. *Applied Sciences*, 11(23), 11523.

Rai, P., Mishra, U. (2022). Numerical simulation of boundary layer flow over a moving plate in the presence of magnetic field and slip condition. *Journal of Advanced Research in Fluid Mechanics and Thermal Sciences* , 95(2), 120–136.

Ramzan, M., Nisa, Z. U., Shafique, A., Nazar, M. (2022). Slip and thermo diffusion effects on the flow over an inclined plate. *Journal of Advanced Research in Fluid Mechanics and Thermal Sciences*, 94(2), 13–28.

Rana, M. D. A., Siddique, S., Raza, A., Naseem, M. (2025). Numerical method for solving the heat transfer in MHD nanofluid over stretching/shrinking surfaces. *Journal of New Horizons in Mathematics*, 1(2), 59–80.

Rashid, U., Liang, H., Ahmad, H., Abbas, M., Iqbal, A., Hamed, Y. (2021). Study of (Ag and TiO_2/water nanoparticles shape effect on heat transfer and hybrid nanofluid flow toward stretching shrinking horizontal cylinder. *Results in Physics*, 21, 103812.

Rossi di Schio, E., Impiombato, A. N., Mokhefi, A., Biserni, C. (2022). Theoretical and numerical study on buongiorno's model with a couette flow of a nanofluid in a channel with an embedded cavity. *Applied Sciences (Switzerland)*, 12(15).

Roy, N. C., Hossain, A., Pop, I. (2022). Flow and heat transfer of MHD dusty hybrid nanofluids over a shrinking sheet. *Chinese Journal of Physics*, 77, 1342–1356.

Roy, N. C., Pop, I. (2021). Dual solutions of magnetohydrodynamic mixed convection flow of an Oldroyd-B nanofluid over a shrinking sheet with heat source/sink. *Alexandria Engineering Journal*, 61(8), 5939–5948.

Saffman, P. G. (1961). On the boundary condition for stream function solutions of the Navier-Stokes equations. *Journal of Fluid Mechanics*, 11(1), 16-30.

Saidur, R., Leong, K. Y., Mohammed, H. A. (2011). A review on applications and challenges of nanofluids. *Renewable and sustainable energy reviews*, 15(3), 1646–1668.

Salameh, T., Alkasrawi, M., Olabi, A. G., Makky, A. Al, Abdelkareem, M. A. (2023). Experimental and numerical analysis of heat transfer enhancement inside concentric counter flow tube heat exchanger using different nanofluids. *International Journal of Thermofluids*, 20, 100432.

Schlichting, H. (1979). Boundary Layer Theory. McGraw-Hill, New York.

Schlichting, H., Gersten, K. (2017). Boundary Layer Theory (9th ed.). Berlin, Germany. *Springer* .

Shah, Z., Asghar, A., Ying, T. Y., Lund, L. A., Alshehri, A., Vrinceanu, N. (2024). Numerical investigation of sodium alginate-alumina/copper radiative hybrid nanofluid flow over a power law stretching/shrinking sheet with suction effect: A study of dual solutions. *Results in Engineering*, 21, 101881.

Shampine, L., Kierzenka, J., Reichelt, M. (2000). Solving boundary value problems for ordinary differential equations in MATLAB with bvp4c. *Tutorial Notes, 75275*, 1–27.

Sobale, S., Tawade, J. V., Ali, A. B., Khidhir, D. M., Norberdiyeva, M., Al-Harbi, F., Satpute, N., Khedher, N. B. (2025). Modeling heat and mass transfer in Williamson nanofluid stagnation flow: Influence of porosity, chemical reaction, and internal heating. *Chemical Engineering Journal Advances*, 25, 100995.

Sohut, F. H., Khan, U., Ishak, A., Soid, S. K., Waini, I. (2023). Mixed convection hybrid nanofluid flow induced by an inclined cylinder with lorentz forces. *Micromachines*, 14(5), 982.

Sudarmozhi, K., Alqahtani, A. A., Niazai, S., Khan, I. (2025). Impact of suction and blowing on radiative heat transfer of maxwell fluid with homogenous heterogenous reactions. *Journal of Radiation Research and Applied Sciences*, 18(2), 101330.

Sudarsana Reddy, P., Chamkha, A. J. (2018). Heat and mass transfer characteristics of nanofluid over horizontal circular cylinder. *Ain Shams Engineering Journal,* , 9(4), 707–716.

Tani, I. (1977). History of Boundary Layer Theory. *Annual Review of Fluid Mechanics*, 9(1), 87–111.

Tripathy, P. K., Samantara, T., Kanungo, S. (2024). Radiation effect on convective boundary layer dusty flow over a stretching surface. *AIP Advances*, 14(3).

Uddin, M. S., Bhattacharyya, K. (2017). Thermal boundary layer in stagnation-point flow past a permeable shrinking sheet with variable surface temperature. *Propulsion and Power Research*, 6(3), 186–194.

Uddin, M. N., Ali, Md. Y. (2024). Similarity solution of unsteady convective MHD flow of viscous incompressible fluid over an inclined porous surface with ohmic heating and viscous dissipation. *In Journal of Applied Science and Engineering*, 28(4), 795–809.

Wahid, N. S., Arifin, N. M., Khashi'ie, N. S., Pop, I. (2020). Hybrid nanofluid slip flow over an exponentially stretching/shrinking permeable sheet with heat generation. *Mathematics* , 9(1), 30.

Waini, I., Alabdulhady, S., Ishak, A., Pop, I. (2023). Viscous dissipation effects on hybrid nanofluid flow over a non-linearly shrinking sheet with power-law velocity. *Heliyon*, 9(10), e20910.

Waini, I., Ishak, A., Pop, I. (2021). Magnetohydrodynamic flow past a shrinking vertical sheet in a dusty hybrid nanofluid with thermal radiation. *Applied Mathematics and Mechanics*, 43(1), 127–140.

Waini, I., Ishak, A., Pop, I. (2020). Mixed convection flow over an exponentially stretching/shrinking vertical surface in a hybrid nanofluid. *Alexandria Engineering Journal*, 59(3), 1881–1891.

Wang, C. Y. (2002). Flow due to a stretching boundary with partial slip - an exact solution of the Navier-Stokes equations. *Chemical Engineering Science*, 57(17), 3745–3747.

Waqas, H., Raza Shah Naqvi, S. M., Alqarni, M. S., Muhammad, T. (2021). Thermal transport in magnetized flow of hybrid nanofluids over a vertical stretching cylinder. *Case Studies in Thermal Engineering*, 27.

Wong, K. V., De Leon, O. (2010). Applications of nanofluids: current and future. *Advances in Mechanical Engineering*.

Yacob, N. A., Dzulkifli, N. F., Salleh, S. N. A., Ishak, A., Pop, I. (2021). Rotating flow in a nanofluid with CNT nanoparticles over a stretching/shrinking Surface. *Mathematics*, 10(1), 7.

Yahaya, R. I., Mustafa, M. S., Md Arifin, N., Pop, I., Md Ali, F., Mohamed Isa, S. S. P. (2023). Hybrid nanofluid flow past a biaxial stretching/shrinking permeable surface with radiation effect: Stability analysis and heat transfer optimization. *Chinese Journal of Physics*, 85, 402–420.

Yan, L., Dero, S., Khan, I., Mari, I. A., Baleanu, D., Nisar, K. S., Sherif, E. S. M., Abdo, H. S. (2020). Dual solutions and stability analysis of magnetized hybrid nanofluid with joule heating and multiple slip conditions. *Processes*, 8(3).

Yashkun, U., Zaimi, K., Bakar, N. A. A., Ferdows, M. (2020). Nanofluid stagnation-point flow using Tiwari and Das model over a stretching/shrinking sheet with suction and slip effects.*Journal of Advanced Research in Fluid*

Mechanics and Thermal Sciences, 70(1), 62–76.

Yusuf, A., Khan, S. U., Hassan, M., Bhatti, M. M., Öztop, H. F. (2025). Heat transfer optimization of MWCNT-Al_2O_3 hybrid nanofluids under convective and irreversible effects. *Journal of Umm Al-Qura University for Applied Sciences*.

Zeeshan, A., Yousif, M. A., Khan, M. I., Latif, M. A., Ali, S. S., Mohammed, P. O. (2025). Non-similar analysis of boundary layer flow and heat transfer in non-Newtonian hybrid nanofluid over a cylinder with viscous dissipation effects. *Energies*, 18(7), 1660.

Zeeshan, Khan, I., Eldin, S. M., Islam, S., Khan, M. U. (2023). Two-dimensional nanofluid flow impinging on a porous stretching sheet with nonlinear thermal radiation and slip effect at the boundary enclosing energy perspective. *Scientific Reports*, 13(1), 1–14.

Zhang, X., Zhang, Y. (2021). Experimental study on enhanced heat transfer and flow performance of magnetic nanofluids under alternating magnetic field. *International Journal of Thermal Sciences*, 164, 106897.

Zhu, A., Ali, H., Ishaq, M., Junaid, M. S., Raza, J., Amjad, M. (2022). Numerical study of heat and mass transfer for Williamson nanofluid over stretching/shrinking sheet along with brownian and thermophoresis effects. *Energies*, 15(16), 5926.

Zukri, N. Z. M., Ilias, M. R., Ishak, S. S., Osman, R., Makhatar, N. a. M., Rahman, M. N. A. (2023). Magnetohydrodynamic effect in mixed convection Casson hybrid nanofluids flow and heat transfer over a moving vertical plate. *CFD Letters* , 15(7), 92–111.

APPENDICES

APPENDIX A
THE SIMILARITY TRANSFORMATION FOR BOUNDARY LAYER FLOW PROBLEM (CHAPTER 5)

A.1 SIMILARITY TRANSFORMATION

The outline of the mathematical formulation is presented in Section 5.2, while the comprehensive formulation is elaborated in this section. The governing equations (5.2.1) and (3.2.22) presented in Chapters 5 and 3 are the momentum and energy equations, respectively, for the hybrid nanofluid phase. The governing equations are subsequently transformed into ordinary differential equations relevant to the problem considered, utilising similarity transformation.

A.1.1 Momentum equation

i. Hybrid nanofluid phase

$$u\frac{\partial u}{\partial x}+v\frac{\partial u}{\partial y}=\frac{\mu_{hnf}}{\rho_{hnf}}\frac{\partial^2 u}{\partial y^2}+\frac{KN}{\rho_{hnf}}(u_p-u)+g\beta^*\left(T-T_\infty\right)cos\alpha,$$

$$u\frac{\partial u}{\partial x}=a^2xf'^2, \tag{A.1}$$

$$v\frac{\partial u}{\partial y}=-a^2xff'', \tag{A.2}$$

$$\frac{\mu_{hnf}}{\rho_{hnf}}\frac{\partial^2 u}{\partial y^2}=\frac{\mu_{hnf}}{\rho_{hnf}}\frac{a^2xf'''}{\nu_f,} \tag{A.3}$$

$$u_p-u=ax\left(f_p'-f'\right), \tag{A.4}$$

$$\frac{KN}{\rho_{hnf}}\left(u_p-u\right)=\frac{KN}{\rho_{hnf}}\left[ax\left(f_p'-f'\right)\right], \tag{A.5}$$

$$g\beta^*\left(T-T_\infty\right)cos\alpha=g\beta^*\theta bx^2cos\alpha. \tag{A.6}$$

Substitute equations (A1)-(A.6) into momentum equation (5.2.1)

$$a^2xf'^2 + \left(-a^2xff''\right) = \frac{\mu_{hnf}}{\rho_{hnf}}\frac{a^2xf'''}{\nu_f} + \frac{KN}{\rho_{hnf}}\left[ax\left(f_p' - f'\right)\right] + g\beta^*\theta bx^2cos\alpha. \quad \text{(A.7)}$$

Multiply both sides with $\left(\dfrac{1}{a^2x}\right)$

$$\frac{\mu_{hnf}}{\rho_{hnf}}\frac{f'''}{\nu_f} + \frac{KN}{\rho_{hnf}}\left(\frac{1}{a}\right)\left(f_p' - f'\right) - f'^2 + ff'' + \frac{g\beta^*\theta bxcos\alpha}{a^2} = 0, \quad \text{(A.8)}$$

$$\frac{\mu_{hnf}}{\rho_{hnf}}\frac{\rho_f}{\mu_f}f''' + ff'' - f'^2 + \frac{\left(\dfrac{m}{\tau_v}\right)N}{\rho_{hnf}}\left(\frac{1}{a}\right)\left(f_p' - f'\right) + \frac{g\left(nx^{-1}\right)\theta bxcos\alpha}{a^2} = 0, \quad \text{(A.9)}$$

where $K = \left(\dfrac{m}{\tau_v}\right)$ and $\beta^* = nx^{-1}$

$$\frac{\mu_{hnf}}{\rho_{hnf}}\frac{\rho_f}{\mu_f}f''' + ff'' - f'^2 + \frac{Nm\left(\dfrac{1}{a\tau_v}\right)}{\rho_{hnf}}\left(f_p' - f'\right) + \lambda^*\theta cos\alpha = 0, \quad \text{(A.10)}$$

where $\lambda^* = \dfrac{gnb}{a^2}$. Then, multiply with $\dfrac{\rho_f}{\rho_f}$

$$\frac{\mu_{hnf}}{\rho_{hnf}}\frac{\rho_f}{\mu_f}f''' + ff'' - f'^2 + \frac{\dfrac{Nm}{\rho_f}\left(\dfrac{1}{a\tau_v}\right)}{\rho_{hnf}/\rho_f}\left(f_p' - f'\right) + \lambda^*\theta cos\alpha = 0, \quad \text{(A.11)}$$

$$\frac{\mu_{hnf}/\mu_f}{\rho_{hnf}/\rho_f}f''' + ff'' - f'^2 + \frac{L\beta_v}{\rho_{hnf}/\rho_f}\left(f_p' - f'\right) + \lambda^*\theta cos\alpha = 0, \quad \text{(A.12)}$$

where, $L = \dfrac{Nm}{\rho_f}$ and $\beta_v = \dfrac{1}{a\tau_v}$.

Then, substitute the value of physical properties of nanofluid and hybrid nanofluid of $\mu_{hnf} = \dfrac{\mu_f}{(1-\phi_1)^{2.5}(1-\phi_2)^{2.5}}$ and $\rho_{hnf} = (1-\phi_2)\left[(1-\phi_1)\rho_f + \phi_1\rho_1\right] + \phi_2\rho_2$ from

Table (3.1) into equation (A.12)

$$\frac{1}{(1-\phi_1)^{2.5}(1-\phi_2)^{3.5}\left[\left[(1-\phi_1)+\phi_1\dfrac{\rho_1}{\rho_f}\right]+\phi_2\dfrac{\rho_2}{\rho_f}\right]}f'''+ff''-f'^2$$
$$+\frac{L\beta_v}{(1-\phi_2)\left[\left[(1-\phi_1)+\phi_1\dfrac{\rho_1}{\rho_f}\right]+\phi_2\dfrac{\rho_2}{\rho_f}\right]}\left(f'_p-f'\right)+\lambda^*\theta cos\alpha=0. \tag{A.13}$$

A.1.2 Energy equation

i. Hybrid nanofluid phase

$$u\frac{\partial T}{\partial x}+v\frac{\partial T}{\partial y}=\frac{k_{hnf}}{(\rho C_p)_{hnf}}\left(\frac{\partial^2 T}{\partial y^2}\right)+\frac{NC_{pf}}{(\rho C_p)_{hnf}\tau_T}(T_p-T)+\frac{N}{(\rho C_p)_{hnf}\tau_v}$$
$$(u_p-u)^2+\frac{\mu_{hnf}}{(\rho C_p)_{hnf}}\left(\frac{\partial u}{\partial y}\right)^2, \tag{A.14}$$

where

$$\theta=\frac{T-T_\infty}{T_w-T_\infty},\theta_p=\frac{T_p-T_\infty}{T_w-T_\infty},$$

$$T_w=T_\infty+bx^2, \tag{A.15}$$

$$T=\theta bx^2+T_\infty, \tag{A.16}$$

$$\frac{\partial T}{\partial x}=2bx\theta, \tag{A.17}$$

$$u\frac{\partial T}{\partial x}=2abx^2f'\theta, \tag{A.18}$$

$$\frac{\partial T}{\partial y}=bx^2\left(\frac{a}{\nu_f}\right)^{\frac{1}{2}}\theta', \tag{A.19}$$

$$v\frac{\partial T}{\partial y}=-abx^2f\theta', \tag{A.20}$$

$$\frac{\partial^2 T}{\partial y^2} = bx^2\left(\frac{a}{\nu_f}\right)\theta'', \tag{A.21}$$

$$(T_p - T) = bx^2\left(\theta_p - \theta\right), \tag{A.22}$$

$$(u_p - u)^2 = \left[ax\left(f_p' - f'\right)\right]^2. \tag{A.23}$$

Find $\frac{k_{hnf}}{(\rho C_p)_{hnf}}\frac{\partial^2 T}{\partial y^2}, \frac{NC_{pf}}{(\rho C_p)_{hnf}\tau_T}(T_p - T), \frac{N}{(\rho C_p)_{hnf}\tau_v}(u_p - u)^2, \frac{\mu_{hnf}}{(\rho C_p)_{hnf}}\left(\frac{\partial u}{\partial y}\right)^2,$

$$\frac{k_{hnf}}{(\rho C_p)_{hnf}}\frac{\partial^2 T}{\partial y^2} = \frac{k_{hnf}}{(\rho C_p)_{hnf}}bx^2\left(\frac{a}{\nu_f}\right)\theta'', \tag{A.24}$$

$$\frac{NC_{pf}}{(\rho C_p)_{hnf}\tau_T}(T_p - T) = \frac{NC_{pf}}{(\rho C_p)_{hnf}\tau_T}bx^2\left(\theta_p - \theta\right), \tag{A.25}$$

$$\frac{N}{(\rho C_p)_{hnf}\tau_v}(u_p - u)^2 = \frac{N}{(\rho C_p)_{hnf}\tau_v}\left[ax\left(f_p' - f'\right)\right]^2, \tag{A.26}$$

$$\frac{\mu_{hnf}}{(\rho C_p)_{hnf}}\left(\frac{\partial u}{\partial y}\right)^2 = \frac{\mu_{hnf}}{(\rho C_p)_{hnf}}a^2x^2f''^2\left(\frac{a}{\nu_f}\right). \tag{A.27}$$

Substitute equations (A.18), (A20), (A24)-(A.27) into energy equation (3.2.22)

$$\begin{aligned}2abx^2f'\theta - abx^2f\theta' &= \frac{k_{hnf}}{(\rho C_p)_{hnf}}bx^2\left(\frac{a}{\nu_f}\right)\theta'' \\ &+ \frac{NC_{pf}}{(\rho C_p)_{hnf}\tau_T}bx^2\left(\theta_p - \theta\right) + \frac{N}{(\rho C_p)_{hnf}\tau_v}\left[ax\left(f_p' - f'\right)\right]^2 \\ &+ \frac{\mu_{hnf}}{(\rho C_p)_{hnf}}a^2x^2f''^2\left(\frac{a}{\nu_f}\right),\end{aligned} \tag{A.28}$$

$$\begin{aligned}&\frac{k_{hnf}}{(\rho C_p)_{hnf}}bx^2\left(\frac{a}{\nu_f}\right)\theta'' + abx^2f\theta' - 2abx^2f'\theta \\ &+ \frac{NC_{pf}}{(\rho C_p)_{hnf}\tau_T}bx^2\left(\theta_p - \theta\right) + \frac{N}{(\rho C_p)_{hnf}\tau_v}(ax)^2\left(f_p' - f'\right)^2 \\ &+ \frac{\mu_{hnf}}{(\rho C_p)_{hnf}}a^2x^2f''^2\left(\frac{a}{\nu_f}\right) = 0.\end{aligned} \tag{A.29}$$

Multiply with $\left(\frac{1}{a}\right)\left(\frac{1}{bx^2}\right)$

$$\frac{k_{hnf}}{(\rho C_p)_{hnf}}\left(\frac{1}{\nu_f}\right)\theta''+f\theta'-2f'\theta+\frac{NC_{pf}}{(\rho C_p)_{hnf}}\frac{1}{a\tau_T}(\theta_p-\theta)$$
$$+\frac{N}{(\rho C_p)_{hnf}}\frac{1}{a\tau_v}\frac{(ax)^2}{bx^2}\left(f_p'-f'\right)^2+\frac{\mu_{hnf}}{(\rho C_p)_{hnf}}\frac{(ax)^2}{bx^2}\left(\frac{1}{\nu_f}\right)f''^2=0, \tag{A.30}$$

$$\frac{k_{hnf}}{(\rho C_p)_{hnf}}\left[\frac{(\rho C_p)_f}{k_f \mathrm{Pr}}\right]\theta''+f\theta'-2f'\theta+\frac{NC_{pf}\beta_T}{(\rho C_p)_{hnf}}(\theta_p-\theta)$$
$$+\frac{N\beta_v}{(\rho C_p)_{hnf}}\frac{(ax)^2}{bx^2}\left(f_p'-f'\right)^2+\frac{\mu_{hnf}}{(\rho C_p)_{hnf}}\left(\frac{\rho_f}{\mu_f}\right)\frac{(ax)^2}{bx^2}f''^2=0, \tag{A.31}$$

where $\beta_T=\frac{1}{a\tau_T},\beta_v=\frac{1}{a\tau_v},\mathrm{Pr}=\frac{(\mu C_p)_f}{k_f}$

$$\frac{k_{hnf}/k_f}{(\rho C_p)_{hnf}/(\rho C_p)_f}\left(\frac{1}{\mathrm{Pr}}\right)\theta''+f\theta'-2f'\theta+\frac{NC_{pf}\beta_T}{(\rho C_p)_{hnf}}(\theta_p-\theta)$$
$$+\frac{N\beta_v}{(\rho C_p)_{hnf}}\frac{(ax)^2}{bx^2}\left(f_p'-f'\right)^2+\frac{\mu_{hnf}/\mu_f}{(\rho C_p)_{hnf}/\rho_f}\left(\frac{\rho_f}{\mu_f}\right)\frac{(ax)^2}{bx^2}f''^2=0, \tag{A.32}$$

$$\frac{k_{hnf}/k_f}{(\rho C_p)_{hnf}/(\rho C_p)_f}\left(\frac{1}{\mathrm{Pr}}\right)\theta''+f\theta'-2f'\theta+\frac{L\beta_T}{m(\rho C_p)_{hnf}/(\rho C_p)_f}(\theta_p-\theta)$$
$$+\frac{L\beta_v\mathrm{Ec}}{m(\rho C_p)_{hnf}/(\rho C_p)_f}\left(f_p'-f'\right)^2+\frac{\mu_{hnf}/\mu_f}{(\rho C_p)_{hnf}/\rho_f}\mathrm{Ec}f''^2=0, \tag{A.33}$$

where, $\mathrm{Ec}=\frac{U_w^2}{(C_p)_f(T_w-T_\infty)}=\frac{(ax)^2}{(C_p)_f bx^2}=\frac{a^2}{(C_p)_f b}$.

Then, substitute the value of physical properties of nanofluid and hybrid nanofluid of $\frac{k_{hnf}}{k_{nf}}=\frac{k_2+2k_{nf}-2\phi_2(k_{nf}-k_2)}{k_2+2k_{nf}+\phi_2(k_{nf}-k_2)}$, $\frac{k_{nf}}{k_f}=\frac{k_1+2k_f-2\phi_1(k_f-k_1)}{k_1+2k_f+\phi_1(k_f-k_1)}$,
$\mu_{hnf}=\frac{\mu_f}{(1-\phi_1)^{2.5}(1-\phi_2)^{2.5}}$, and $(\rho C_p)_{hnf}=(1-\phi_2)\left[(1-\phi_1)(\rho C_p)_f+\phi_1(\rho C_p)_1\right]$
$+\phi_2(\rho C_p)_2$ from Table (3.1) into equation (A.33)

$$\frac{\left[\dfrac{k_2+2k_{nf}-2\phi_2(k_{nf}-k_2)}{k_2+2k_{nf}+\phi_2(k_{nf}-k_2)}\right]\left[\dfrac{k_1+2k_f-2\phi_1(k_f-k_1)}{k_1+2k_f+\phi_1(k_f-k_1)}\right]}{(1-\phi_2)\left[(1-\phi_1)+\phi_1\dfrac{(\rho C_p)_1}{(\rho C_p)_f}\right]+\phi_2\dfrac{(\rho C_p)_2}{(\rho C_p)_f}}\left(\frac{1}{\mathrm{Pr}}\right)\theta''+f\theta'-2f'\theta$$

$$+\frac{L\beta_T}{m(1-\phi_2)\left[(1-\phi_1)+\phi_1\dfrac{(\rho C_p)_1}{(\rho C_p)_f}\right]+\phi_2\dfrac{(\rho C_p)_2}{(\rho C_p)_f}}(\theta_p-\theta)$$

$$+\frac{L\beta_v\mathrm{Ec}}{m(1-\phi_2)\left[(1-\phi_1)+\phi_1\dfrac{(\rho C_p)_1}{(\rho C_p)_f}\right]+\phi_2\dfrac{(\rho C_p)_2}{(\rho C_p)_f}}\left(f_p'-f'\right)^2$$

$$+\frac{1}{(1-\phi_1)^{2.5}(1-\phi_2)^{3.5}\left[(1-\phi_1)+\phi_1\dfrac{(\rho C_p)_1}{(\rho C_p)_f}\right]+\phi_2\dfrac{(\rho C_p)_2}{(\rho C_p)_f}}\mathrm{Ec}f''^2=0. \quad \text{(A.34)}$$

CHAPTER B
THE SIMILARITY TRANSFORMATION FOR BOUNDARY LAYER FLOW PROBLEM (CHAPTER 6

B.1 SIMILARITY TRANSFORMATION

Section 6.2 outlines the mathematical formulation employed, whereas this section provides a detailed formulation of the outline. Similarity transformations are utilised to reduce the governing equation (6.2.1) in Chapter 6, expressing the momentum equation of the hybrid nanofluid phase to ordinary differential equations.

B.1.1 Momentum Equation

i. Hybrid nanofluid phase

$$u\frac{\partial u}{\partial x}+v\frac{\partial u}{\partial y}=\frac{\mu_{hnf}}{\rho_{hnf}}\frac{\partial^2 u}{\partial y^2}+\frac{KN}{\rho_{hnf}}(u_p-u)+g\beta^*(T-T_\infty),$$

$$u\frac{\partial u}{\partial x}=a^2xf'^2, \tag{B.1}$$

$$v\frac{\partial u}{\partial y}=-a^2xff'', \tag{B.2}$$

$$\frac{\mu_{hnf}}{\rho_{hnf}}\frac{\partial^2 u}{\partial y^2}=\frac{\mu_{hnf}}{\rho_{hnf}}\frac{a^2xf'''}{\nu_f}, \tag{B.3}$$

$$u_p-u=ax\left(f_p'-f'\right) \tag{B.4}$$

$$\frac{KN}{\rho_{hnf}}(u_p-u)=\frac{KN}{\rho_{hnf}}\left[ax\left(f_p'-f'\right)\right], \tag{B.5}$$

$$g\beta^*(T-T_\infty)=g\beta^*\theta bx^2. \tag{B.6}$$

Substitute equation (B.1)-(B.6) into momentum equation (6.2.1)

$$a^2xf'^2+\left(-a^2xff''\right)=\frac{\mu_{hnf}}{\rho_{hnf}}\frac{a^2xf'''}{\nu_f}+\frac{KN}{\rho_{hnf}}\left[ax\left(f_p'-f'\right)\right]+g\beta^*\theta bx^2. \tag{B.7}$$

Multiply both sides with $\left(\dfrac{1}{a^2x}\right)$

$$\frac{\mu_{hnf}}{\rho_{hnf}}\frac{f'''}{\nu_f}+\frac{KN}{\rho_{hnf}}\left(\frac{1}{a}\right)\left(f_p'-f'\right)-f'^2+ff''+\frac{g\beta^*\theta bx}{a^2}=0, \tag{B.8}$$

$$\frac{\mu_{hnf}}{\rho_{hnf}}\frac{\rho_f}{\mu_f}f'''+ff''-f'^2+\frac{\left(\dfrac{m}{\tau_v}\right)N}{\rho_{hnf}}\left(\frac{1}{a}\right)\left(f_p'-f'\right)+\frac{g\left(nx^{-1}\right)\theta bx}{a^2}=0, \tag{B.9}$$

where, $K=\left(\dfrac{m}{\tau_v}\right)$ and $\beta^*=nx^{-1}$

$$\frac{\mu_{hnf}}{\rho_{hnf}}\frac{\rho_f}{\mu_f}f'''+ff''-f'^2+\frac{Nm\left(\dfrac{1}{a\tau_v}\right)}{\rho_{hnf}}\left(f_p'-f'\right)+\lambda^*\theta=0, \tag{B.10}$$

where $\lambda^*=\dfrac{gnb}{a^2}$. Then, multiply with $\dfrac{\rho_f}{\rho_f}$

$$\frac{\mu_{hnf}}{\rho_{hnf}}\frac{\rho_f}{\mu_f}f'''+ff''-f'^2+\frac{\dfrac{Nm}{\rho_f}\left(\dfrac{1}{a\tau_v}\right)}{\rho_{hnf}/\rho_f}\left(f_p'-f'\right)+\lambda^*\theta=0, \tag{B.11}$$

$$\frac{\mu_{hnf}/\mu_f}{\rho_{hnf}/\rho_f}f'''+ff''-f'^2+\frac{L\beta_v}{\rho_{hnf}/\rho_f}\left(f_p'-f'\right)+\lambda^*\theta=0, \tag{B.12}$$

where, $L=\dfrac{Nm}{\rho_f}$ and $\beta_v=\dfrac{1}{a\tau_v}$.

Then, substitute the value of physical properties of nanofluid and hybrid nanofluid of

$\mu_{hnf}=\dfrac{\mu_f}{(1-\phi_1)^{2.5}(1-\phi_2)^{2.5}}$ and $\rho_{hnf}=(1-\phi_2)\left[(1-\phi_1)\rho_f+\phi_1\rho_1\right]+\phi_2\rho_2$

from Table (3.1) into equation (B.12)

$$\begin{aligned}&\frac{1}{(1-\phi_1)^{2.5}(1-\phi_2)^{3.5}\left[(1-\phi_1)+\phi_1\dfrac{\rho_1}{\rho_f}\right]+\phi_2\dfrac{\rho_2}{\rho_f}}f'''+ff''-f'^2\\&+\frac{L\beta_v}{(1-\phi_2)\left[(1-\phi_1)+\phi_1\dfrac{\rho_1}{\rho_f}\right]+\phi_2\dfrac{\rho_2}{\rho_f}}\left(f_p'-f'\right)+\lambda^*\theta=0.\end{aligned} \tag{B.13}$$

CHAPTER C
MATLAB PROGRAM FOR PROBLEM CONSIDERED IN CHAPTER 4

```
function Dhia_Problem2_DiffEcwithS

format long g

%Define all parameters
global phi1 phi2 Pr lambda sigma1 sigma2 L Bv BT m Eckert s epsilon A1 A2 A3 A4 A5

%Boundary layer thickness & stepsize
etaMin = 0;
etaMax1 = 10; %blt 1st solution
etaMax2 = 10; %blt 2nd solution
stepsize1 = etaMax1;
stepsize2= etaMax2;

%Input for the parameters

phi1 = 0.01; %nanoparticle volume fraction
phi2 = 0.01;
Pr = 6.2;  %Prandtl number %Pr=6.2 water
lambda = -1.0; %stretching/shrinking parameter
L = 1.0; %mass concentration
Bv = 0.5; %fluid partcle interaction (velocity)
BT = 0.5; %fluid particle interaction (temperature)
m = 1.0; %mass concentration fixed to 1
Eckert = 0.5; % Eckert number
epsilon = 1.0; %ratio specific heat
s = 1.52026; %suction
sigma1 = 0.2;
sigma2 = 0.2;


rho_f = 997.1; k_f = 0.6130; C_f = 4179; %base fluid (water)
rho_1 = 3970; k_1 = 40; C_1 = 765;  %Al2O3
rho_2 = 8933; k_2 = 400; C_2 = 385; %Cu

A1 = 1/[((1-phi1)^(2.5))*((1-phi2)^(2.5))];
A2 = (1-phi2)*[(1-phi1)+phi1*(rho_1/rho_f)]+(phi2*(rho_2/rho_f));
A3 = (1-phi2)*[(1-
phi1)+phi1*((rho_1*C_1)/(rho_f*C_f))]+(phi2*((rho_2*C_2)/(rho_f*C_f)));
A4 = (k_1+2*k_f-2*phi1*(k_f-k_1))/(k_1+2*k_f+phi1*(k_f-k_1));
A5 = [(k_2+(2*A4*k_f)-2*phi2*(A4*k_f-k_2))/(k_2+(2*A4*k_f)+phi2*(A4*k_f-k_2))]*A4;


%%%%%%%%%%%%%%%%%%%%%%%%   first solution   %%%%%%%%%%%%%%%%%%%%%%%%%%%%%%%%%%%%%

    options = bvpset('stats','off','RelTol',1e-10);
    solinit = bvpinit (linspace (etaMin, etaMax1, stepsize1), @OdeInit1);
    sol = bvp4c (@OdeBVP, @OdeBC, solinit, options);
    eta = linspace (etaMin, etaMax1, stepsize1);
    y = deval (sol, eta);

    figure(1)
    plot(sol.x,sol.y(2,:),'r')
    xlabel('\eta')
    ylabel('f`(\eta)')
```

```
    hold on

    figure(2)
    plot(sol.x,sol.y(5,:),'b')
    xlabel('\eta')
    ylabel('F`(\eta)')
    hold on

    figure(3)
    plot(sol.x,sol.y(6,:),'g')
    xlabel('\eta')
    ylabel('t(\eta)')
    hold on

    figure(4)
    plot(sol.x,sol.y(8,:),'k')
    xlabel('\eta')
    ylabel('tp(\eta)')
    hold on

    %Saving the output in txt file for first solution
    descris = [sol.x; sol.y];
    save 'upper_HN.txt' descris -ascii

    %Displaying the output for first solution
    fprintf('\nFirst solution:\n');
    fprintf('A1 = %7.9f\n',A1);
    fprintf('A5 = %7.9f\n',A5);
    fprintf('f"(0) = %7.9f\n',y(3));
    fprintf('F`(0) = %7.9f\n',y(5));
    fprintf('-t`(0) = %7.9f\n',-y(7));
    fprintf('tp(0) = %7.9f\n',y(8));
    fprintf('\n');

%%%%%%%%%%%%%%%%%%%%%%%%   second solution   %%%%%%%%%%%%%%%%%%%%%%%%%%%%%%%%%%%

    options = bvpset('stats','off','RelTol',1e-10);
    solinit = bvpinit (linspace (etaMin, etaMax2, stepsize2), @OdeInit2);
    sol = bvp4c (@OdeBVP, @OdeBC, solinit, options);
    eta = linspace (etaMin, etaMax2, stepsize2);
    y = deval (sol, eta);

    figure(1)
    plot(sol.x,sol.y(2,:),'--r')
    xlabel('\eta')
    ylabel('f`(\eta)')
    hold on

    figure(2)
    plot(sol.x,sol.y(5,:),'--b')
    xlabel('\eta')
    ylabel('F`(\eta)')
    hold on

    figure(3)
```

```
    plot(sol.x,sol.y(6,:),'--r')
    xlabel('\eta')
    ylabel('t(\eta)')
    hold on

    figure(4)
    plot(sol.x,sol.y(8,:),'--b')
    xlabel('\eta')
    ylabel('tp(\eta)')
    hold on

    %Saving the output in txt file for second solution
    descris = [sol.x; sol.y];
    save 'lower_HN.txt' descris -ascii

    %Displaying the output for second solution
    fprintf('\nSecond solution:\n');
    fprintf('f"(0) = %7.9f\n',y(3));
    fprintf('F`(0) = %7.9f\n',y(5));
    fprintf('-t`(0)= %7.9f\n',-y(7));
    fprintf('tp(0) = %7.9f\n',y(8));
    fprintf('\n');

%%%%%%%%%%%%%%%%%%%%%%%%%%%%%%%%%%%%%%%%%%%%%%%%%%%%%%%%%%%%%%%%%%%%%%%%%%%%

%Define the ODE function
function ff = OdeBVP (x, y, Pr, L, Bv, BT, m, Eckert, epsilon, A1, A2, A3, A5)

global Pr L Bv BT m Eckert epsilon A1 A2 A3 A5

 ff = [y(2)
       y(3)
      (A2/A1)*(-y(1)*y(3)+((y(2))^2)-((L*Bv)/A2)*(y(5)-y(2)))
       y(5)
       (1/y(4))*((y(5))^2-Bv*(y(2)-y(5)))
       y(7)
       ((Pr*A3)/A5)*(-y(1)*y(7)+2*y(2)*y(6)-((L*BT)/(m*A3))*(y(8)-y(6)) ...
       -((L*Bv*Eckert)/(m*A3))*((y(5)-y(2))^2)-((A1/A3)*(Eckert*(y(3)^2))))
       (1/y(4))*(2*y(5)*y(8)-epsilon*BT*(y(6)-y(8)))];

%Define the boundary condition
function res = OdeBC (ya, yb, lambda, s, sigma1, sigma2)

global lambda s sigma1 sigma2
res = [ ya(1)-s
        ya(2)-lambda-sigma1*ya(3)
        ya(6)-1-sigma2*ya(7)
        yb(2)
        yb(5)
        yb(4)-yb(1)
        yb(6)
        yb(8)];

%Setting the initial guess for first solution
function v = OdeInit1 (x, lambda)
```

```
global lambda
%1
%     v = [0.2   %0.98 0.2 1.8 1.2
%          0
%          0
%          0
%          0
%          0
%          0
%          3.21];   %3.21

%2
%v = [1.112+exp(-x) % lower branch 0.0112 1.112
%       exp(-x)   %-
%       exp(-x)
%       exp(-x)
%       exp(-x)
%       exp(-x)
%       exp(-x)
%       exp(-x)];

%3
%v = [1.112+exp(-x)*exp(-x)
%        exp(-x)
%        exp(-x)
%        0.01+exp(-x)
%        exp(-x)
%        exp(-x)
%        exp(-x)
%        0.01+exp(-x)];

%4
%v = [-1.1167/exp(-x)-exp(-x)
%        exp(-x)
%       exp(-x)
%        0.15+exp(-x)
%        exp(-x)
%        exp(-x)
%        exp(-x)
%        0.15+exp(-x)];

%5
%v = [1.1124+exp(-x) % lower branch 0.0112 1.112
%       exp(-x)   %-
%      exp(-x)
%       exp(-x)
%       exp(-x)
%       exp(-x)
%       exp(-x)
%       exp(-x)];
```

```
%Setting the initial guess for second solution
function v1 = OdeInit2 (x, lambda)

global lambda

%1
v1 = [4.912/exp(-x) % lower branch 1.12 1.2 0.912 0.7912
       exp(-x)   %-
       exp(-x)
       exp(-x)
       exp(-x)
       exp(-x)
       exp(-x)
       exp(-x)];

%2
%v1 = [3.5*exp(-x) %contoh coding senang dapat
%         exp(-x)
%         exp(-x)
%         exp(-x)
%         exp(-x)
%         0.15-exp(-x)
%         exp(-x)
%         0.15-exp(-x)];

%3
%v1 = [3.5*exp(-x)  %lambda 3-2.6 (1.0)
%        exp(-x)
%        exp(-x)
%        exp(-x)
%        exp(-x)
%        0.72-exp(-x)
%        exp(-x)
%        0.72-exp(-x)];
```

CHAPTER D
MATLAB PROGRAM FOR PROBLEM CONSIDERED IN CHAPTER 5

```
function Dhia_Problem3_New2025_DiffLambdavsEc

format long g

%Define all parameters
global phi1 phi2 Pr lambda sigma1 sigma2 L Bv BT m Eckert s epsilon A1 A2 A3 A4 A5 Gr
X

%Boundary layer thickness & stepsize
etaMin = 0;
etaMax1 = 9; %blt 1st solution
etaMax2 = 9; %blt 2nd solution
stepsize1 = etaMax1;
stepsize2= etaMax2;

%Input for the parameters

phi1 = 0.01; %nanoparticle volume fraction
phi2 = 0.01;
Pr = 6.2;  %Prandtl number %Pr=6.2 water
lambda = -1.667; %stretching/shrinking parameter
L = 1.0; %mass concentration
Bv = 0.5; %fluid particle interaction (velocity)
BT = 0.5; %fluid particle interaction (temperature)
m = 1.0; %mass concentration fixed to 1
Eckert = 0.5; % Eckert number
epsilon = 1.0; %ratio specific heat
s = 2.0; %suction
sigma1 = 0.2; %velocity slip parameter
sigma2 = 0.2; %thermal slip parameter
Gr = 0.001; %mixed convection
X = pi/4; %inclination angle in rad

rho_f = 997.1; k_f = 0.6130; C_f = 4179; %base fluid (water)
rho_1 = 3970; k_1 = 40; C_1 = 765;  %Al2O3
rho_2 = 8933; k_2 = 400; C_2 = 385; %Cu

A1 = 1/[((1-phi1)^(2.5))*((1-phi2)^(2.5))];
A2 = (1-phi2)*[(1-phi1)+phi1*(rho_1/rho_f)]+(phi2*(rho_2/rho_f));
A3 = (1-phi2)*[(1-
phi1)+phi1*((rho_1*C_1)/(rho_f*C_f))]+(phi2*((rho_2*C_2)/(rho_f*C_f)));
A4 = (k_1+2*k_f-2*phi1*(k_f-k_1))/(k_1+2*k_f+phi1*(k_f-k_1));
A5 = [(k_2+(2*A4*k_f)-2*phi2*(A4*k_f-k_2))/(k_2+(2*A4*k_f)+phi2*(A4*k_f-k_2))]*A4;


%%%%%%%%%%%%%%%%%%%%%%    first solution    %%%%%%%%%%%%%%%%%%%%%%%%%%%%%%%%%%

    options = bvpset('stats','off','RelTol',1e-10);
    solinit = bvpinit (linspace (etaMin, etaMax1, stepsize1), @OdeInit1);
    sol = bvp4c (@OdeBVP, @OdeBC, solinit, options);
    eta = linspace (etaMin, etaMax1, stepsize1);
    y = deval (sol, eta);

     figure(1)
     plot(sol.x,sol.y(2,:),'r')
```

```
     xlabel('\eta')
     ylabel('f`(\eta)')
     hold on

    figure(2)
    plot(sol.x,sol.y(5,:),'b')
    xlabel('\eta')
    ylabel('F`(\eta)')
    hold on

    figure(3)
     plot(sol.x,sol.y(6,:),'g')
     xlabel('\eta')
     ylabel('t(\eta)')
     hold on

    figure(4)
    plot(sol.x,sol.y(8,:),'k')
    xlabel('\eta')
    ylabel('tp(\eta)')
    hold on

    %Saving the output in txt file for first solution
    descris = [sol.x; sol.y];
    save 'upper_HN.txt' descris -ascii

    %Displaying the output for first solution
    fprintf('\nFirst solution:\n');
    fprintf('A1 = %7.9f\n',A1);
    fprintf('A5 = %7.9f\n',A5);
    fprintf('f"(0) = %7.9f\n',y(3));
    fprintf('F`(0) = %7.9f\n',y(5));
    fprintf('-t`(0) = %7.9f\n',-y(7));
    fprintf('tp(0) = %7.9f\n',y(8));
    fprintf('\n');

%%%%%%%%%%%%%%%%%%%%%%   second solution   %%%%%%%%%%%%%%%%%%%%%%%%%%%%%%%%

    options = bvpset('stats','off','RelTol',1e-10);
    solinit = bvpinit (linspace (etaMin, etaMax2, stepsize2), @OdeInit2);
    sol = bvp4c (@OdeBVP, @OdeBC, solinit, options);
    eta = linspace (etaMin, etaMax2, stepsize2);
    y = deval (sol, eta);

    figure(1)
    plot(sol.x,sol.y(2,:),'--r')
    xlabel('\eta')
    ylabel('f`(\eta)')
    hold on

    figure(2)
    plot(sol.x,sol.y(5,:),'--b')
    xlabel('\eta')
    ylabel('F`(\eta)')
    hold on
```

```
    figure(3)
    plot(sol.x,sol.y(6,:),'--r')
    xlabel('\eta')
    ylabel('t(\eta)')
    hold on

    figure(4)
    plot(sol.x,sol.y(8,:),'--b')
    xlabel('\eta')
    ylabel('tp(\eta)')
    hold on

    %Saving the output in txt file for second solution
    descris = [sol.x; sol.y];
    save 'lower_HN.txt' descris -ascii

    %Displaying the output for second solution
    fprintf('\nSecond solution:\n');
    fprintf('f"(0) = %7.9f\n',y(3));
    fprintf('F`(0) = %7.9f\n',y(5));
    fprintf('-t`(0)= %7.9f\n',-y(7));
    fprintf('tp(0) = %7.9f\n',y(8));
    fprintf('\n');

%%%%%%%%%%%%%%%%%%%%%%%%%%%%%%%%%%%%%%%%%%%%%%%%%%%%%%%%%%%%%%%%%%%%%%%%%%%%

%Define the ODE function
function ff = OdeBVP (x, y, Pr, L, Bv, BT, m, Eckert, epsilon, A1, A2, A3, A5, Gr, X)

global Pr L Bv BT m Eckert epsilon A1 A2 A3 A5 Gr X

 ff = [y(2)
       y(3)
      (A2/A1)*(-y(1)*y(3)+((y(2))^2)-((L*Bv)/A2)*(y(5)-y(2))-(Gr*y(6))*(cos(X)))
       y(5)
       (1/y(4))*((y(5))^2-Bv*(y(2)-y(5)))
       y(7)
       ((Pr*A3)/A5)*(-y(1)*y(7)+2*y(2)*y(6)-((L*BT)/(m*A3))*(y(8)-y(6))-
((L*Bv*Eckert)/(m*A3))*((y(5)-y(2))^2)-((A1/A3)*(Eckert*(y(3)^2))))
       (1/y(4))*(2*y(5)*y(8)-epsilon*BT*(y(6)-y(8)))];


%Define the boundary condition
function res = OdeBC (ya, yb, lambda, s, sigma1, sigma2)

global lambda s sigma1 sigma2
res = [ ya(1)-s
        ya(2)-lambda-sigma1*ya(3)
        ya(6)-1-sigma2*ya(7)
        yb(2)
        yb(5)
        yb(4)-yb(1)
        yb(6)
        yb(8)];
```

```
%Setting the initial guess for first solution
function v = OdeInit1 (x, lambda)

global lambda
%1
%     v = [1.2   %0.98 0.2 1.8 1.2
%          0
%          0
%          0
%          0
%          0
%          0
%          0];   %3.21

%2
%v = [-2.45*exp(-x) % lower branch 0.0112 1.112
%       exp(-x)   %-
%       -exp(-x)
%       exp(-x)
%       exp(-x)
%       exp(-x)
%       -exp(-x)
%       exp(-x)];

%3
%v = [-1.1167/exp(-x)-exp(-x)
%        exp(-x)
%        exp(-x)
%        0.15+exp(-x)
%        exp(-x)
%        exp(-x)
%        exp(-x)
%        0.15+exp(-x)];

%4
% v = [-1.1167/exp(-x)-exp(-x)
%         exp(-x)
%         exp(-x)
%         0.15+exp(-x)
%         exp(-x)
%         exp(-x)
%         exp(-x)
%         0.15+exp(-x)];

%5
%v = [1.1124+exp(-x) % lower branch 0.0112 1.112
%       exp(-x)   %-
%      exp(-x)
%       exp(-x)
%       exp(-x)
%       exp(-x)
%       exp(-x)
%       exp(-x)];
```

```
% %6
v = [1.112+exp(-x)*exp(-x)
        exp(-x)
        exp(-x)
        0.15+exp(-x)
        exp(-x)
        exp(-x)
        exp(-x)
        0.15+exp(-x)];

%7
%v = [-sin(pi*x)
%       exp(-x)
%       exp(-x)
%       exp(-x)
%       exp(-x)
%       exp(-x)
%       exp(-x)
%       exp(-x)];


%Setting the initial guess for second solution
function v1 = OdeInit2 (x, lambda, s)

global lambda s

%1
%v1 = [7.4273/exp(-x) % lower branch 1.12 1.2 0.912 0.7912
%       exp(-x)   %-
%       exp(-x)
%       exp(-x)
%       exp(-x)
%       exp(-x)
%       exp(-x)
%       exp(-x)];

%2
%v1 = [1.12+exp(-x) %contoh coding senang dapat
%         exp(-x)
%         exp(-x)
%         exp(-x)
%         exp(-x)
%         0.5+exp(-x)
%         exp(-x)
%         0.5+exp(-x)];

%3
%v1 = [3.5/exp(-x)  %lambda 3-2.6 (1.0)
%        exp(-x)
%        exp(-x)
%        exp(-x)
%        exp(-x)
%        1.5+exp(-x)
%        exp(-x)
%        1.5+exp(-x)];
```

CHAPTER E
MATLAB PROGRAM FOR PROBLEM CONSIDERED IN CHAPTER 6

```
function Dhia_Problem3NewVD2025_SL

format long g

%Define all parameters
global phi1 phi2 Pr lambda sigma1 sigma2 L Bv BT m Eckert s epsilon A1 A2 A3 A4 A5 Gr

%Boundary layer thickness & stepsize
etaMin = 0;
etaMax1 = 10; %blt 1st solution
etaMax2 = 10; %blt 2nd solution
stepsize1 = etaMax1;
stepsize2= etaMax2;

%Input for the parameters

phi1 = 0.01; %nanoparticle volume fraction
phi2 = 0.01;
Pr = 6.2;  %Prandtl number %Pr=6.2 water
lambda = -1.0; %stretching/shrinking parameter
L = 0; %dust particle mass concentration
Bv = 0.5; %fluid particle interaction (velocity)
BT = 0.5; %fluid particle interaction (temperature)
m = 1.0; %mass concentration fixed to 1
Eckert = 2.0; % Eckert number
epsilon = 1.0; %ratio specific heat
s = 1.8; %suction
sigma1 = 0.2; %velocity slip parameter
sigma2 = 0.2; %thermal slip parameter
Gr = 0.001; %mixed convection

rho_f = 997.1; k_f = 0.6130; C_f = 4179; %base fluid (water)
rho_1 = 3970; k_1 = 40; C_1 = 765;  %Al2O3
rho_2 = 8933; k_2 = 400; C_2 = 385; %Cu

A1 = 1/[((1-phi1)^(2.5))*((1-phi2)^(2.5))];
A2 = (1-phi2)*[(1-phi1)+phi1*(rho_1/rho_f)]+(phi2*(rho_2/rho_f));
A3 = (1-phi2)*[(1-phi1)+phi1*((rho_1*C_1)/(rho_f*C_f))]+(phi2*((rho_2*C_2)/(rho_f*C_f)));
A4 = (k_1+2*k_f-2*phi1*(k_f-k_1))/(k_1+2*k_f+phi1*(k_f-k_1));
A5 = [(k_2+(2*A4*k_f)-2*phi2*(A4*k_f-k_2))/(k_2+(2*A4*k_f)+phi2*(A4*k_f-k_2))]*A4;


%%%%%%%%%%%%%%%%%%%%%%   first solution   %%%%%%%%%%%%%%%%%%%%%%%%%%%%%%%%%%

    options = bvpset('stats','off','RelTol',1e-10);
    solinit = bvpinit (linspace (etaMin, etaMax1, stepsize1), @OdeInit1);
    sol = bvp4c (@OdeBVP, @OdeBC, solinit, options);
    eta = linspace (etaMin, etaMax1, stepsize1);
```

```
 figure(1)
 plot(sol.x,sol.y(2,:),'r')
 xlabel('\eta')
 ylabel('f`(\eta)')
 hold on

figure(2)
plot(sol.x,sol.y(5,:),'b')
xlabel('\eta')
ylabel('F`(\eta)')
hold on

figure(3)
 plot(sol.x,sol.y(6,:),'g')
 xlabel('\eta')
 ylabel('t(\eta)')
 hold on

figure(4)
plot(sol.x,sol.y(8,:),'k')
xlabel('\eta')
ylabel('tp(\eta)')
hold on

%Saving the output in txt file for first solution
descris = [sol.x; sol.y];
save 'upper_HN.txt' descris -ascii

%Displaying the output for first solution
fprintf('\nFirst solution:\n');
fprintf('A1 = %7.9f\n',A1);
fprintf('A5 = %7.9f\n',A5);
fprintf('f"(0) = %7.9f\n',y(3));
fprintf('F`(0) = %7.9f\n',y(5));
fprintf('-t`(0) = %7.9f\n',-y(7));
fprintf('tp(0) = %7.9f\n',y(8));
fprintf('\n');

%%%%%%%%%%%%%%%%%%%%   second solution   %%%%%%%%%%%%%%%%%%%%%%%%%%%%%%%%

options = bvpset('stats','off','RelTol',1e-10);
solinit = bvpinit (linspace (etaMin, etaMax2, stepsize2), @OdeInit2);
sol = bvp4c (@OdeBVP, @OdeBC, solinit, options);
eta = linspace (etaMin, etaMax2, stepsize2);
y = deval (sol, eta);
```

```
    figure(1)
    plot(sol.x,sol.y(2,:),'--r')
    xlabel('\eta')
    ylabel('f`(\eta)')
    hold on

    figure(2)
    plot(sol.x,sol.y(5,:),'--b')
    xlabel('\eta')
    ylabel('F`(\eta)')
    hold on

    figure(3)
    plot(sol.x,sol.y(6,:),'--r')
    xlabel('\eta')
    ylabel('t(\eta)')
    hold on

    figure(4)
    plot(sol.x,sol.y(8,:),'--b')
    xlabel('\eta')
    ylabel('tp(\eta)')
    hold on

    %Saving the output in txt file for second solution
    descris = [sol.x; sol.y];
    save 'lower_HN.txt' descris -ascii

    %Displaying the output for second solution
    fprintf('\nSecond solution:\n');
    fprintf('f"(0) = %7.9f\n',y(3));
    fprintf('F`(0) = %7.9f\n',y(5));
    fprintf('-t`(0)= %7.9f\n',-y(7));
    fprintf('tp(0) = %7.9f\n',y(8));
    fprintf('\n');

%%%%%%%%%%%%%%%%%%%%%%%%%%%%%%%%%%%%%%%%%%%%%%%%%%%%%%%%%%%%%%%%%%%%%%%%%%%

%Define the ODE function
function ff = OdeBVP (x, y, Pr, L, Bv, BT, m, Eckert, epsilon, A1, A2, A3, A5, Gr)

global Pr L Bv BT m Eckert epsilon A1 A2 A3 A5 Gr
```

```
 ff = [y(2)
       y(3)
      (A2/A1)*(-y(1)*y(3)+((y(2))^2)-((L*Bv)/A2)*(y(5)-y(2))-(Gr*y(6)))
       y(5)
       (1/y(4))*((y(5))^2-Bv*(y(2)-y(5)))
       y(7)
       ((Pr*A3)/A5)*(-y(1)*y(7)+2*y(2)*y(6)-((L*BT)/(m*A3))*(y(8)-y(6))- ...
      ((L*Bv*Eckert)/(m*A3))*((y(5)-y(2))^2)-((A1/A3)*(Eckert*(y(3)^2))))
       (1/y(4))*(2*y(5)*y(8)-epsilon*BT*(y(6)-y(8)))];


%Define the boundary condition
function res = OdeBC (ya, yb, lambda, s, sigma1, sigma2)

global lambda s sigma1 sigma2
res = [ ya(1)-s
        ya(2)-lambda-sigma1*ya(3)
        ya(6)-1-sigma2*ya(7)
        yb(2)
        yb(5)
        yb(4)-yb(1)
        yb(6)
        yb(8)];

%Setting the initial guess for first solution
function v = OdeInit1 (x, lambda)

global lambda
%1
%  v = [1.2   %0.98 0.2 1.8 1.2
%          0
%          0
%          0
%          0
%          0
%          0
%          0];   %3.21

%2
%v = [-2.45*exp(-x) % lower branch 0.0112 1.112
%       exp(-x)   %-
%       -exp(-x)
%       exp(-x)
%       exp(-x)
%       exp(-x)
%       -exp(-x)
%       exp(-x)];
```

```
%Setting the initial guess for second solution
function v1 = OdeInit2 (x, lambda, s)

global lambda s

%1
%v1 = [7.4273/exp(-x) % lower branch 1.12 1.2 0.912 0.7912
%       exp(-x)   %-
%       exp(-x)
%       exp(-x)
%       exp(-x)
%       exp(-x)
%       exp(-x)
%       exp(-x)];

%2
%v1 = [1.12+exp(-x) %contoh coding senang dapat
%         exp(-x)
%         exp(-x)
%         exp(-x)
%         exp(-x)
%         0.5+exp(-x)
%         exp(-x)
%         0.5+exp(-x)];

%3
%v1 = [3.5/exp(-x)  %lambda 3-2.6 (1.0)
%        exp(-x)
%        exp(-x)
%        exp(-x)
%        exp(-x)
%        1.5+exp(-x)
%        exp(-x)
%        1.5+exp(-x)];

%4
% v1  = [1.63  % run M=0.1
%         0  %
%         0
%         0
%         0
%         0
%         0
%         0];
```

AUTHOR'S PROFILE

The author, Dhia Azeem binti Khairil Anwar, was born on the 14th of May 1999 in Ipoh, Perak. She began her primary education at Methodist Girls Primary School, Ipoh and then continued to Methodist Girls Secondary School, Ipoh for her secondary education. Upon finishing her secondary education, she pursued a Diploma in Mathematical Sciences at Universiti Teknologi Mara (UiTM) Perak, Kampus Tapah. Upon completing her Diploma, she continued her education by enrolling in the Bachelor of Science (Hons.) Mathematics at UiTM Negeri Sembilan, Kampus Seremban. In 2023, she pursued her Master of Science (Mathematics) at UiTM Pahang, Kampus Jengka.

LIST OF PUBLICATIONS

Anwar, D. A. K., Yacob, N. A., Dzulkifli, N. F., Ilyas, R., Anuar, N. S., Ishak, A., Pop, I. (2025). Flow and heat transfer characteristics of dusty hybrid nanofluid over vertical stretching/shrinking surface with slip conditions. *CFD Letters* , 17(11), 106–122.

Khairil Anwar, D. A., Yacob, N. A., Dzulkifli, N. F., Dasman, A., Ilias, M. R., Anuar, N. S., Ishak, A., Pop, I. (2025). Analysis of dusty hybrid nanofluid flow and heat transfer characteristics over shrinking and stretching sheets: Role of viscous dissipation and slip conditions. *Propulsion and Power Research*, 1–12.